Experimental Investigation of Temperature Effects on Microparticle Sand Rebound Characteristics at Gas Turbine Representative Conditions

Jacob Michael Delimont

Dissertation submitted to the faculty of the Virginia Polytechnic Institute and State University in partial fulfillment of the requirements for the degree of

Doctor of Philosophy
In
Mechanical Engineering

Wing F. Ng
Srinath V. Ekkad
Danesh K. Tafti
Todd Lowe
Gary R. Pickrell

March 26, 2014
Blacksburg, Virginia, USA

Keywords: Sand Ingestion, Coefficient of Restitution, Microparticle Impact, Deposition

Experimental Investigation of Temperature Effects on Microparticle Sand Rebound Characteristics at Gas Turbine Representative Conditions

Jacob Michael Delimont

ABSTRACT

When a gas turbine operates in a particle laden environment, such as a desert, small solid particles are ingested into the engine. The ingested sand particles can cause damage to engine components and reduce the service life of the engine. Particle ingestion causes the erosion of metal blades and vanes, and, if the firing temperature is hot enough, deposition of molten particles in the hot sections of the engine. Both deposition and erosion phenomena can severely reduce overall engine performance. The Coefficient of Restitution (COR) is a measure of the particle-wall interaction, and has been widely used to quantify particle rebound characteristics in past particle impact studies. This work investigates the effects of temperature on sand particle impact characteristics by measuring the COR and other deposition related impact parameters.

The first study presented as part of the dissertation contains a description of a novel method used to measure COR using a Particle Tracking Velocimetry (PTV) method. This is combined with Computational Fluid Dynamics (CFD) flow field to allow for an accurate determination of the particle impact velocity. The methodology described in this paper allows for measurement of the COR in a wide range of test conditions in a relatively simple manner. The COR data for two different sizes of Arizona Road Dust (ARD) and one size of glass beads are presented in this paper. Target material was stainless steel 304 and the impact angle was varied from 25 to 85 degrees.

The second study details the first quantification of the COR of san particles at elevated temperatures. Temperatures used in this study were 533 K, 866 K, and 1073 K. In this study the mass flow rate through the experimental setup was fixed. This meant that velocity and temperature were coupled. Target material for this study was stainless steel 304 and the impact angle was varied from 30° to 80°. The COR was found to decrease substantially at the temperatures and velocity increased. It was determined that the decrease in COR was almost certainly caused by the increase in velocity, and not the decrease in temperature.

The third study contains COR results at elevated temperatures. Significant improvements from the method used to calculate COR in the first paper are described. The particle used for these tests was an ARD sand of 20-40 μm size. Target materials used were stainless steel 304 and Hastelloy X. The particles impinged on the target coupon at a velocity of 28m/s. Tests were performed at three different temperatures, 300 K (ambient), 873 K, and 1073 K to simulate temperatures seen in gas turbine cooling flows. The angle of impingement of the bulk flow sand on the coupon was varied between 30° and 80°. A substantial decrease in COR was discovered at the elevated temperatures of this experiment. Hastelloy X exhibited a much larger decrease in COR than does stainless steel 304. The results were compared to previously published literature.

The final study also used the ARD size of 20-40 μm. The target material was a nickel alloy Hastelloy X. Experiments for this study were performed at a constant velocity of 70m/s. Various temperatures ranging from 1073 K up to and including 1323 K were studied. Particle angle of impact was varied between 30° and 80°. Significant deposition was observed and quantified at the highest two temperatures. The COR of the ARD sand at the highest temperatures was found not to change despite the occurrence of deposition. At elevated temperatures, many of the particles are not molten due to sand's non-homogeneous and crystalline nature. These particles rebound from the target with little if any change in COR.

Preface

This dissertation is written in manuscript format and contains three papers directly related to the PhD dissertation. Although the author is not the first author on the first and second paper included, he was directly involved in all aspects of the experiments described in this paper and wrote parts of the final papers. The remaining two publications of this work the author is the primary author, and was directly involved with all the aspects of the work published. Other details of the work not discussed in the main body of the dissertation can be found in the appendix.

In order to measure COR, a variety of methods have been used. The most prominent works involving COR measurements for gas turbine related particles were performed by Tabakoff [1-3]. These experiments were performed using Laser Doppler Velocimetry (LDV) to measure the particle velocity before impact on the coupon and then again as the particle leaves the coupon. This method has limitations in that the velocity of particles can only be measured at one location at a time, and the complicated setup requiring the intersection of two laser beams makes measurements slow and expensive. Other measurements have been made in past research, such as the work of Sommerfeld *et al.* [4] using high frame rate photography. This method allows for the same particle to be tracked before and after the impact. This has significant advantages in that no calculation is needed to determine COR. The limitation of this method is providing a light source intense enough to illuminate microparticles is difficult. To date, this method has only been used to measure the impact characteristics of particles larger than 100μm. None of the previous literature pertaining to COR measurements for gas turbine relevant particles contain any study of the temperature impact on COR values for sand particles.

The first paper [5] primarily contains a description of a new Particle Tracking Velocimetry (PTV) technique augmented by Computational Fluid Dynamics (CFD) in a unique fashion to remove overcome some of the shortcomings of previous methods. This paper was first published in conference format at the ASME-IGTI Turbo Expo 2012, and was subsequently published in the Journal of Measurement Science and Technology. Stainless steel 304 was used as the target for these ambient temperature test method validation tests. Results from two different sizes of ARD and one type of glass bead are presented in this study and compared to past literature.

The method developed for this project and described in the first paper is an improvement on past methods in several ways. Unlike the LDV method, the current PTV method is relatively simple to set up and allows for measurement of a wide range of particle impacts simultaneously instead of just a point measurement. The size of particles found in gas turbines are generally on the order of 10μm which makes methods that rely on normal photographic light sources unsuitable for studying deposition related particle impacts. The hybrid technique allows for use of lasers to illuminate small microparticles and overcomes many of the short comings of other techniques when applied to the problem of high temperature impact.

Between the time when the first paper presented in this dissertation was published and the completion of the experiments detailed in the third and fourth chapters a paper was published which measured the COR at elevated temperatures in the VT Aerothermal Rig. The paper was originally presented at the ASME IGTI 2013 conference by the author and subsequently published in the Journal of Engineering for Gas Turbines and Power [6]. This paper received a "Best Paper Award" from the Coal, Biomass, and Fuels Committee at the ASME IGTI 2013 conference where it was presented.

While this study was conducted there was no control over the mass flow rate of the test rig. This meant that when the temperature was increased the velocity of the air hitting the target coupon also increased. The particles used in this study were the 20-40μm range of ARD sand particles. The data produced from this study is very interesting in that it is the first time that temperature has been used as a variable of study in the measurement of COR. The conclusions from this paper were that the temperature was responsible for very little of the decrease in COR observed in the results. It was believed that the increases in velocity due to the coupled nature of the velocity and temperature were responsible for the decreases in COR. This conclusion was proven to be partially correct by the data from the second and third papers, in that above the temperature at which the oxide layer form temperature seems to play little if any role.

The third chapter of this dissertation is a paper [7] that has been accepted for publication at ASME-IGTI Turbo Expo 2014 and is being submitted for journal publication as well. The paper describes significant advances made in the method for calculating COR over the previous method used in the first paper. These advances in COR calculation rely on statistical methods that were not used in any previous studies on COR. All past works completed at Virginia Tech as well as those by Tabakoff's group used a mean incoming velocity and angle to calculate the

COR. This neglects the variation in incoming particle velocity. The new method takes into account the variation in the incoming velocity and angle when calculating the COR and gives a more accurate measure of the variation of COR.

The paper describes the effects of particle impact behavior at an impact velocity of 28m/s and at temperatures of ambient (300 K), 873 K, and 1073K. The angle of impact of the particles was measured from 30° to 80°. The target materials used were stainless steel 304 and Hastelloy X. As the temperature of the particles rises above ambient, a thick oxide layer begins to form on the surface of the metal which affects the impact characteristics. This oxide layer leads to a significant drop in COR. This drop is seen in both target metals, but is much more substantial in the Hastelloy X. This effect of the oxide layer formation has not been observed by others studying particle impact, because temperature has not been an experimental parameter in past studies.

The final paper [8] of the dissertation is the culminating of study of the particle impact characteristics. This paper has also been accepted for publication at ASME-IGTI Turbo Expo 2014 and has been submitted for journal publication. The test temperatures tested were 1073 K, 1173 K, 1223 K, 1273 K, and 1323 K. The test velocity of this work was increased to 70m/s from the 28m/s used in the previous study. Particle deposition was observed to occur at the two highest temperatures. A method of calculating the ratio of rebounding to incoming particles was used to get a measure of the percentage of particle depositing. Additionally, counts of the deposited particles per unit area were made using a microscope.

Surprisingly, the COR of the sand particles did not change at the higher temperatures. It is hypothesized that, due to the non-homogeneous and crystalline nature of sand, some particle types begin to deposit while other compositions are still fully crystalline and thus do not exhibit any decrease in COR. The effect of the non-homogeneous nature of the sand particles has never been discussed in open literature, and will require a careful characterization of the percentage of particle types sticking. The results from these experiments are a large step forward towards understanding the impact characteristics of sand on hot metal components inside a gas turbine engine. The results obtained can be used to validate sticking models or used directly as empirical data to allow design to mitigate the effects of sand deposition.

[1] Eroglu, H., and Tabakoff, W., 1991, "3-D LDV Measurements of Particle Rebound Characteristics," AIAA-91-0011.

[2] Tabakoff, W., Malak, M.F., and Hamad, A., 1987, "Laser Measurements of Solid-Particle Rebound Parameters mpacting on 2024 Aluminum and 6A1-4V Titanium Alloys," AIAA Journal, 25(5), pp. 721-726.

[3] Tabakoff, W., 1991, "Measurements of Particles Rebound Characteristics on Materials Used in Gas Turbines," J. of Propulsion and Power, 7(5), pp. 805-813.

[4] Sommerfeld, M., and Huber, N., 1999, "Experimental analysis and modelling of particle-wall collisions," International Journal of Multiphase Flow, 25, pp. 1457-1489.

[5] Reagle C., D. J., Ng W., Ekkad S., Rajendran V., 2013, "Measuring the coefficient of restitution of high speed microparticle impacts using a PTV and CFD hybrid technique," Measurement Science and Technology, 24(10).

[6] Reagle CJ, D. J., Ng WF, Ekkad SV, 2014, "Study of Microparticle Rebound Characteristics Under High Temperature Conditions," Journal of Engineering for Gas Turbines and Power, 136(1).

[7] Delimont JM, M. M., Ng WF, Ekkad, SV, 2014, "Effect of Temperature on Microparticle Rebound Characteristics at a Constant Impact Velocity," ASME Turbo Expo 2014, ASME, Dusseldorf, Germany.

[8] Delimont JM, M. M., Ng WF, Ekkad, SV, 2014, "Effect of Near Melting Temperatures on Microparticle Sand Rebound Characteristics at Constant Impact Velocity," ASME Turbo Expo 2014, ASME, Dusseldorf, Germany.

Acknowledgements

I would first and most importantly like to thank my wife, Ashley, for her loving support throughout my time as a graduate student at Virginia Tech. I would not be writing this without her help along the way. I thank you for always encouraging me and providing the love and support I needed when times were tough. I also want to thank my two sons James and Levi for being so wonderful to come home to, and providing me with a reason to play with toys when I come home. I love you all and truly appreciate everything you have done for me. I want to thank my parents Mike and Colette for the many trips to see museums, mountains, beaches, and the many other things we went to visit that inspired my desire to learn.

Thank you to my co-advisors Dr. Wing Ng, and Dr. Srinath Ekkad for the opportunity to work on this project. I also thank them for the guidance and direction on this project, pushing the project to meet goals, and providing insight when problems were encountered. Dr. Danesh Tafti has contributed many insightful comments and discussion on the physics of particle collision for which I am very grateful. To my other committee members Dr. Todd Lowe and Dr. Gary Pickrell for being a resource on laser systems and the materials portions of this project, thank you. I acknowledge the work of Colin Reagle and long hours he spent getting the test rig working properly. To Sukhjinder Singh, thank you for the many insightful discussions involving sand transport phenomena. A special thanks goes to Matt Murdock for the good work done, car repair help, and the late nights spent running experiments to meet the deadlines. A special thanks to Mike Fertall for the hard work he put in during the facility startup phase of this project and the expertise and positive attitude he brought to the project. Thanks also to Adam Shoemaker, Avi Freidman, Raul Otero, and David Mayo, Jr., for their help in making the necessary experiments happen. Also thanks to the shop guys Johnny, Bill, James, and Tim for their advice and help on numerous machining and welding jobs. A very special thank you goes to Diana Israel for her assistance with purchasing and advice on many things related to Virginia Tech.

I would like to thank Rolls Royce for sponsoring this project and donating some of the hardware used for the test rig. I would like to specifically thank Brett Barker, Kwen Hsu, Veera Rajendran, Paul Davis, Nathan Wagers, and M.S. Anand for the many tough questions asked that led to great improvements in the experiment.

Table of Contents

1 Paper #1: Measuring the Coefficient of Restitution of High Speed Microparticle Impacts Using a PTV and CFD Hybrid Technique 1

1.1 Abstract 1

1.2 Introduction 1

1.2.1 Nomenclature 3

1.3 Experimental Setup and Instrumentation 4

1.3.1 Aerothermal Rig 4

1.3.2 Instrumentation 7

1.3.3 Particles 8

1.4 Data Reduction 10

1.4.1 Particle Tracking 11

1.4.2 COR Calculation 15

1.4.3 CFD 17

1.5 Results 19

1.5.1 Deviation 19

1.5.2 Glass Beads 19

1.5.3 Arizona Road Dust 21

1.5.4 Normal & Tangential COR 24

1.6 Conclusions 30

1.7 Acknowledgments 30

1.8 References 31

2 Paper #2 Study of Microparticle Rebound Characteristics Under High Temperature Conditions 33

2.1 Abstract 33

2.2 Introduction 33

2.2.1 Nomenclature 35

2.3 Experimental Setup and Instrumentation 36

2.3.1 Aerothermal Rig 36

2.3.2 Instrumentation 38

2.3.3 Test Conditions and Material Properties 41

2.4 Data Reduction *42*
2.5 Results *44*
2.5.1 Standard Deviation and Uncertainty 44
2.5.2 Total Coefficient of Restitution 46
2.5.3 Normal Coefficient of Restitution 47
2.5.4 Tangential Coefficient of Restitution 48
2.6 Discussion on Temperature/Velocity Effects *50*
2.6.1 Power Law 50
2.6.2 Perfectly Plastic Collisions 52
2.6.3 Kinetic Energy 53
2.7 Conclusions *54*
2.8 Acknowledgments *55*
2.9 References *55*
3 Paper #3: Effect of Temperature on Microparticle Rebound Characteristics at Constant Impact Velocity **58**
3.1 Abstract *58*
3.2 Introduction *58*
3.2.1 Nomenclature 62
3.3 Experimental Setup and Instrumentation *63*
3.3.1 Aerothermal Rig 63
3.3.2 Test Conditions 65
3.3.3 Instrumentation 66
3.3.4 Particles 67
3.4 Data Reduction *68*
3.4.1 Particle Tracking 69
3.4.2 Coefficient of Restitution Calculations 71
3.4.3 Curve Fitting 73
3.5 Results *75*
3.5.1 COR 75
3.5.2 Normal COR 77
3.5.3 Tangential COR 78

3.5.4 Literature Comparison 80
3.6 Conclusions ***83***
3.7 Acknowledgments ***84***
3.8 References ***84***
3.9 Appendix A ***86***
4 Paper #4: Effect of Near Melting Temperatures on Microparticle Sand Rebound Characteristics at Constant Impact Velocity 87
4.1 Abstract ***87***
4.2 Introduction ***87***
4.2.1 Nomenclature 91
4.3 Experimental Setup ***92***
4.3.1 Aerothermal Rig 92
4.3.2 Test Conditions 94
4.3.3 Instrumentation 95
4.3.4 Particles 96
4.4 Data Reduction ***98***
4.4.1 Particle Tracking 98
4.4.2 Coefficient of Restitution Calculations 99
4.5 Results ***101***
4.5.1 COR 101
4.5.2 Normal COR 103
4.5.3 Tangential COR 104
4.5.4 Effect of Temperature on COR 106
4.5.5 Rebound Ratio Calculations 106
4.5.6 Deposition Measurement 108
4.6 Effects of Sand Particle Characteristics ***111***
4.7 Conclusions ***114***
4.8 Acknowledgments ***114***
4.9 References ***114***
4.10 Appendix B ***116***
5 Conclusion and Future Work 117

6 Appendices 120

6.1 Appendix C: Two Pass Channel Experiment 120

6.2 Appendix D: Modifications Made to the Test Rig 123

6.2.1 Controlling the Mass Flow Rate of the rig 123

6.2.2 Equilibration Tube Design 125

6.2.3 Expanding the Operating Envelop 126

6.2.4 Camera Cooling Modifications 130

6.2.5 Exhaust Quenching System 131

6.2.6 Rig Controls 133

6.2.7 Hastelloy X Target Coupons 134

6.3 Appendix E: Buckingham Pi Analysis of Impact Variables 136

6.4 Appendix F: Data Reduction Code 140

6.4.1 Post_Processing_v5.1 142

List of Figures

Figure 1-1. VT Aerothermal Rig configured for sand testing 5
Figure 1-2. Schematic of coupon setup..... 6
Figure 1-3. Pitot-Static Traverse 8.13 cm Upstream of Coupon 7
Figure 1-4. Size distribution of particles..... 9
Figure 1-5. Particle tracking software results for 70^{o} angle..... 12
Figure 1-6. Example tracked ARD 20-40 µm history 14
Figure 1-7. Values for ARD 10-20 µm, coupon angle 60^{o} 15
Figure 1-8. Values for glass beads, coupon angle 60^{o} 16
Figure 1-9. Impact velocity vs. angle for ARD 20-40 µm..... 17
Figure 1-10. CFD domain with W velocity contour..... 18
Figure 1-11. W velocity CFD w/ rebounding particle tracks..... 19
Figure 1-12. Glass bead results..... 20
Figure 1-13. ARD 10-20 µm results 22
Figure 1-14. ARD 20-40 µm results 22
Figure 1-15. Comparison with literature COR vs angle 24
Figure 1-16. Tangential COR vs angle for ARD 20-40 µm 25
Figure 1-17. Tangential velocity vs angle for ARD 20-40 µm..... 26
Figure 1-18. Normal COR vs angle for ARD 20-40 µm 27
Figure 1-19. Normal velocity vs angle for ARD 20-40 µm..... 28
Figure 1-20. Tangential COR vs angle for ARD 20-40 µm 29
Figure 1-21. Normal COR vs angle for ARD 20-40µm 29
Figure 2-1. VT Aerothermal Rig configured for sand 37
Figure 2-2. Schematic of instrumentation setup 39
Figure 2-3. Traverse 8.13 cm upstream of coupon, 533 K..... 39
Figure 2-4. Temperature ratio 1.78 cm upstream of coupon 40
Figure 2-5. Data points with mean and standard deviation lines plotted..... 45
Figure 2-6. ARD 20-40 µm results COR vs angle..... 46
Figure 2-7. ARD 20-40 µm normal COR vs angle..... 47
Figure 2-8. ARD 20-40 µm tangential COR vs angle 48
Figure 2-9. ARD 20-40 µm COR vs Velocity..... 51

Figure 2-10. ARD 20-40 µm COR vs KE (12mv2) 54
Figure 3-1. V-22 Osprey [Department of Defense] 59
Figure 3-2. Diagram of Incoming and Rebounding Particle Trajectories 60
Figure 3-3. VT Aerothermal Rig 64
Figure 3-4. Schematic of instrumentation setup 65
Figure 3-5. Particle tracks generated by the Lagrangian particle tracking algorithm 70
Figure 3-6. Power law curve fit and raw data for the mean COR 74
Figure 3-7. Plot of COR vs. angle of impact for SS304 and Hastelloy X 76
Figure 3-8. Plot of normal COR vs. angle of impact for SS304 and Hastelloy X 77
Figure 3-9. Plot of tangential COR vs. angle of impact for SS304 79
Figure 3-10. Plot of ambient COR vs. angle of impact comparison to literature 81
Figure 3-11. Plot of ambient normal COR vs. angle of impact comparison to literature . 82
Figure 3-12. Plot of ambient tangential COR vs. angle of impact comparison to literature 83
Figure 4-1. Example of sand ingestion in desert conditions 88
Figure 4-2. Diagram of incoming and rebounding particle trajectories 89
Figure 4-3. VT Aerothermal Rig 93
Figure 4-4. Schematic of instrumentation setup 94
Figure 4-5. Plot of total COR vs. angle of impact 102
Figure 4-6. Plot of normal COR vs. angle of impact 103
Figure 4-7. Plot of tangential COR vs. angle of impact 105
Figure 4-8. Plot of COR vs. temperature for different impact angles 106
Figure 4-9. Averaged rebound ratio of angles 108
Figure 4-10. Image of sand deposition at 1323 K at 60° angle of attack and 200X optical magnification 109
Figure 4-11. Deposition per mm^2 at several angles and at various temperatures 110
Figure 4-12. Image taken sand particles prior to testing at 200X optical magnification 112
Figure 4-13. Hypothesized non-homogeneous sand particle impact behavior 113
Figure C-1. Two pass internal cooling channel geometry 120
Figure C-2. Experimental test setup used for two pass deposition test 121
Figure C-3. Two-sided sticky tape attached on end walls, underneath ribs 121

Figure C-4. Deposition results from the 180° turn portion of the test rig..... 122
Figure D-1. Pressure regulator and flow control valve setup 124
Figure D-2. Graph of the percentage of air flow velocity and temperature versus position of target particle 126
Figure D-3. Burner operation envelop in current configuration 127
Figure D-4. Stainless steel burner insert with areas of high energy losses shown 129
Figure D-5. Finished combustor liner as installed in the VT Aerothermal Rig..... 129
Figure D-6. Camera blackout shroud..... 130
Figure D-7. Cooling air routed to camera..... 131
Figure D-8. Exhaust quenching system 132
Figure D-9. Control panel used to operate the VT Aerothermal Rig..... 134
Figure D-10. a) Shows the scaling damage to the surface coating that occurs to stainless steel 304 after cooling. b) Shows the new visible light image of Hastelloy X coupon at 1323 K..... 135

List of Tables

Table 1-1. Test Dust Chemical Composition 9
Table 1-2. Test Dust Size Properties 10-20 µm 10
Table 1-3. Test Dust Size Properties 20-40µm 10
Table 1-4. Representative Size Properties for Glass Beads 10
Table 2-1. Chemical composition of ARD 41
Table 2-2. Test Dust Properties 29.25 µm mean by volume values 41
Table 2-3. Average Deviation from Mean Values 45
Table 2-4. Power Law curve fit parameters 51
Table 3-1. Test Temperatures and Velocities 66
Table 3-2. Test Dust Stokes Numbers at Extreme Values 68
Table 3-3. Estimated COR Standard Deviation for SS304 and HX 76
Table 3-4. Normal COR Estimated Standard Deviation for SS304 and HX 78
Table 3-5. Tangential COR Estimated Standard Deviation for SS304 and HX 80
Table A-1. Power Law Coefficients for SS304 and HX COR 86
Table A-2. Power Law Coefficients for SS304 and HX Normal COR 86
Table A-3. Power Law Coefficients for SS304 Tangential COR 86
Table 4-1. Test Temperatures and Velocities 95
Table 4-2. Test Dust Stokes # Extreme Values 97
Table 4-3. Total COR Estimated Standard Deviations 102
Table 4-4. Normal COR Estimated Standard Deviation 104
Table 4-5. Tangential COR Estimated Standard Deviation 105
Table B-1. Curve fit coefficients for total COR 116
Table B-2. Curve fit coefficients for normal COR 117
Table B-3. Curve fit coefficients for tangential COR 117
Table D-1. Air energy compared to water energy at 1073 K and 28 m/s 128

1 Paper #1: Measuring the Coefficient of Restitution of High Speed Microparticle Impacts Using a PTV and CFD Hybrid Technique

1.1 Abstract

A novel Particle Tracking Velocimetry (PTV) / Computational Fluid Dynamics (CFD) hybrid method for measuring Coefficient of Restitution (COR) has been developed which is relatively simple, cost-effective, and robust. A laser and camera system is used in the Virginia Tech Aerothermal Rig to measure velocity trajectories of microparticles. The method solves for particle impact velocity at the impact surface using a CFD solution and lagrangian particle tracking. The methodology presented here attempts to characterize a difficult problem by a combination of established techniques, PTV and CFD, which have not been used in this capacity before. Erosion and deposition are functions of particle/wall interactions and COR is a fundamental property of these interactions. COR depends on impact velocity, angle of impact, temperature, particle composition, and wall material. Two sizes of Arizona Road Dust (ARD) and one size of glass beads are impacted on to a 304 stainless steel coupon. The particles are entrained into a free jet of 27 m/s at room temperature. Impact angle was varied from 85 to 25 degrees depending on particle. Mean results collected using this new technique compare favorably with trends established in literature. The utilization of this technique to measure COR of microparticle sand will help develop a computational model and serve as a baseline for further measurements at elevated air and wall temperatures

1.2 Introduction

Understanding when particles will rebound and when they will stick to a surface is a problem that is not well understood or documented for many scenarios. The process of tracking particles and their interactions with the fluid flow of a system can be performed relatively easily using computational methods. The difficulty in understanding where the particles will travel in the system comes from modeling the interaction between the particle and the solid surfaces. This aspect of a particle's journey through a system has been the subject of a great deal of research throughout the years.

The theory of colliding solids has been around since Heinrich Hertz fathered the field of contact mechanics by combining classical elasticity theory with continuum mechanics [1]. Hertzian theory has been widely applied as the basis of solutions for stress, compression, time, and separation of impacting solids. Since then, numerous researchers have proposed improvements to account for phenomenon, such as plastic deformation, associated with colliding solids. With the introduction of plastic deformation to Hertzian theory, approximations can be made for coefficient of restitution of real particles at higher impacting velocities. The contact is broken up into phases of elastic compression, plastic deformation, and restitution of stored elastic strain energy. After solving the necessary equations, an approximation for coefficient of restitution (2-1) is produced [2]

$$e = \frac{2}{v_0}\left[\frac{2E}{m(1-\nu^2)}\right]\left\{\frac{2}{15}u_0^{5/2} + \frac{r^2}{3}u_0^{3/2}\right\}^{1/2} \tag{1-1}$$

where v_0 is the impact velocity, E is the modulus of elasticity, m is the mass, ν is Poisson's ratio, u_0 is deformation, and r is radius of permanent deformation. A slightly different equation is proposed in [3] based on dynamic yield strength. However, both of these expressions are based on approximations. When the effects of surface roughness, particle/material combination, temperature, impact angle and impact velocity are introduced, these equations are analytical estimates at best.

Many of the general trends predicted by theory are correct. However, in real impacts the impact parameters vary statistically. Tabakoff *et al.* [4] used high speed photography to measure particle trajectories and found that, as predicted, COR generally decreases as particle velocity increases. COR is generally a measure of energy transfer between particle and surface of which the tangential component is found to be the determining factor in erosive behavior. A general correlation of COR was presented by Tabakoff [5] by averaging Laser Doppler Velocimetry (LDV) data of 15 μm fly ash impacting different gas turbine material samples. LDV was necessary to capture the small particle sizes in this study. However, this study also showed the percent difference in mean COR was higher than 25% for different materials. This shows a distinct effect of impacting particle/material combination on rebound characteristics. Tabakoff *et al.* [6] later went on to repeat many of these same experiments using 100-200 μm sand particles impacting aerospace materials. Comparing the mean results led to a notable difference in COR

values compared with the fly ash particles.

While tangential and normal COR have been presented, out of plane measurements made by Eroglu and Tabakoff [7] using three dimensional LDV measurements, found that out of plane COR was insensitive to changes in impact angle. Sommerfeld and Huber [8] experimented with 100 μm and 500 μm glass beads and non-spherical quartz particles on smooth and rough surfaces. Surface roughness and particle roundness were shown to have similar effects on COR and rebound angles. Wall *et. al.* [9] utilized an LDV system and calculated a 1-D velocity correction based on very small tracer particle measurements at different heights.

In reported literature, high speed imaging [4] and LDV [5-9] are the two main methods of measuring COR. High speed imaging has its limitations with respect to particle size and high resolution/speed cameras can make this measurement technique quite expensive. While LDV provides high quality data, the technique requires precise setup and seeding for a single point measurement. LDV becomes even more difficult to set up when the effects of thermal expansion must also be accounted for.

The technique utilized in the current work is important as it allows for COR measurements in 2-D forced flow field. The technique can also be used at high temperatures in future experiments. After initial set-up, the test section components may thermally expand as they are heated, moving the impact surface.

The previous studies have highlighted the important parameters of COR research, however the current techniques for measuring COR have stagnated. To accurately model these phenomena a wide range of impact scenarios must be measured. The current technique allows measurement of many very small particles simultaneously during a short test interval. Angle of impact and impact velocity can be varied. Particle and material combinations can be interchanged quickly and measurements repeated easily. All without the use of an expensive, high resolution and high frame rate camera. A novel method of Particle Velocimetry Tracking (PTV) using a CFD simulated flow field is presented.

1.2.1 Nomenclature

ARD	Arizona Road Dust
a	acceleration

C_d	Drag Coefficient
CFD	Computational Fluid Dynamics
COR	Coefficient of Restitution
d	diameter
e	Coefficient of Restitution (COR)
E	Modulus of elasticity
F_d	Drag force
L	length
LDV	Laser Doppler Velocimetry
m	mass
PTV	Particle Tracking Velocimetry
r	radius of permanent deformation
Stk	Stokes Number
t	time
u_0	deformation
v	Velocity
Greek	
β	impact angle
ν	Poisson's ratio
ρ	density
subscript	
n	normal
p	particle
t	tangential
∞	freestream

1.3 Experimental Setup and Instrumentation

1.3.1 Aerothermal Rig

Virginia Tech Aerothermal Rig was donated to Virginia Tech by Rolls-Royce in September 2010. This rig was used in previous heat transfer studies conducted at their facility in

Indianapolis, IN. Hylton *et al.* [10] used the same facility to conduct a series of tests on shower head and film cooling heat transfer at a temperature of 700 K. Nealy *et al.* [11] used the rig at temperatures of 811 K to measure heat transfer on nozzle guide vanes at different transonic Mach numbers. The operational specifications for this rig when installed in Indianapolis were reported as 2.2 kg/s at a maximum of 16 atm and 2033 K by Rolls-Royce.

At Virginia Tech the pressure and temperature capabilities for this rig are being brought up gradually in steps as the rig is fully recomissioned. For the present study the Aerothermal Rig has been reconfigured to allow for sand injection into the flow as seen in Figure 1-1. A compressor supplies air to the rig at a constant rate of 0.15 kg/s.

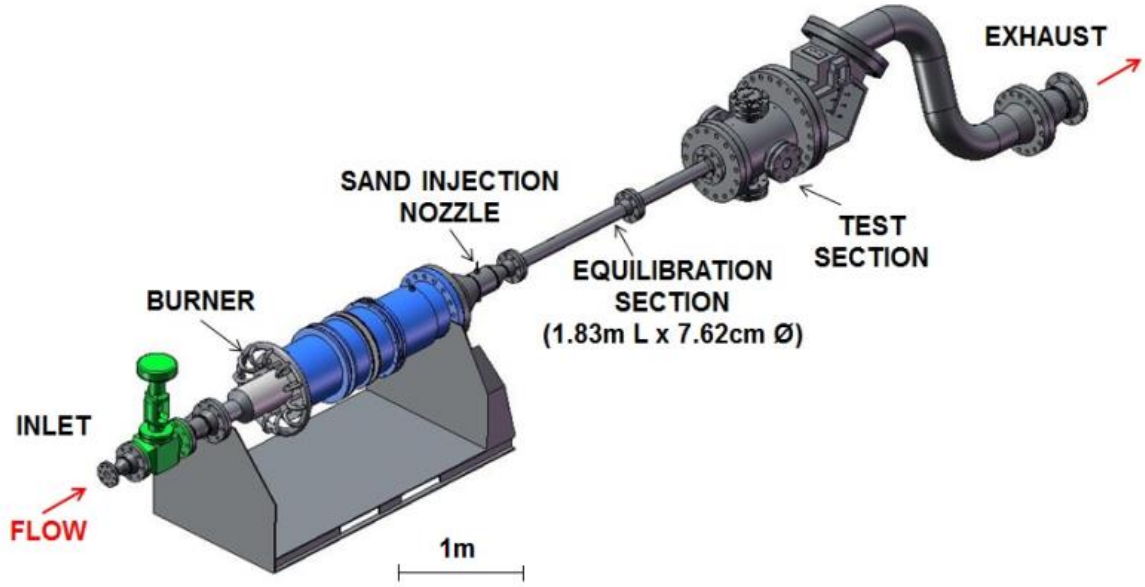

Figure 1-1. VT Aerothermal Rig configured for sand testing

The flow is regulated upstream with a 10.2 cm globe valve. The air then passes through a sudden expansion burner capable of heating the flow. The burner is not used to heat the flow in the current study.

At the exit downstream of the burner, the cross-section of the flow is reduced in diameter from 30.5 cm to 7.62 cm. During the contraction section, the test particles are injected into the mainstream flow. The particles are entrained in a compressed air flow that has been bled from the main compressor upstream of the burner. The particles then enter a 1.83 m long, 7.62 cm

diameter equilibration tube which enables particles of various sizes to reach the same speed and temperature as the rest of the flow. The flow exits the equilibration tube as a free jet into the test section and impinges on the test surface.

The test section contains a test coupon, on which the impacts occur, and a support to allow for rotation of the coupon. The test section has a laser access port as well as optical access for the camera to image the area in front of the coupon. The test coupon has a height of 3.81 cm and is 6.35 cm long as shown in Figure 1-2. The longer side allows a reasonable projected area perpendicular to the flow at shallow angles of attack. The coupon itself is made from SAE 304 stainless steel and can be rotated 360 degrees in 10 degree increments. Before testing the coupon is polished to a mirror finish with an average roughness < 500 Å as measured by a surface profilometer.

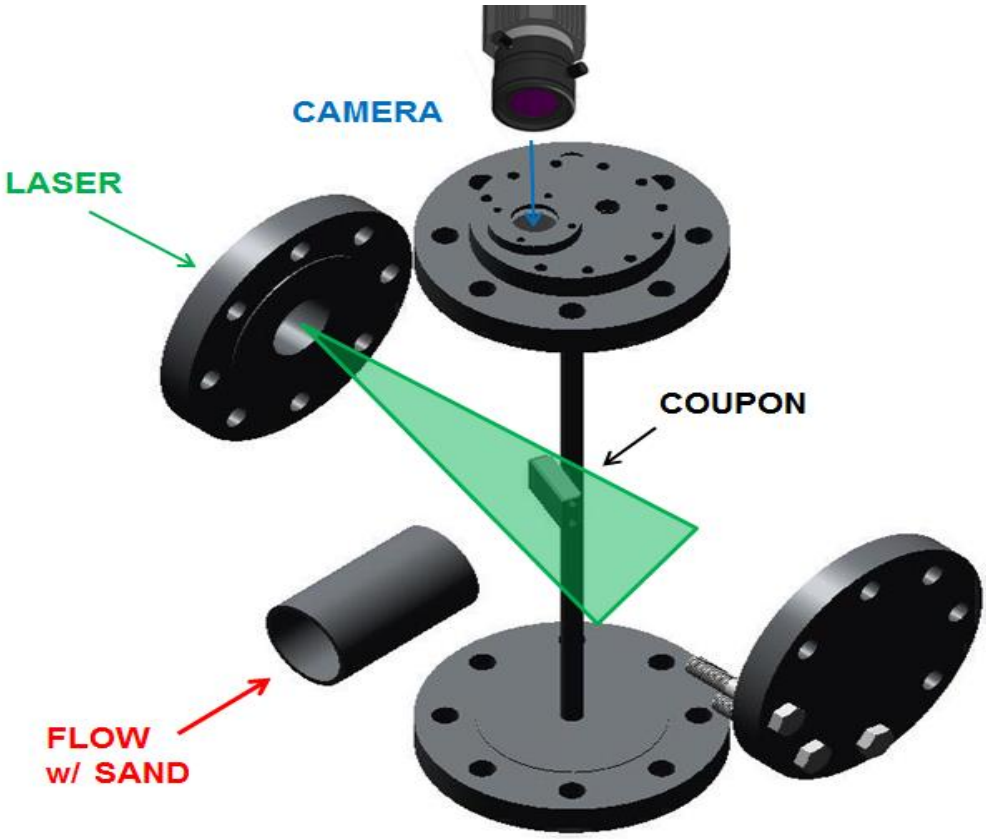

Figure 1-2. Schematic of coupon setup

1.3.2 Instrumentation

The Pitot-static probe survey, seen in Figure 1-3, was taken at a distance of 8.13 cm upstream from the coupon face to quantify the fully developed velocity profile. The probe is moved out of the test section during particle injection. The Reynolds number at the survey location is 128,000 based on the diameter of the pipe and mean velocity of the flow.

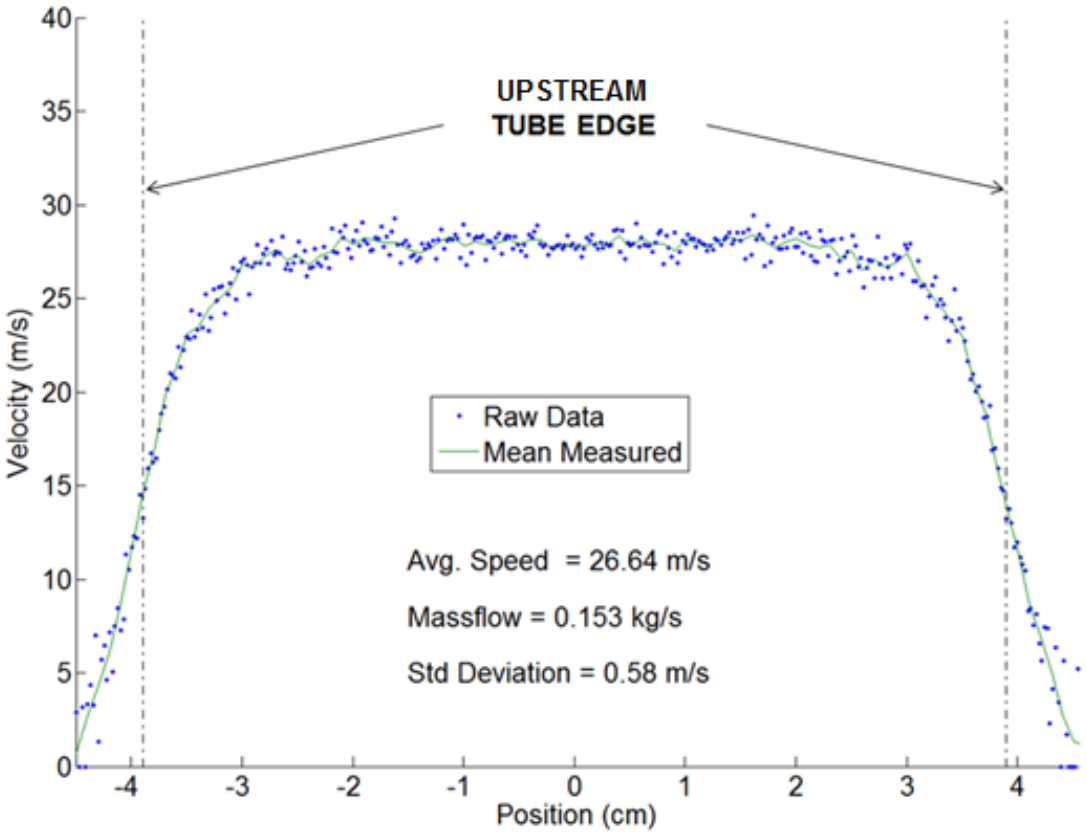

Figure 1-3. Pitot-Static Traverse 8.13 cm Upstream of Coupon

The laser for illuminating the particles is a twin head Litron Nd:YAG laser that emits approximately 55 mJ at 532 nm wavelength. The laser is capable of emitting two pulses of light within a few microseconds. The laser light is projected in a plane at the center of the test coupon as shown in Figure 1-2. A Dantec Dynamics® FlowSense camera equipped with a Zeiss® Makro-Planar 2/50 lens is used to capture the particle images at 2048x2048 resolution. This resolution allows for one to two pixels per particle in the interrogation region. Both the laser and the camera are synced by a timer box ensuring illumination and imaging occurs concurrently.

The system can take image pairs with a 5μs, however, the maximum sampling frequency for image pairs is 7.4 Hz.

1.3.3 Particles

The sand particles used were Arizona Road Dust (ARD) or Arizona Test Dust. Intermediate Grades of Nominal 10-20 μm and also Nominal 20-40 μm were tested in this experiment. ARD has been widely used as a standard test dust for filtration, automotive and heavy equipment testing. Glass beads with large Stokes number (Stk) were also tested in this experiment to help verify the technique. This case limited variation in the impact conditions and particle sphericity.

Stk is dimensionless parameter that relates the characteristic response time of the particle to the response time of the fluid. It is defined as

(1-2) $$Stk = \frac{\rho_p d_p^2}{18\mu}\frac{v_\infty}{L_c}$$

where ρ_p is the density of the particle, d_p is the diameter of the particle, v_∞ is the velocity at the pipe exit, and L_c is the length of the coupon face. The smaller the Stk is, the smaller the deviation of the particle from the flow. In this experiment, all of the sand particles have a finite Stk and do not follow the streamlines exactly. The smallest particles have the smallest Stk and will never impact the coupon. The largest particles will impact at almost the same flow conditions as are found at the exit of the 7.62 cm pipe.

Size distributions for the specific batches of test dust used, as well as a representative size distribution for the glass beads are shown in Figure 1-4. Size properties of ARD are presented in, Table 1-2, and Table 1-3 below. The size properties of the glass beads are presented in Table 1-4. Stk of the various particle sizes are also presented in these tables.

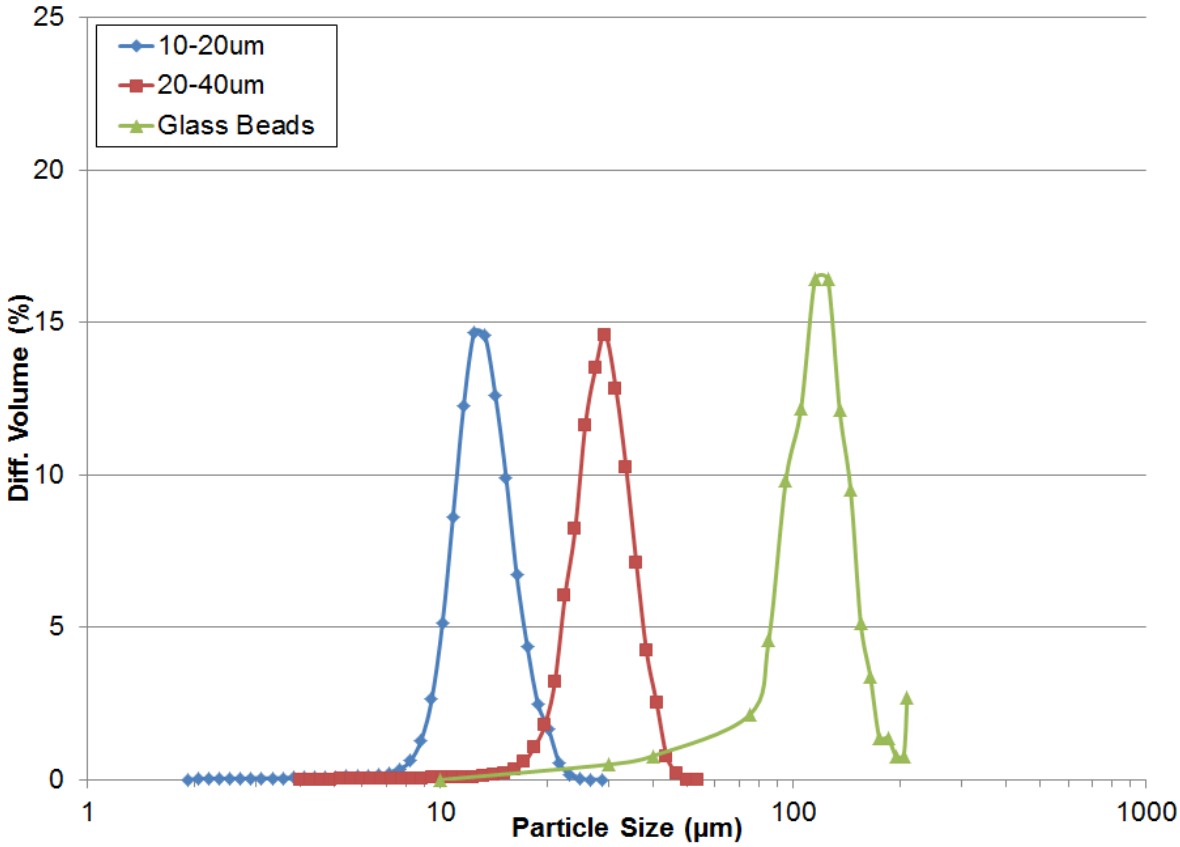

Figure 1-4. Size distribution of particles

Table 1-1. Test Dust Chemical Composition

Chemical	% Weight
Quartz (SiO_2)	68-76
Aluminum Oxide (Al_2O_3)	10-15
Iron Oxide (Fe_2O_3)	2-5
Sodium Oxide (Na_2O)	2-4
Calcium Oxide (CaO)	2-5
Magnesium Oxide (MgO)	1-2
Titanium Dioxide (TiO_2)	0.5-1
Potassium Oxide (K_2O)	2-5

Table 1-2. Test Dust Size Properties 10-20 µm

Particle Size	Cumulative. % Vol.	Stk
< 6.667µm	< 1.04%	0.146
< 13.46µm	< 50%	0.597
< 21.66 µm	< 99.24%	1.55

Table 1-3. Test Dust Size Properties 20-40µm

Particle Size	Cumulative % Vol.	Stk
< 15.10µm	< 1.16%	0.752
< 29.25µm	< 50%	2.82
< 40.91 µm	< 99.04%	5.52

Table 1-4. Representative Size Properties for Glass Beads

Particle Size	Cumulative % Vol.	Stk
< 90µm	< 7.98%	25.4
< 110µm	< 29.96%	37.9
< 150 µm	< 84.46%	70.5

1.4 Data Reduction

Coefficient of restitution is defined by the particle velocities just before and just after impact by equation (1-3).

(1-3) $$e = \frac{v_{reb}}{v_{in}}$$

The hardware used in the VT Aerothermal Rig has a maximum repetition rate of 7.4 Hz per image pair. This does not allow for continuous tracking of microparticles at high speeds. This has two consequences. First is that the majority of the particle measurements are made some distance away from the coupon. Second is that an impacting particle cannot be uniquely identified before and after impact. The experimental approach discussed below mitigates these consequences without the purchase of exotic or expensive imaging hardware or software. The current setup also allows for high temperature measurements of COR, which is the end goal of this line of research. The methodology discussed below is meant to establish the technique and

provide a baseline for future COR measurements.

1.4.1 Particle Tracking

The first step is to take each image pair and determine particle velocities. The particle tracking is accomplished with an open source code developed by Grier, Crocker and Weeks and coded for Matlab® by Blair and Dufresne.

The raw images are first filtered to increase resolution between the particles and background. The particle centers are then located to sub pixel accuracy in each frame of each image pair. The particles are then tracked by correlating particles between frames to minimize total displacement. A balance between particle seeding density, velocity, and time between frames must be held so that maximum particle displacement between frames does not approach mean particle spacing. If there are multiple particle in an image that could possibly correlate to a single particle, the particle with multiple possibilities will not be used to eliminate the possibility of erroneous tracks being introduced. The current experiment uses image pairs in which the illuminating pulses occur 15 μs apart. A tracked image pair is presented in Figure 1-5 with the circles representing particles found in frame 1 and particles in frame 2, and black arrows as tracked velocities between frames 1 and 2.

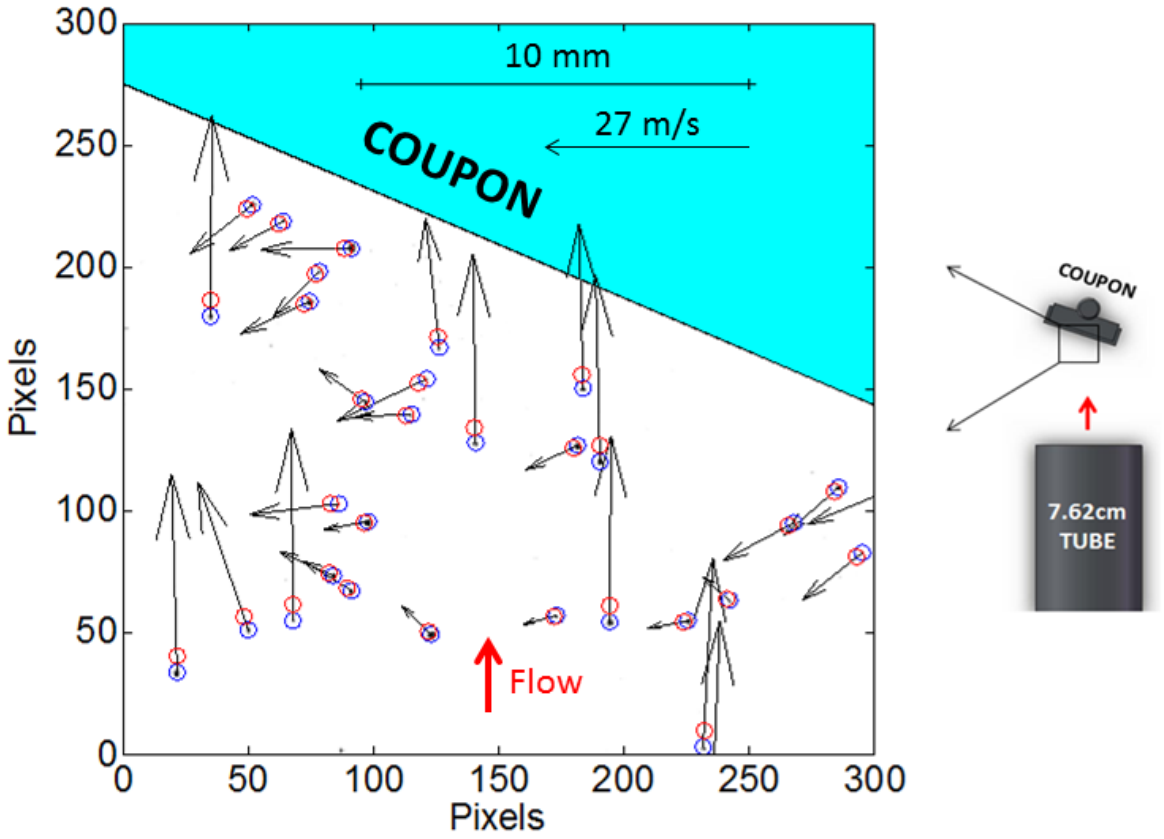

Figure 1-5. Particle tracking software results for 70° angle

The current technique uses a laser and camera system to measure many particle velocities near the coupon using an established Particle Tracking Velocimetry (PTV) technique. Assuming that the flow field is steady in front of the coupon, these measured particle trajectories can be calculated forward or backwards to yield velocities just before hitting the coupon face. The flow field is predicted with sufficient spatial resolution using CFD. The impacting and rebounding velocities become a function of the measured particle velocity (from PTV), the aerodynamic flow field (from CFD), particle mass, and particle size. The change in velocity over a small time step is calculated

(1-4) $$v = v_0 + at$$

where acceleration is defined as

(1-5) $$a = F_d/m$$

and the drag force, F_d, is defined as

(1-6) $$F_d = {}^1/_8\, C_d \pi d^2 \rho v_{rel}^2$$

where v_{rel} is the relative velocity difference between the particle and the local air velocity. The drag coefficient, C_d, is determined by

(1-7) $$C_d = \frac{24}{Re} + \frac{2.6\left({}^{Re}/_{5.0}\right)}{1+\left({}^{Re}/_{5.0}\right)^{1.52}} + \frac{0.411\left({}^{Re}/_{263{,}000}\right)^{-7.94}}{1+\left({}^{Re}/_{263{,}000}\right)^{-8.00}} + \frac{Re^{0.80}}{461{,}000}$$

which is a correlation developed by Morrison[12] to capture smooth sphere drag coefficients for Reynolds numbers up to 10^6.

The equations used for calculating particle trajectories are relatively straightforward with the exception of v_{rel}. Traditional PIV calculates the flow field using a seeding particle that follows the streamlines very closely, v_{rel} is assumed to be equal to zero and small changes in velocity of the flow are reflected instantaneously in the particle's trajectory.

At the exit of the pipe, v_{rel} is close to zero. However, as the sand particles approach the coupon, the velocity gradients in the forced flow field, have a tangible effect. To account for this effect a CFD flow field is calculated in front of the coupon, for the sole purpose of estimating the relative velocity difference between the particle and the flow at its calculated location. This is where the novelty of the hybrid PTV/CFD technique is witnessed, the calculation of v_{rel} for a particle with a moderate Stk.

PTV typically captures sparsely seeded particles through multiple images to determine their trajectories. When following microparticles, high resolution over a small area must be used to accurately locate the individual particles. However, to continuously track the particles at high speed, a high frame rate must also be used. This becomes a very expensive piece of hardware just to record the images without even considering illumination. CFD can typically capture particle trajectories quite well; however, particle impact is not accurately modeled, leading to false trajectories after an impact. By combining the PTV measurements with CFD predictions

the advantages of each technique are maintained, while the shortcomings are negated.

To combine the PTV and CFD data, a zero point is chosen for referencing the location of the coupon face in both the images and the CFD. The coupon face is located in the raw image to select valid impact areas at different coupon angles. The particle measurements are then scaled, translated, and rotated onto the CFD results.

The measurements are then filtered into two categories, incoming and rebounding. This categorization is a function of the current angle of trajectory compared with the plate angle. Particles that have impacted the coupon will rebound and move away from it at an angle different than the incoming particles. The rebounding particles are stepped backwards to the coupon face, while the incoming particles are stepped forward until they hit the coupon face. A set of image pairs is plotted in Figure 1-6 with the trace history of both incoming and rebounding particle velocities.

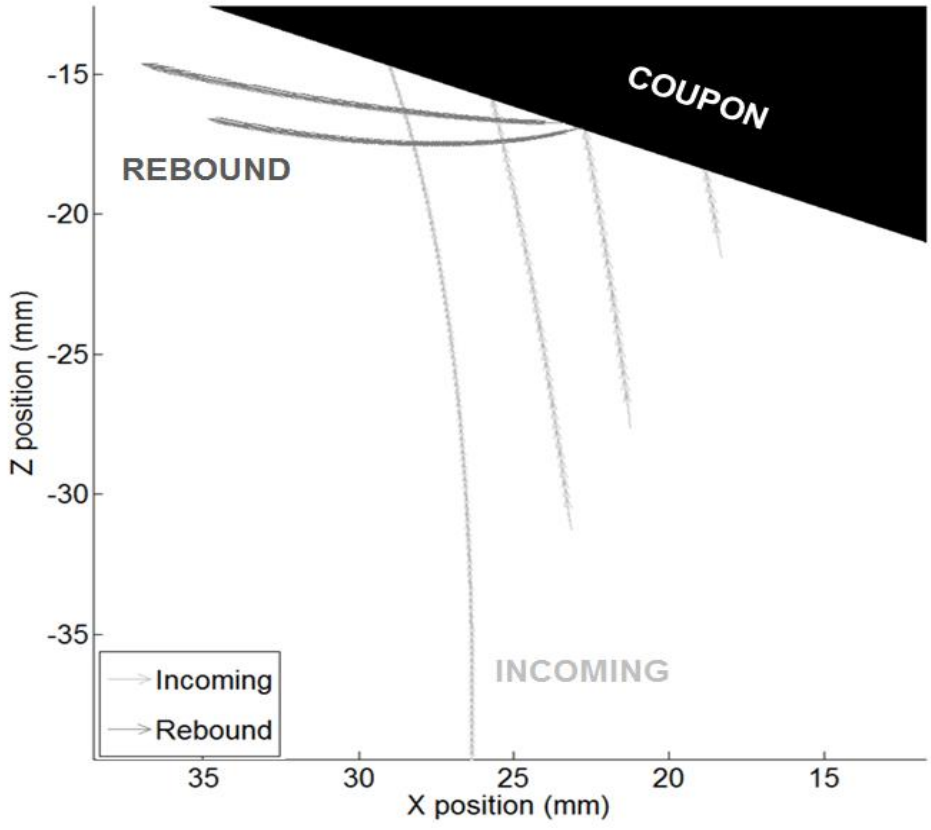

Figure 1-6. Example tracked ARD 20-40 µm history

1.4.2 COR Calculation

As mentioned previously, the particles cannot be uniquely identified before and after impact so an average incoming velocity and angle are used. The incoming velocity is a function of impact location along the coupon face. The flow near the edges tends to turn more than the flow in the center of the coupon (near the stagnation point) and the particles impinge at steeper angles. The representative incoming data is plotted along with the raw rebounding data. An example for a given coupon angle of 60 degrees is presented in Figure 1-7 for ARD 10-20 µm and in Figure 1-8 for glass beads. From these figures, it can be seen that a range of impact angle conditions are achieved from a single coupon angle, one of the advantages of this technique.

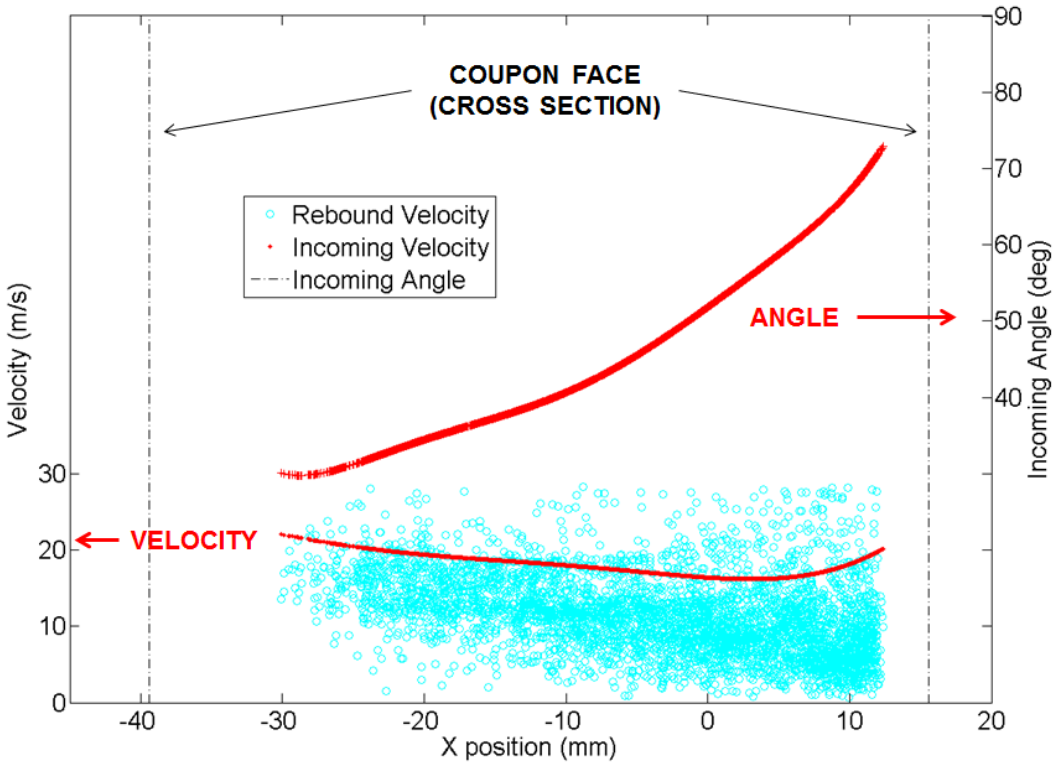

Figure 1-7. Values for ARD 10-20 µm, coupon angle 60°

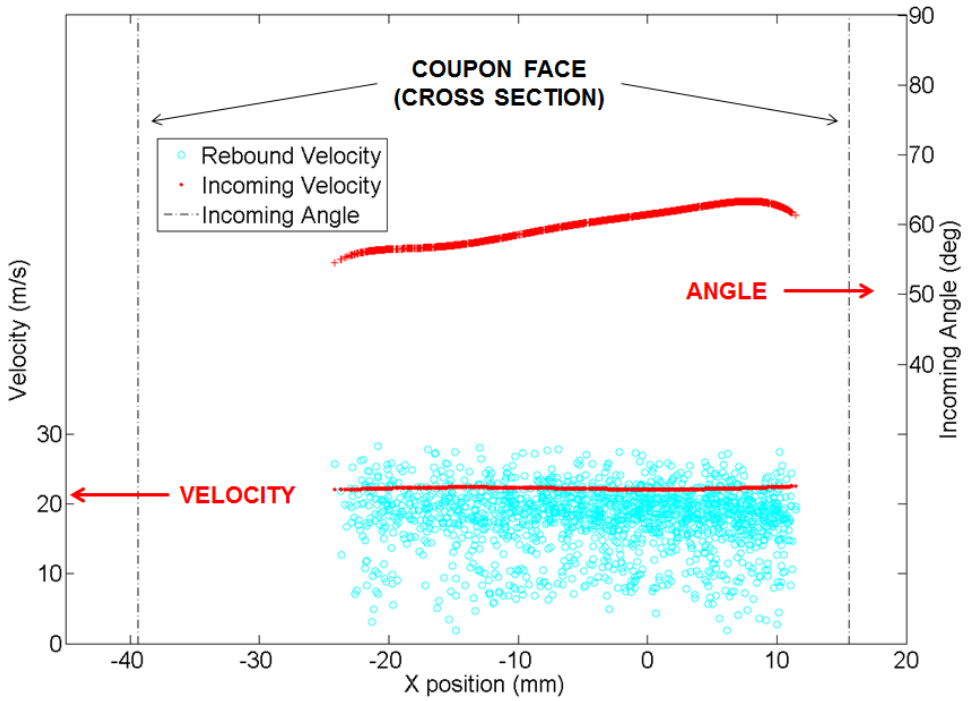

Figure 1-8. Values for glass beads, coupon angle 60°

The forced flow field around the coupon also causes particles to decelerate when approaching the impact location. For the glass beads and the ARD 20-40 µm, this effect is relatively small, however, as particle size and Stk decrease so does the impact velocity. In Figure 1-8, the 10-20 µm particles impacting near the stagnation point decelerate to approximately 14 m/s while the particles near the edge impact at approximately 19 m/s. This can have a tangible effect on the COR results for a finite size distribution using this technique and must be accounted for. In this technique, each rebounding particle is tracked backwards to its impacting location, and the average incoming velocity and impact angle at that position along the coupon face is used to calculate COR for one particle.

Figure 1-9 shows the cumulative effect of incoming velocity versus impact angle for six different coupon angles. The 30 degree coupon angle has the smallest blockage and particle deceleration resulting in the highest impact velocity of 26.3 m/s The 80 degree coupon angle has the highest blockage and highest particle deceleration. This results in the lowest incoming velocity of 21.3 m/s. There is also some overlap between angle of impact at different coupon angles which contributes to the deviation of the data at these angles. It should be noted that conditions exiting the equilibration tube are identical for all coupon angles.

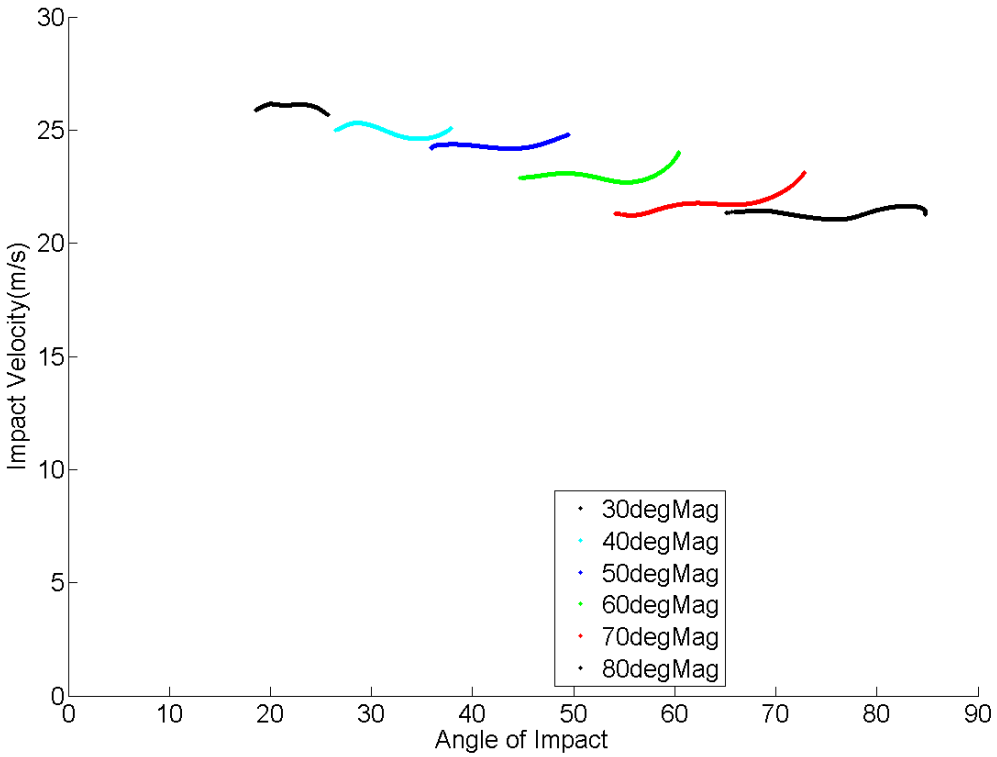

Figure 1-9. Impact velocity vs. angle for ARD 20-40 μm

1.4.3 CFD

As there are numerous iterations for different angles, the grid was kept relatively coarse. ANSYS® CFX® was used for the solution. The outlet of the domain is an opening at atmospheric pressure. The 7.62 cm pipe boundary was an inlet condition with total pressure set to match the velocities in the Pitot-static survey in Figure 1-3. There are approximately 600,000 cells calculated for each case with a layered grid on the coupon faces and an unstructured grid in the body of the domain. The CFD domain and region of interest is plotted in Figure 1-10. The W velocity contour after being imported into Matlab® is plotted in Figure 1-11 along with the measured, rebounding particle tracks.

The aerodynamic CFD is of secondary importance to the particle tracking measurements in this experiment. Sensitivity studies were conducted to ensure undue influence was not being exerted by incorrect velocity predictions. The aerodynamic flow field was artificially increased by 15% and the data re-reduced using this new flow field. Mean results were shown to decrease by 6.8%. Measurement uncertainty was calculated at 5.4% for the inlet Pitot-static velocity

traverse used to match the CFD data to the experiment. The standard deviation in these measurements was 2.2%. These statistics taken together suggest that errors related to the CFD are less than 1.0% of total COR. By comparison, the average run to run repeatability of the total COR mean values for two different data sets was 1.5%.

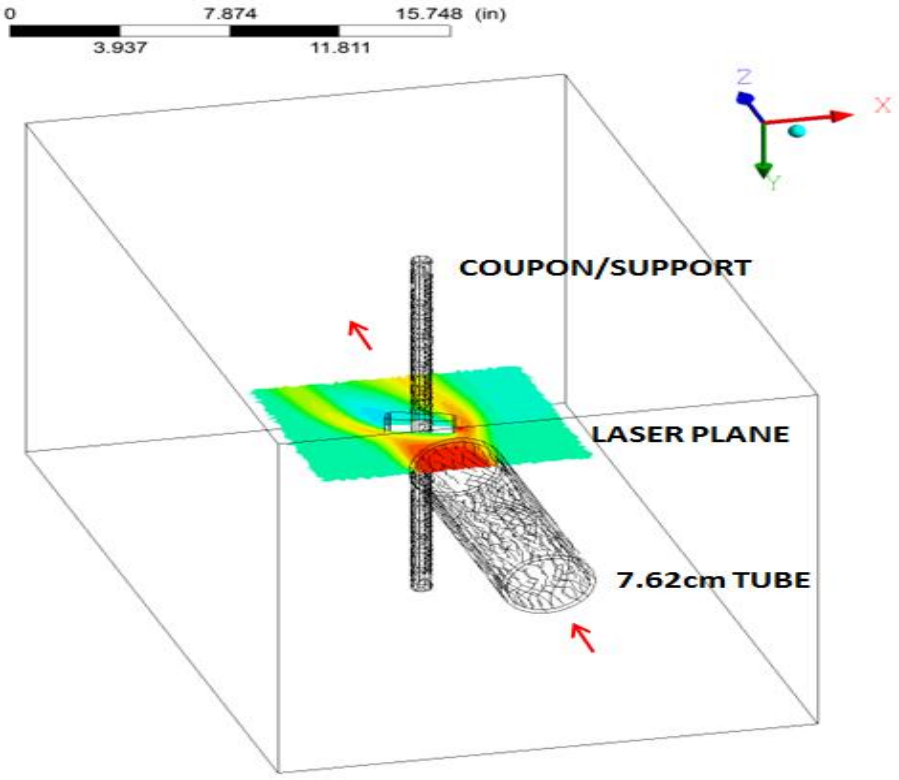

Figure 1-10. CFD domain with W velocity contour

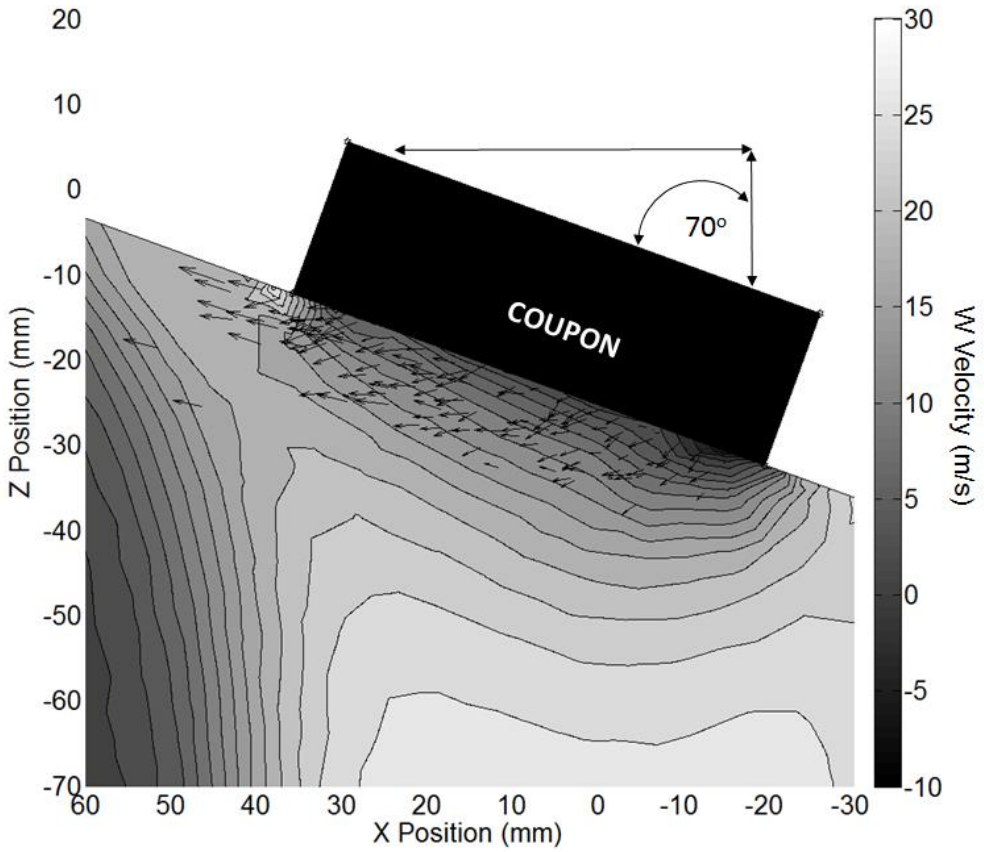

Figure 1-11. W velocity CFD w/ rebounding particle tracks

1.5 Results

1.5.1 Deviation

In the following results, raw data, mean COR, and values corresponding to one standard deviation from the mean value are plotted. To calculate the statistical values, the data is sorted into bins by integer value of angle of impact. In each bin, at least 100 impact events are captured and averaged to calculate the mean. This is an advantage in technique also, as traditional methods capture fewer impacts at only a few angles of impact. The standard deviation is calculated for each bin and plotted accordingly.

1.5.2 Glass Beads

Glass beads were tested in this experiment to help validate the technique. They were

relatively smooth on the surface and large enough not to be significantly affected by the flow field downstream of the jet. Sets of data were taken at three coupon angles, 80°, 70°, and 60°, where 90° is normal to the flow direction. This resulted in particle impact angles from 56° to 83° for the beads. The average COR values for each set of data is plotted in Figure 1-12 along with a median curve fit, upper and lower bounds.

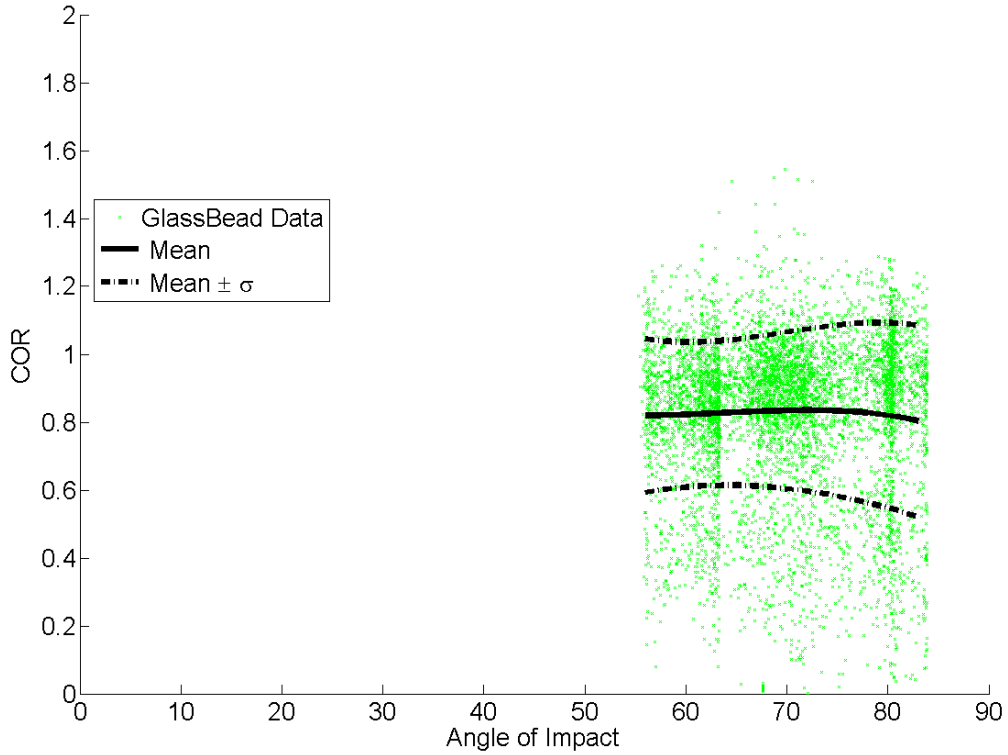

Figure 1-12. Glass bead results

The glass bead values are in agreement with literature for glass/steel impact events. Dunn *et. al.* [13], while studying microparticle adhesion, found 8.6 µm mean diameter Ag-coated glass spheres impacting stainless steel at 21 m/s and 90°, to have a mean COR of 0.84. Adhesion was not found to affect these particles at less than 15 m/s. At an 80° impact angle, the glass beads in the current study had a mean COR of 0.81. Li *et. al.* [14] measured low velocity (< 1.6m/s) impact of 70 µm mean diameter stainless steel spheres on a $Si0_2$ surface at different angles. The mean COR stayed relatively constant at 0.70 for different angles above 50°. However, microparticle adhesion did play a role at such low velocities which helps explain the lower values of COR. Finally, [8] studied 100 µm glass beads impacting polished steel at shallow

angles of impact (< 50°). A relatively constant mean COR between 0.85 and 0.8 from impact angles of 10° to 40° was measured. Both glass and stainless steel are rigid, hard materials which at low relatively low velocities should transfer their energy efficiently resulting in a high COR. At these impact conditions, results are relatively constant between 0.79 and 0.83 with the mean value at 0.82, which is in consistent agreement with similar experiments.

1.5.3 Arizona Road Dust

Impact of ARD was measured at different coupon angles. The 10-20 μm distribution was tested at 80°, 70°, 60°, and 50° coupon angles resulting in particle impact angles from 22° to 85°. The ARD 20-40 μm particles were tested at coupon angles from 30-80°, in 10° increments, resulting in particle impacts at angles from 19° to 84°. Equation (1-8) is the total COR polynomial curve fit for the ARD 20-40 μm results versus angle of impact. The total COR values for each size distribution are plotted in Figure 1-13 and Figure 1-14.

$$e = 1.25 - 2.95 \times 10^{-2}\beta + 7.04 \times 10^{-4}\beta^2 - 9.80 \times 10^{-6}\beta^3 + 4.97 \times 10^{-8}\beta^4 \quad (1\text{-}8)$$

The experiment captures a decreasing trend as particle impact angle approaches 90°, where the highest amount of energy is transferred through irreversible plastic deformation. At oblique angles, particles can glance off the surface and lose less of their total energy during impact.

The sand has a lower COR than the glass beads in general. This is expected from reviewing literature [5, 8]. The non-spherical sand particles can impact on a point, increasing localized stress in the particle, thus causing further plastic deformation and reduction in COR. The sand particles are also smaller in size than the glass beads and therefore carry less energy into an impact.

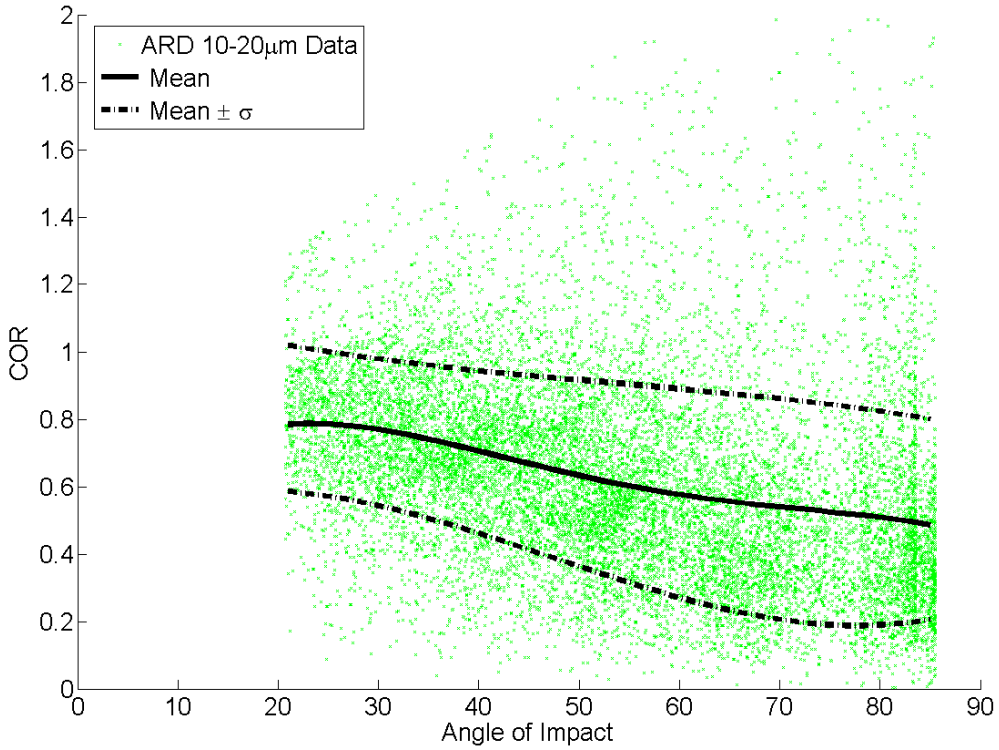

Figure 1-13. ARD 10-20 μm results

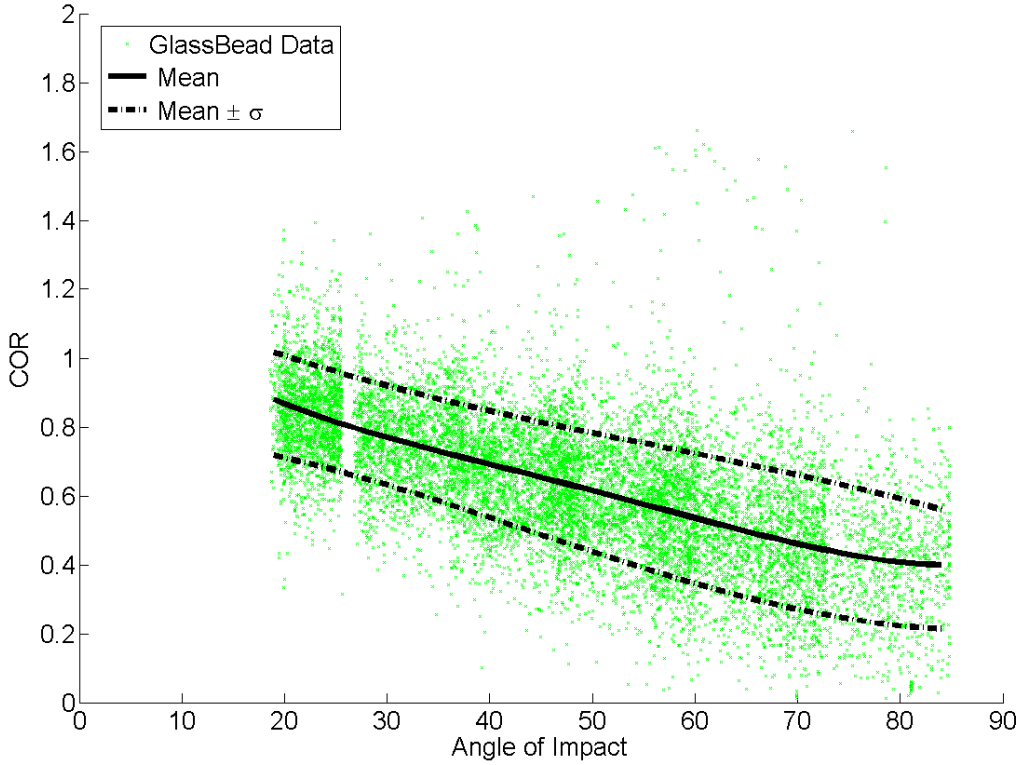

Figure 1-14. ARD 20-40 μm results

There is significant scatter at higher impact angles which can be explained given a finite size distribution of the impacting particles and the nature of the experiment. The impacting particles are treated at the mean value for the distribution. However, the individual particle sizes cannot be accurately resolved from the images. For the trajectory calculations of ARD 10-20 μm, the mean diameter of 13.46 μm was assumed, even though particles ranged from 6-22 μm. The acceleration parameter used to calculate trajectory is dependent on drag force and mass, both of which are particle size dependent. For a given v_{rel}, increasing diameter will cause acceleration to decrease for all Reynolds numbers considered in this experiment. For particles larger than the mean, the incoming velocity should be larger than that calculated by the hybrid PTV/CFD method; the rebounding velocity should be smaller than calculated. This results in higher than expected values of COR being calculated for large particles. The effects are reversed for smaller particles with a high enough Stk to impact the coupon, these smaller particles will contribute to lower than expected COR values. The COR values above one in Figure 1-13 and Figure 1-14 are not physically possible. They are a result of statistical processing in this technique but are included so an accurate mean can be reported for this ARD distribution.

Even with the size distribution accounted for, scatter would still be expected; COR experiments are statistical in nature [5, 6]. In even the most controlled experiments non-spherical particles and minute surface roughness will cause variation in the measured data due to the shadow effect documented in [8]. Other researchers have also documented the effects of adhesion in microparticle impacts at low velocity which is not exhibited at larger particle sizes at the same speeds [9].

Figure 1-15 compares mean values with [5, 6], a similar trend is exhibited for fly ash and sand impacts. A few caveats must be noted, first, that the sand particles in the comparison experiment are 150 μm while the fly ash is 15 μm. The fly ash is included for a size comparison even though it possesses a different chemical composition. The impact speeds are greater than 91 m/s, this means both of these particles impact with greater kinetic energy than the ARD particles in this study. Also different grades of steel are used as impact surfaces. With that said, these are the closest experimental comparisons available in open literature for microparticle sand and ash at different angles of impact. The comparison is quite good with the differences in impact energy accounting for lower values of COR.

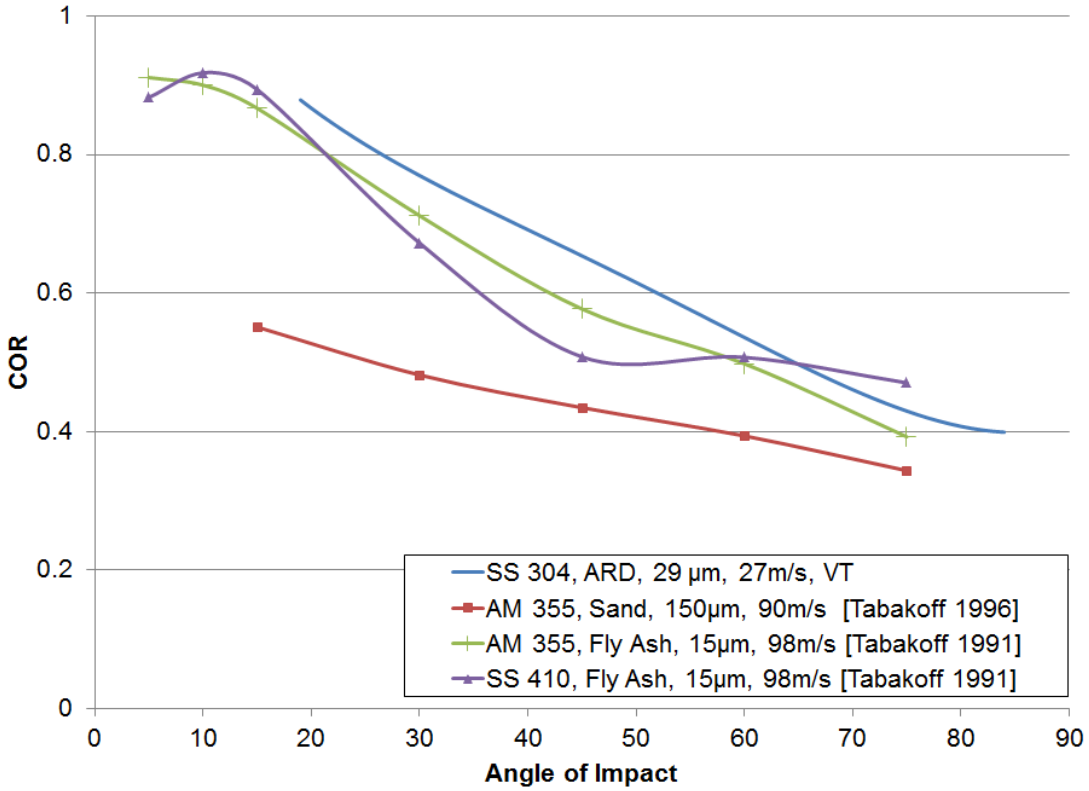

Figure 1-15. Comparison with literature COR vs angle

1.5.4 Normal & Tangential COR

As the ultimate goal of this work is to measure high temperature impact conditions and how they relate to impact, erosion, and deposition, it is also important to look at the role of tangential and normal components of COR. These components can be extracted from the data by looking at the rebound trajectory as predicted at the coupon surface and comparing to the representative incoming values for angle and velocity magnitude.

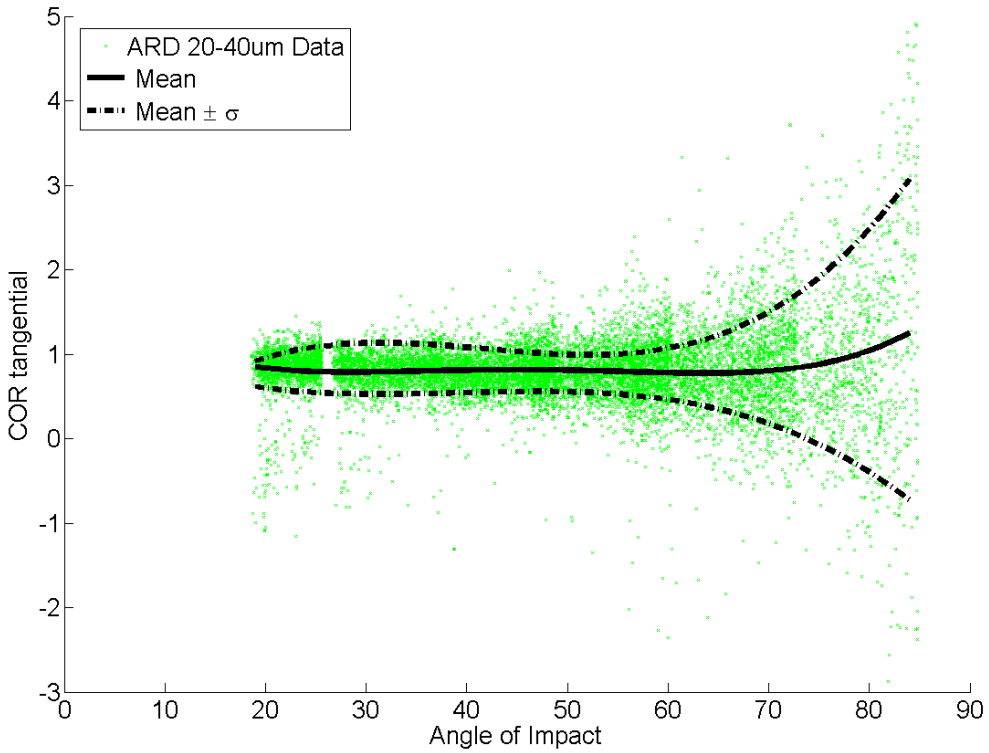

Figure 1-16. Tangential COR vs angle for ARD 20-40 μm

Figure 1-16 shows the mean and deviation for tangential COR versus angle of impact. Equation (1-9) gives the polynomial relationship for the mean value of tangential COR as a function of angle of impact.

$$e_t = 1.91 - 0.115\beta + 4.20 \times 10^{-3}\beta^2 - 6.46 \times 10^{-5}\beta^3 + 3.55 \times 10^{-7}\beta^4 \quad (1\text{-}9)$$

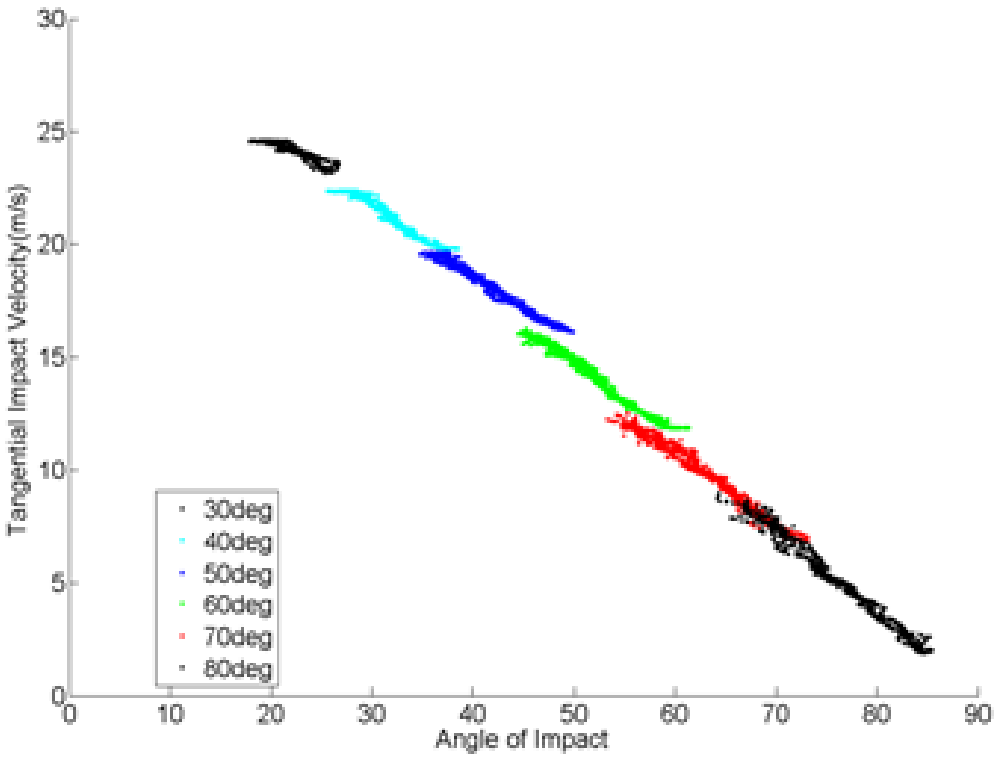

Figure 1-17. Tangential velocity vs angle for ARD 20-40 μm

Figure 1-17 is also included to show the relationship between the representative tangential impact velocity and the angle of impact. From these results, the large variation (and negative values) seen in Figure 1-16 at high impact angles can be explained by the low tangential component of velocity at high angles of impact. Any noise introduced by normal particle variation during rebound will be magnified by the small denominator in equation 1-3.

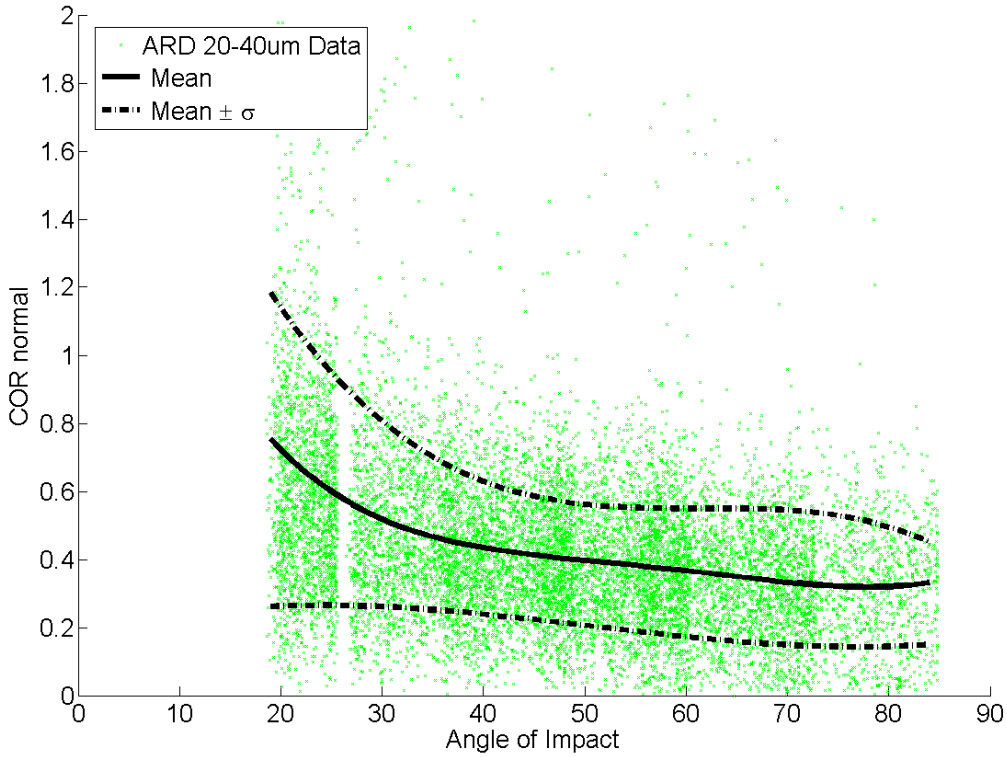

Figure 1-18. Normal COR vs angle for ARD 20-40 μm

Figure 1-18 plots normal COR vs angle of impact. Low angles of impact show the most deviation, which can be accounted for by the low values of normal impact velocity shown in Figure 1-19.

Equation (1-10) also shows the mean values of normal COR as a function of angle of impact for 20-40 μm ARD impacting 304 stainless steel at the specified test conditions.

$$(1\text{-}10)\quad e_n = 1.95 - 0.103 + 2.67 \times 10^{-3}\beta^2 - 3.11 \times 10^{-5}\beta^3 + 1.35 \times 10^{-7}\beta^4$$

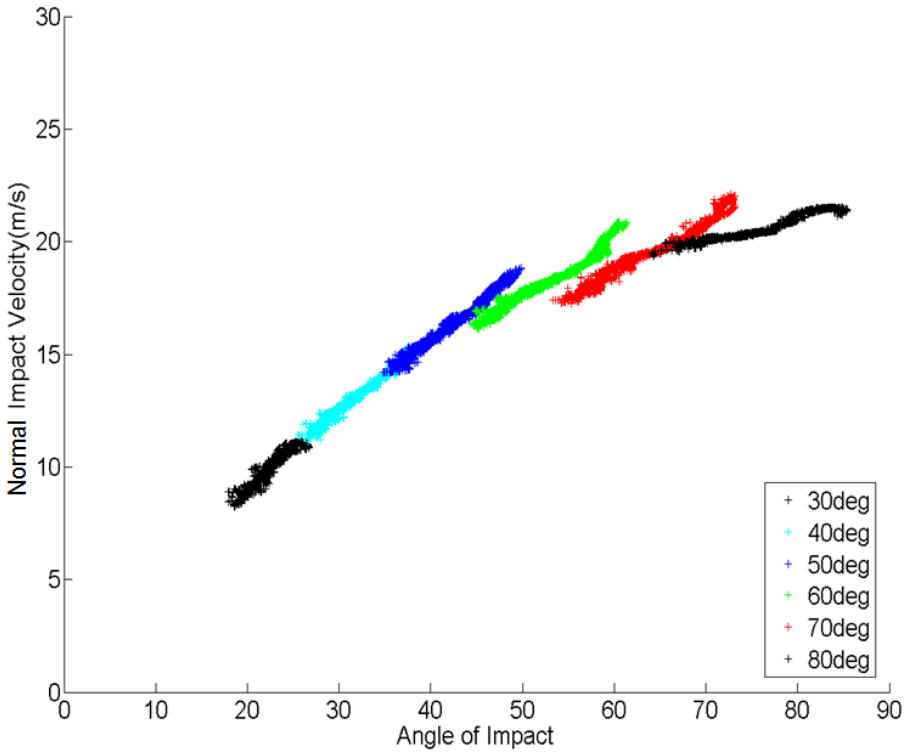

Figure 1-19. Normal velocity vs angle for ARD 20-40 µm

Figure 1-20 and Figure 1-21 show the comparison between tangential and normal components of COR compared with the work of Tabakoff *et. al*. [5, 6]. The values provided by this novel technique appear quite reasonable. The levels are slightly higher for both tangential and normal COR which is to be expected based on the difference in impact energy.

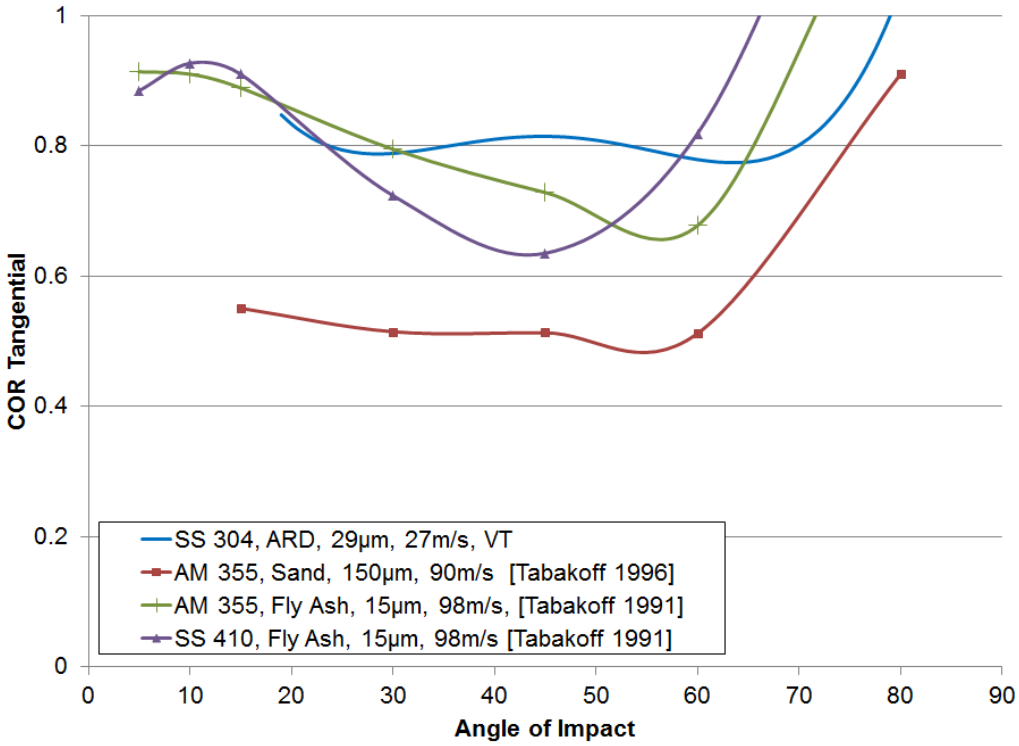

Figure 1-20. Tangential COR vs angle for ARD 20-40 µm

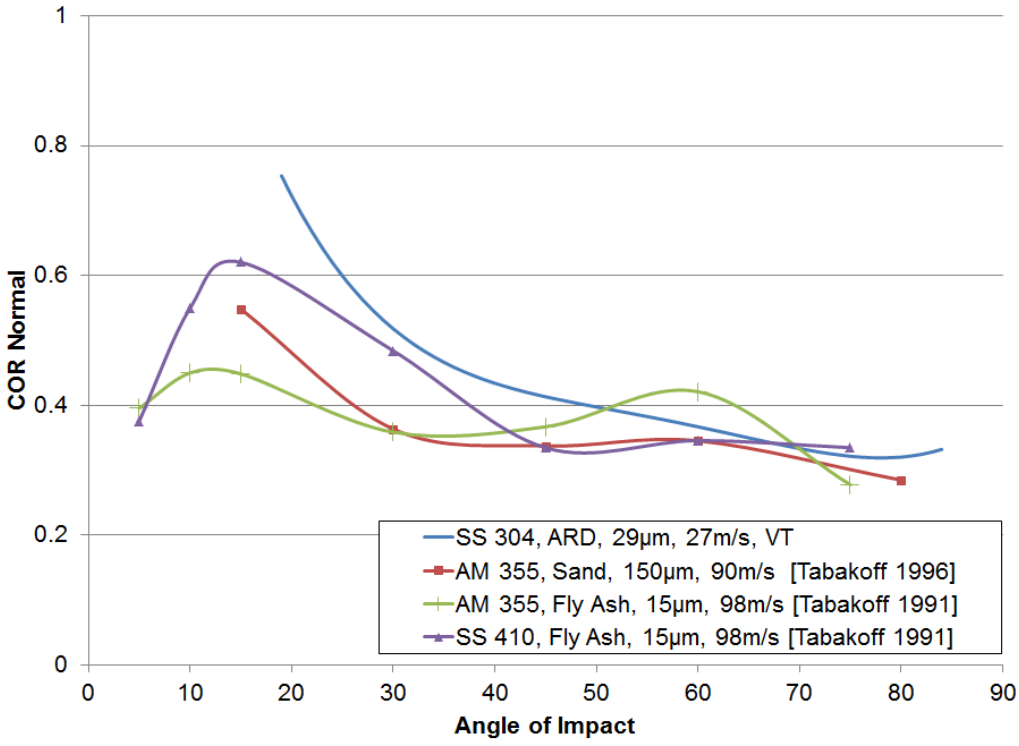

Figure 1-21. Normal COR vs angle for ARD 20-40µm

The past and current results highlight the fickle nature of microparticle impacts in realistic scenarios. A complete quantification of impact conditions is required to predict particle behavior and there exists a large range of impact conditions with little or no experimental measurements reported. An enhanced understanding of microparticle impacts can lead to better prediction and modeling. This knowledge allows engineers to tailor designs with the intention of limiting particle impact effects on critical surfaces.

1.6 Conclusions

A new hybrid PTV/CFD technique was presented to measure Coefficient of Restitution for microparticle impacts. Data from a 27 m/s free jet was presented at different angles for microparticle glass beads and sand, impacting 304 stainless steel. The empirical data presented here is intended to provide an estimate of both the sample mean and sample deviation expected from an impact of these specific materials at a given angle and velocity. The actual behavior cannot be computationally determined without investing significant resources. The results are in qualitative and quantitative agreement with past experiments for microparticles at similar, but not identical, sizes, angles, and velocities. This technique captures a large quantity of particle impacts over a wider range of impact angles than previously utilized techniques. The large sample size helps to refine the mean and standard deviation of COR, better capturing the probabilistic nature of impact. The technique can also be applied to a high temperature environment for measuring impacts. The technique does not require continuous tracking of high speed microparticles. The resulting data is of acceptable quality and can be obtained with economical, readily available hardware and software. This allows for accurate modeling of particle transport and identification of areas susceptible to particle impact effects.

1.7 Acknowledgments

The work detailed here would not be possible without the support and direction of Rolls-Royce, especially N. Wagers, K. Hsu, M. Creason, and B. Barker. The authors would also like to thank D.K. Tafti and S. Singh from Virginia Tech for their thoughtful discussion, analysis and advice.

1.8 References

[1] Hertz, H., 1896, "Miscellaneous Papers by H. Hertz," MacMillan, London, pp. 142-162.

[2] Goldsmith, W., 2002, Impact : the theory and physical behaviour of colliding solids, Dover Publications, Mineola, N.Y.

[3] Johnson, K. L., 1985, Contact Mechanics, Cambridge University Press, Cambridge, UK.

[4] Tabakoff, W., Grant, G., and Ball, R., 1974, "An Experimental Investigation of Certain Aerodynamic Effects on Erosion," AIAA-74-639.

[5] Tabakoff, W., 1991, "Measurements of Particles Rebound Characteristics on Materials Used in Gas Turbines," J. of Propulsion and Power, 7(5), pp. 805-813.

[6] Tabakoff. W, H., A., and Murugan, D.M, 1996, "Effect of Target Materials on the Particle Restitution Characteristics for Turbomachinery Application," J. of Propulsion and Power, 12(2), pp. 260-266.

[7] Eroglu, H., and Tabakoff, W., 1991, "3-D LDV Measurements of Particle Rebound Characteristics," AIAA-91-0011.

[8] Sommerfeld, M., and Huber, N., 1999, "Experimental analysis and modelling of particle-wall collisions," International Journal of Multiphase Flow, 25, pp. 1457-1489.

[9] Wall, S., John, W., Wang H.C., and Goren, S. L., 1990, "Measurements of Kinetic Energy Loss for Particles Impacting Surfaces," Aerosol Science and Technology, 12, pp. 926-946.

[10] Hylton, L., Nirmalan, V., Sultanian, B., Kaufman, R., 1988, "The Effects of Leading Edge and Downstream Film Cooling on Turbine Vane Heat Transfer," NASA Contractor Report 182133.

[11] Nealy, D., Mihelc, M., Hylton, L., Gladden, H., 1984, "Measurements of Heat Transfer Distribution Over the Surfaces of Highly Loaded Turbine Nozzle Guide Vanes," Journal of Engineering for Gas Turbines and Power, 106, pp. 149-158.

[12] Morrison, F. A., "Data Correlation for Drag Coefficient for Sphere," Department of Chemical Engineering, Michigan Technological University, Houghton, MI.

[13] Dunn, P. F., Brach, R. M., and Caylor, M. J., 1995, "Experiments on the Low-Velocity Impact of Microspheres with Planar Surfaces," Aerosol Science and Technology, 23(1), pp. 80-95.

[14] Li, X., Dunn, P.F., and Brach, R.M., 2000, "Experimental and Numerical Studies of Microsphere Oblique Impact with Planar Surfaces," Aerosol Science and Technology, 31(5), pp. 583-594.

2 Paper #2 Study of Microparticle Rebound Characteristics Under High Temperature Conditions

2.1 Abstract

Large amounts of tiny microparticles are ingested into gas turbines over their operating life, resulting in unexpected wear and tear. Knowledge of such microparticle behavior at gas turbine operating temperatures is limited in published literature. In this study, Arizona Road Dust (ARD) is injected into a hot flow field to measure the effects of high temperature and velocity on particle rebound from a polished 304 Stainless Steel (SS) coupon. The results are compared with baseline (27 m/s) measurements at ambient (300 K) temperature made in the Virginia Tech Aerothermal Rig, as well as previously published literature. Mean Coefficient of Restitution (COR) was shown to decrease with the increased temperature/velocity conditions in the VT Aerothermal Rig. The effects of increasing temperature and velocity led to a 12% average reduction in COR at 533 K (47 m/s), 15% average reduction in COR at 866 K (77 m/s), and 16% average reduction in COR at 1073 K (102 m/s) compared with ambient results. The decrease in COR appeared to be almost entirely a result of increased velocity that resulted from heating the flow. Trends show that temperature plays a minor role in energy transfer between particle and impact surface below a critical temperature.

2.2 Introduction

As global transportation and energy needs continue to expand, gas turbine engines are increasingly called upon to provide mechanical power. Many of these new or expanding markets require engines to operate in harsh, particle laden environments. These particles can cause performance deterioration through erosion and deposition of turbine parts.

A number of studies have looked at these mechanisms but there is a lack of fundamental understanding of particle trajectory after impact at engine representative conditions. Erosive particles will continue on through the engine after the initial impact and may cause subsequent damage to other areas downstream. The engine conditions that cause deposition are being investigated by a number of researchers but many upstream or secondary flows in the engine do not meet the temperature or velocity requirements to initiate deposition. There will likely be several impacts upstream before these particles may be ejected through film cooling holes or

combustion liners and deposit on hot section parts. The accurate trajectory modeling of these particles after impact can lead to a better understanding of the precise regions most susceptible to the effects of particle ingestion.

In many modeling scenarios the effects of impact are modeled using Coefficient of Restitution (COR). COR is defined

$$e = \frac{v_{reb}}{v_{in}} \tag{2-1}$$

where v_{in} is the incoming particle velocity, and v_{reb} is the velocity after impact. COR depends on a number of parameters such as material properties, velocity, particle size, impact angle, particle spin, particle sphericity, surface roughness, and temperature. The effects of these impact parameters have been well documented by researchers studying a variety of topics. Goldsmith [1] provided a wealth of knowledge on classical impacts investigated during the 20th century. In this reference, COR is shown to decrease with increasing velocity, increasing size, and decreasing hardness. Armstrong *et. al.* [2] documented that particle spin could result in curved trajectories after impact due to Magnus forces. Sommerfeld and Huber [3] documented the effects of surface roughness and sphericity. Their study showed rougher surfaces or less spherical particles tend to have lower COR and a wider scatter due to strong local deformations. The effects of temperature have been largely ignored when considering COR.

There exist few studies that can even be loosely applied to the physics of engine realistic impacts at high temperature. Mok and Duffy [4] looked at 1" steel and 2017 aluminum balls impacting lead or 6061-T6 aluminum plates at velocities of 0-5 m/s and temperatures from 294-755 K. COR results versus velocity were presented at 90^{o} impact angle. The effect of temperature on the steel ball, lead specimen impact event was negligible, likely due to the relative softness of lead. The effect of temperature on the steel ball, aluminum alloy specimen impact event was notable. COR was decreased ~0.08 at different impact velocities by increasing temperature from 294 K to 755 K.

Brenner *et al.* [5] impinged three types of iron spheres on iron plates in a hydrogen atmosphere to look at the various effects. Impact area, sticking probability and COR results were presented at 90^{o} impact angles. COR results were shown for 973 and 1073 K, type II spheres (melted drops of 120 μm thick wire) impacting an Al_2O_3 coated iron plate at velocities up to 3

m/s. COR was reduced by ~0.03 between these two temperatures. COR was shown to be proportional to $v^{-1/4}$ at one of the 1073 K test cases.

These two studies, although involving metal-metal impact at 90° impact angle, are the closest experiments involving temperature and COR that are available in open literature. Though the comparison is not ideal, evidence of temperature effects, as well as the relationship between COR and velocity, will be compared in the results section for sand-metal impacts as a sanity check.

Erosive behavior of aerospace materials has been associated with COR through a number of works by Tabakoff *et. al.* [6-9]. In these works, COR is shown to be statistical in nature. These works also show that erosion is primarily a function of tangential COR. At shallow impact angles erosion is the highest, even though bounce-back is quite efficient at these angles, resulting in a high overall COR. This was evidenced previously in the models of Finnie [10] for ductile erosion. Wakeman and Tabakoff [11] looked at erosive behavior at temperatures up to 978 K, impact velocities up to 274 m/s, and different impact angles for 150-180 μm quartz sand particles. A power law relationship was shown to fit the erosive data for increasing velocity quite well, though the coefficients varied with changing impact angle and material.

Still, COR has not been transparently presented for high temperature, engine representative particles at different angles and velocities. It is clear that more study is needed on the topic to accurately represent particle transport and energy transfer mechanisms in computational models. This work is intended to help fill in the gap between erosion and deposition experiments in literature. Erosive experiments neglect the particle after impact and deposition experiments only quantify a sticking probability associated with high temperature impact. With the current hardware at Virginia Tech and the measurement technique established by the authors, the problem of high temperature microparticle impact is investigated in the following work.

2.2.1 Nomenclature

ARD	Arizona Road Dust
e	Coefficient of Restitution (COR)
E	Elastic (Young's) Modulus
L	Length

m	mass
SS	Stainless Steel
St	Stokes Number
v	Velocity
Y	Yield Strength (0.2% Offset)

Greek

β	angle of impact
μ	viscosity
ρ	density
σ	standard deviation

Subscript

in	incoming
n	normal
p	particle
reb	rebound
t	tangential

2.3 Experimental Setup and Instrumentation

2.3.1 Aerothermal Rig

The Virginia Tech Aerothermal Rig was donated by Rolls-Royce in September 2010. This rig was used in previous heat transfer studies conducted at their facility in Indianapolis, IN by Hylton *et al.* [12] and Nealy *et al.* [13]. The operational specifications for this rig when installed in Indianapolis were reported as 2.2 kg/s at a maximum of 16 atm and 2033 K by Rolls-Royce. For the present study the VT Aerothermal Rig has been reconfigured to allow for sand injection into the main burner flow path as seen in Figure 2-1. The rig was used by Reagle *et. al.* [14] in this configuration to measure the baseline results at ambient temperature.

At Virginia Tech, the pressure and temperature capabilities for this rig are being brought up in steps as the rig is fully re-commissioned. The first step in this gradual process is igniting

the burner, which is water cooled, to temperatures within the safe operating limits of the uncooled equilibrate and test sections.

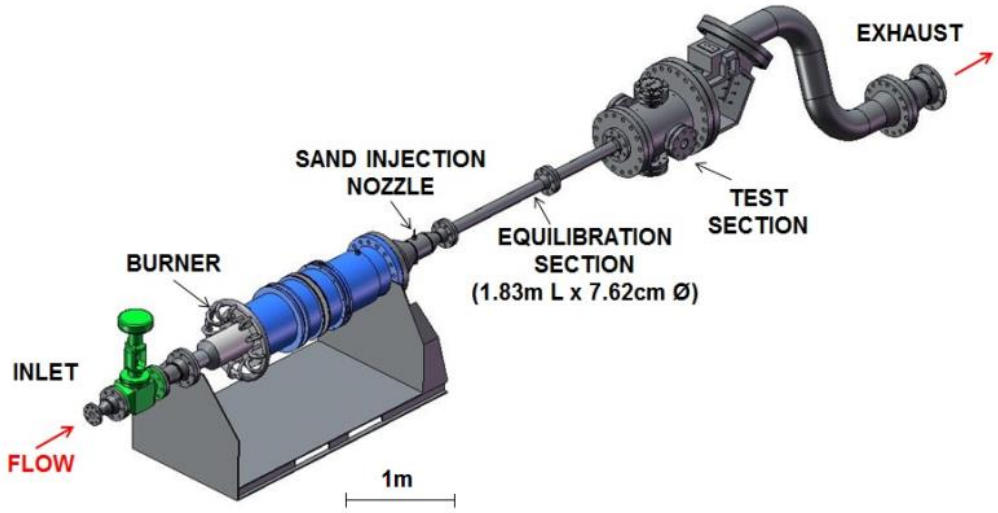

Figure 2-1. VT Aerothermal Rig configured for sand

A compressor supplies air to the rig at a constant rate of 0.15 kg/s. The flow is regulated upstream with a 10.2 cm globe valve then passes through a sudden, step expansion, into the burner section. The methane flows through a fuel ring capable of supplying 12 nozzles. The fuel exiting these nozzles mixes with the air and is ignited using a hydrogen/air pilot light. In the current study, temperature levels between 533 K, the minimum stable operating limit of the burner, and 1073 K, the current safe operating limit for the uncooled materials, are tested. The VT Aerothermal Rig is typically heated for one hour prior to the first test. Once thermocouples on the coupon, in the contraction, and in the exhaust all reach steady values, particles are injected and measurements are obtained. Due to the fixed mass flow rate being used in this test configuration, the velocity and temperature are not controlled independently. This means that as temperature increases, the velocity also increases in a proportional manner.

At the exit downstream of the burner, the cross-section of the flow is reduced in diameter from 30.5 cm to 7.62 cm. Inside the contraction section, the test particles are injected into the mainstream flow. The particles are entrained in a compressed air flow that is bled from the main

flow upstream of the burner. This relatively cool flow of sand and air is then injected and mixed with the hot mainstream flow. The particles then enter a 1.82 m long, 7.62 cm diameter equilibration tube which enables particles of various sizes to accelerate to the same speed (and temperature) as the rest of the flow. The flow exits the equilibration tube as a free jet into the test section and impinges on the test surface.

The test section shown in Figure 2-1, contains a test coupon, on which the impacts occur, and a support to allow for rotation of the coupon. The test section has a laser access port as well as optical access for the camera to image the area in front of the coupon. The camera is actively cooled using a ventilation fan to ensure consistent operation during heated testing. The test coupon has a height of 3.81 cm and is 6.35 cm long. The longer side allows a reasonable projected area perpendicular to the flow at shallow angles of attack. The coupon itself is made from SAE 304 stainless steel and can be rotated 360 degrees in 10 degree increments. The coupon has been polished to a mirror finish with an average roughness less than 500 Å as measured by a surface profilometer.

2.3.2 Instrumentation

To fully document the flow at the exit of the pipe, a Pitot-static probe and a thermocouple probe are traversed upstream of the coupon. A schematic of the test section is shown in Figure 2-2.

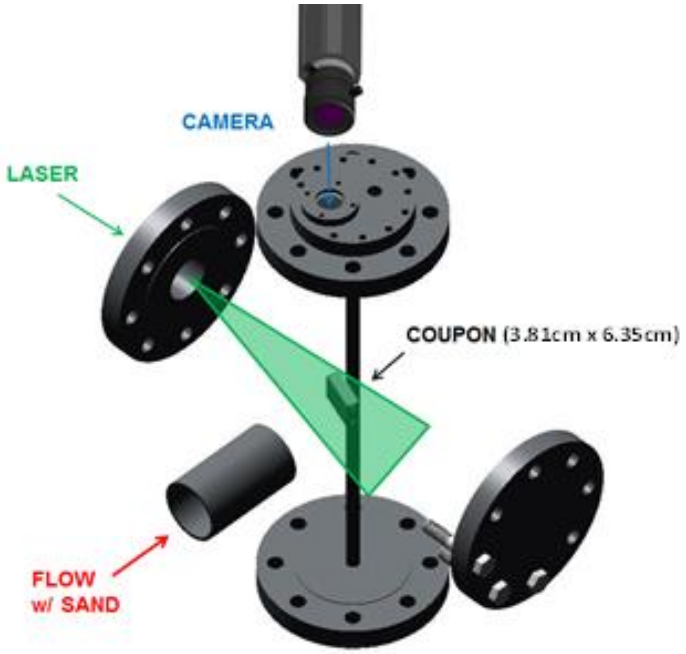

Figure 2-2. Schematic of instrumentation setup

The Pitot-static probe survey, seen in Figure 2-3, was taken at a distance of 8.13 cm upstream from the coupon face to quantify the fully developed velocity profile. The Reynolds number at the survey location is 94,000 for the 533 K case, 69,000 for the 866 K case, and 60,000 for the 1073 K case based on the diameter of the pipe.

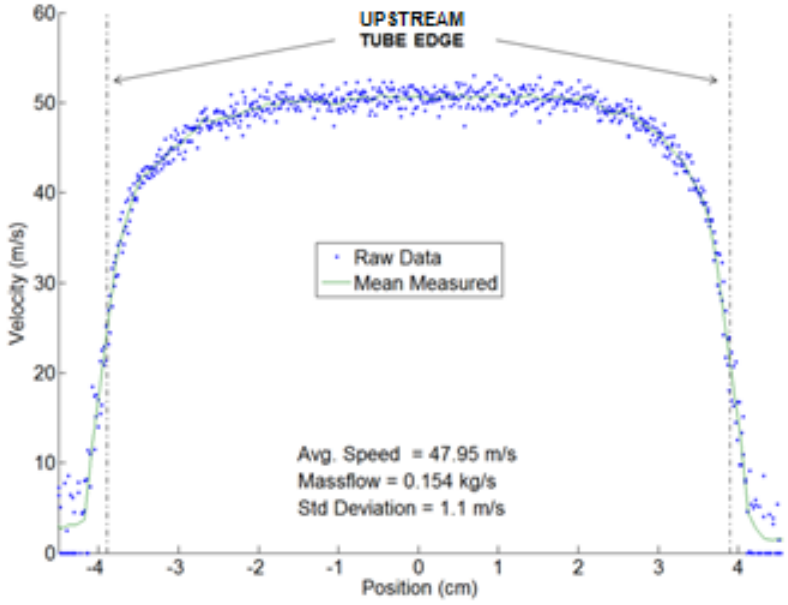

Figure 2-3. Traverse 8.13 cm upstream of coupon, 533 K

The thermocouple survey shown in Figure 2-4 plots the value of the temperature ratio between the probe measurement location, and a fixed thermocouple downstream of the test section. The survey shows a flat temperature profile upstream of the coupon. Both the Pitot probe and the thermocouple are fully withdrawn while COR data is being taken.

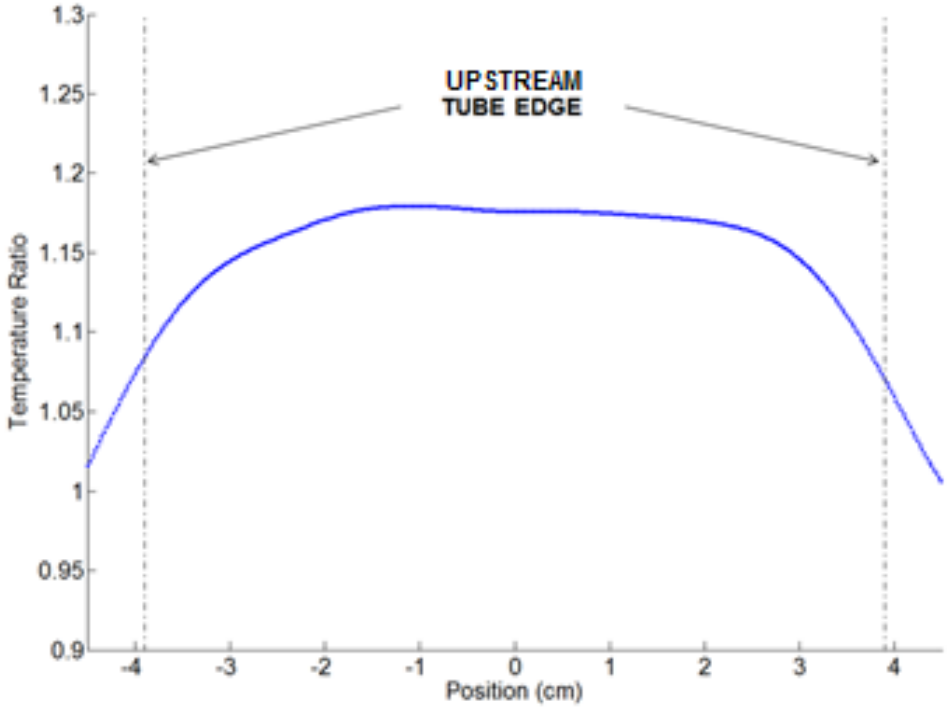

Figure 2-4. Temperature ratio 1.78 cm upstream of coupon

The laser for illuminating the particles is a twin head Litron Nd:YAG laser that emits approximately 55 mJ at 532 nm wavelength. The laser is capable of emitting two pulses of light within a few microseconds. The laser light is projected in a plane at the center of the test coupon as shown in Figure 2-2. A Dantec Dynamics® FlowSense camera equipped with a Zeiss® Makro-Planar 2/50 lens is used to capture the particle images at 2048x2048 resolution. This resolution allows for one to two pixels per particle in images taken. Both the laser and the camera are synced by a timer box ensuring illumination and imaging occur concurrently. The system can take two images within a 5 μs interval, however, the maximum sampling frequency for image pairs is 7.4 Hz.

2.3.3 Test Conditions and Material Properties

The sand particles used were Arizona Road Dust (ARD) also called Arizona Test Dust. Intermediate grades of nominal 20-40 μm were tested in this experiment. ARD has been widely used as a standard test dust for filtration, automotive and heavy equipment testing. It is also an excellent choice for studying sand ingestion in jet engines as it has very similar properties to sands found throughout the world and is readily available. The mean size by volume is 29.25 μm. More detailed information on the test dust size can be found in [14]. The chemical composition and melting point of the various constituents is presented in Table 2-1. Based on SiO_2 composition, these particles fall somewhere between pure silica sand and fly ash. Tests conducted by Walsh *et al*. [15] in a temperature controlled kiln show that a similar mixture of sand began to have visible temperature effects at 1203 K with complete melting occurring by 1363 K

Table 2-1. Chemical composition of ARD

Chemical	**% Weight**	**Melting Point (K)**
Quartz (SiO_2)	68-76	1983
Aluminum Oxide (Al_2O_3)	10-15	2323
Iron Oxide (Fe_2O_3)	2-5	1838
Sodium Oxide (Na_2O)	2-4	1548
Calcium Oxide (CaO)	2-5	2845
Magnesium Oxide (MgO)	1-2	3073
Titanium Dioxide (TiO_2)	0.5-1	3116
Potassium Oxide (K_2O)	2-5	373 (Boiling)

Table 2-2. Test Dust Properties 29.25 μm mean by volume values

Test Condition (K)	**Bulk Velocity**	**St#**
300 [14]	27	2.82
533	47	3.35
866	77	4.01
1073	102	7.44

In the current setup for the VT Aerothermal Rig, the velocity is coupled with the temperature. As the flow temperature is increased, the velocity is also increased. This effect on

the bulk velocity as well as the Stokes number, defined as a particle's inertial response compared to changes in a flow field, is presented in Table 2-2.

$$St = \frac{\rho_p d_p^2}{18\mu} \frac{v_\infty}{L_c} \tag{2-2}$$

where ρ is density, d is diameter, v is velocity, μ is viscosity, and L is the characteristic length of the system.

The temperature case of 533 K was the lowest stable operating point of the rig with heated flow. At this temperature, Potassium Oxide (K_2O), which makes up 2-5% by weight, was expected to undergo physical changes related to temperature. Potassium Oxide was of interest in this study as the pure compound is highly reactive, boiling easily at atmospheric pressure. Schairer and Bowen [16] showed that increased amounts of K_2O in a K_2O-SiO_2-Al_2O_3 system causes reduced melting points. These three components comprise between 80-96% of the particles. The rest of the pure components in the ARD have melting points in excess of experimental capabilities and exist in quantities less than or approximately equal to K_2O.

The temperature case of 866 K was chosen because SiO_2 undergoes a crystal transformation from α-quartz to β-quartz at a temperature of 846 K and normal pressure. This change occurs quite suddenly and comes with a change in bond angle and an expansion from 2.65 g/cm^3 to 2.53 g/cm^3 [17].

The 1073 K test case was chosen as an acceptable operating limit for the stainless steel test section components which were not actively cooled. It was hypothesized that this high of temperature would cause a relative change in material properties between the particle and the coupon leading to a significant reduction in COR. This was within 130 K of the first visible signs of temperature effects for the particles as shown in [15].

2.4 Data Reduction

Coefficient of restitution is defined by the particle velocities just before and just after impact. The hardware used in the VT Aerothermal Rig has a maximum repetition rate of 7.4Hz per image pair. This does not allow for continuous tracking of particles at engine representative speeds because almost all of the particles move out of the interrogation region between image

frames. This has two consequences. First is that the majority of the particle measurements are made some distance away from the coupon. Second is that an impacting particle cannot be uniquely identified before and after impact. The experimental approach discussed in [14] mitigates these consequences without the purchase of exotic or expensive imaging hardware or software. A brief summary is presented below.

The first step is to take each image pair and determine particle velocities. The particles are tracked by correlating particle locations between frames to minimize total displacement. Only particles that can be uniquely correlated are kept. The particles are then classified as incoming or rebounding based on their trajectory angle with respect to the coupon angle. Assuming that the flow field is steady in front of the coupon, the flow field can be used calculate particle paths, forward for incoming or backwards for rebounding, in time using a finite difference method to yield velocities just before hitting the coupon face. The impacting and rebounding velocities become a function of the measured particle velocity, the particle velocity relative to the flow field (v_{rel}), particle mass, and particle size.

The equations used for calculating particle trajectories are relatively straightforward with the exception of the relative velocity between the particle and the flow, v_{rel}. At the exit of the pipe, v_{rel} is close to zero. However, as the sand particles approach the plate, the velocity gradients in the forced flow field have a tangible effect on the particle trajectory. To account for this effect, a CFD flow field is calculated in front of the coupon for the sole purpose of estimating the relative velocity difference between the particle and the flow at its current location in the finite difference calculation. The particle measurements are then mapped onto the CFD flow field and tracked to the coupon face.

The average incoming velocity and impact angle is then calculated as a function of impact location along the coupon face. The rebounding velocity for each individual particle is then compared with the average incoming particle data at the impact location to calculate a single COR data point. All of the runs at a given temperature/velocity condition are then combined and analyzed to calculate a mean and a standard deviation

This results in a range of particle impact angles for a single coupon angle. Figure 2-5 shows the compilation of multiple coupon angles to show the overlap between different angles of the coupon plate. At high temperatures, the cost of testing for extended periods can be quite high, especially as more mass flow is added and the rig is brought up to full capability. The

current technique allows for collection of thousands of impact events in a relatively short data taking window. This also helps to eliminate the effects of erosion on the coupon, which can significantly affect results. Surface roughness measurements following a set of heated runs showed average roughness to have increased, but still remained less than 1000Å.

2.5 Results

The results published here document the effects of temperature/velocity on microparticle sand impacting stainless steel 304 at different angles. In the following results, only the mean COR values are plotted for clarity.

2.5.1 Standard Deviation and Uncertainty

It is important to note that the majority of the variation seen in the data is real variation due to the non-spherical nature of the particles, surface asperity, particle spin, and variations in particle size. This means that particles impacting at exactly the same velocity can have a very different COR based on differences in the previously mentioned parameters. The standard deviation and the mean of the COR are the method most commonly used to quantify the probability distribution that results from this variation in particle COR. A sample of the data obtained through the data reduction method as well as the mean and standard deviation lines used to define the probability distribution are shown in Figure 2-5.

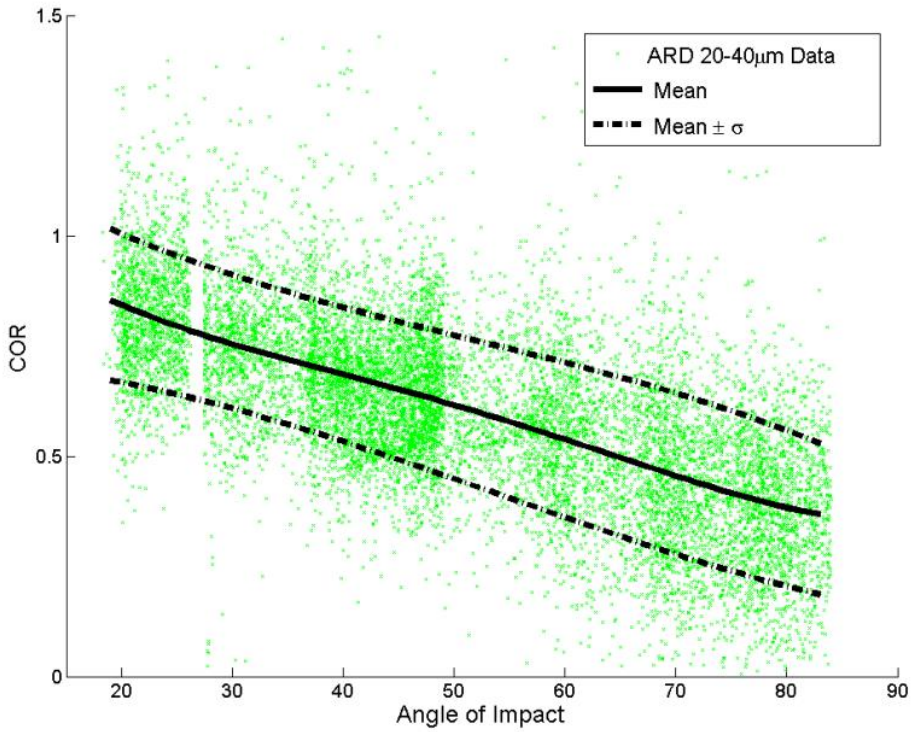

Figure 2-5. Data points with mean and standard deviation lines plotted

The average standard deviation for COR across all test cases is $\sigma = 0.17$. The values for normal and tangential components varied widely with angle. At angles up to 48°, σ_t was less than 0.3 for all cases while angles above 74° resulted in σ_t values above 1 for all cases. For normal COR, σ_n decreased from a maximum of 0.43 at 19° angle of impact to less than 0.2 at angles greater than 40° for all compared cases. Table 2-3 shows representative values of standard deviation for COR, tangential COR, and normal COR.

Table 2-3. Average Deviation from Mean Values

Angle of Impact	**σ**	**σ_t**	**σ_n**
25	0.14	0.25	0.26
35	0.15	0.27	0.21
45	0.17	0.24	0.17
55	0.18	0.31	0.17
65	0.19	0.56	0.18
75	0.18	0.95	0.16

2.5.2 Total Coefficient of Restitution

Impact of Arizona Road Dust impacting a polished SS 304 coupon was measured at coupon angles from 30-80° at four temperatures/velocities. Figure 2-6 shows the total COR results for all four temperature/velocity conditions vs angle of impact. COR vs angle of impact was shown to decrease at all angles as temperature/velocity increased. The raw data has been fit to a polynomial and Equations (2-3), (2-4), and (2-5) present the COR as a function of impact angle for the three heated test cases. The average decrease in COR for the increased temperature and velocity conditions was 12% for the 533 K (47 m/s), 15% for the 866 K (77 m/s) case, and 16% for the 1073 K (102 m/s) case.

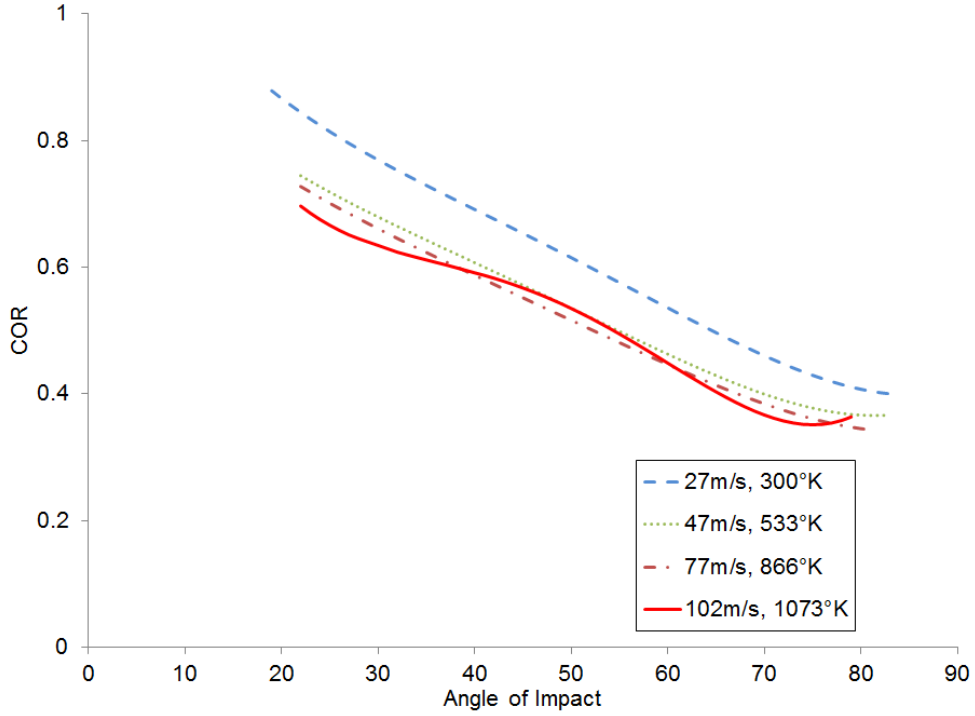

Figure 2-6. ARD 20-40 µm results COR vs angle

(2-3) $e_{v,533K} = 1.06 - 2.28 \times 10^{-2}\beta + 5.37 \times 10^{-4}\beta^2 - 8.02 \times 10^{-6}\beta^3 + 4.40 \times 10^{-8}\beta^4$

(2-4) $e_{v,866K} = 1.03 - 2.09 \times 10^{-2}\beta + 4.43 \times 10^{-4}\beta^2 - 6.32 \times 10^{-6}\beta^3 + 3.39 \times 10^{-8}\beta^4$

(2-5) $e_{v,1073K} = 1.72 - 9.23 \times 10^{-2}\beta + 2.9 \times 10^{-3}\beta^2 - 4.05 \times 10^{-5}\beta^3 + 1.99 \times 10^{-7}\beta^4$

2.5.3 Normal Coefficient of Restitution

Figure 2-7 shows the normal COR vs angle for all temperature/velocity conditions. Equations (2-6), (2-7), and (2-8) present normal COR as a function of impact angle for the heated test conditions. The heated cases were within 1.5% of each other on average. The experimental repeatability for the ambient data was 1.5% as documented in [14]. The shallow angle of impact data less than 35° showed all the heated trends crossing over the ambient trend but it should be noted that these angles of impact had the highest deviation.

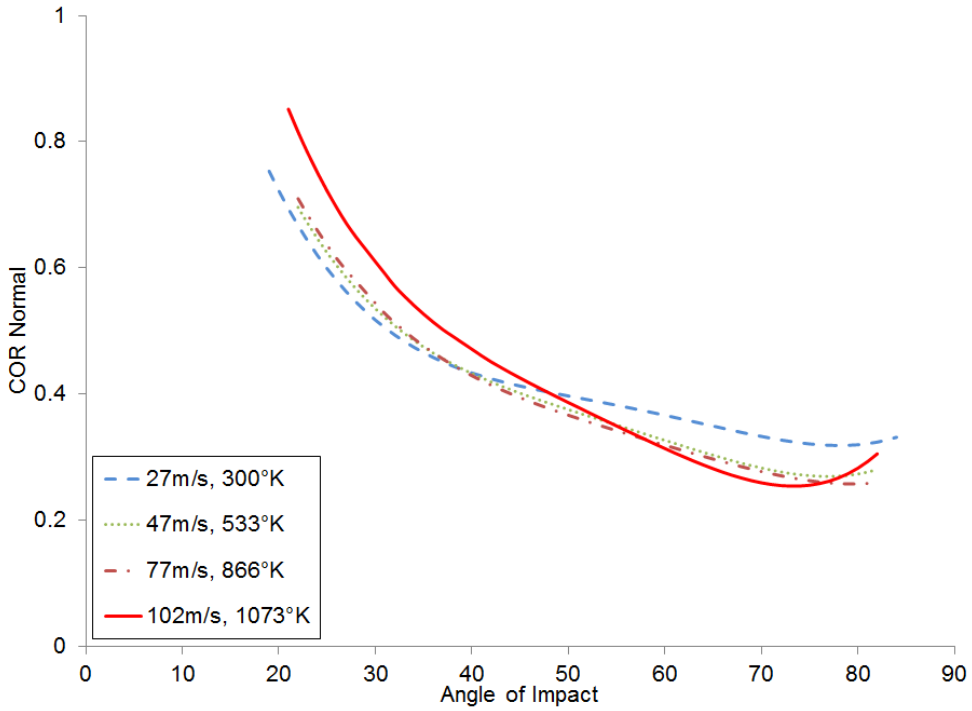

Figure 2-7. ARD 20-40 µm normal COR vs angle

(2-6) $e_{n,533K} = 1.98 - 0.102\beta + 2.60 \times 10^{-3}\beta^2 - 3.09 \times 10^{-5}\beta^3 + 1.38 \times 10^{-7}\beta^4$

(2-7) $e_{n,866K} = 1.93 - 9.34 \times 10^{-2}\beta + 2.24 \times 10^{-3}\beta^2 - 2.52 \times 10^{-5}\beta^3 + 1.08 \times 10^{-7}\beta^4$

(2-8) $e_{n,1073K} = 2.28 - 1.146 \times 10^{-1}\beta + 2.8 \times 10^{-3}\beta^2 - 3.28 \times 10^{-5}\beta^3 + 1.45 \times 10^{-7}\beta^4$

2.5.4 Tangential Coefficient of Restitution

Figure 2-8 shows the tangential COR vs angle of impact for all temperature/velocity conditions. Equations (2-9), (2-10), and (2-11) present COR as a function of impact angle for the heated test conditions. Tangential COR was shown to decrease with increasing temperature/velocity.

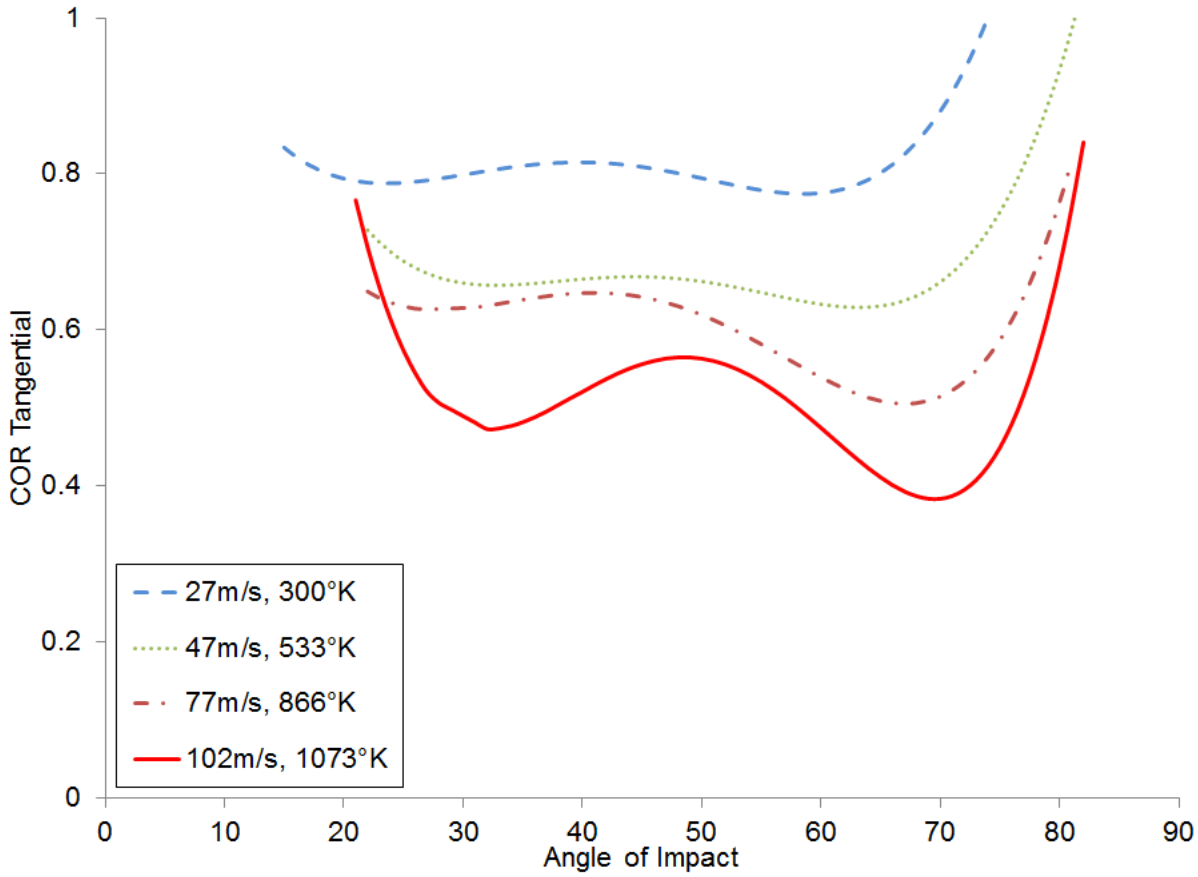

Figure 2-8. ARD 20-40 µm tangential COR vs angle

(2-9) $e_{t,533K} = 2.31 - 0.157\beta + 5.40 \times 10^{-3}\beta^2 - 7.97 \times 10^{-5}\beta^3 + 4.26 \times 10^{-7}\beta^4$

(2-10) $e_{t,866K} = 1.98 - 0.142\beta + 5.34 \times 10^{-3}\beta^2 - 8.39 \times 10^{-5}\beta^3 + 4.63 \times 10^{-7}\beta^4$

(2-11) $e_{t,1073K} = 7.39 - 0.628\beta + 2.03 \times 10^{-2}\beta^2 - 2.76 \times 10^{-4}\beta^3 + 1.34 \times 10^{-6}\beta^4$

While this study does not measure erosion, Erosion has been shown to be a function of tangential COR [6, 7]. Results for quartz sand impacting SS410 in [6] indicate a local minimum of tangential COR at approximately 30° which corresponds with the angle of maximum erosion. Erosion rate at this angle is more than twice as severe as subsequent measurements at 45°. Ductile materials typically have a shallow angle of impact associated with maximum erosion rates that corresponds with a local minimum of tangential COR. Brittle materials have been shown to have a different erosion mechanism with maximum erosion at higher angles of impact. The ductile model of material removal has been developed by Finnie [10] but does not account for erosion at 90° impact angles. Aside from ductile erosion at shallow angles of impact, there is not much agreement in open literature over the erosion mechanisms at normal impact angles or with brittle materials.

Unfortunately, the quartz sand study [6] is the only published work to look at both tangential COR and erosion. In the current study, as seen in Figure 2-8, there is a relatively flat trend for ambient and 533 K (47 m/s) and a relatively flat trend with a distinct local minima at 68° for the 866 K (77 m/s) case. The 1073 K (102 m/s) case also exhibits this minima but has an additional minima at approximately 31° degree also. These may indicate the onset of erosion due to the higher velocities for the microparticles impacting stainless steel, but further study is needed. Future experiments documenting the relationship between tangential COR and erosion would be beneficial in helping to predict the effects of particle ingestion at engine realistic conditions.

2.6 Discussion on Temperature/Velocity Effects

The main source of energy loss during impact is the result of plastic deformation. Dislocations and imperfections in the crystal structure are moved through the material, attempting to distribute the impulse and find equilibrium during compression. At increased temperatures, the atoms vibration amplitude increases, increasing the position between stable atom locations. This leads to decreased bond strength in the material allowing dislocations in the crystal structure to relocate with less force, thus increasing plastic deformation and reducing COR.

Many of the relationships that have been analytically developed, and are available in sources such as Fischer-Cripps [18] for elastic-plastic impact, involve the ratio E/Y, where E is the elastic modulus and Y is the Yield Strength. However, much of the experimental rebound data does not exhibit a clear relationship between the material properties of E, Y or Hardness. The complex interplay between these changes in material properties over a rapid impact event can prove very difficult to predict. While the effects of temperature on COR have not been thoroughly documented, some empirical data has been correlated COR to changes in velocity.

2.6.1 Power Law

Various references [5, 19] have suggested that COR decreases proportionally with velocity according to the equation

(2-12) $$e = av^{-b}$$

where a and b are constants. These sources have shown a to be related to the impact conditions (i.e. materials, angle, etc.) and b to be equal to ¼ for 90° impacts. Similar variation of the rebound velocity vs impact velocity at oblique angles was measured by Hutchings *et. al.* [20] for hardened steel spheres impacting mild steel targets, however, tabulated data was not available for accurate comparison with the current trends.

As there are no correlations in open literature for the relationship between temperature, velocity and COR, the current discussion uses Equation (2-12) as a starting point for analysis,

where v is the coupled temperature/velocity conditions in the VT Aerothermal Rig. Temperature has been shown to decrease COR and eventually lead to deposition. It is hypothesized that coupling a temperature increase with a velocity increase would substantially decrease COR.

The first step in this analysis is to assume Equation (2-12) is true for oblique, sand-metal impacts and see if the equation fits the data for changes in velocity impact conditions. The analysis in Figure 2-9 plots the total COR results for a few angles on the y-axis versus velocity on the x-axis utilizing a log-log scale. The corresponding power law coefficients are also attached in Table 2-4.

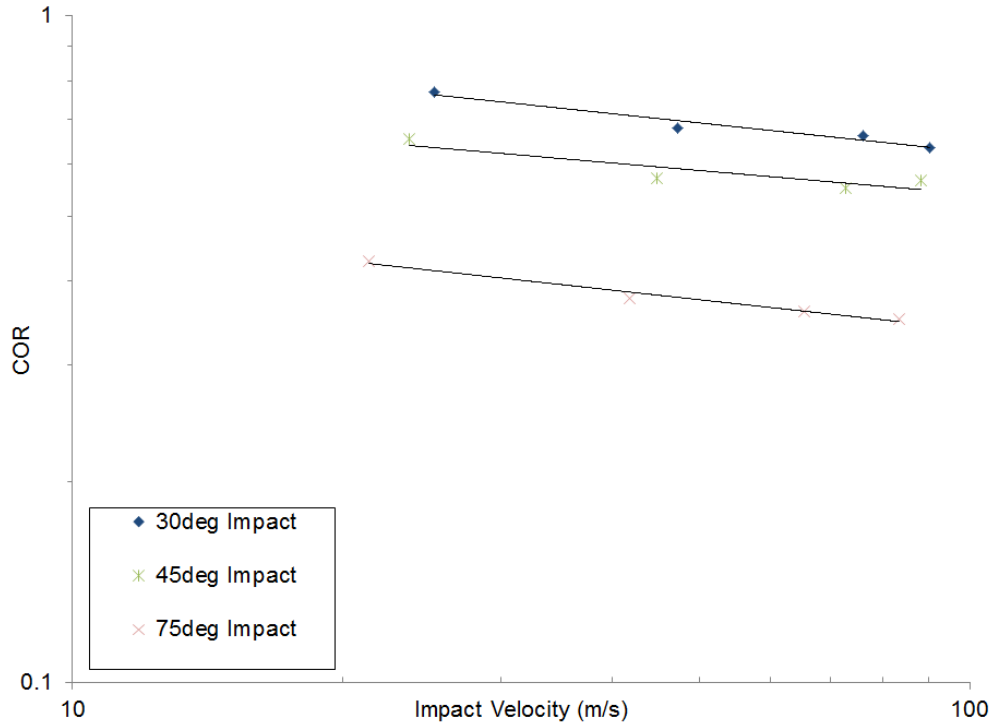

Figure 2-9. ARD 20-40 µm COR vs Velocity

Table 2-4. Power Law curve fit parameters

Angle	**a**	**b**	**R^2**
25	1.3021	0.148	0.944
30	1.2074	0.143	0.954
35	1.1049	0.124	0.944
40	1.0074	0.124	0.889
45	0.9237	0.116	0.807
50	0.863	0.115	0.768

55	0.8221	0.122	0.798
60	0.7989	0.136	0.878
65	0.7814	0.152	0.947
70	0.7487	0.162	0.974
75	0.6678	0.147	0.975

The coefficient of determination (R^2) indicates good agreement over most of the dataset. However, there is relatively poor agreement from 40-60 degrees, where the 1073 K (102 m/s) COR vs angle trend line intersects the lower temperature/velocity cases as shown in Figure 1-14. This data is within the uncertainty of the measurement technique.

The *b* trend is also of interest to this study because it appears much lower than the 0.25 value found in previous studies. A *b* value of 0.25 would predict that COR would decrease more (for the same increase in velocity) than was measured in the current set of experiments. The 0.25 value was measured by other researchers at constant temperature. It was hypothesized that increased temperature would further decrease COR leading to *b* values greater than 0.25, which were not witnessed in the current study. The 0.25 value was found for metal spheres, larger than 120 μm, impacting metal plates whereas the current study has 20-40 μm rough sand impacting metal. This may account for the difference in *b* seen in this study but more experimentation is necessary to confirm this relationship.

2.6.2 Perfectly Plastic Collisions

While the literature available for COR at different temperatures is limited and applies loosely to the current study, there is much larger body of work involving deposition, which can be interpreted as a special case, where COR = 0, a perfectly plastic collision.

It has been shown by a number of researchers studying deposition that above a critical temperature, particles begin to stick to the impacting surface. The critical temperature was determined by Crosby *et. al.* [21] to be 1233 K for 3 μm coal ash which had approximately 47.4% Si by weight. Above the critical temperature, deposition increased exponentially. This is in agreement with the computational model developed by Sreedharan and Tafti [22] that bases deposition on critical viscosity.

Assuming, based on deposition research and modeling, that at 1363 K (the 100% melting point of ARD [15]) the sticking probability is 100%, COR = 0. At the ARD melting temperature of 1363 K, (~130 m/s if tested in the VT Aerothermal Rig) the trend lines from the current dataset would predict COR values at different impact angles in the range of 0.32-0.63. The trend developed in the current set of experiments would have to deviate sharply between 1073 K and 1363 K to agree with deposition research in published literature. It is hypothesized that there exists a critical temperature greater than 1073 K at which COR of ARD-SS impacts will decrease exponentially, similar to the exponential increase in sticking probability seen in deposition experiments.

2.6.3 Kinetic Energy

Attempts were made to normalize the existing data for comparison due to lack of experimental research under engine representative impact conditions. In Figure 2-10, COR at a given angle was plotted on a log-log scale against average incoming particle kinetic energy (KE). Data from Tabakoff *et al.* [8, 9] was included to see if the velocity and size differences between experiments could be mitigated. The KE of the fly ash data fell in between the ambient and 533^{o}K data set, the sand data had a much higher KE.

Qualitatively, it appears a smooth relationship between COR and KE exists at higher impact angles. However, it did not hold a power law relationship, thus COR must scale differently with mass/material properties. This exercise, while informative, did not lead to an overall correlation between COR and KE. There were not enough points to satisfactorily determine a polynomial relationship without directly solving for coefficients. Developing a universal relationship for COR with engine realistic impact conditions would be a major breakthrough in the study of particle ingestion effects.

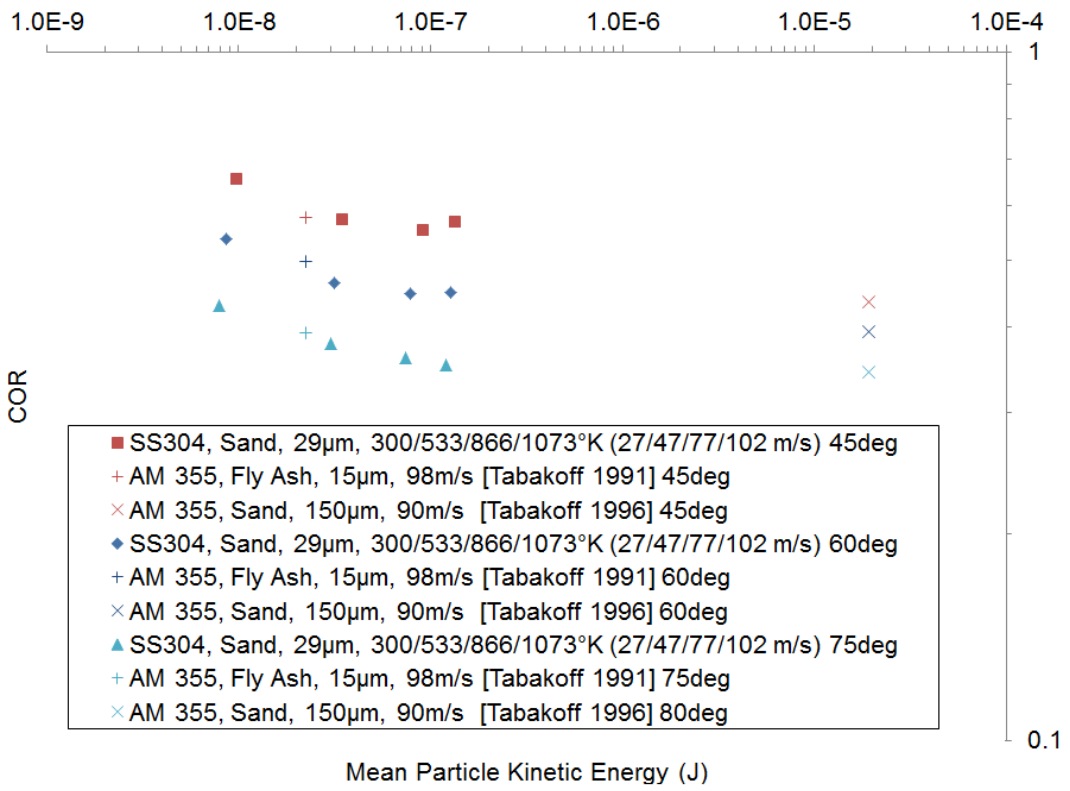

Figure 2-10. ARD 20-40 µm COR vs KE ($^1/_2\, mv^2$)

2.7 Conclusions

The discussed work begins to document uninvestigated areas of impact research. Oblique impacts at high temperature have only been documented with respect to the deposits formed or material removed. Previous normal impacts experiments at high temperature involve materials and sizes that are not engine representative. The empirical correlations developed here can be readily integrated into commercial CFD code. When run on engine geometry, the subsequent modeling of impact and re-entrainment into the flow can predict areas susceptible to erosion in secondary flows and accurate particle trajectories exiting cooling channels into hot gas paths where deposition is a concern.

Datasets at engine realistic particle size and temperature were presented at different angles and velocities for microparticle sand impacting 304 Stainless Steel. The data presented here is intended to provide an estimate of both the mean and variance expected from an impact of these specific materials at a given angle, temperature, and velocity, which has not been

presented in prior gas turbine literature. Experimental results presented at 533 K (47 m/s), 866 K (77 m/s), and 1073 K (102 m/s) show that COR is reduced by an average of 12%, 15%, and 16% respectively over ambient baseline results. This is attributed primarily to the increase in velocity that is coupled to the temperature increase in the VT Aerothermal Rig. The reduction in elastic modulus and yield strength of the steel, along with the material changes in the ARD, were expected to play a larger part in the impact mechanics as temperature increased. Temperatures up to 1073 K do not appear to significantly reduce COR, as has been witnessed at higher temperatures where plastic collisions can result in deposition.

2.8 Acknowledgments

The work detailed here would not be possible without the support and direction of Rolls-Royce, Indianapolis, IN. The authors would also like to thank D.K. Tafti and S. Singh from Virginia Tech for their thoughtful discussion, analysis and advice.

2.9 References

[1] Goldsmith, W., 2002, Impact : the theory and physical behaviour of colliding solids, Dover Publications, Mineola, N.Y.

[2] Armstrong, J. D., Collings, N., and Shayler, P.J., 1984, "Trajectory of Particles Rebounding Off Plane Targets," AIAA, 22(2), pp. 214-218.

[3] Sommerfeld, M., and Huber, N., 1999, "Experimental analysis and modelling of particle-wall collisions," International Journal of Multiphase Flow, 25, pp. 1457-1489.

[4] Mok, C. H., and Duffy, J., 1964, "THE BEHAVIOUR OF METALS AT ELEVATED TEMPERATURES UNDER IMPACT WITH A BOUNCING BALL," Int J Mech Sci, 6, pp. 161-175.

[5] Brenner, S. S., Wriedt, H. A., and Oriani, R. A., 1981, "Impact adhesion of iron at elevated temperatures," Wear, 68(2), pp. 169-190.

[6] Tabakoff, W., Grant, G., and Ball, R., 1974, "An Experimental Investigation of Certain Aerodynamic Effects on Erosion," AIAA-74-639.

[7] Grant, G., and Tabakoff, W., 1975, "Erosion Prediction in Turbomachinery Resulting from Environmental Solid Particles," J. Aircraft, 12(5), pp. 471-478.
[8] Tabakoff, W., 1991, "Measurements of Particles Rebound Characteristics on Materials Used in Gas Turbines," J. of Propulsion and Power, 7(5), pp. 805-813.
[9] Tabakoff. W, H., A., and Murugan, D.M, 1996, "Effect of Target Materials on the Particle Restitution Characteristics for Turbomachinery Application," J. of Propulsion and Power, 12(2), pp. 260-266.
[10] Finnie, I., 1960, "Erosion of surfaces by solid particles," Wear, 3(2), pp. 87-103.
[11] Wakeman, T., and Tabakoff, W., 1979, "Erosion Behavior in a Simulated Jet Engine Environment," J. Aircraft, 16(12), pp. 828-833.
[12] Hylton, L., Nirmalan, V., Sultanian, B., Kaufman, R., 1988, "The Effects of Leading Edge and Downstream Film Cooling on Turbine Vane Heat Transfer," NASA Contractor Report 182133.
[13] Nealy, D., Mihelc, M., Hylton, L., Gladden, H., 1984, "Measurements of Heat Transfer Distribution Over the Surfaces of Highly Loaded Turbine Nozzle Guide Vanes," Journal of Engineering for Gas Turbines and Power, 106, pp. 149-158.
[14] Reagle, C. J., Delimont, J.M., Ng, W.F., and Ekkad, S.V., 2012, "A NOVEL TECHNIQUE FOR MEASURING THE COEFFICIENT OF RESTITUTION OF MICROPARTICLE IMPACTS IN A FORCED FLOWFIELD," GT2012-68252.
[15] Walsh, W. S., Thole, K. A., and Joe, C., 2006, "Effects of Sand Ingestion on the Blockage of Film-Cooling Holes," ASME Conference Proceedings, 2006(4238X), pp. 81-90.
[16] Schairer, J. F., and Bowen, N.L., 1947, "Melting Relations in the systems Na2O-Al2-O3-SiO2 and K2O-Al2-O3-SiO2," American Journal of Science, 245(4), pp. 193-204.
[17] Wenk , H.-R., and Bulakh, A., 2003, Minerals - Their Constitution and Origin, Cambridge University Press, Cambridge, UK.
[18] Fischer-Cripps, A. C., 2000, Introduction to Contact Mechanics, Springer.
[19] Johnson, K. L., 1985, Contact Mechanics, Cambridge University Press, Cambridge, UK.
[20] Hutchings, I. M., Macmillan, N. H., and Rickerby, D. G., 1981, "Further studies of the oblique impact of a hard sphere against a ductile solid," International Journal of Mechanical Sciences, 23(11), pp. 639-646.

[21] Crosby, J. M., Lewis, S., Bons, J. P., Ai, W., and Fletcher, T. H., 2008, "Effects of Temperature and Particle Size on Deposition in Land Based Turbines," Journal of Engineering for Gas Turbines and Power, 130(5), p. 051503.

[22] Sreedharan, S. S., and Tafti, D. K., 2011, "Composition dependent model for the prediction of syngas ash deposition in turbine gas hotpath," International Journal of Heat and Fluid Flow, 32(1), pp. 201-211.

3 Paper #3: Effect of Temperature on Microparticle Rebound Characteristics at Constant Impact Velocity

3.1 Abstract

Many gas turbine engines operate in harsh environments where the engines ingest solid particles. Ingested particles accelerate the deterioration of engine components and reduce the engine's service life. Understanding particle impacts on materials used in gas turbines at representative engine conditions leads to improved designs for turbomachinery operating in particle-laden environments. Coefficient of Restitution (COR) is a measure of particle/wall interaction and is used to study erosion and deposition. In the current study, the effect of temperature (independent of velocity) on COR was investigated. Arizona Road Dust (ARD) of 20-40μm size was injected into a flow field to measure the effects of temperature and velocity on particle rebound. Target coupon materials used were 304 stainless steel and Hastelloy X. Tests were performed at three different temperatures, 300 K (ambient), 873 K, and 1073 K while the velocity of the flow field was held constant at 28 m/s. The impingement angle of the bulk sand on the coupon was varied from 30° to 80° for each temperature tested. The COR was found to decrease substantially from the ambient case to the 873 K and 1073 K cases. This decrease is believed to be due to the changes in the surface of both materials due to oxide layer formation which occurs as the target material is heated. The Hastelloy X material exhibits a larger decrease in COR than the stainless steel 304 material. The results are also compared to previously published literature.

3.2 Introduction

Gas turbines are a popular source of mechanical power. Many of these engines operate in particle-laden environments which is detrimental to engine performance. Aircraft operating in remote locations or at low altitudes are particularly prone to particle ingestion. Engines operating in desert environments will be subject to sand, dust, and other particulate ingestion (See Figure 3-1). Natural disasters such as volcanic eruptions and dust storms can lift significant amounts solid particulate to aircraft cruising altitudes. Particle ingestion reduces engine life and performance through both erosion and deposition.

Figure 3-1. V-22 Osprey [Department of Defense]

Several computational studies have investigated the effects of erosion and deposition on gas turbines. These computational studies involving particle impact have used either empirical impact correlations, which have only previously been reported for low temperatures, or analytical impact models. Analytical models make many assumptions to simplify the collision so that a simplified model can be developed. The present study presents the impact and rebound characteristics of microparticle sand to enable more accurate impact modeling for use in computational analysis of sand transport inside gas turbine geometry.

Coefficient of Restitution (COR) is a measure of the particle/wall interactions and is used to study erosion and deposition. COR is defined as:

$$e = \frac{V_2}{V_1} \tag{3-1}$$

where V_2 is the velocity after impact and V_1 is the velocity before impact. Figure 3-2 displays a diagram of a particle's trajectory before and after impact. The solid lines in Figure 3-2 represent

the particles' actual velocity while the dotted lines represent the normal and tangential components of velocity.

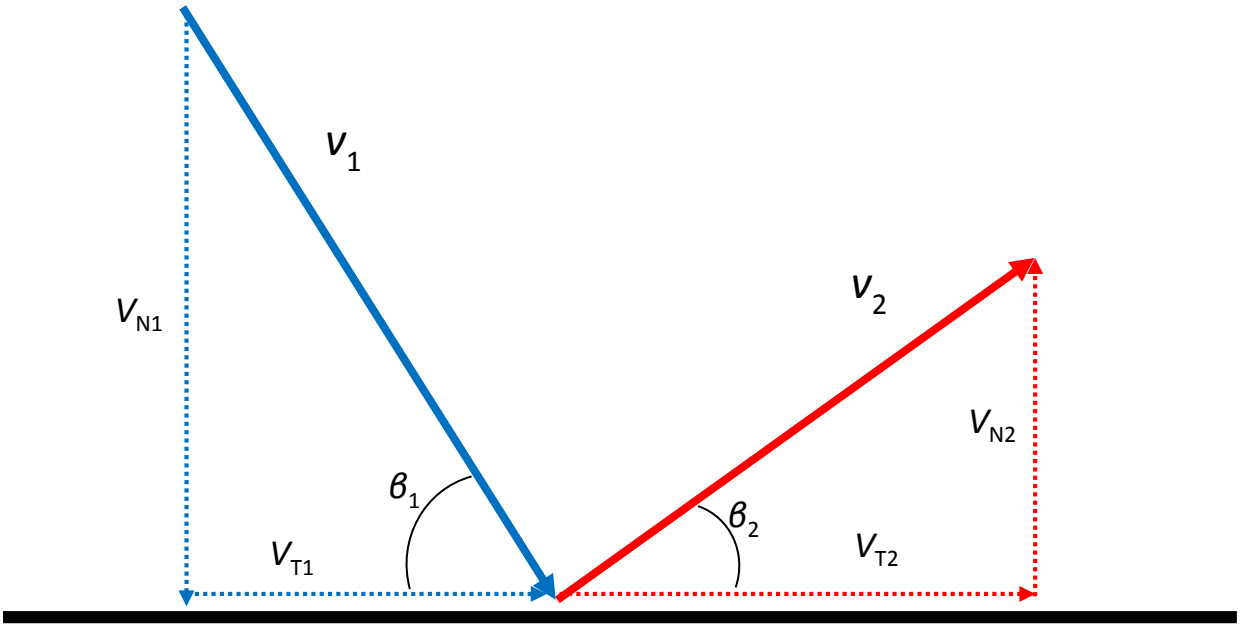

Figure 3-2. Diagram of Incoming and Rebounding Particle Trajectories

COR for the normal and tangential components of velocity are also important quantities for studying particle impact. The normal and tangential CORs are defined as:

(3-2) $$e_N = \frac{V_{N2}}{V_{N1}}$$

(3-3) $$e_T = \frac{V_{T2}}{V_{T1}}$$

where V_{N2} is the normal component of the rebounding velocity, V_{N1} is the normal component of the incoming velocity, V_{T2} is the tangential component of the rebounding velocity, and V_{T1} is the tangential component of the incoming velocity.

COR depends on many factors such as: particle velocity, particle size, particle and surface temperature, surface roughness, surface hardness, particle spin, particle shape, adhesion, and material properties. Some of these factors such as particle shape and surface roughness are essentially random, and are primarily responsible for the statistical nature of COR when it is

measured. In order for COR data to be useful in understanding sand transport in gas turbine engines, the mean as well as some measure of the variation in the COR must be presented.

Several studies have been done to investigate the effects of some of these factors on COR. However, very little research has been done at the high temperatures seen in gas turbines, and with the exception of a couple of papers, nothing has done experimentally using sand. None of the papers that have studied sand have done so at elevated temperatures or with particles approaching the size of sand particles that are seen in the hot sections of gas turbines.

Some of the first studies on particle impact mechanics were done by Goldsmith [1] published in 1960. From this work, COR was found to decrease with increasing velocity, increasing particle size, and decreasing surface hardness. Tabakoff *et. al*. [2] confirmed that in general, COR decreases as particle velocity increases. Li *et. al.* [3] studied 70 μm mean diameter SS316 spheres impacting a silicon crystal wafer at different angles and velocities. The velocities measured were very low, 45 m/s, 1.05 m/s, and 1.6 m/s. The COR was relatively constant at 0.7 for angles between 50° and 85°. Microparticle adhesion is important at these low velocities and contributes to the low COR values. The study by Sommerfeld and Huber [4] shows that rougher surfaces and more oblong particles tend to have a lower COR and wider scatter due to local deformations that absorb impact energy.

Past studies have mostly neglected the study of the effects of temperature on COR. Most of these studies are only marginally relevant to the current sand research. Mok and Duffy [5] studied solid steel balls of 1 in and ½ in diameter balls impacting cylindrical targets made from 6061-T6 aluminum. The balls impacted the target at 90° with a range of velocities from 0-5 m/s and temperatures from 294-755 K. Temperature did have an effect on the COR for the steel ball/aluminum target impact. It was found that as temperature increased, COR decreased. Brenner *et. al.* [6] studied the impacts of three types of iron spheres on aluminum oxide covered iron plates at 973 and 1073 K at 90° impact angle. COR results were presented for velocities up to 3 m/s. COR was found to decrease as the temperature increased and was found to be proportional to $V^{-1/4}$.

Tabakoff *et. al.* [7-10] completed a number of studies on the erosive effects of particles on metals. The COR was used to find a correlation between kinetic energy lost and erosion. These works showed that erosion of metals is mainly a function of the tangential COR; meaning that erosion is highest at shallow angles of impact. These works also clearly show that COR is a

probabilistic function. Wakeman and Tabakoff [9] studied the erosive behavior of 150-180μm quartz sand at temperatures up to 978 K and velocities up to 274 m/s at different impact angles, but no COR was reported. Relationships were proposed for erosion based on incoming velocity. Tabakoff *et. al.* [8] studied 150 μm sand particles impacting several common turbomachinery target materials at 90.85 m/s and at different angles of impact. The COR trends versus angle of impact for all of the materials were similar, but the values of the COR were different for each of the materials. Reagle *et. al.* [11, 12] tested the effects of temperature and velocity on COR for sand particles. In these studies velocity was not controlled independently of temperature, and velocity increased with temperature increases. This makes it impossible to decouple the effect of increasing temperature from the effect of increasing velocity. The current study controls velocity independent of temperature, allowing for the effects of temperature to be studied.

COR of sand microparticles has not been studied at high temperatures independent of velocity. The current study aims to document the COR at temperatures ranging from ambient up to 1073 K. This study and its companion study[13], which covers the effects of temperature up to and including deposition, help fill the gap between past deposition studies and previous research done in erosion.

3.2.1 Nomenclature

ARD	Arizona Road Dust
C_d	drag coefficient
CFD	Computational Fluid Dynamics
COR	Coefficient of Restitution
d	diameter
e	Coefficient of Restitution (COR)
L	length
PTV	Particle Tracking Velocimetry
pdf	probability density function
RMS	Root Mean Squared
Stk	Stokes Number
t	time
V	velocity

$\bar{x}$	mean

Greek Letter Symbols

β	impact angle
ρ	density
σ	Standard Deviation
μ	viscosity

subscript

c	characteristic
N	normal
p	particle
T	tangential
∞	freestream

3.3 Experimental Setup and Instrumentation

3.3.1 Aerothermal Rig

The Virginia Tech Aerothermal Rig was used for all the testing presented in this paper. The VT Aerothermal Rig was donated by Rolls Royce in 2010. It was previously used in Indianapolis, Indiana, for heat transfer studies by Nealy *et. al.* [14] and Hylton *et. al*. [15]. The original operation specifications for this rig reported by Rolls Royce were 2.2 kg/s at a maximum pressure of 16 atm and temperature of 2033 K.

The rig has been reconfigured to allow for sand to be injected into the heated flow. Figure 3-3 is an image of a CAD model of the Aerothermal Rig in its current setup. The rig was used previously by Reagle [16]. Since that study the equilibration tube has been changed to allow for a higher maximum operating temperature. The current maximum operating temperature of the rig is 1323 K.

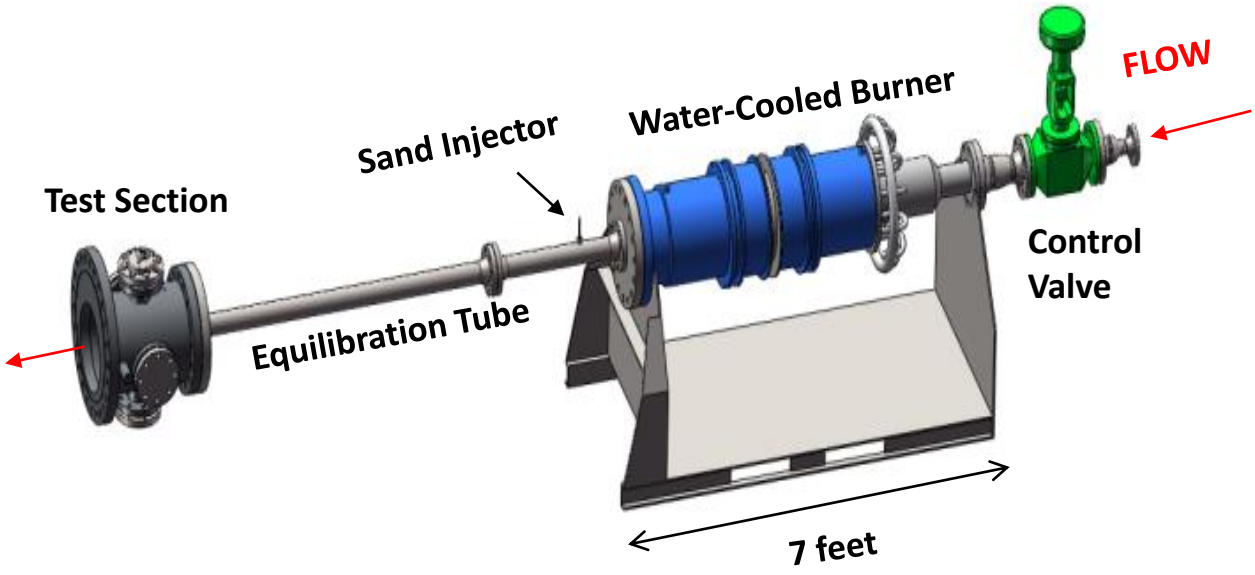

Figure 3-3. VT Aerothermal Rig

A compressor supplies compressed air to a buffer tank at 0.15 kg/s. From the buffer tank the air goes through a series of regulator valves before passing through the main control valve. The pressure regulators and control valves are adjustable and allow the mass flow rate of the rig to be controlled precisely. This allows temperature and velocity of the rig to be controlled independently.

After passing through the control valve, the air flow passes through a sudden-expansion, water-cooled burner that heats the flow using methane as fuel. The fuel flow rate is controlled by a regulator and pneumatically actuated control valve. This allows fuel flow rate to be controlled to maintain temperatures to an accuracy of +/-3 K. The sand particles are entrained in a flow separate from the main flow and are injected into the main flow downstream of the burner. The flow travels through the 7.62 cm diameter, 1.82 m equilibration tube to allow the sand particles to reach the temperature and velocity of the flow. The flow then exits the equilibration tube as a free jet into the test section and impinges on the test coupon. During a test run, time is allowed for the temperature in the test section to reach equilibrium, before the sand particles are injected and measurements taken.

A CAD image of the test section without the outer casing is shown in Figure 3-4. The figure shows the test coupon supported by the support rod that can be rotated in 10° increments. A quartz viewing window in the top flange allows for a camera to view the test coupon. The test

section also has a quartz laser access port to allow illumination of the particles during testing. The camera is located directly above the hot test section, so it is necessary to cool it by means of an air conditioner to ensure proper temperature of the camera electronics. The test coupon on which particle impacts occur is 3.81 cm by 6.35 cm. The coupon is rectangular in shape to allow for a sufficient area to be projected normal to the flow when testing at shallow impingement angles. The test coupons are made from either SAE 304 stainless steel or a nickel alloy Hastelloy X. The coupons are polished to a mirror finish with an RMS average roughness less than 0.2 μm prior to testing.

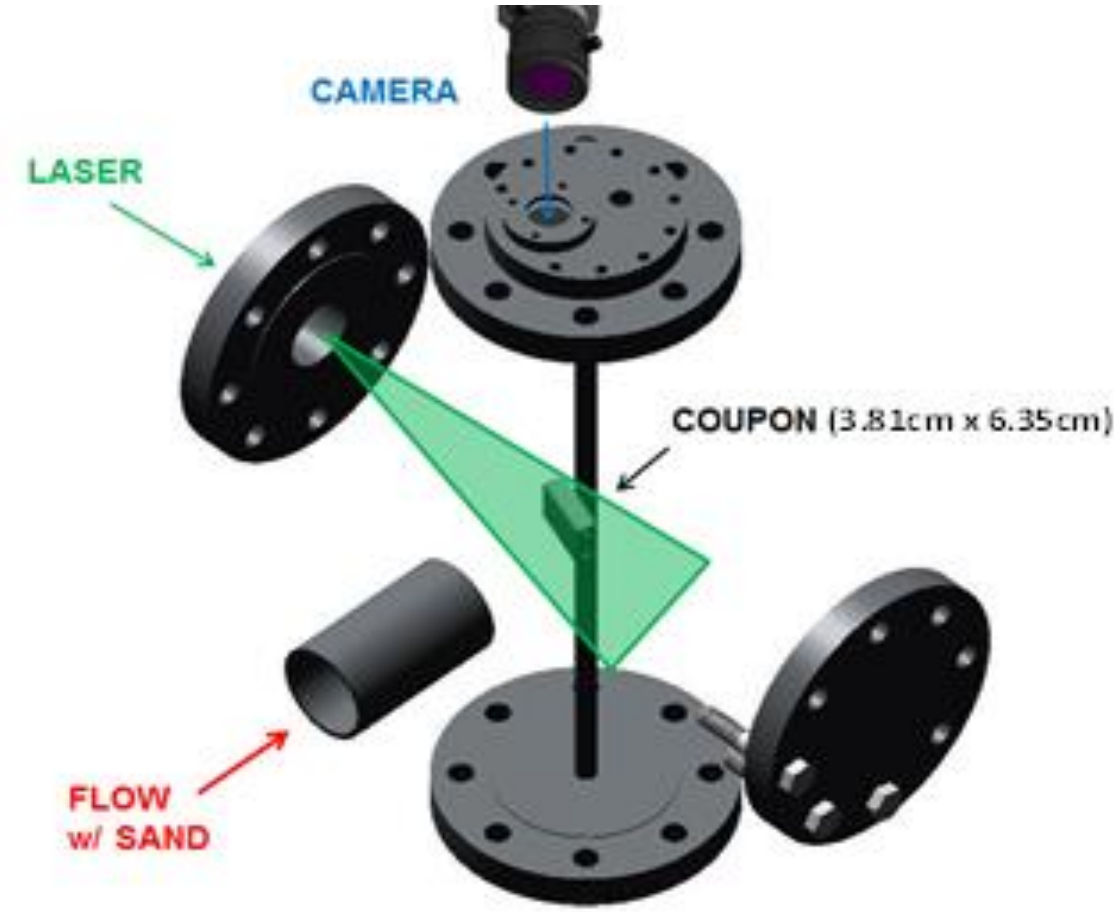

Figure 3-4. Schematic of instrumentation setup

3.3.2 Test Conditions

In previous works published using this experimental setup by Reagle *et. al*. [11, 12], there was no method to precisely control the mass flow of the test rig. This meant that as the air

temperature was increased, the velocity increased as well. For the current study, the mass flow rate can be controlled which allows for a constant velocity at any temperature. The velocity chosen for this work was 28 m/s. Table 3-1 below shows the test conditions for the experiments described in this paper as compared to the previously published work performed with this rig. It is important to note that the temperature of the metal coupon is substantially lower than the air and particle temperature. The reason for the lower temperature is due to conduction through the coupon support material and radiation heat transfer losses to the surrounding environment. At 1073 K, the coupon is 140 K cooler than the air and particles impinging on its surface. Hot particle impact on cooler surfaces is a phenomenon which often occurs in gas turbines on cooled vanes and blades. The 1073 K temperature is in the range which is experienced by some hot section components.

Table 3-1. Test Temperatures and Velocities

Air Temp (K)	**Coupon Temp. (K)**	**Bulk Velocity (m/s)**	**Velocity of Past Work (m/s) [12]**
~300	~300	28	28
873	803	28	77
1073	933	28	102

3.3.3 Instrumentation

In order to determine the velocity of the flow exiting the equilibration tube, a Pitot-static probe is mounted on a traversing mechanism. The probe used for this is specially designed to handle the extreme temperature environment in which it operates. The traversing mechanism allows the Pitot-static probe to be placed into the main flow in order to measure the velocity of the flow, and then retracted from the flow so as not to be damaged or clogged by the flow of sand particles through the rig. Another Pitot-static probe is placed upstream of the burner to verify mass flow rate of air entering the burner.

To measure the temperature of the air impinging on the coupon, a type K thermocouple is placed above the coupon to measure the air temperature. Additionally, a thermocouple is buried inside the metal of the coupon itself, in order to accurately measure the temperature of the coupon. There are many other thermocouples and pressure transducers used in each experiment

that mainly serve safety functions to monitor the temperature of the air, cooling water, and metal of the rig at other locations to ensure that the rig is not damaged by excess temperature exposure.

A Litron Nd:YAG laser is used to illuminate the particles in the test section. The laser can be set to emit up to 55 mJ per laser pulse at 532 nm wavelength. For the camera settings used in this experiment, it was found that setting the laser to 55 mJ produced the best images. The thickness of the laser sheet where it intersects the coupon is ~4 mm. The camera used is a Dantec Dynamics® FlowSense camera equipped with a Zeiss® Makro-Planar 2/50 lens. Figure 3-4 shows the relation of the laser light, camera, equilibration tube, and coupon. The camera is a monochrome camera which captures images with a 2048x2048 resolution. The laser-camera system is able to refresh at a rate of 7.4 Hz between image pairs captured. The camera is focused such that a single particle is captured in one or two pixels on each image. With the air velocity set to 28 m/s, it was found that 15 μs between images was the best setting for the laser and camera image pair speed. This small time interval allows the particles to move up to 10 pixels between images. This is enough distance to get an accurate measure of the particle's velocity. If the particles move too far between the two images of the image pair, it becomes very difficult to correctly match a particle from the first image with the particle that appears in the second image. This produces many false velocity vectors, which is why it is very important to set the timing correctly. The 15 μs chosen is small enough to almost eliminate the possibility of false velocity vectors.

3.3.4 Particles

The sand particles used for this test are Arizona Road Dust (ARD). ARD is a test dust that is often used to represent desert sands in experimental tests of filtration, automotive, and other equipment testing. The particle size of the ARD used for this test was a narrow size range of 20-40 μm. The mean by number of particles was 24.67 μm based on batch statistics provided by the manufacturer. A narrow size range of particles is extremely important so the effects of particle size do not affect the test results. The complete chemical composition as well as description of particle size distribution of this test dust range can be found in the previous work by Reagle *et. al.* [11]. Small microparticles have a tendency to clump together while being stored due to atmospheric moisture. In order to achieve correct test results for microparticles, the

particles cannot be allowed to clump together. To achieve this it is necessary to heat the particles for several hours in an oven to remove moisture from the particles thereby preventing the clumping that would otherwise occur.

The Stokes number (Stk) is a ratio of the particle response time to fluid response time. This physically means that the Stk quantifies the degree to which particles suspended in a fluid flow will follow the fluid motion. A particle with a Stk much larger than unity will not follow the fluid flow, but instead its momentum will force it to keep traveling in its original direction. The Stk is calculated using the following equation:

$$Stk = \frac{\rho_p d_p^2}{18\mu} \frac{V_\infty}{L_c} \tag{3-4}$$

where ρ_p is density of the particle, d_p is diameter of the particle, V_∞ is fluid velocity, μ is fluid viscosity, and L_c is the characteristic length of the system, in this case the 6.35 cm width of the coupon. The Stk governs only the particle-fluid interactions, and particle impact characteristics are not directly affected by the particle's Stk. However, it is still important to know the Stk of the particles, because at very low Stk no impact on the target coupon will occur. The Stk at the different experimental conditions is given in Table 3-2 below for the smallest and largest particles in the size range.

Table 3-2. Test Dust Stokes Numbers at Extreme Values

Test Condition (K)	Bulk Velocity (m/s)	Stokes 20 μm Sand	Stokes 40μm Sand
300	28	1.38	5.52
873	28	0.66	2.63
1073	28	0.58	2.32

3.4 Data Reduction

The data reduction method used for this experiment is very similar to that which was used in past studies [11, 12] involving this experimental setup. A few significant changes have been made to the method to improve accuracy. Because the particle velocity is always measured at a distance from the target coupon, some velocity correction is needed. Past works by other researchers using similar methods of determining particle velocity have assumed that the

measured velocity at some distance from the target was the velocity with which the particle would arrive at or leave the target. While this may be a valid assumption for large Stk particles, it is not true for smaller particles which are strongly influenced by the fluid flow. This necessitates the use of a velocity correction in order to obtain the velocity at the moment of impact with the target coupon.

3.4.1 Particle Tracking

The Particle Tracking Velocimetry (PTV) method involves first implementing a band pass filter on the image to remove large objects (coupon, thermocouples, etc.), locating the particles, and then using a radius of gyration calculation to find the particle centroid to sub-pixel accuracy. After the particle locations have been determined, the particles are then correlated between the image pair to determine particle velocity. If there is more than one possible correlation option within the circle of possible correlation for the particle, then that particle velocity track is disregarded to prevent any false velocity vectors.

Once the particle velocity has been measured, the velocity is used as an initial condition for a Lagrangian particle tracking algorithm which uses a flow field calculated from ANSYS CFX for the Eulerian phase of the calculation. This computational flow field is validated against velocity surveys taken with the Pitot-static probe immediately upstream of the coupon to ensure accuracy. Additionally a study was performed to assess the errors introduced by the particle tracking method. This was done by varying the distance particles were allowed to be from the coupon face. This study found that the results were independent of the distance from the face, and therefore not biased by the particle tracking. This Lagrangian tracking scheme uses only particle drag force based on the relative velocity of the particles as calculated by the coefficient of drag equation provided by Morrison [17]. Magnitude of the other forces acting on the particles were calculated and were found to be orders of magnitude smaller than the drag force and are thus neglected. The measurements taken by the PTV system do not allow for measurement of spin, so unfortunately no calculation of the Magnus force is possible. This would be particularly interesting to investigate for rebounding particles at low angles of attack where any particle friction in the collision will cause the particle to rotate.

Although the basic method used by Reagle *et. al.* [11, 12] in previous works has been retained, one significant change has been made to the particle tracking algorithm. In the method used for this work, there is a limit to how far a rebounding particle may be from the coupon to still be used in the data reduction scheme. This limit is set to fifty time steps of the Langrangian particle path algorithm. This means that rebounding particles must have travelled less than 2 cm from the point of impact to be counted. This constraint helps to eliminate any error that may be created by use of the Langrangian correction to the particle velocity.

The result of this particle tracking scheme for particle velocity correction are the actual velocities of the particles when impact with the plate occurred. This impact or rebound velocity at the moment just before or just after the impact is what is needed to accurately calculate COR. Figure 3-5 below shows the particle tracks output by the Lagrangian particle tracking scheme.

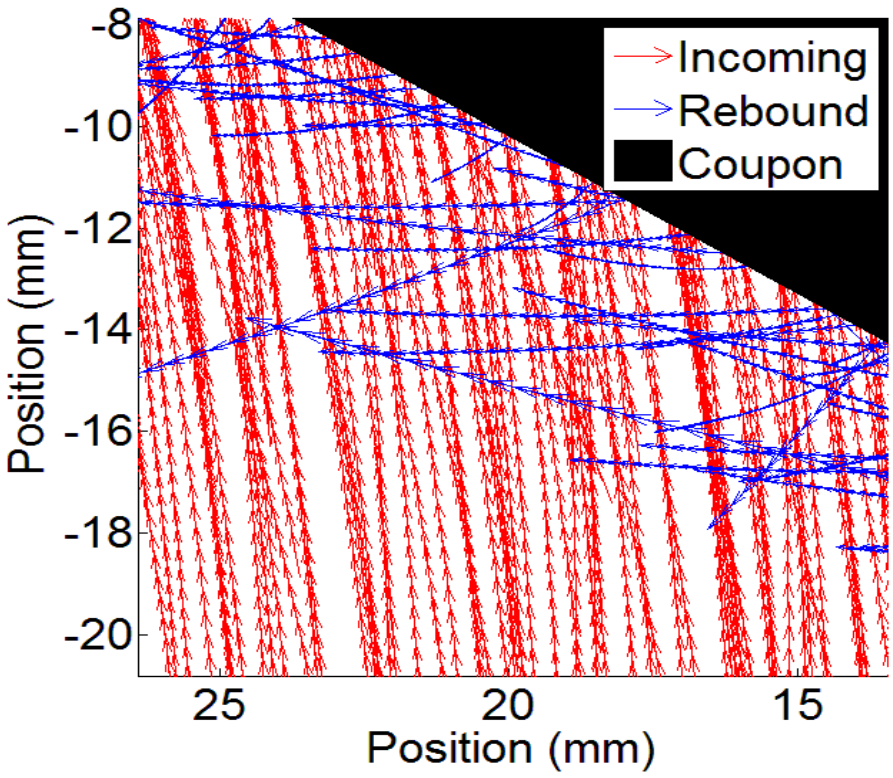

Figure 3-5. Particle tracks generated by the Lagrangian particle tracking algorithm

Figure 3-5 clearly shows that the incoming particles only have slight deviation from a purely ballistic trajectory; however, the rebounding particles deviate more substantially from a ballistic course because of their higher relative velocity with respect to the flow. It can be seen

for Figure 3-5 that some particles do not deviate much while others deviate quite substantially. The mean of the angle change for incoming particles is 2.5° while the rebounding is closer to 6°. Some rebounding particles change direction as much as 15° which is a very significant change in direction.

3.4.2 Coefficient of Restitution Calculations

In order to determine the COR, the coupon face where the impacts occur is divided into segments 2 mm in width. A compilation of all the particles that impacted on each of the 2 mm "bin" widths is made. There is generally a smaller number of rebounding particles than incoming particles, so the number of rebounding particles per bin was monitored. No bin was observed to contain fewer than 30 rebounding particles and there are many cases where particle counts upwards of 200 per bin were observed. Each of these bins contains a distribution of incoming and rebounding velocities and an angle of impact. With this distribution it is then possible to compute the statistics on each of these distributions. A mean and a standard deviation are calculated for the total, as well as the normal and tangential velocity components as well as the angle of impact.

Each of these distributions is further analyzed to verify its normality. A Lilliefors normality test is used on each of the incoming and rebounding distributions to verify that the distribution is in fact normal. The Lilliefors test takes into account the skewness and kurtosis of the sample, as well as the sample size in testing the sample for normality. The null hypothesis is rejected if the test statistic is less than 0.05, as is the standard for many statistical tests. Roughly 5% of the distributions tested fail the normality test; this is usually because these rebounding distributions tend to be "tail heavy" and the incoming distributions do exhibit some small amount of negative skewness. Once each of the distributions has been established as statistically significant, the COR can be calculated from the statistics.

In the past works, such as those by Tabakoff *et. al.* [7, 8] and Reagle *et. al.* [11, 12], that have measured COR and have not directly tracked particles during the impact have neglected the variation in the incoming particles. This assumption has been justified by the fact that the incoming distribution has a much smaller range of variation than the rebounding distribution. Making this assumption does not substantially affect the mean of the COR when it is calculated;

however, it does cause significant overestimation of the variation of the COR. This is because by making the assumption of no incoming variation, all of the rebounding variation is assumed to be a result of the impact itself. In fact some of the rebounding variation is a result of a variation in impacting velocity and angle. The amount of overestimation depends strongly on the amount of incoming variation. In the data collected for this paper at 28 m/s, not using the ratio distribution method would result in a 7% overestimation of the standard deviation. This results in the variation of the COR appearing larger than it physically is. If the incoming variation were larger, then overestimation is also larger.

In order to properly calculate the distribution of the COR about the mean while taking into account the variation of incoming particles, it is necessary to perform a ratio distribution of V_2 and V_1. The equation for the ratio distribution of two variables was derived by Hinkley in his 1969 work [18]. This derivation requires that the two distributions be Gaussian, which is verified during the data reduction process. Because V_2 and V_1 are statistically independent over the 2 mm bin width the equation for the probability density function (pdf) of the ratio distribution can be simplified to the following format:

$$p.d.f.(z) = \frac{b(z)*c(z)}{\sqrt{(2\pi)}\sigma_1\sigma_2 a^3(z)} \left[\Phi\left(\frac{b(z)}{a(z)}\right) - \Phi\left(-\frac{b(z)}{a(z)}\right) \right] + \frac{1}{a^2(z)\pi\sigma_1\sigma_2} e^{-\frac{1}{2}\left(\frac{\bar{x}_1{}^2}{\sigma_1^2} + \frac{\bar{x}_2{}^2}{\sigma_2^2}\right)} \tag{3-5}$$

Where

$$a(z) = \sqrt{\frac{1}{\sigma_1^2}z^2 + \frac{1}{\sigma_2^2}}, \quad b(z) = \frac{\bar{x}_1{}^2}{\sigma_1^2}z + \frac{\bar{x}_2{}^2}{\sigma_2^2}$$

$$c(z) = e^{\frac{1}{2}\frac{b^2(z)}{a^2(z)} - \frac{1}{2}\left(\frac{\bar{x}_1{}^2}{\sigma_1^2} + \frac{\bar{x}_2{}^2}{\sigma_2^2}\right)}, \quad \Phi(z) = \int_{-\infty}^{z} \frac{1}{\sqrt{2\pi}} e^{-\frac{1}{2}u^2} du$$

where σ_1 is standard deviation of the incoming velocity, $\bar{x}_1$ is the mean of the incoming velocity, σ_2 is standard deviation of the rebounding velocity, $\bar{x}_2$ is the mean of the rebounding velocity, and z is the ratio variable, in this case the COR.

The resulting distribution from performing the ratio distribution on two independent variables is a Cauchy distribution. Since Cauchy distributions do not have a mathematically definable mean or standard deviation, we estimate these values based on the probability density

function. These estimated mean and standard deviation values for e, e_N, e_T are presented for each of the test cases in the results section.

3.4.3 Curve Fitting

In order to present COR in a manner that is most useful it is generally plotted against incoming incidence angle. In the case of this data the mean incidence angle of the incoming data collected for each of the 2 mm bin widths was used as the incidence angle. The standard deviation of the incoming incidence angle was found to be around 1.5°. For each of the bins a combined, normal, and tangential COR as well as a standard deviation for each type of COR are paired with the mean incidence angle in order to provide the raw data from which a curve fit can be performed.

A power law equation was used to curve fit that data. A power law type curve fit was chosen as the most appropriate type of curve fit for the data as it was taken. The two coefficient form of the power law equation can be seen in Equation (3-6) below where β_1 is in degrees.

$$e = A\beta_1^B \tag{3-6}$$

The curve fitting of this equation to the data was performed using MATLAB.

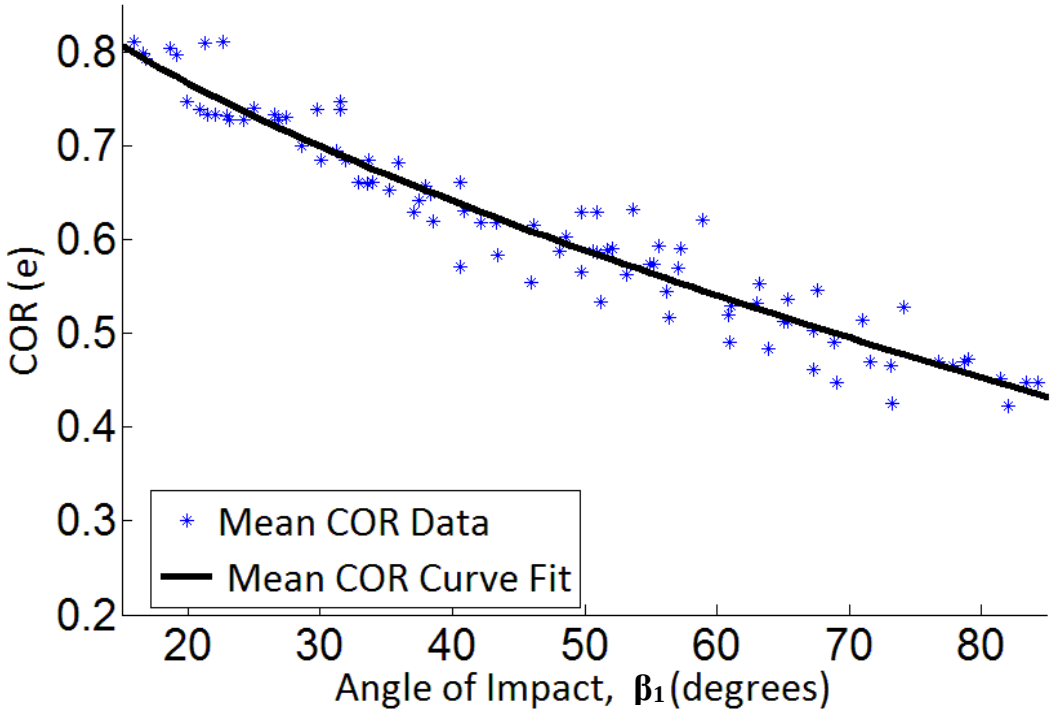

Figure 3-6 contains an example of the amount of scatter and the curve fit as it has been applied to the mean data generated from the probability density function of the COR output from the ratio distribution.

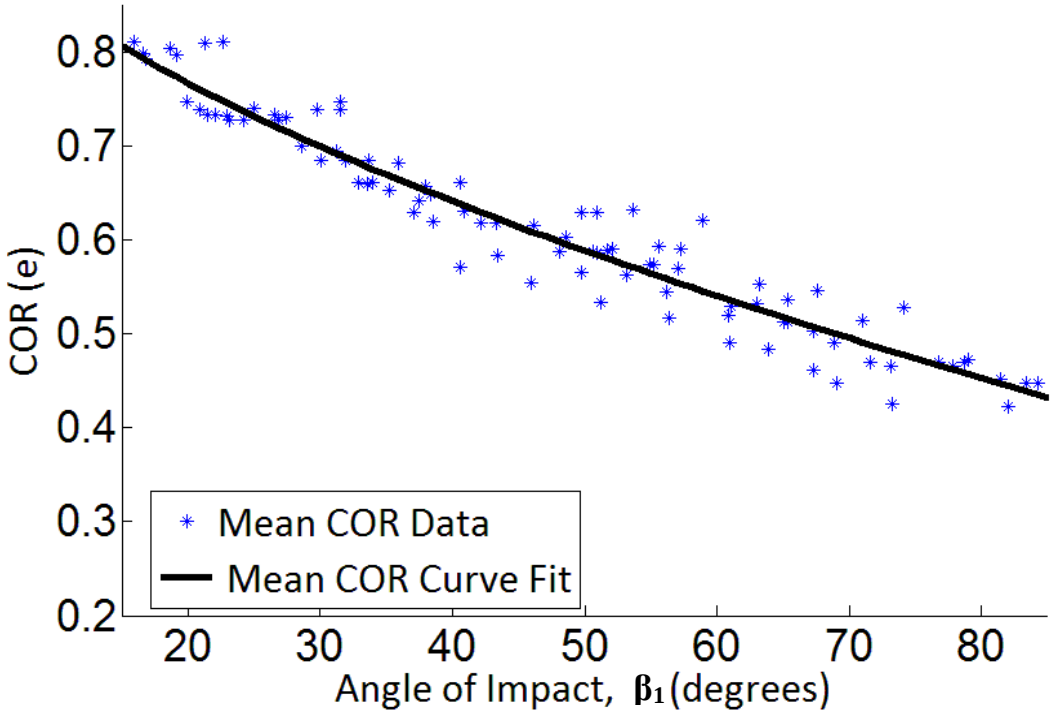

Figure 3-6. Power law curve fit and raw data for the mean COR

3.5 Results

The impacts of 20-40 μm ARD impacting polished stainless steel 304(SS304) and Hastelloy X(HX) coupons were recorded for angles ranging from 30° to 80° for three different temperatures. Each temperature was tested at a constant velocity of 28 m/s. The repeatability of the experiment is very good. Less than 1% variation was found during tests to verify the repeatability of the data. In addition the power law curve fit coefficients for all of the COR as well as normal and tangential COR components are tabulated in the Appendix.

3.5.1 COR

Figure 3-7 displays the sample mean for COR vs. angle of impact on both SS304 and HX for the three temperatures studied in this experiment. The trends for COR are similar for the three temperatures. All of the cases show a trend of decreasing COR as the angle of impact increases. This is an expected result and has been seen in other papers reporting COR of various particles at ambient temperatures. Both the HX and the SS304 data have almost identical COR at ambient conditions. At these conditions the particles impact on and erode the surface in similar manners.

As can be seen in Figure 3-7, at elevated temperatures both SS304 and HX experience a significant drop in COR as compared to the COR at ambient. This is believed to be the result of the protective oxide layer that both stainless steel and nickel alloys form at elevated temperatures. As the metal increases in temperature the metal itself becomes softer, but at the same time the oxide layer protecting the metal becomes thicker and in the case of the HX the composition of the oxide layer undergoes significant changes as the temperature increases. In addition, Wright *et. al.* [19] found that particle bombardment can actually increase the rate of oxide layer formation in Inconel alloys. This is caused by the particles breaking up the original oxide layer and allowing oxygen penetration into the metal substrate much quicker. All of these changes are believed to be the cause of the significant drop in COR. The drop from the ambient temperature to 873 K and 1073 K for the SS304 metal is an average of 1.5%. For the HX coupon this drop is substantially more at 12%. The low angles of attack exhibit substantially more drop in COR the high angles of attack do.

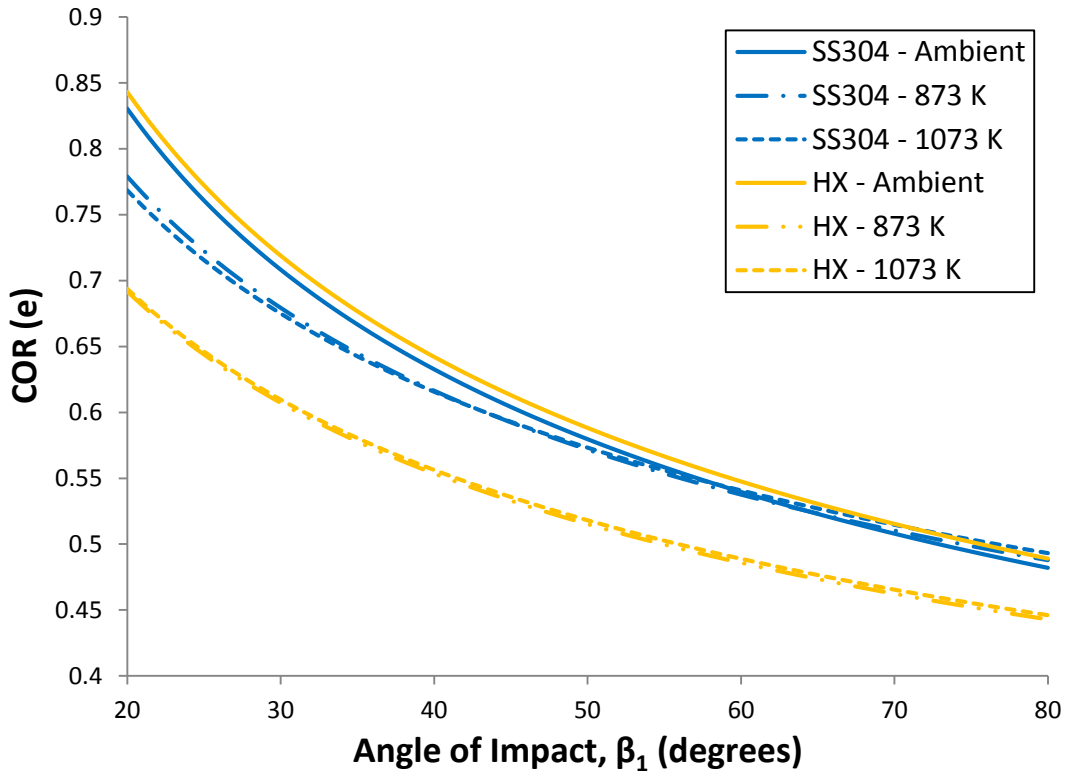

Figure 3-7. Plot of COR vs. angle of impact for SS304 and Hastelloy X

Table 3-3 displays the estimated standard deviations for the sample mean for impact angles 30° to 80° for the two metals at the three temperatures. The standard deviation is fairly constant throughout the range of angles tested in this experimental study.

Table 3-3. Estimated COR Standard Deviation for SS304 and HX

Mean COR Estimated Standard Deviation						
	SS304			HX		
Angle	Ambient	873 K	1073 K	Ambient	873 K	1073 K
20	0.07	0.17	0.17	0.06	0.12	0.13
30	0.11	0.18	0.18	0.10	0.14	0.15
40	0.13	0.19	0.19	0.12	0.15	0.15
50	0.14	0.19	0.19	0.12	0.15	0.15
60	0.15	0.19	0.19	0.13	0.15	0.15
70	0.15	0.19	0.19	0.13	0.15	0.15
80	0.15	0.18	0.19	0.13	0.15	0.15

3.5.2 Normal COR

Figure 3-8 shows the SS304 and HX normal COR vs. angle of incidence for the three different temperatures at 28 m/s. The trend of the two ambient runs on both SS304 and HX follow nearly identical trends, while the four experimental conditions at higher temperature in which the thicker oxide layer exists follow a significantly different trend. It is believed that the formation of a chromium oxide layer, in addition to roughness due to erosion, increases the surface roughness of the coupon. The surface roughness was measured to have a peak-to-peak roughness of 2 μm. This causes transfer of energy from the tangential to the normal direction due to the "shadow effect" noted by Sommerfeld and Huber[4]. In addition it is possible that at the low angles of impact, the particle does not have sufficient normal velocity to penetrate the hard oxide surface layer. The substantially higher COR observed between 20° and 40° angle of impact is believed to be due to these effects.

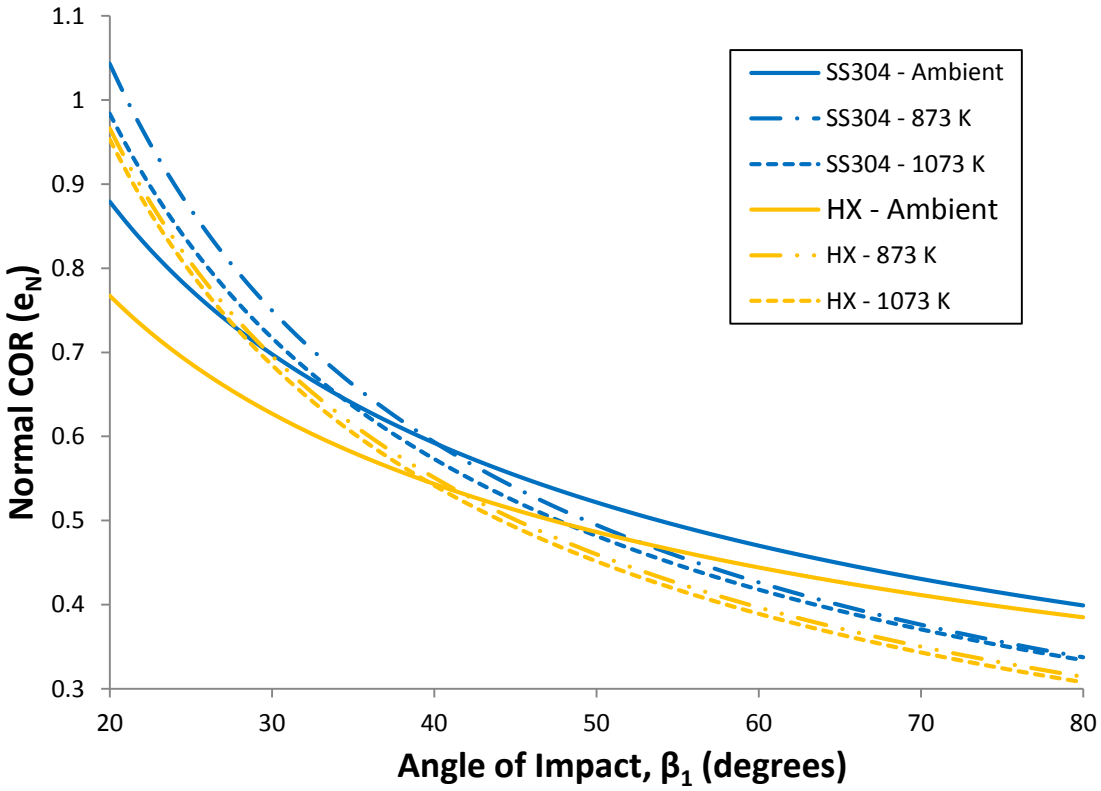

Figure 3-8. Plot of normal COR vs. angle of impact for SS304 and Hastelloy X

Table 3-4 displays the estimated standard deviations for the trends in Figure 3-8. The table shows that the shallow angles of impact have the highest deviation. It should be noted that

the velocity measured in the normal direction is very small for the data between 20° and 30°. This makes the signal-to-noise ratio large and explains why the standard deviations at low angles of impact are much larger. This effect has been noted by others who have reported standard deviations on normal COR.

Table 3-4. Normal COR Estimated Standard Deviation for SS304 and HX

Normal COR Estimated Standard Deviation						
	SS304			HX		
Angle	Ambient	873 K	1073 K	Ambient	873 K	1073 K
20	0.27	0.41	0.39	0.24	0.36	0.37
30	0.23	0.30	0.29	0.20	0.26	0.26
40	0.20	0.24	0.23	0.18	0.21	0.21
50	0.18	0.20	0.19	0.16	0.17	0.17
60	0.17	0.18	0.17	0.15	0.15	0.15
70	0.16	0.16	0.15	0.14	0.13	0.13
80	0.15	0.14	0.13	0.13	0.12	0.12

3.5.3 Tangential COR

Figure 3-9 displays the SS304 and HX tangential COR vs. angle for the three different temperatures for 28m/s. The trends for all temperatures are similar. There is a significant decrease in tangential COR for both materials as the temperature rises above ambient, but there is not a large decrease from 873 K to 1073 K. The decrease for the SS304 from ambient to the elevated temperatures is 6.7% for both 873 K and 1073 K. The HX material shows substantially larger decrease in COR with both elevated cases showing a decrease in COR of 25%.

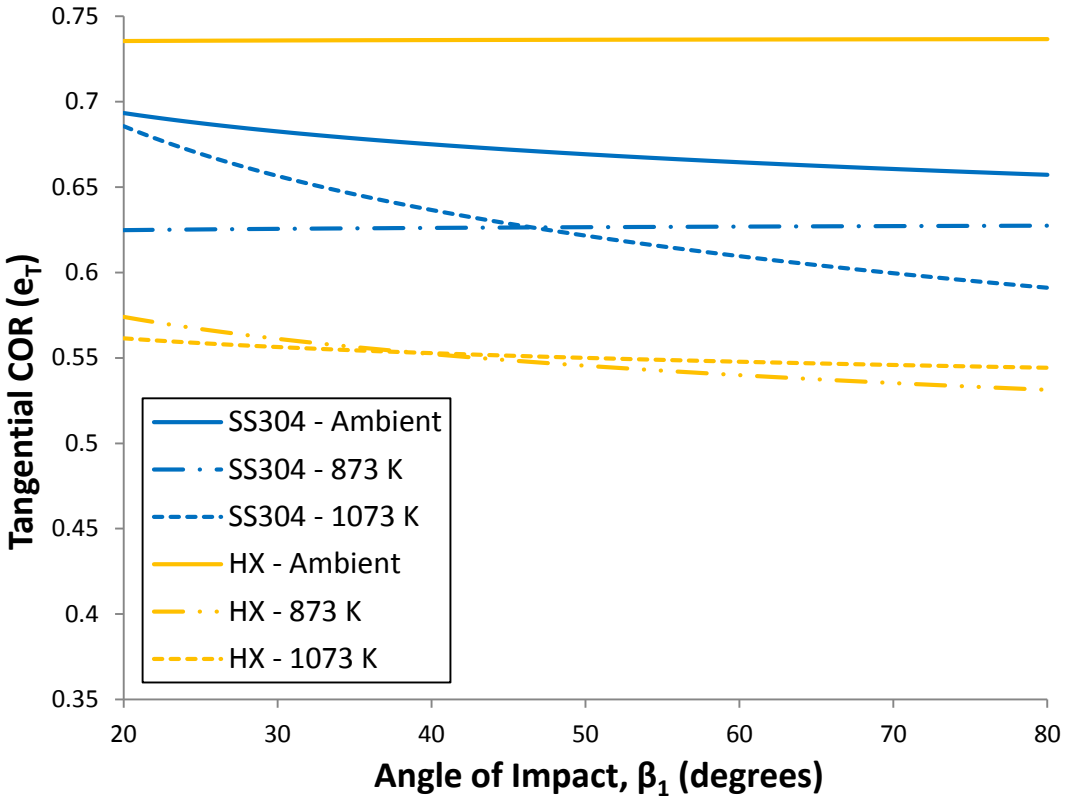

Figure 3-9. Plot of tangential COR vs. angle of impact for SS304

Table 3-4 displays the estimated standard deviations for the trends in Figure 3-9. The table shows that larger angles of impact have the highest deviation. One of the reasons for this is due to the small magnitude of the tangential velocity at these high angles of impact. This creates a very small velocity to measure which is then easily influenced by other factors. This is similar to the reason for the higher variation of the normal COR at low angles of incidence.

Table 3-5. Tangential COR Estimated Standard Deviation for SS304 and HX

Tangential COR Estimated Standard Deviation						
	SS304			HX		
Angle	Ambient	873 K	1073 K	Ambient	873 K	1073 K
20	0.06	0.19	0.22	0.12	0.14	0.23
30	0.09	0.25	0.26	0.14	0.17	0.23
40	0.15	0.33	0.34	0.16	0.23	0.27
50	0.24	0.45	0.44	0.23	0.34	0.33
60	0.38	0.59	0.56	0.34	0.49	0.46
70	0.57	0.77	0.70	0.53	0.70	0.66
80	0.82	0.98	0.86	0.82	0.96	0.96

Surface roughness and particle irregularities cause the particles to bounce at unexpected angles. Any deviation of the rebound angle will cause substantial exchange of energy from normal to tangential direction. Since the effects of particle irregularities and surface roughness are essentially random, they cause a great increase in the scatter of the data at the very high angles of incidence. This effect has been seen in other literature that reported standard deviation of the tangential COR.

3.5.4 Literature Comparison

In comparing the data collected in this experiment to literature it is important to compare data sets that are roughly similar. Most of the existing literature examines particles that are significantly larger than the 24.7 μm particle used in this study. Larger particles will have significantly lower COR than the particles used in this study, which makes comparison of results difficult. For example Sommerfeld *et. al*. [4] conducted studies using primarily glass spheres of 100 μm and 500 μm, a much larger size than the particles used in this study. Additionally spheres have also been shown to have substantially different COR trends than non-spherical angular particles.

The velocity, particle size, particle composition, and target material all should be similar in order to accurately compare results. Three data sets from Tabakoff's [7] study of 15 μm fly ash impacts at ambient temperatures were compared to the ambient data taken in the current

study. The trends for RENE 41, a nickel alloy, AM 355 and SS410, stainless steel alloys, were used. Figure 3-10 displays the plot of COR vs. angle of impact for the different metals. A similar trend is found in both fly ash and ARD impacts.

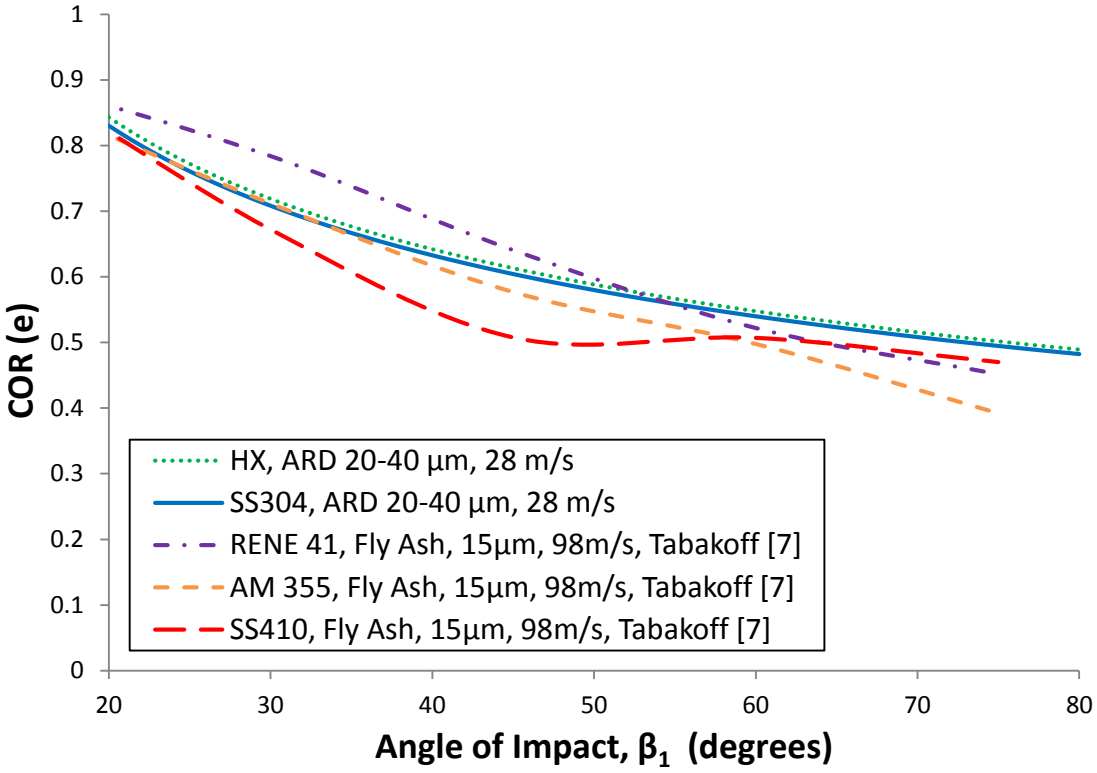

Figure 3-10. Plot of ambient COR vs. angle of impact comparison to literature

It should be noted that the impact speed for the fly ash particle is 98 m/s which is much higher than the 28 m/s for the ARD in this experiment. The faster velocity of the fly ash data should lower the COR as compared to the sand data presented in this paper; however, the smaller size of the fly ash particles causes COR to be higher. Given that these two differences offset, it is not surprising that the trends of the fly ash data and the ARD data sets appear very similar.

Figure 3-11 compares the normal COR of the same two material and particle cases that were compared in Figure 3-10. It should be noted that Tabakoff's [7] work presented the COR and the directional COR, which the ratio of incoming to rebounding angle. In order to compare the data to the normal and tangential COR it is necessary to calculate the normal and tangential components of COR from the data Tabakoff provided. The trend is similar for the RENE 41 and SS410 materials but the stainless steel AM 335 differs in the low angle.

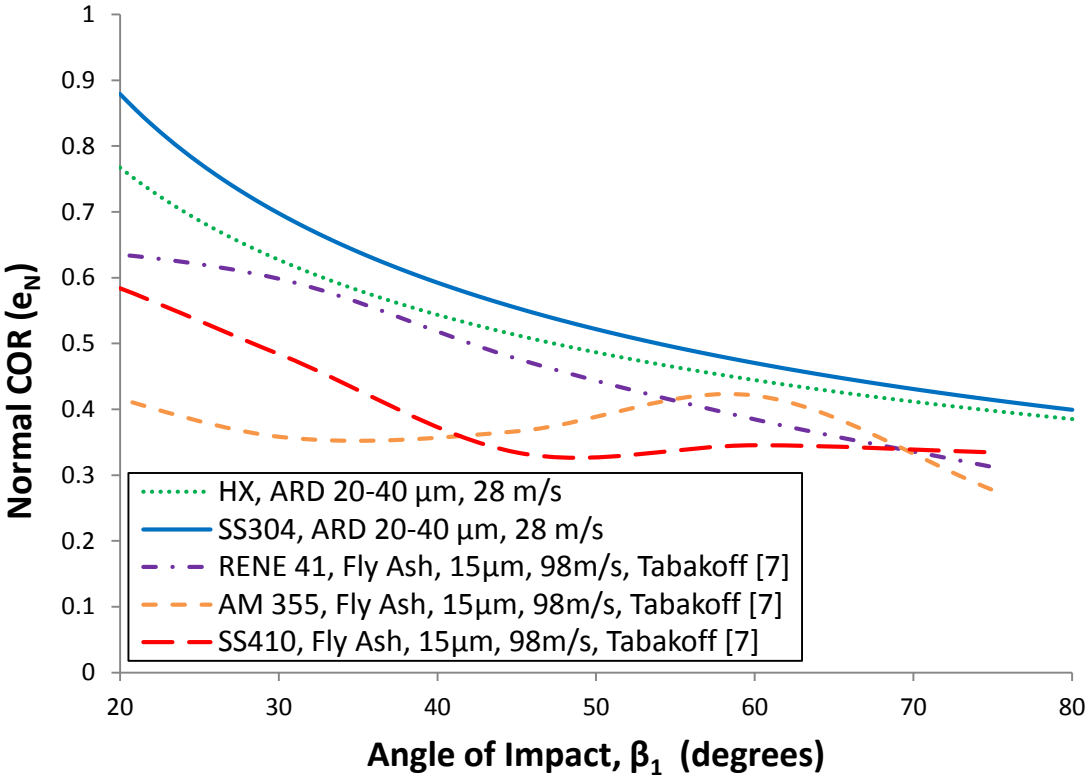

Figure 3-11. Plot of ambient normal COR vs. angle of impact comparison to literature

Figure 3-12 contains a comparison of the same three material types. The ARD trends have a similar magnitude to the fly ash trends; however, the trends vary substantially in the high angle of attack region. The curve fits provided by Tabakoff [7] are only valid to 75° angle of impact. At high impacting angle it is apparent by the COR values much larger than unity that something is wrong with the curve fits. This much higher magnitude of COR is seen in the region which contains extremely high noise, so it is possible that this contributes to the higher than physically possible tangential COR values reported. The remainder of the trend is similar to the trends observed with the 24.7 µm ARD reported in this paper.

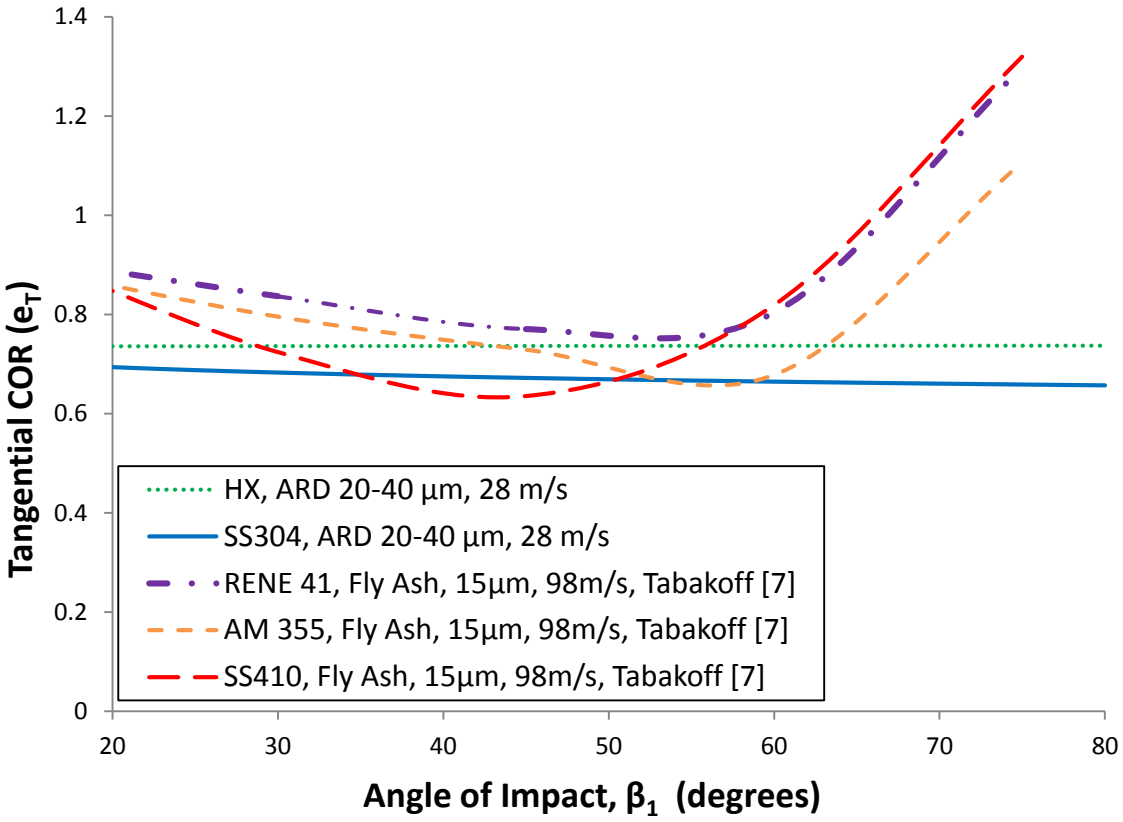

Figure 3-12. Plot of ambient tangential COR vs. angle of impact comparison to literature

3.6 Conclusions

The current study investigated the effects on temperature on COR for 20-40 µm ARD impacting Stainless Steel 304 and Hastelloy X coupons at a constant 28 m/s velocity and different impact angles varying from 30° to 80°. The data presented here is intended to give an estimate of the mean and variance from the specific test conditions performed in the VT Aerothermal Rig that have not been presented in previous literature. A new method of calculating COR, the ratio distribution, was used to compute a probability density function of the COR. This more accurate method of calculating COR variation has not been utilized in any previous studies. Results presented at ambient, 873 K, and 1073 K show that as the temperature increases, the COR generally decreases. For Hastelloy X the average decrease in COR from ambient to 873 K was 12.8% and from ambient to 1073 K was 12.3%. For SS304 the average decrease in COR from ambient to 873 K was 1.7% and from ambient to 1073 K was 1.6%. The formation of oxide layers at higher temperature significantly affects the COR when compared to

ambient conditions. The data is presented in a manner that can be easily integrated into a computational model to help improve the design of gas turbine components which will face sand particle ingestion. Temperature effects on normal COR and their relation to surface roughness are also discussed. Tangential COR was found to generally decrease with increase in temperature.

3.7 Acknowledgments

The work detailed here would not be possible without the support and direction of Rolls-Royce, especially B. Barker, K. Hsu, P. Davis, and N. Wagers. The authors would also like to thank D.K. Tafti and S. Singh from Virginia Tech for their thoughtful discussion, analysis, and advice.

3.8 References

[1] Goldsmith, W., 2002, Impact : the theory and physical behaviour of colliding solids, Dover Publications, Mineola, N.Y.

[2] Tabakoff, W., Grant, G., and Ball, R., 1974, "An Experimental Investigation of Certain Aerodynamic Effects on Erosion," AIAA-74-639.

[3] Li, X., Dunn, P.F., and Brach, R.M., 2000, "Experimental and Numerical Studies of Microsphere Oblique Impact with Planar Surfaces," Aerosol Science and Technology, 31(5), pp. 583-594.

[4] Sommerfeld, M., and Huber, N., 1999, "Experimental analysis and modelling of particle-wall collisions," International Journal of Multiphase Flow, 25, pp. 1457-1489.

[5] Mok, C. H., and Duffy, J., 1964, "The Behaviour of Metals at Elevated Temperatures Under Impact with a Bouncing Ball," Int J Mech Sci, 6, pp. 161-175.

[6] Brenner, S. S., Wriedt, H. A., and Oriani, R. A., 1981, "Impact adhesion of iron at elevated temperatures," Wear, 68(2), pp. 169-190.

[7] Tabakoff, W., 1991, "Measurements of Particles Rebound Characteristics on Materials Used in Gas Turbines," J. of Propulsion and Power, 7(5), pp. 805-813.

[8] Tabakoff. W, H., A., and Murugan, D.M, 1996, "Effect of Target Materials on the Particle Restitution Characteristics for Turbomachinery Application," J. of Propulsion and Power, 12(2), pp. 260-266.

[9] Wakeman, T., and Tabakoff, W., 1979, "Erosion Behavior in a Simulated Jet Engine Environment," J. Aircraft, 16(12), pp. 828-833.

[10] Hamad A., T. W., "Experimental and Numerical Simulation of the Effects of Ingested Particles in Gas Turbine Engines," Proc. AGARD, NATO.

[11] Reagle C., Delimont. J., Ng W., Ekkad S., Rajendran V., 2013, "Measuring the coefficient of restitution of
high speed microparticle impacts using a
PTV and CFD hybrid technique," Measurement Science and Technology, 24(10).

[12] Reagle CJ, Delimont. J., Ng WF, Ekkad SV, 2014, "Study of Microparticle Rebound Characteristics Under High Temperature Conditions," Journal of Engineering for Gas Turbines and Power, 136(1).

[13] Delimont JM, Murdock MK., Ng WF, Ekkad, SV, 2014, "Effect of Near Melting Temperatures on Microparticle Sand Rebound Characteristics at Constant Impact Velocity," Submitted to ASME Turbo Expo 2014, ASME, Dusseldorf, Germany.

[14] Nealy, D., Mihelc, M., Hylton, L., Gladden, H., 1984, "Measurements of Heat Transfer Distribution Over the Surfaces of Highly Loaded Turbine Nozzle Guide Vanes," Journal of Engineering for Gas Turbines and Power, 106, pp. 149-158.

[15] Hylton, L., Nirmalan, V., Sultanian, B., Kaufman, R., 1988, "The Effects of Leading Edge and Downstream Film Cooling on Turbine Vane Heat Transfer," NASA Contractor Report 182133.

[16] Reagle, C., 2012, "Technique for Measuring the Coefficient of Restitution for Microparticle Sand Impacts at High Temperature for Turbomachinery Applications," PhD, Virginia Tech, Blacksburg, Virginia, USA.

[17] Morrison, F. A., "Data Correlation for Drag Coefficient for Sphere," Department of Chemical Engineering, Michigan Technological University, Houghton, MI.

[18] Hinkley, D. V., 1969, "On the Ratio of Two Correlated Normal Random Variables," Biometrika, 56(3), pp. 635-639.

[19] Wright, I. G., Nagarajan, V., Stringert, V., 1986 "Observations on the Role of Oxide Scales in High-Temperature Erosion-Corrosion of Alloys," Oxidation of Metals, 25(3/4).

3.9 Appendix A

Table A-1. Power Law Coefficients for SS304 and HX COR

HX	COR	
Temp. (K)	A	B
HX, Amb.	2.7365306	-0.3929858
HX, 873 K	2.1413619	-0.3375113
HX, 1073 K	2.0044913	-0.3200114
SS304, Amb.	2.6905989	-0.3923721
SS304, 873 K	2.1413619	-0.3375113
SS304, 1073 K	2.0044913	-0.3200114

Table A-2. Power Law Coefficients for SS304 and HX Normal COR

HX	Normal COR	
Temp. (K)	A	B
HX, Amb.	2.7365306	-0.3929858
HX, 873 K	2.1413619	-0.3375113
HX, 1073 K	2.0044913	-0.3200114
SS304, Amb.	2.6905989	-0.3923721
SS304, 873 K	2.1413619	-0.3375113
SS304, 1073 K	2.0044913	-0.3200114

Table A-3. Power Law Coefficients for SS304 Tangential COR

HX	Tangential COR	
Temp. (K)	A	B
HX, Amb.	2.7365306	-0.3929858
HX, 873 K	2.1413619	-0.3375113
HX, 1073 K	2.0044913	-0.3200114
SS304, Amb.	2.6905989	-0.3923721
SS304, 873 K	2.1413619	-0.3375113
SS304, 1073 K	2.0044913	-0.3200114

4 Paper #4: Effect of Near Melting Temperatures on Microparticle Sand Rebound Characteristics at Constant Impact Velocity

4.1 Abstract

When gas turbine engines operate in environments where the intake air has some concentration of particles, the engine will experience degradation. Very few studies of microparticles at temperatures approaching the melting temperature of the particles are available in open literature. Coefficient of Restitution (COR), a measure of the particles' impact characteristics, was measured for microparticles using a particle tracking technique. This study presents data taken using the Virginia Tech Aerothermal Rig and Arizona Road Dust (ARD) of 20-40 μm size range. Data was taken at temperatures up to and including 1323 K, where significant deposition of the sand particles was observed. The velocity at which the particles impact the surface was held at a constant 70 m/s for all of the temperature cases. The target on which the particles impacted was made of a nickel alloy, Hastelloy X. The particle angle of impact was also varied between 30° and 80°. The COR of the particles decreases slightly as some of the particles approach their glass transition point and start to become molten. Other particles, which do not become molten due to different particle composition, rebound and maintain a relatively high COR. Images were taken using a microscope to examine the particle deposition that occurs at various angles. A rebound ratio is formulated to give a measure of the number of particles which deposit on the surface. The results show an increase in deposition as the temperature approaches the melting temperature of sand.

4.2 Introduction

Gas turbines are a popular source of power for aerospace and land-based applications. Particle ingestion can reduce engine life and performance through erosion and deposition. There are several different situations where particles can be ingested. Volcanic eruptions and dust storms can send particulate to aircraft cruising altitudes. Also, aircraft operating in remote locations or at low altitude can be subjected to particle ingestion, especially in desert environments (See Figure 4-1).

Figure 4-1. Example of sand ingestion in desert conditions

Sand and dust effect gas turbine engines in several ways. In the cold section of the engine, erosion is the primary mechanism of damage. Once the particulate passes through the burner, sand melting and deposition becomes the primary mechanism of sand particulate damage. Deposition on gas turbine blades and vanes causes changes in aerodynamic profiles, deposits of surface coatings on combustor and turbine components, deterioration of film cooling efficiency, and blockages of cooling systems, all of which can lead to premature engine failure.

In the past, erosion and deposition have been modeled in several computational studies for gas turbines. These studies have used empirical impact correlations and analytical models to determine the behavior of the particles at impact. The current study expands the data available for empirical impact correlations by presenting impact and rebound characteristics of microparticle sand at temperatures near the melting point of sand. This will enable more accurate models and computational analysis of sand transport in gas turbines.

Coefficient of Restitution (COR) is a measure of the particle/wall interactions and is used to study erosion and deposition. COR is defined as:

(4-1) $$e = \frac{V_2}{V_1}$$

where V_2 is the velocity after impact and V_1 is the incoming velocity before impact. The particle impact is an extremely complex phenomenon which involves variables such as: particle material, particle shape, particle temperature, particle velocity, particle spin, wall material, wall roughness, and wall temperature. Figure 4-2 displays a diagram of a particles trajectory before and after impact. The solid lines in Figure 4-2 represent the particles' actual velocity while the dotted lines represent the normal and tangential components of velocity.

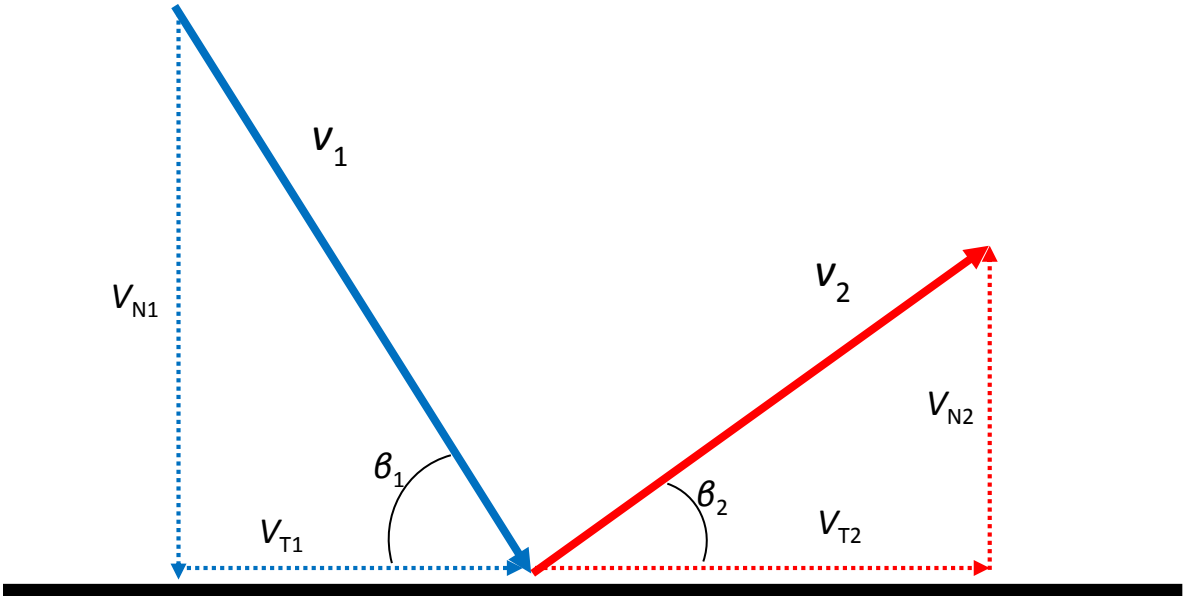

Figure 4-2. Diagram of incoming and rebounding particle trajectories

COR for the normal and tangential components of velocity are also important quantities for studying particle impacts. The normal and tangential CORs are defined as:

(4-2) $$e_N = \frac{V_{N2}}{V_{N1}}$$

(4-3) $$e_T = \frac{V_{T2}}{V_{T1}}$$

where V_{N2} is the normal component of the rebounding velocity, V_{N1} is the normal component of the incoming velocity, V_{T2} is the tangential component of the rebounding velocity, and V_{T1} is the tangential component of the incoming velocity.

Several studies have investigated how different conditions affect COR. Some of the first studies of impact mechanics were done by Goldsmith [1] in the 20th century. From this work COR is found to decrease with increasing velocity, increasing particle size, and decreasing surface hardness. Tabakoff [2] confirms that in general COR decreases as particle velocity increases. Li *et. al.* [3] studied 70 μm mean diameter SS316 spheres impacting a silicon crystal wafer at different angles and velocities. The velocities measured were very low, 1.6 m/s, 1.05 m/s, and .45 m/s. The COR was relatively constant at 0.7 for angles between 50° and 85°. Microparticle adhesion is an issue at these low velocities and contributes to the low COR values. Sommerfeld and Huber [4] found that rougher surfaces and more oblong particles tend to have a lower COR and wider scatter due to local deformation.

Past studies have mostly neglected the effects of temperature on COR. Only a few studies are relevant to the current research. Mok and Duffy [5] studied solid steel balls impacting cylindrical targets made from 6061-T6 aluminum. The balls impacted the target at 90° with a range of velocities from 0-5 m/s and temperatures from 294-755 K. Temperature did have an effect on the COR for the steel ball/aluminum target impact. It was found that as temperature increased, COR decreased. Brenner *et. al.* [6] studied the impacts of three types of iron spheres on aluminum oxide covered iron plates at 973 and 1073 K at 90° impact angle. COR results were presented for velocities up to 3 m/s. COR was found to decrease as the temperature increased.

Tabakoff *et. al.* [7-10] completed a number of studies on the erosive effects of particles on metals. COR has been used in these studies to find a correlation between COR and erosion. These works show that erosion is mainly a function of the tangential COR. These works also clearly show that COR is a statistical function. Wakeman and Tabakoff [9] studied the erosive behavior of 150-180μm quartz sand at temperatures up to 978 K and velocities up to 274 m/s at different impact angles. It was concluded that as velocity increased for the erosive data, a power law relationship fit the data very well. The coefficients for the relationship vary with material and angle of impact. Tabakoff *et. al.* [8] studied 150 μm sand particles impacting several turbomachinery target materials at 90.85 m/s for different angles of impact. The COR trends for

all of the materials were similar, but the characteristics of the COR were different for each of the materials. Reagle *et. al.* [11, 12] tested the effects of temperature and velocity on COR for sand particles. In those studies, velocity was not controlled independently of temperature and increased with temperature. The current study controls velocity independent of temperature allowing for the effects of temperature to be studied.

Several studies have been performed to study the effect of temperature on particle deposition. Walsh *et. al*. [13] performed sand deposition studies and found that the temperature at which sand begins to deposit to be between 1273 K and 1353 K in their experimental setup. Crosby *et. al.* [14] found that fly ash experiences a sharp decrease in deposit quantities at temperatures below 1233 K. All of these as well as several others have studied deposition patterns, but have not characterized impact behavior. These studies do indicate that deposition should be seen in the VT Aerothermal Rig at 1273 K and 1323 K.

COR has not been documented at near-deposition temperatures for engine representative sand microparticles at different angles. More study is needed before particle transport and energy transfer mechanisms of microparticles can be confidently included in computation models. This study provides new insight into the effect of temperature on particles that will help bridge the gap between previous research done at ambient conditions and deposition. The companion work to this study [15] which investigates a lower temperature and velocity regime than the near-deposition regime investigated in this study will allow for significant new insights into particle impact. The results are immediately applicable to enhancing the accuracy of numerical simulations.

4.2.1 Nomenclature

ARD	Arizona Road Dust
CFD	Computational Fluid Dynamics
COR	Coefficient of Restitution
d	diameter
e	Coefficient of Restitution (COR)
L	length
PDF	Probability Density Function

PTV	Particle Tracking Velocimetry
RMS	Root Mean Squared
Stk	Stokes Number
t	time
V	Velocity
$\bar{x}$	mean

Greek Letter Symbols

β	impact angle
σ	Standard Deviation
ρ	density
μ	viscosity

subscript

c	characteristic
N	normal
p	particle
T	tangential
∞	freestream

4.3 Experimental Setup

4.3.1 Aerothermal Rig

The Virginia Tech Aerothermal Rig was donated by Rolls Royce to Virginia Tech in 2010. It was previously used in Indianapolis, Indiana, for heat transfer studies by Nealy *et. al.* [16] and Hylton *et. al*. [17]. The original operation specifications for this rig were reported by Rolls Royce as 2.2 kg/s at a maximum pressure of 16 atm and temperature of 2033 K. The VT Aerothermal Rig was used to conduct all the experiments discussed in this paper

The rig has been modified from its original configuration to allow sand to be injected immediately downstream of the burner. Figure 4-3 is an image of CAD model of the VT Aerothermal Rig showing its layout in the current configuration. The rig was used previously by Reagle [11, 12] to study sand ingestion at temperatures lower than 1073 K. Since the work by Reagle, the equilibration tube has been changed to allow for a higher maximum operating

temperature. The current maximum test section temperature of the rig constrained by the limits of the uncooled equilibration tube is 1323 K.

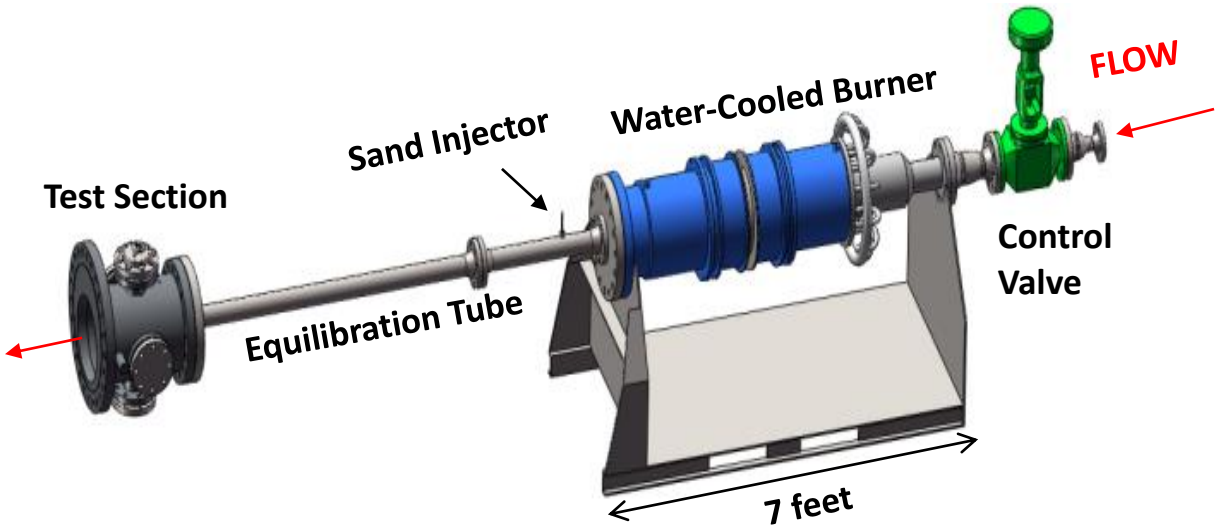

Figure 4-3. VT Aerothermal Rig

A compressor supplies compressed air to a buffer tank at a mass flow rate of 0.15 kg/s. A series of regulator valves control the flow rate of the air before it goes through the main control valve, which is used to make fine adjustments. The regulator control valves are adjustable so that any mass flow rate less than 0.15 kg/s can be maintained. These regulators allow the mass flow rate of the rig to be controlled precisely, which in turn allows temperature and velocity to be controlled independently.

After passing through the control valve, the air flow passes through the sudden-expansion, water-cooled burner that heats the flow using methane as fuel. The sand particles are entrained in a flow separate from the main flow and are injected into the main flow after the burner. The flow travels through the 7.62 cm diameter, 1.82 m equilibration tube to allow the sand particles to reach the temperature and velocity of the flow. The flow then exits the equilibration tube as a free jet in the test section and impinges on the test coupon. During each test, a sufficient amount of time is allowed for the temperature of the rig to reach equilibrium before sand particles are injected and measurements of the particles are taken.

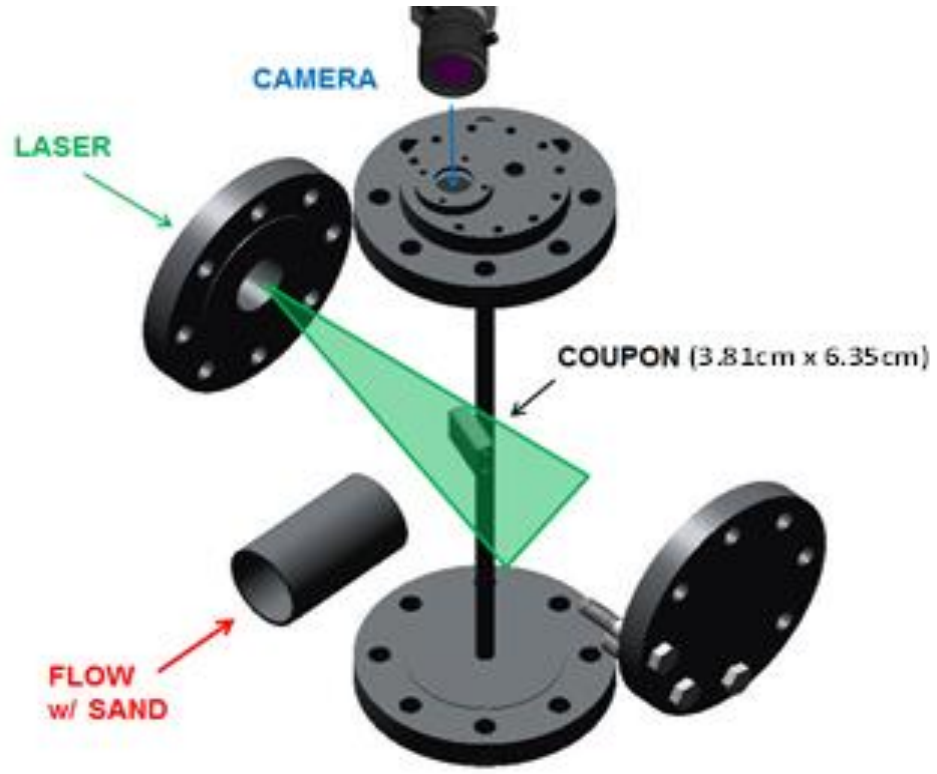

Figure 4-4. Schematic of instrumentation setup

A CAD image of the test section without the outer casing walls is shown in Figure 4-4. The figure shows the test coupon support that can be rotated in 10° increments. This allows for various angles of impingement to be studied. A quartz viewing window in the top flange allows for a camera to view the test coupon. The test section also has a quartz laser access port to allow illumination of the coupon and particles during testing. The test coupon on which the impacts occur is 3.81 cm by 6.35 cm. The coupon is rectangular in shape to allow for a sufficient area to be projected normal to the flow when testing at shallow impingement angles. The test coupon is made from Hastelloy X, which is a high temperature nickel alloy. The coupon is polished to a mirror finish with a measured RMS roughness less than 0.2μm before every testing run to ensure surface roughness effects are minimized.

4.3.2 Test Conditions

In previous works published using this experimental setup by Reagle *et. al.* [11, 12] there was no method for precisely controlling the mass flow rate in the test rig. This means that as the

air temperature was raised, the velocity of the flow increased as well. As discussed in the section on the VT Aerothermal Rig, modifications made for this study allowed a constant velocity independent of temperature. The velocity chosen for this work was at 70m/s. For each temperature that tests were conducted, the coupon was rotated in 10° increments from angle of incidence 30° to 80°. Also it is important to note that the temperature of the metal coupon is substantially lower than the air and particle temperature. This lower temperature is due to conduction through the support and radiation heat transfer losses that affect the coupon. Table 4-1 below shows the test conditions for the experiments described in this paper. These test conditions were chosen after studying the experiments of Walsh *et. al.* [13] and Crosby and Bons [14]. Temperatures near and below the temperature at which all of the particles can be assumed to deposit on impact were chosen to observe the effects of near-melting temperature on COR. An additional run was performed at 1073 K to verify the repeatability of the data and data reduction method. It was found that the data was repeatable within 0.01 on the COR scale.

Table 4-1. Test Temperatures and Velocities

Air Temp (K)	Coupon Temp. (K)	Bulk Velocity (m/s)
1073	933	70
1173	1033	70
1223	1073	70
1273	1133	70
1323	1183	70

4.3.3 Instrumentation

In order to determine the velocity of the flow exiting the equilibration tube, a Pitot-static probe is mounted to a traversing mechanism and placed at the exit of the equilibration tube. Because the probe is mounted to a traverse mechanism it can be placed in the flow to verify test conditions prior to the run and then removed so as not to be damaged or clogged by sand while particles are being injected into the flow.

To measure the temperature of the air exiting the equilibration tube, a type K thermocouple is placed above the coupon. Additionally, a thermocouple is buried inside the metal of the coupon itself, and sealed with high temperature cement, in order to accurately

measure the temperature of the coupon. There are many other thermocouples which are also placed on and in the rig. These thermocouples are used to insure that the rig has reached equilibrium temperature and to make sure that the rig does not go over its safe temperature limits.

A Litron Nd:YAG laser is used to illuminate the particles in the test section. The laser can be set to emit up to 55 mJ per laser pulse at 532 nm wavelength. For the camera settings used in this experiment, it was found that setting the laser to 55 mJ produced the best images. The thickness of the laser sheet where it intersects the coupon is ~4 mm. The camera used is a Dantec Dynamics® FlowSense camera equipped with a Zeiss® Makro-Planar 2/50 lens. Figure 4-4 shows the relation of the laser light, camera, equilibration tube, and coupon. The camera is a monochrome camera which captures images with a 2048x2048 resolution. The laser-camera system is able to refresh at a rate of 7.4 Hz between image pairs captured. The camera is focused such that a single particle is captured in one or two pixels on each image. With the air velocity set to 70 m/s, it was found that 6 μs between images was the best setting for the laser and camera image pair speed. This small time allows the particles to move ~9 pixels between images. This particle movement is enough distance to get an accurate measure of the particle's velocity. If the particles move too far between the two images it becomes very difficult to correctly match a particle from the first image with a particle from the second image. This will produce many false velocity vectors. The 6 μs time between images is small enough to almost eliminate the possibility of false velocity vectors. In addition the measured particles are filtered to remove particles that have more than one possible match to remove any remaining false velocity vectors.

4.3.4 Particles

The sand particles used for this test are Arizona Road Dust (ARD). The particle size of the ARD used for this test was a narrow size range of 20-40 μm. The numerical mean particle size was calculated from particle batch analysis provided by the particle manufacturer of the ARD used in the experiments. A narrow size range of particles is extremely important so that the possible effects of particle size do not contaminate the test results. The chemical composition as well as description of particle size distribution of this test dust range can be found in the previous work by Reagle *et. al.* [11]. The chemical composition reported is the bulk

chemical composition of the ARD. Individual particles will vary significantly in composition from the composition shown for the bulk materials. Small microparticles have a tendency to clump together while being stored due to moisture. In order to achieve accurate test results for microparticles, the particles cannot be allowed to clump together. To avoid clumping, it is necessary to heat the particles for several hours in an oven to drive all possible moisture from the particles. This prevents much of the clumping that would otherwise occur.

The Stokes number (Stk) is the ratio of particle relaxation time to fluid relaxation time. The Stk quantifies the degree to which particles suspended in a fluid flow will follow the fluid motion. This means that a particle with a Stk much larger than unity will not follow the fluid flow, but instead its momentum will force it to keep traveling in its original direction. The equation used to calculate the Stk is shown in the following equation:

(4-4) $$Stk = \frac{\rho_p d_p^2}{18\mu} \frac{V_\infty}{L_c}$$

where ρ_p is density of the particle, d_p is diameter of the particle, V_∞ is fluid velocity, μ is fluid viscosity, and L_c is the characteristic length of the system in this case the width of the coupon. The Stk determines how the particle will behave in a fluid flow. Particle impact characteristics are not directly affected by the particle Stk; however, it is still important to know the Stk of the particles, because at very low Stk no particle impact on the target coupon will occur. The Stk at the different experimental conditions is given in Table 4-2 below.

Table 4-2. Test Dust Stokes # Extreme Values

Test Condition	Bulk Velocity	Stokes # 20µm	Stokes # 40µm
1073	70	1.45	5.79
1173	70	1.37	5.49
1223	70	1.34	5.36
1273	70	1.31	5.23
1323	70	1.28	5.12

4.4 Data Reduction

The data reduction method used for this experiment is very similar to that which was used in past studies [11, 12] involving this experimental setup. A few significant changes have been made to improve the accuracy of the method. Because the particle velocity is always measured at a distance from the target coupon, some velocity correction is needed. Past works by other researchers using similar methods of determining particle velocity have assumed that the measured velocity at some distance from the target was the velocity with which the particle would arrive at or leave the target. While this may be true for large Stk particles, it is not true for smaller particles which are strongly influenced by the fluid flow. The particles which are being studied in this paper are strongly influenced by the flow field; this necessitates the use of a velocity correction in order to obtain the velocity at the moment of impact with the target coupon.

4.4.1 Particle Tracking

The PTV method used in this study involves implementing a band pass filter on the image to remove large objects (coupon, thermocouples, etc.), locating the particles, and then using a radius of gyration calculation to find the particle centroid to sub-pixel accuracy. After the particle locations have been determined, the particles are then correlated between the images in the image pair to determine particle velocity. If there is more than one possible correlation option within the circle of possible movement for the particle, then that particle velocity is disregarded.

Once the particle velocity has been measured, the velocity is used as a starting point for a Lagrangian particle tracking algorithm which uses a flow field calculated from ANSYS CFX for the Eulerian phase of the calculation. This CFX flow field is validated against velocity surveys taken with the Pitot-static probe immediately upstream of the coupon to ensure accuracy. The output from this Lagrangian scheme for velocity correction is the velocity at which a particle, measured at a distance from the coupon, had at the moment of impact. An incoming particle which is detected and measured at some finite distance away from the target will have a different velocity when it strikes the target coupon. This impact or rebound velocity at the moment just before or just after the impact is what is needed to calculate COR.

Although the basic method used by Reagle *et. al.* [11, 12] in previous works has been retained, one significant change has been made to the particle tracking algorithm. In the reduction method used for this work there is a limit to how far a rebounding particle may be from the coupon to still be used in the data reduction scheme. This limit is set to fifty 6μs time steps of the Lagrangian particle path algorithm. This means that rebounding particles must have travelled less than 2 cm from the point of impact to be counted. This constraint helps to eliminate any error that could be created by use of the Lagrangian correction to the particle velocity. It also helps to remove potential bias effects of particle size variation. This is because larger particles are capable of retaining their velocity in the face of the contrary velocity gradient much better than the smaller particles, and therefore can travel farther from the coupon than small particles. By being limited to particles which are very close to the coupon, this potential source of bias is removed. During the course of a test run it is normal for approximately two thousand rebounding particles to be captured and a like number of incoming particles at each of the six angles at which experiments are conducted.

4.4.2 Coefficient of Restitution Calculations

Once the particles have been tracked the COR can be calculated. A full description of the details the method used to calculate COR can be found in the companion work to this paper by Delimont *et. al*. [15], but a shorter description is provided in this paper. In order to determine the COR, incoming and rebounding particles are sorted into bins by the location of impact on the target coupon. The width of the coupon area allocated to each bin is 2 mm. Once all impacts have been sorted into their appropriate bin based on impact location, a mean total, normal, and tangential velocity are calculated for both incoming and rebounding particles. Calculating the distribution of the COR around the mean is a complicated task.

In order to properly calculate the distribution of the COR about the mean, it is necessary to perform a ratio distribution of V_2 and V_1. The equation for the ratio distribution of two variables was derived by Hinkley in his 1969 work [18]. This derivation requires that the two distributions be Gaussian, which is verified during the data reduction process. Hinkley's work provides an equation that utilizes a correlation coefficient for dependent data sets. The correlation coefficient between V_2 and V_1 was calculated to be on the order of 0.01, which means

the data is statistically independent. Because V_2 and $V_1$are statistically independent over the 2 mm width of coupon face, the equation for the probability density function (pdf) of the ratio distribution can be simplified to the following format:

$$p.d.f.(z) = \frac{b(z)*c(z)}{\sqrt{(2\pi)}\sigma_1\sigma_2 a^3(z)} \begin{bmatrix} \Phi\left(\frac{b(z)}{a(z)}\right) - \\ \Phi\left(-\frac{b(z)}{a(z)}\right) \end{bmatrix} + \frac{1}{a^2(z)\pi\sigma_1\sigma_2} e^{-\frac{1}{2}\left(\frac{\bar{x}_1{}^2}{\sigma_1^2}+\frac{\bar{x}_2{}^2}{\sigma_2^2}\right)} \tag{4-5}$$

Where

$$a(z) = \sqrt{\frac{1}{\sigma_1^2}z^2 + \frac{1}{\sigma_2^2}}, \quad b(z) = \frac{\bar{x}_1{}^2}{\sigma_1^2}z + \frac{\bar{x}_2{}^2}{\sigma_2^2}$$

$$c(z) = e^{\frac{1}{2}\frac{b^2(z)}{a^2(z)}-\frac{1}{2}\left(\frac{\bar{x}_1{}^2}{\sigma_1^2}+\frac{\bar{x}_2{}^2}{\sigma_2^2}\right)}, \ \Phi(z) = \int_{-\infty}^{z}\frac{1}{\sqrt{2\pi}} e^{-\frac{1}{2}u^2}\, du$$

where σ_1 is standard deviation of the incoming velocity, $\bar{x}_1$ is the mean of the incoming velocity, σ_2 is the standard deviation of the rebounding velocity, $\bar{x}_2$ is the mean of the rebounding velocity, and z is the variable for which the probability density function is calculated, in this case COR.

The resulting distribution from performing the ratio distribution on two independent variables is a Cauchy distribution. Since Cauchy distributions do not have mathematically definable means or standard deviations, we estimate these values based on the probability density function. These estimated mean and standard deviation values for e, e_N, e_T are presented for each of the test cases in the results section.

A power law equation was used to curve fit the COR data. The choice of the power law curve fit was made after examining the different possible curve fits and determining that the power law matched the data the best. The two coefficient form of the power law equation used for the curve fitting can be seen in Equation (4-6) below.

$$e = A\beta_1^B \tag{4-6}$$

where $\beta_1$is in degrees and A and B are the coefficients. The curve fitting of this equation to the data was performed using MATLAB.

4.5 Results

Data was recorded for impacts of 20-40 μm ARD impacting a polished Hastelloy X coupon for angles ranging from 30° to 80° for each of the five different temperatures near beginning of the melting point of sand. The COR as well as the normal and tangential components of the COR are presented in this section. The Appendix contains the coefficients for the all power law curve fits used in the results section. Additionally two different methods are used to quantify the amount of particles that deposit on the coupon.

4.5.1 COR

Figure 4-5 displays the sample mean for COR vs. angle of impact for the different temperatures. The trends for COR are similar for the different temperatures. There is a decrease in COR at the high angle of impact as has been seen in many other studies. This is believed to be due to the higher normal velocity in combination with softer particles allowing more energy to be absorbed in plastic deformation of the particle material. The change in COR as temperature increases is negligible. This is somewhat surprising in that the particles are beginning to deposit at 1273 K and a substantial portion are depositing at 1323 K. It is important to realize that the method that has been chosen for this work to measure the COR will only capture particles that rebound from the surface of the coupon.

Sand particles, especially microparticle sand, vary in composition from particle to particle. This means that some percentage of the particles will be fully molten at temperatures tested in these experiments, while others will retain most of their crystalline structure, and thus rebound from the target. While deposition was observed in the 1273 K and 1323 K cases, most of the particles retained enough of their solid state characteristic to rebound and be recorded by the experiment as a COR data point.

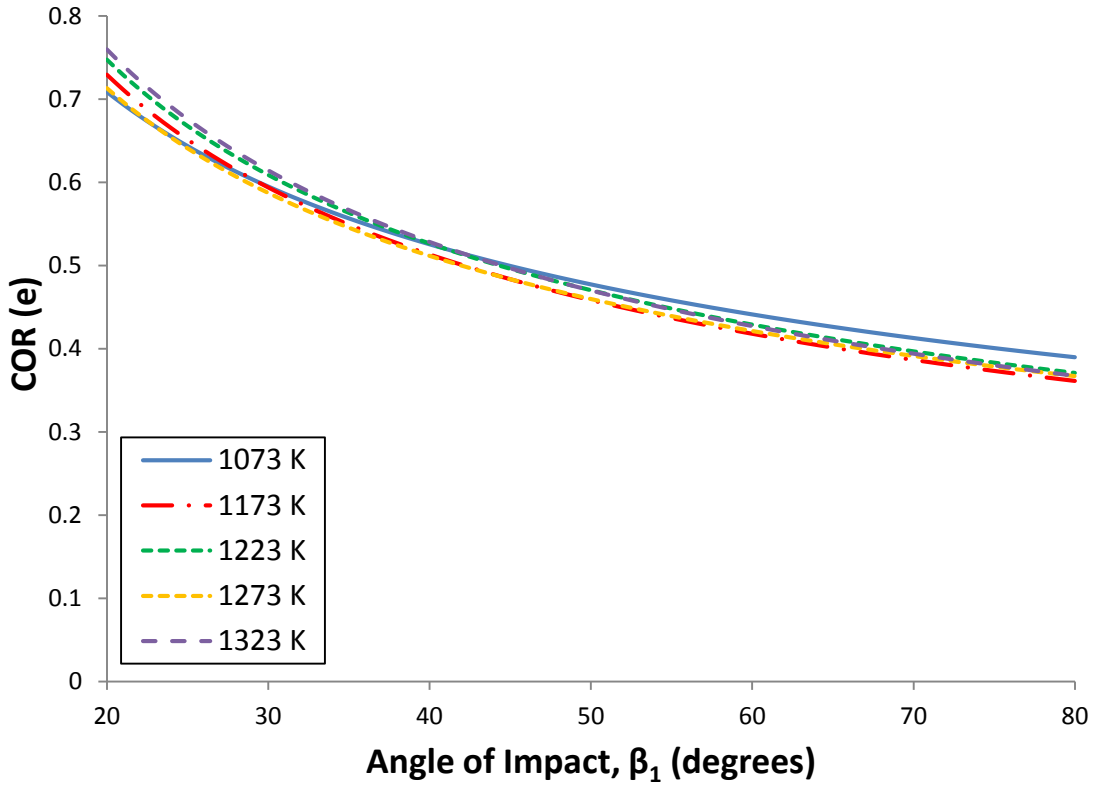

Figure 4-5. Plot of total COR vs. angle of impact

Table 4-3 below shows the standard deviation that was calculated for each of the test runs at various angles. It is worth noting that the standard deviation show a remarkable uniformity between the different test runs.

Table 4-3. Total COR Estimated Standard Deviations

Mean COR Estimated Standard Deviation					
Angle	**1073 K**	**1173 K**	**1223 K**	**1273 K**	**1373 K**
20	0.08	0.10	0.08	0.09	0.09
30	0.11	0.12	0.12	0.12	0.11
40	0.13	0.13	0.13	0.13	0.12
50	0.13	0.13	0.14	0.13	0.12
60	0.14	0.13	0.14	0.13	0.12
70	0.14	0.13	0.14	0.13	0.12
80	0.14	0.13	0.14	0.13	0.12

4.5.2 Normal COR

Figure 4-6 displays the normal COR vs. angle for the different temperatures. Similar to what has been seen at lower temperatures, a chromium oxide layer forms on the surface of the Hastelloy X coupon. The higher COR observed between 20° and 40° angle of impact is believed to be due to the significantly lower normal velocity which the particles have when they strike the surface. The overall trends of normal COR are nearly identical for all temperatures examined in this study.

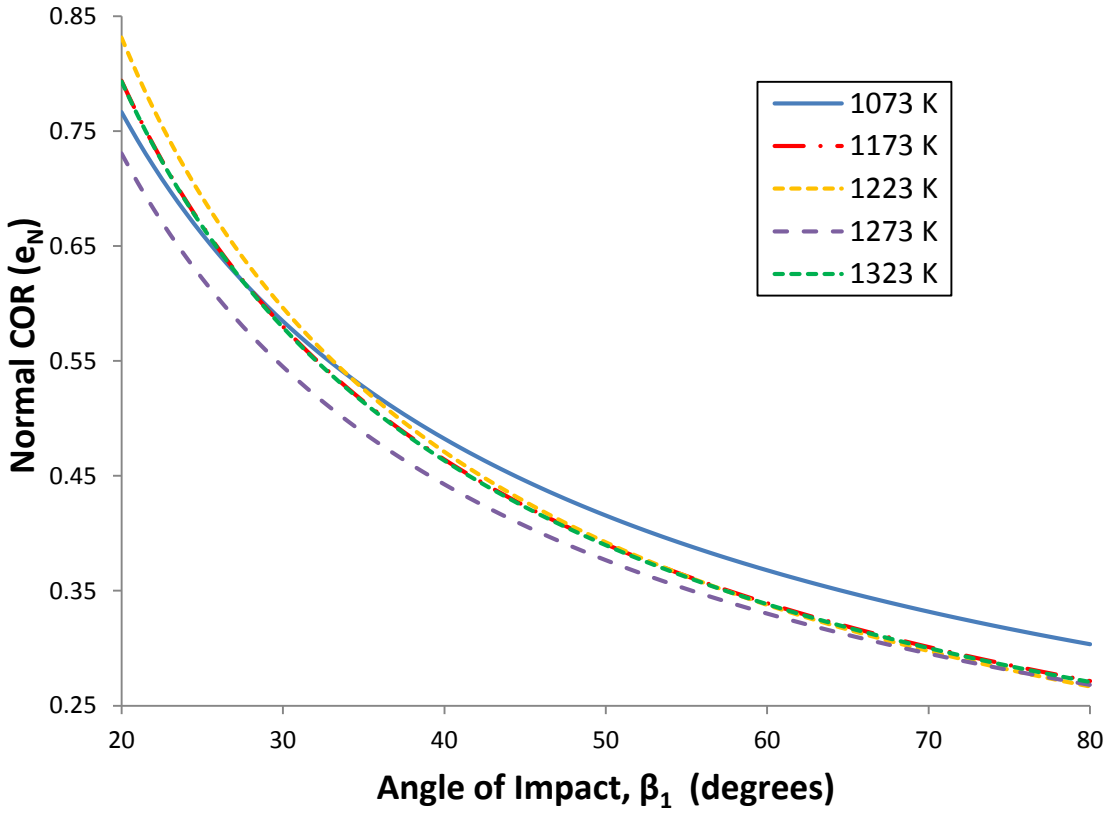

Figure 4-6. Plot of normal COR vs. angle of impact

Table 4-4 displays the estimated standard deviations for the curves shown in Figure 4-6. It should be noted that the amount of velocity component measured in the normal direction is very small for the data taken between 20° and 30°. This makes the signal-to-noise ratio larger and explains why the standard deviations at low angles of impact are much larger. This has been observed in a great deal of the literature which has examined normal COR over the full range of impact angles.

Table 4-4. Normal COR Estimated Standard Deviation

Normal COR Estimated Standard Deviation					
Angle	**1073 K**	**1173 K**	**1223 K**	**1273 K**	**1373 K**
20	0.31	0.31	0.36	0.29	0.29
30	0.23	0.22	0.25	0.21	0.21
40	0.18	0.17	0.20	0.17	0.16
50	0.16	0.14	0.16	0.14	0.13
60	0.14	0.12	0.14	0.12	0.12
70	0.12	0.11	0.12	0.11	0.10
80	0.11	0.10	0.11	0.10	0.09

4.5.3 Tangential COR

Figure 4-7 displays the tangential COR vs. angle for the different temperatures. Table 4-5 displays the estimated standard deviations for the trends in Figure 4-7. All of the trends of tangential COR are relatively similar, although a larger amount of variation is seen in the trends as compared to the other two measures of COR presented here. This is partially due to the large amount of variation that is seen in the high angles. This makes the curve fitting process very susceptible to groupings of extreme data that occur in the 75°+ region. The reason for this is the small tangential velocity at high angles. This creates a very small signal which, similar to the low angles at normal impact, is easily influenced by random factors. At high angles, these effects lead to an extremely large increase in standard deviation as can be seen in Table 4-5 which shows one standard deviation as +/- 0.85.

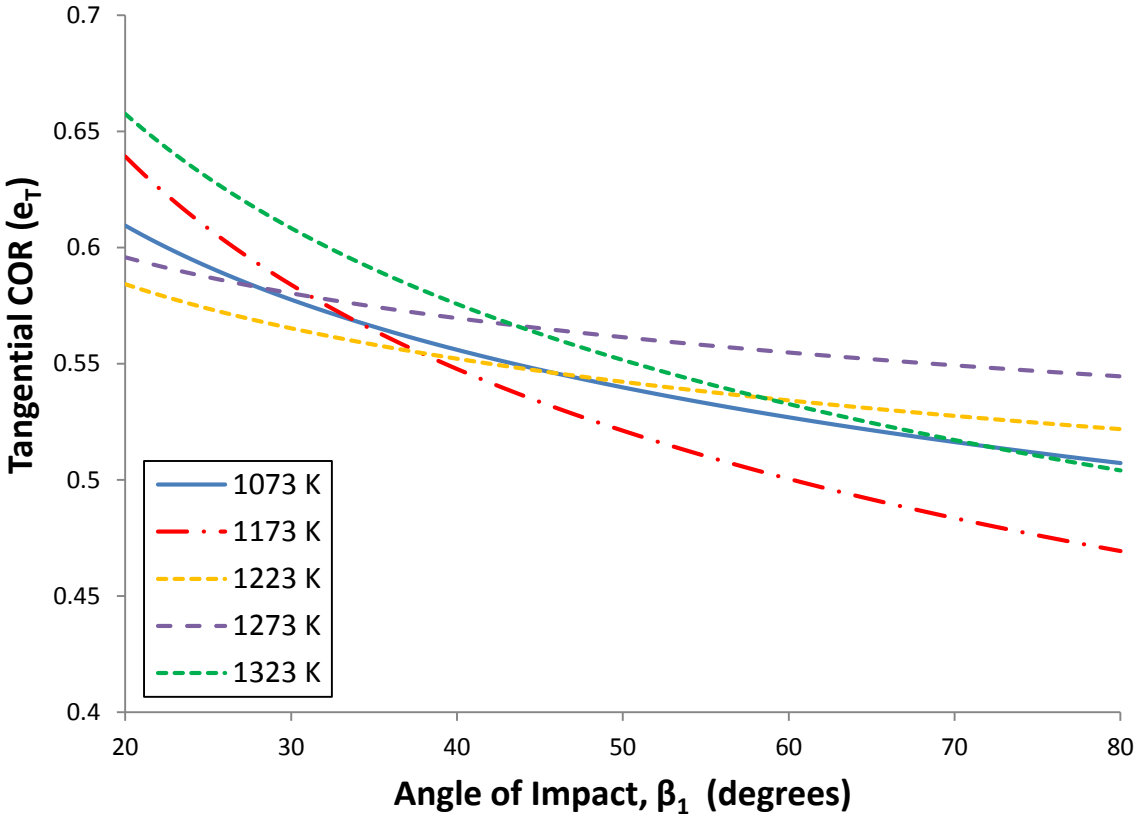

Figure 4-7. Plot of tangential COR vs. angle of impact

Table 4-5. Tangential COR Estimated Standard Deviation

Tangential COR Estimated Standard Deviation					
Angle	**1073 K**	**1173 K**	**1223 K**	**1273 K**	**1373 K**
20	0.09	0.20	0.14	0.09	0.15
30	0.12	0.16	0.17	0.13	0.15
40	0.19	0.17	0.24	0.20	0.19
50	0.30	0.24	0.34	0.30	0.28
60	0.44	0.37	0.47	0.43	0.43
70	0.60	0.60	0.62	0.59	0.63
80	0.81	0.96	0.80	0.78	0.91

4.5.4 *Effect of Temperature on COR*

Figure 4-8 displays a plot of COR vs. temperature for three different impact angles and the four different temperature cases. It is apparent from this plot that the COR does not vary with temperature. As was mentioned earlier, this is believed to be caused by the non-homogeneous nature of the particles. This leads to certain compositions of particles softening much sooner than others. It is known that pure quartz crystals will melt at temperatures around 1900 K; however the addition of impurities can cause the melting temperature of quartz to lower significantly.

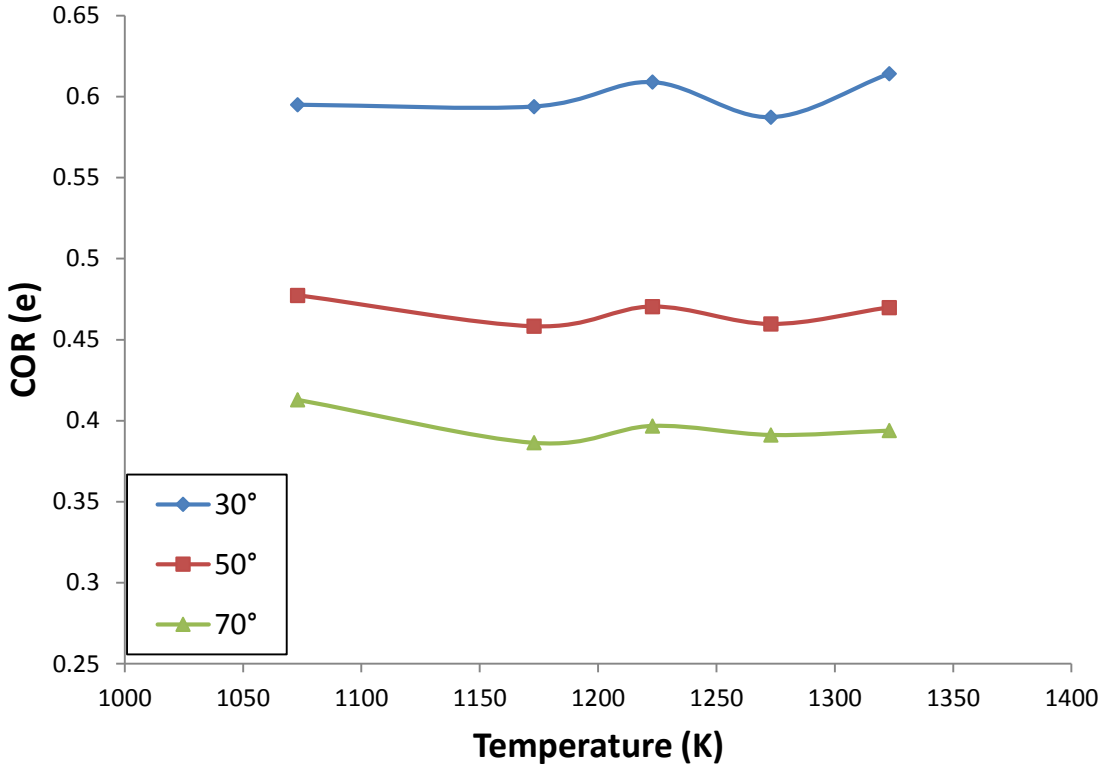

Figure 4-8. Plot of COR vs. temperature for different impact angles

4.5.5 *Rebound Ratio Calculations*

Even though deposition begins to occur at 1323 K, it is certain from the COR results that a large portion of the particles are still rebounding from the target coupon while some particles are depositing. In order to quantify the number particles that deposit onto the target within the

constraints of the experimental method, it was necessary to examine the number of particles which rebound from the surface compared to the number of incoming particles. A rebound ratio was defined in the following manner:

$$Rebound\ Ratio = \frac{Number\ of\ V_2}{Number\ of\ V_1} \tag{4-7}$$

This means that if the number of rebounding particles is the same as incoming particles, the ratio will equal unity. It is expected that this ratio will never equal unity due to particles rebounding out of plane, the larger incoming interrogation region, and many other reasons.

A rebound ratio is calculated for each angle of the coupon at each different temperature. In order for the rebound ratio to be of value for studying deposition it needs to be normalized so that it is equal unity when no deposition occurs. By normalizing the rebound ratio by the rebound ratio at a temperature where no deposition occurs, it should be possible to measure the increase in deposition at higher temperatures. For example, at 70° and 1073 K there are 1.55 times the number of incoming particles compared to the number of rebounding particles, and at 1323 K the ratio drops to 1.35 times as many. Normalizing the rebound ratio at 1323 K by rebound ratio by the 1073 K case will yield a normalized ratio of approximately 0.9 for this example. Capturing the rebound ratio in this manner is fairly noisy and the error bands are +/- 5%. Figure 4-9 shows the normalized rebound ratio averaged over all angles of impact. The results show that the normalized rebound ratio decreases to 0.87 at the highest temperature. Unity minus the rebound ratio yields the sticking ratio, meaning that 13% of the particles deposit on the surface at 1323 K.

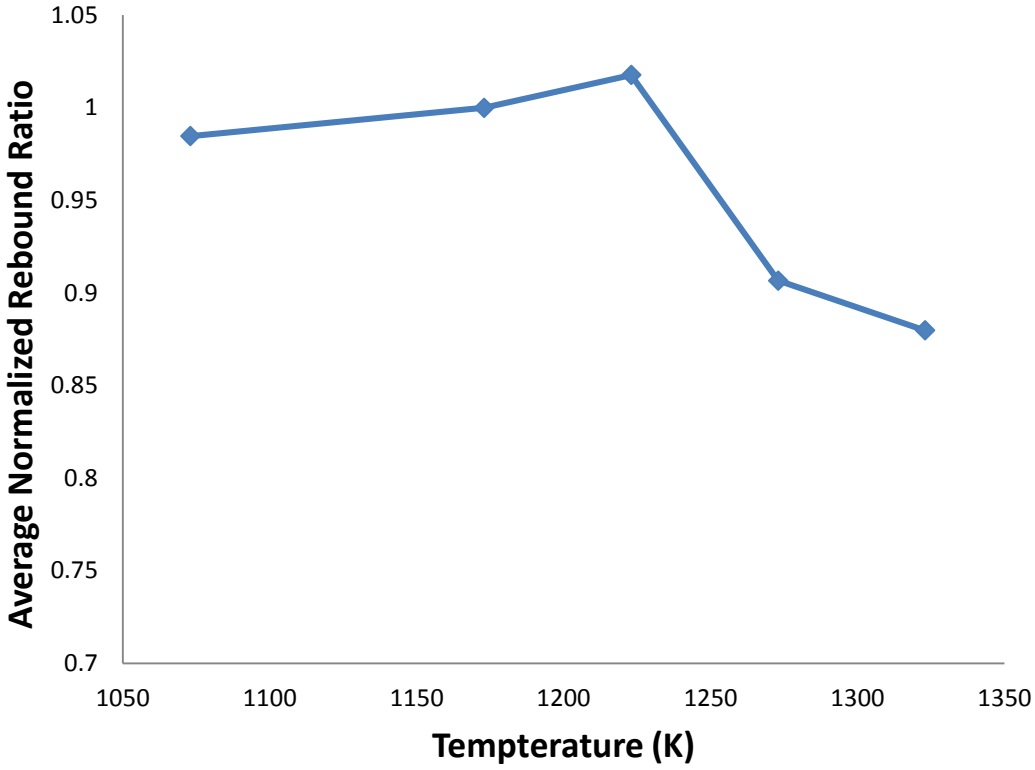

Figure 4-9. Averaged rebound ratio of angles

4.5.6 Deposition Measurement

In order to better understand the amount of deposition occurring during the test, it is possible to actually count the number of particles that have deposited in a given area. Images were taken of the deposition on the coupon after testing at 1273 K and 1323 K, using an Axiovert 200M optical microscope. Figure 4-10 below shows and example of the deposition that was observed at the highest two temperature cases. Some of the sand particles retain a great deal of their out of plane height, causing them to be out of focus, while others are small enough to be in focus and observe their surface characteristics. There is very little reason to suspect that these small particles are breaking free of the surface as the coupon cools. Their small size does not allow for very large stress buildup due to differences in thermal expansion as the coupon cools.

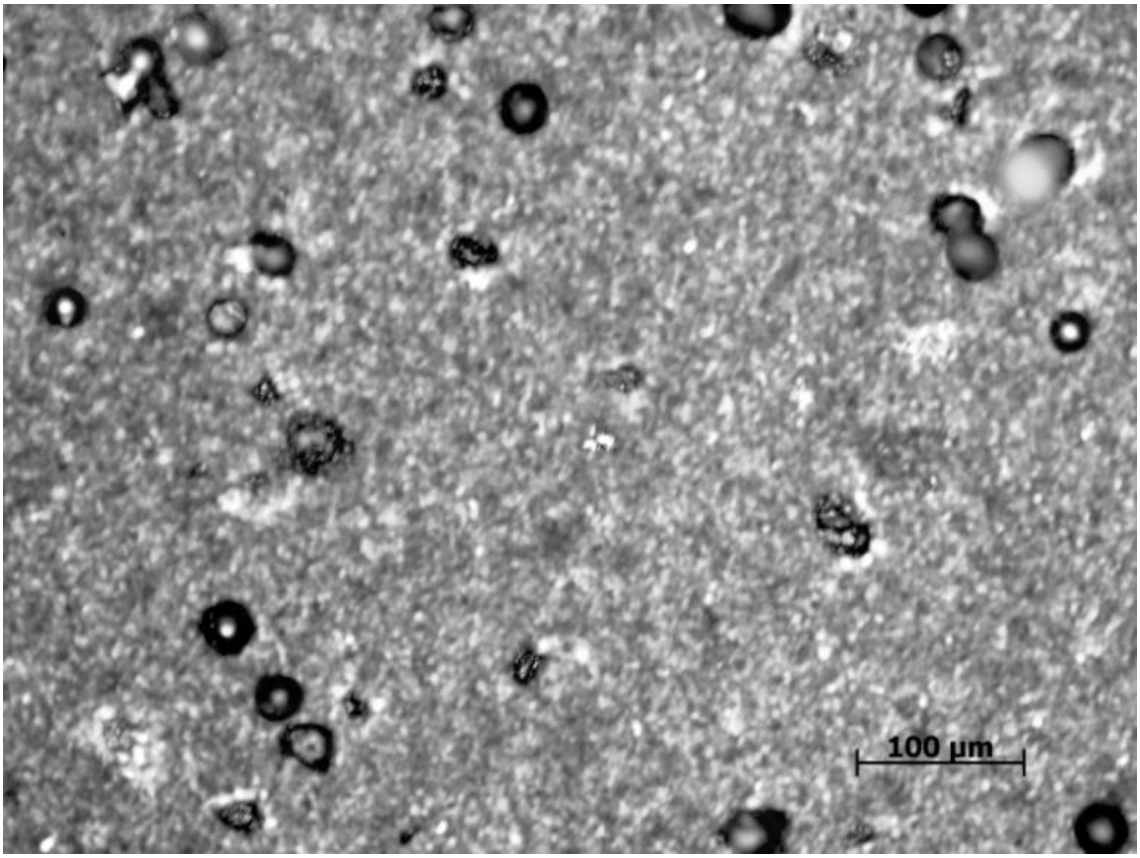

Figure 4-10. Image of sand deposition at 1323 K at 60° angle of attack and 200X optical magnification

Multiple images were taken after testing of selected runs. It was then possible to count individual sand particles in the image to gain a measure of the amount of deposition that occurs at each set of conditions. In order to directly compare deposition amounts exactly the same quantity of sand, 59 g, was put through the rig for each of the runs in which images were taken. The number of particles were counted and then averaged by area. The particle count from multiple images was averaged to get an accurate measure of the number of depositing particles per mm^2. Although no accurate measure of the change in weight of the coupon was made, it is certain, given the weight of the total input of particles and the amount of deposited particles, that the percentage of particles which deposit of the coupon is small compared to the number of particles which strike the coupon.

Figure 4-11 below shows a large increase in deposition that occurs at elevated temperatures. The increase from in temperature from 1273 K to 1323 K shows a roughly ten

times increase in deposition for the same angle. Each of the three angles shows nearly identical levels of increase over the same angle at the lower temperature. This increase from 1273 K to 1323 K is not seen at the same level in the rebound ratio measurement; this is believed to be due to the noise in that measurement and the small percentage of particles depositing.

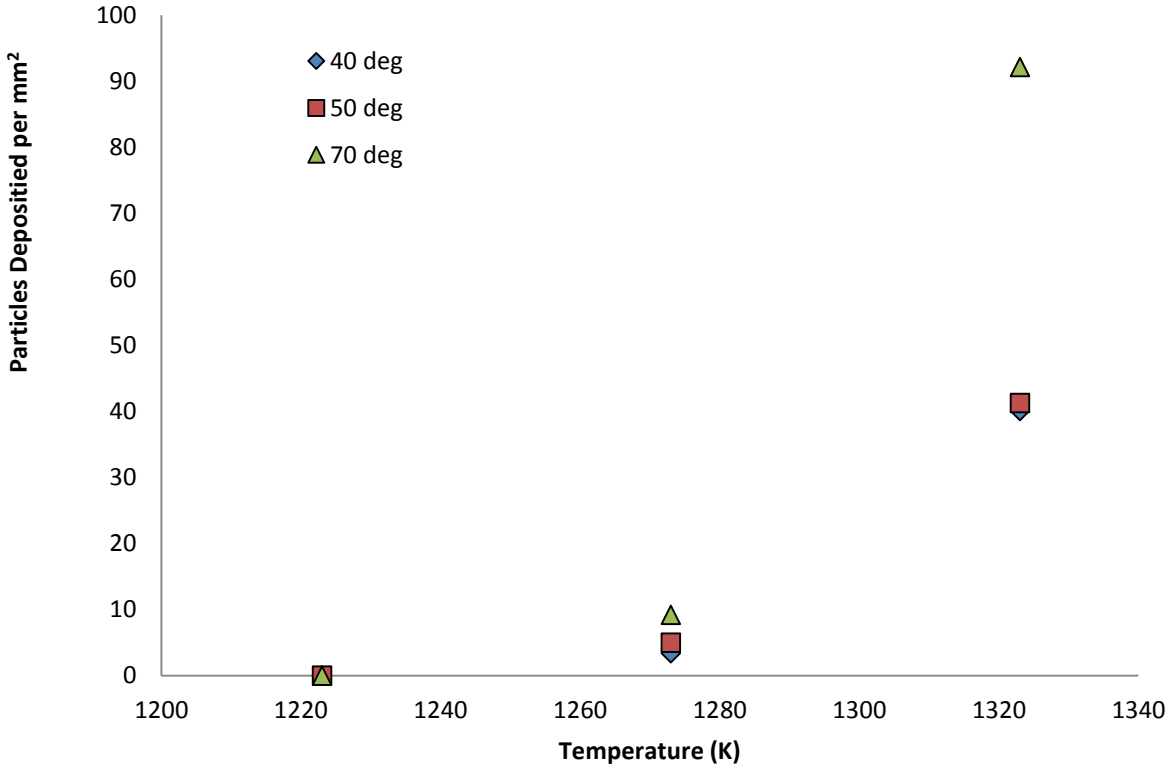

Figure 4-11. Deposition per mm^2 at several angles and at various temperatures

Additional information can be gained regarding the effects of the angle of impact on the deposition rate as well. The 40° and 50° angle of attack show roughly 45% of the deposition that occurs at 70° angle of attack. This percentage for the lower angles is almost identical for both temperatures at which deposition was observed. This is due to the much smaller normal velocity component at low angles which is primarily responsible for the deposition of particles of this size.

4.6 Effects of Sand Particle Characteristics

In the past literature there have been no studies that have attempted to characterize the COR of particles in the temperature range at which particles start to deposit. There are past works that have characterized the percent of particles that deposit on surfaces, but those have been done with homogeneous particle types. Further, many of these experiments have used either fly ash or glass particles – both of which have amorphous non-crystalline structures. Desert sand from a wide variety of locations has been shown to contain almost entirely particles of crystalline structure [19]. This crystalline structure causes several differences from a fly ash or other particle with an amorphous structure. The major difference is that crystalline mineral particles do not soften as do amorphous particles. This means that even though temperatures are approaching deposition there is no decrease in COR due to this effect. Additionally a crystalline particle generally melts at a higher temperature than an amorphous particle of the same chemical composition.

Figure 4-12 shows an image of the sand particles before experiments were run, taken with the same microscope used to count deposited particles. The image clearly shows four distinct colors of particles, meaning that there at least four distinct compositions composing this ARD sand and likely more compositions as literature on the mineralogy of desert sands show a great deal of variation in sand grain composition. Each of these materials has a potentially different melting temperature. This is a significant difference from a more homogeneous particle type where there is little difference in particle composition from one particle to another. The literature associated with melting of rock mineral is conclusive that sand melted in bulk will melt at a significantly lower temperature than individual particles [20, 21]. This is caused by chemical interactions that lower the melting temperature of the bulk material. In gas turbine application sand will experience elevated temperatures as individual particles and will melt at the individual particle temperatures.

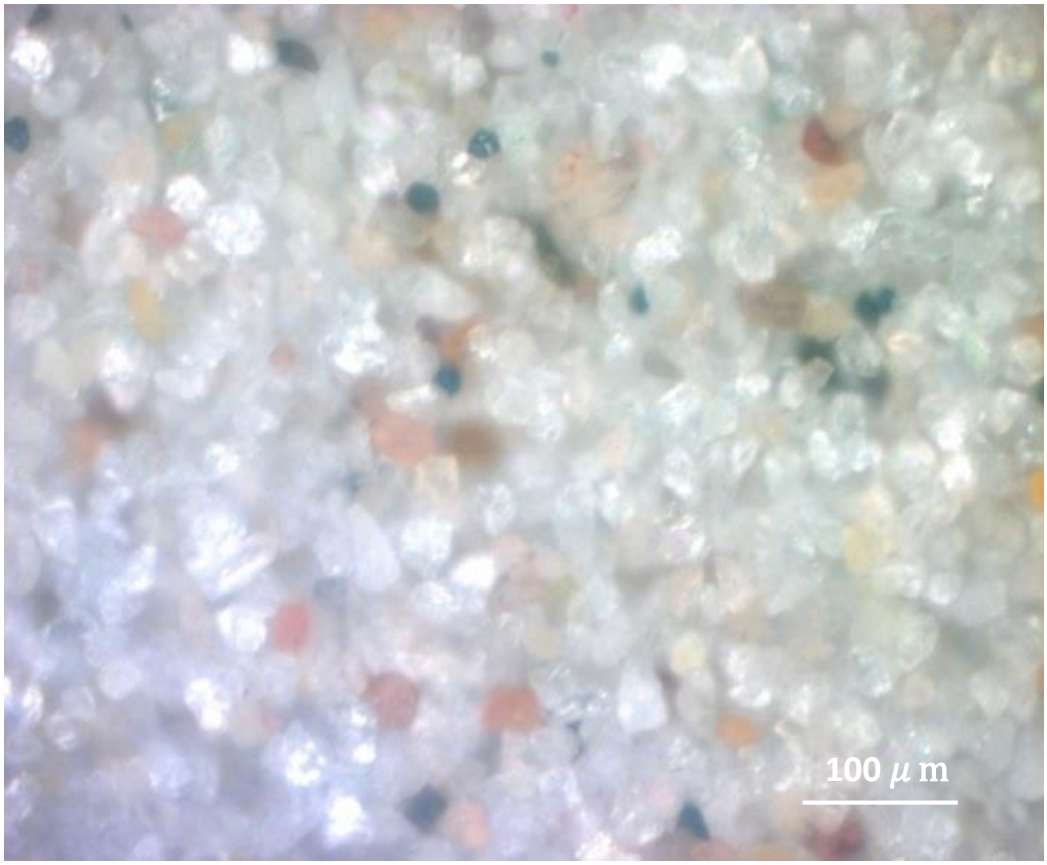

Figure 4-12. Image taken sand particles prior to testing at 200X optical magnification

In this experiment, deposition was observed to begin at 1273 K, but pure quartz melts in the 1900 K temperature range. It seems likely that the deposition observed was composed of a few select particle compositions while other particles which melt at much higher temperatures rebounded from the target. Particles which have not yet been effected by the temperature will rebound from the target and very little if any change in the COR of these rebounding particles is seen in the results.

Figure 4-13 shows hypothesized curves for the sticking ratio as well as the COR based on the idea that different constituent sand particles will melt and deposit at very different temperatures. As each individual particle composition melts, it will deposit; but once 100% of that particle type is deposited there is potential for a plateau in the sticking ratio as temperature rises. This is significantly different than the behavior that is expected from the behavior of a homogeneous particle composition. It is also possible that for some sands, the melting points of different constituent sand particle types are close enough together that the rise of the sticking

ratio with temperature will be more or less constant. If this is the case, it is still certain that the range of temperature from the onset of deposition to temperature at which complete deposition occurs will be much larger than the temperature range of a single homogeneous particle composition. Another factor that will affect the sticking ratio curve of non-homogeneous particles is the sticking of un-melted particles to fully molten previously deposited particles. This effect is also important, but it is dependent on the total particle throughput, which is a function of time in a gas turbine, and is not discussed in detail here.

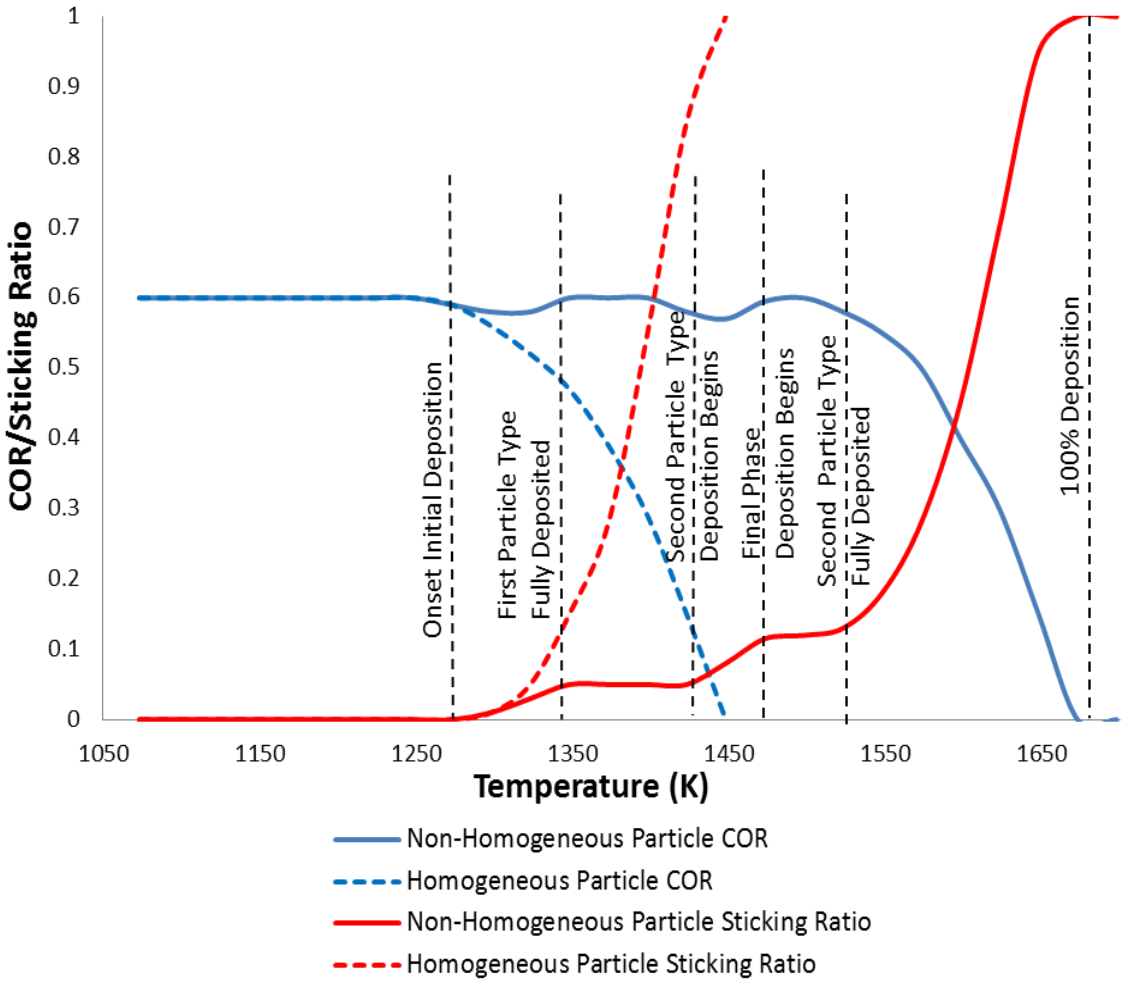

Figure 4-13. Hypothesized non-homogeneous sand particle impact behavior

Given this hypothesized particle behavior, it is expected that a large drop in COR would not be observed until a particle type which is a very large percent of the total particle count begins to soften. As it softens, the particle absorbs more kinetic energy into plastic deformation

leaving less rebound velocity and thus a lower COR. There may be small decreases in COR as smaller constituent particle types start to soften. This will further affect the COR of the rebounding particles until the particle type is fully deposited; and then the effects of that deposited particle type will no longer be counted in the COR of the rebounding particles.

4.7 Conclusions

The current study investigated the effects of temperature on COR for 20-40μm ARD impacting a Hastelloy X coupon at a constant 70m/s velocity and different impact angles varying from 30° to 80°. The data presented shows the mean and standard deviation of the COR as well as normal and tangential COR components. Results presented at 1073 K, 1173 K, 1273 K, and 1323 K show that there is not a major drop of the COR of rebounding particles. However, the normalized rebound ratios as well as deposited particle counts show that there is a significant increase in deposition in the 1273 K to 1323 K range. It is theorized that sand, which does not have a homogeneous composition from one particle to another and is crystalline in structure, may behave in a significantly different fashion from a homogeneous particle mixture that have been the exclusive focus of study in the past. The work is presented in this study in such a way that it can be integrated into a computational model to help improve the design of turbomachinery components susceptible to particle ingestion.

4.8 Acknowledgments

The work detailed here would not be possible without the support and direction of Rolls-Royce, especially B. Barker, K. Hsu, and N. Wagers. The authors would also like to thank D.K. Tafti and S. Singh from Virginia Tech for their thoughtful discussion, analysis and advice.

4.9 References

[1] Goldsmith, W., 2002, Impact : the theory and physical behaviour of colliding solids, Dover Publications, Mineola, N.Y.

[2] Tabakoff, W., Grant, G., and Ball, R., 1974, "An Experimental Investigation of Certain Aerodynamic Effects on Erosion," AIAA-74-639.

[3] Li, X., Dunn, P.F., and Brach, R.M., 2000, "Experimental and Numerical Studies of Microsphere Oblique Impact with Planar Surfaces," Aerosol Science and Technology, 31(5), pp. 583-594.

[4] Sommerfeld, M., and Huber, N., 1999, "Experimental analysis and modelling of particle-wall collisions," International Journal of Multiphase Flow, 25, pp. 1457-1489.

[5] Mok, C. H., and Duffy, J., 1964, "The Behaviour of Metals at Elevated Temperatures Under Impact with a Bouncing Ball," Int J Mech Sci, 6, pp. 161-175.

[6] Brenner, S. S., Wriedt, H. A., and Oriani, R. A., 1981, "Impact adhesion of iron at elevated temperatures," Wear, 68(2), pp. 169-190.

[7] Tabakoff, W., 1991, "Measurements of Particles Rebound Characteristics on Materials Used in Gas Turbines," J. of Propulsion and Power, 7(5), pp. 805-813.

[8] Tabakoff. W, H., A., and Murugan, D.M, 1996, "Effect of Target Materials on the Particle Restitution Characteristics for Turbomachinery Application," J. of Propulsion and Power, 12(2), pp. 260-266.

[9] Wakeman, T., and Tabakoff, W., 1979, "Erosion Behavior in a Simulated Jet Engine Environment," J. Aircraft, 16(12), pp. 828-833.

[10] Hamad A., T. W., "Experimental and Numerical Simulation of the Effects of Ingested Particles in Gas Turbine Engines," Proc. AGARD, NATO.

[11] Reagle C., D. J., Ng W., Ekkad S., Rajendran V., 2013, "Measuring the coefficient of restitution of high speed microparticle impacts using a PTV and CFD hybrid technique," Measurement Science and Technology, 24(10).

[12] Reagle CJ, D. J., Ng WF, Ekkad SV, 2014, "Study of Microparticle Rebound Characteristics Under High Temperature Conditions," Journal of Engineering for Gas Turbines and Power, 136(1).

[13] Walsh, W. S., Thole, K. A., and Joe, C., 2006, "Effects of Sand Ingestion on the Blockage of Film-Cooling Holes," ASME Conference Proceedings, 2006(4238X), pp. 81-90.

[14] Crosby, J. M., Lewis, S., Bons, J. P., Ai, W., and Fletcher, T. H., 2008, "Effects of Temperature and Particle Size on Deposition in Land Based Turbines," Journal of Engineering for Gas Turbines and Power, 130(5), p. 051503.

[15] Delimont JM, M. M., Ng WF, Ekkad, SV, 2014, "Effect of Temperature on Microparticle Rebound Characteristics at a Constant Impact Velocity," ASME Turbo Expo 2014, ASME, Dusseldorf, Germany.

[16] Nealy, D., Mihelc, M., Hylton, L., Gladden, H., 1984, "Measurements of Heat Transfer Distribution Over the Surfaces of Highly Loaded Turbine Nozzle Guide Vanes," Journal of Engineering for Gas Turbines and Power, 106, pp. 149-158.

[17] Hylton, L., Nirmalan, V., Sultanian, B., Kaufman, R., 1988, "The Effects of Leading Edge and Downstream Film Cooling on Turbine Vane Heat Transfer," NASA Contractor Report 182133.

[18] Hinkley, D. V., 1969, "On the Ratio of Two Correlated Normal Random Variables," Biometrika, 56(3), pp. 635-639.

[19] White, W. A., 1939, "The Mineralogy of Desert Sands," American Journal of Science, 239, p. 742.

[20] Charles Herman Fulton, W. J. S., 1929, A Manual of Fire Assaying, McGraw-Hill Book Company, New York.

[21] Larsen, E. S., 1929, "The Temperatures of Magmas," American Mineralogist, 14, pp. 81-94.

4.10 Appendix B

Table B-1. Curve fit coefficients for total COR

HX	Total COR Coefficients	
Temp. (K)	A	B
HX, 1073 K	2.5788647	-0.4311932
HX, 1173 K	3.3336001	-0.5072069
HX, 1223 K	3.3976463	-0.5054238
HX, 1273 K	2.9975939	-0.4792643
HX, 1323 K	3.6512507	-0.5240972

Table B-2. Curve fit coefficients for normal COR

HX	Normal COR Coefficients	
Temp. (K)	A	B
HX, 1073 K	5.680224	-0.6685572
HX, 1173 K	8.0699347	-0.7741545
HX, 1223 K	9.7006588	-0.8201193
HX, 1273 K	6.3752274	-0.7230662
HX, 1323 K	8.1125756	-0.7760539

Table B-3. Curve fit coefficients for tangential COR

HX	Tangential COR Coefficients	
Temp. (K)	A	B
HX, 1073 K	0.9063855	-0.1325015
HX, 1173 K	1.2451098	-0.2226254
HX, 1223 K	0.7458812	-0.0815212
HX, 1273 K	0.7236329	-0.0649107
HX, 1323 K	1.1676401	-0.1917286

5 Conclusion and Future Work

The results obtained through the studies presented herein are new and add significantly to the body of existing literature in the study of high temperature sand deposition and the interaction of the metal oxide layer with sand particle impact characteristics. The project sponsors are seeking the development of a model, whether semi-empirical or fully empirical, which explains the rebound of a sand particle impacting a surface in gas turbine representative conditions. The final results from this work add substantially to the base of experimental data from which a model for particle impact can be developed.

The understanding of the sand particle behavior at gas turbine relevant temperatures and velocities is extremely important to improving gas turbine components for tolerance to the effects of sand ingestion. The results from this work offer a great insight into what is occurring during microparticle impact at elevated temperatures. The current body of literature is lacking in any measurement of microparticle rebound characteristics at gas turbine representative conditions. All previous studies which have reported COR for particles likely to be found in gas

turbines have performed their studies at ambient temperatures only. This work is groundbreaking with the inclusion of the temperature variable in the study of sand particle COR as well as the methodology used to measure the COR.

The method developed for use in the studies included in this dissertation will allow for further effective exploration of the parameters governing particle impact at gas turbine representative conditions. The use of the novel CFD-based velocity correction for determining the velocity of impact is an improvement on existing techniques for the study of COR of microparticles. It allows for a large amount of impact data to be gathered in a relatively simple and inexpensive manner.

The improvements in the data reduction technique discussed in the second paper allow for a more accurate determination of the variation in the probabilistic nature of the sand particle impact. The use of power law curve fits as shown in this paper also improves the ability to draw conclusions from the COR results. Additionally, the COR was measured for the same velocity at ambient temperature and at elevated temperatures at which oxide layers form. The presence of an oxidizing atmosphere that allows for the quick formation of oxide layers, due to elevated temperature, significantly decreases the COR of sand particles as compared to the ambient results. This has never before been documented through the measurement of COR, although results from erosion-corrosion experiments have shown a similar increase in erosion rate as temperature rises. The increase in erosion rate has been strongly correlated with decreasing COR by a number of past studies which have measured both COR and erosion rate.

Some of the most interesting results come from the final paper. It shows that the COR of rebounding particles does not change substantially as the particles begin to deposit, which is contrary to what was previously believed would occur as sand particles begin to deposit on the surface of the target metal. These results indicate that no bulk softening due to increased temperature is occurring in the rebounding particles. This measured COR result is supported by the fact that sand is primarily crystalline in nature and therefore it does not soften as it is heated. It is hypothesized that the deposited particles observed in the experiment is one of the particle types which melts at a lower temperature than other particles. In addition, the direct counts of deposited particles show significant deposition trends with both temperature and angle of impact. These trends have never been reported for sand in open literature. These deposition results, in

combination with the COR results, lead to a hypothesized behavior for a non-homogeneous mixture of sand particles at elevated temperatures.

The results from the experiments conducted as part of the dissertation offer new insight into the physical phenomena of the particle impact and deposition. Based on these insights, there are several areas of further research that will improve upon what has been done for in these studies. There is a further need to raise the operating temperature of the test rig several hundred Kelvins in order to study the deposition of other constituent types of sand particles that have not yet begun to soften at the 1323 K temperature reached in this study. With the test rig capable of operating at those higher temperatures, it will be important to not only measure the COR of the rebounding particles, but to accurately measure the deposition ratio of the particles. By measuring the percentage of particles that stick and the energy of particles that rebound from the surface, a full understanding of the rebound behavior of the sand particles will be gained. The results from these studies are extremely exciting and provide a great step forward in the understanding of sand particle collision behavior.

Several other parameters are also available for further exploration. The velocity of the particle impacting the surface is known to be a primary factor governing the COR, so exploring the exact effects of velocity on COR is important. There is also a distinct possibility that an interaction exists between temperature and velocity of the impacting particle. This potential interaction has never been explored in open literature. Other factors that are known to affect the impact characteristics but have not been fully quantified are the surface roughness of the target material, and the size of the impacting particle. Additionally, there is likely a significant amount of useful information derived from the exact chemical composition of the particles that deposit on the surface at different temperatures. The composition of the ARD test sand used for these experiments also varies significantly from the sand that is found in Saudi Arabia, the Sahara desert, or the deserts of Afghanistan.

6 Appendices

6.1 Appendix C: Two Pass Channel Experiment

At the very start of the sand ingestion project a simple experiment was conducted in part to become familiar with some of the issues involved with experiments involving particles. This experimental work, along with the modeling done by Sukhjinder Singh and Dr. Danesh Tafti was presented in the International Journal of Heat and Fluid Flow [2].

This work was completed primarily while the some of the major construction work was being done on the Aerothermal Rig facility was being completed, and no experiments were possible using the Aerothermal Rig. The geometry was a two pass internal cooling channel geometry. The channels were 2"x2" in cross section with 0.125" high ribs and a schematic of the geometry can be seen in Figure C-1. The ribs were spaced with a pitch to height ratio of 9.28. The Reynolds number of the air flow through the test section was 25,000. The particles used for this test were "Fine" ARD with a size range of 1-25 μm.

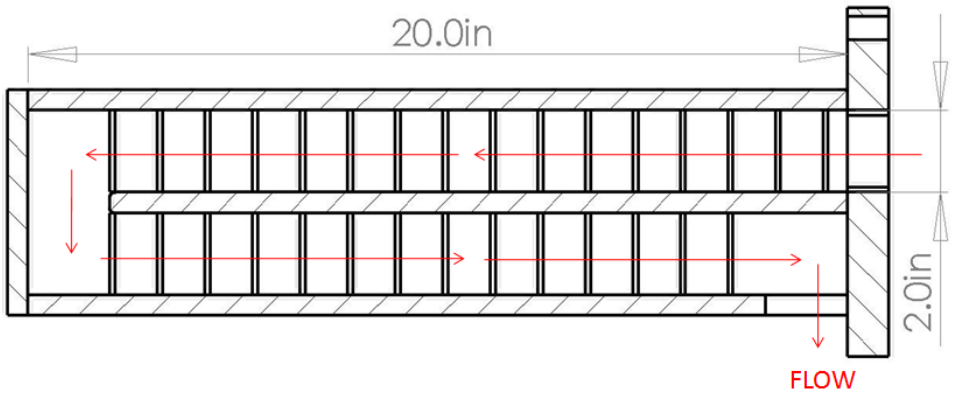

Figure C-1. Two pass internal cooling channel geometry

The experimental test setup included many the aspects that were later included in the high temperature testing done in the Aerothermal Rig. These aspects include the equilibration tube, control valves, flow meters, and particle hopper. A schematic of this setup can be seen in Figure C-2 below. The air flow of both the particle injector as well as the main air inlet must be metered and the combined flow rate counted due to the relatively large size of the particle injector flow in comparison to the main flow.

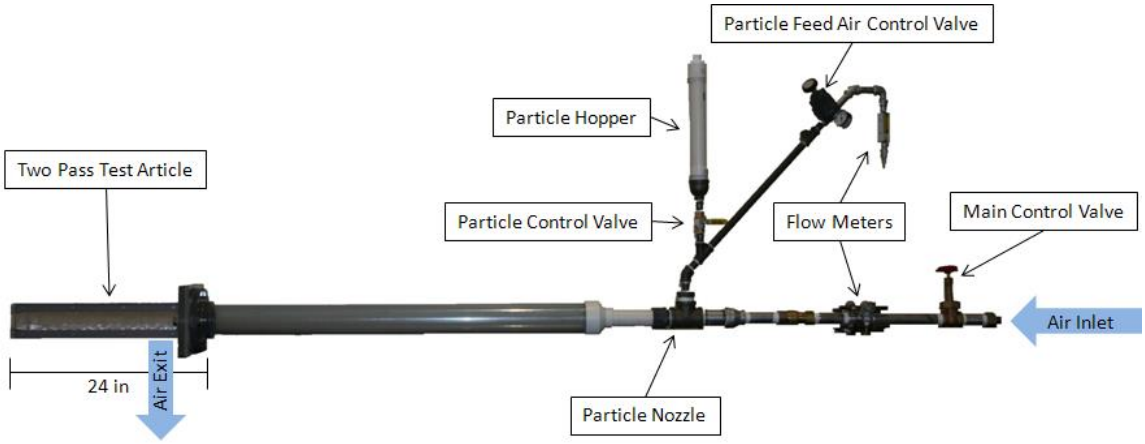

Figure C-3. Experimental test setup used for two pass deposition test

The two pass test section was carefully covered with 3M Very High Bond double sided tape which was attached to all of the side walls as well as all the end walls. The ribs were then bonded to the top of the sticky tape. The tape was not applied over the top of due the significant change in the geometry of the ribs that would result due to the tape thickness being on the same order of size as the rib height. An image of the two-sided sticky tape setup is shown in Figure C-3 below.

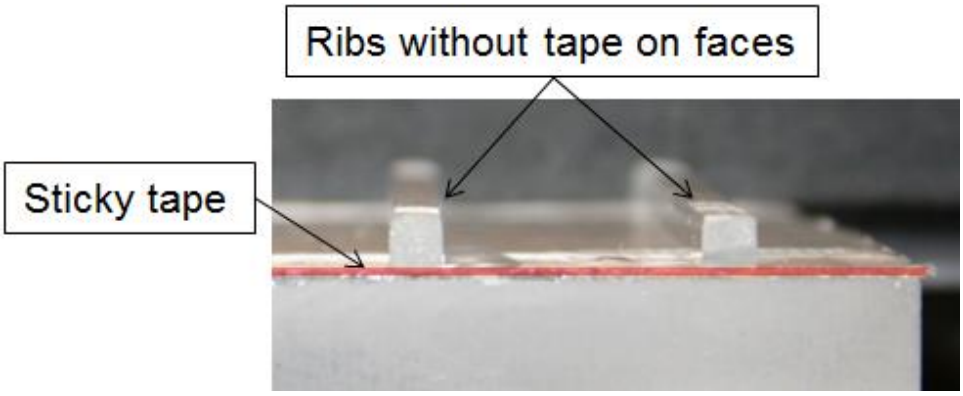

Figure C-4. Two-sided sticky tape attached on end walls, underneath ribs

The results from this experiment were purely qualitative understanding of the deposition patterns of the ARD particles. The quantitative patterns were obtained by disassembling the test set up and laying the particle coated tape directly on a black background and capturing images of the deposited particle pattern. A sample image showing the 180° turn region can be seen in Figure C-4. This turn region produced some of the most interesting patterns seen in this

experiment. The results from this test matched with the particle transport models and LES simulation used in [2] with the exception of some of the more complicated patterns in the turn.

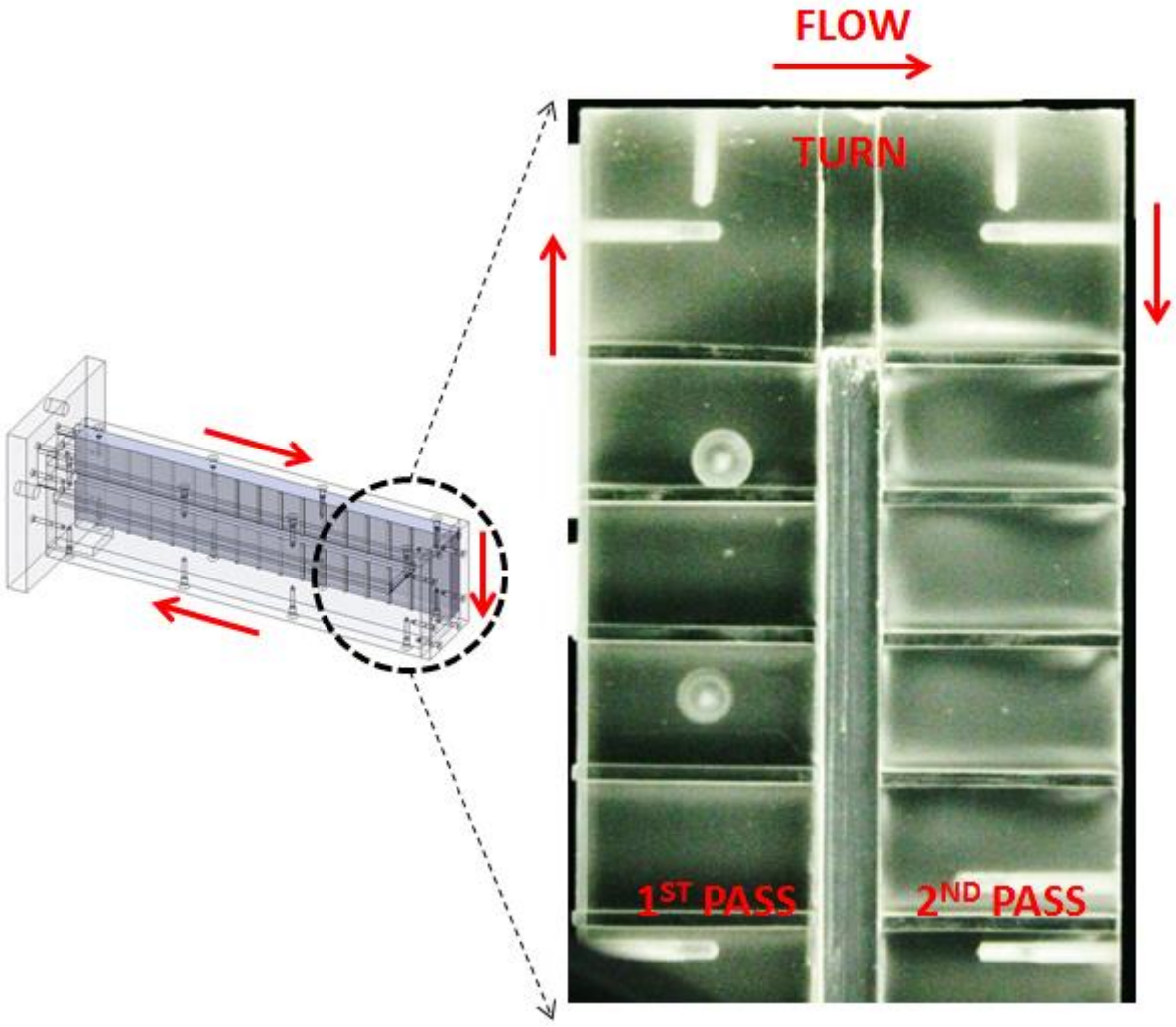

Figure C-5. Deposition results from the 180° turn portion of the test rig

[2] Singh, S., Tafti, D. , Reagle, C., Delimont, J., Ng, W., Ekkad, E., 2014, "Sand Transport in a Two Pass Internal Cooling Duct with Rib Turbulators," International Journal of Heat and Fluid Flow, 46, pp. 158-167.

6.2 Appendix D: Modifications Made to the Test Rig

A great deal of the time invested in this project was in the refurbishing of the VT Aerothermal Rig. The rig had not been used in 30 years prior to Virginia Tech taking possession of the rig. In addition in order to reach the high temperatures required for deposition many parts of the rig needed to be substantially upgraded. This appendix describes some of the major work done by the author to improve the VT Aerothermal Rig.

6.2.1 Controlling the Mass Flow Rate of the rig

During the year of 2012 experiments were run in the Virginia Tech Aerothermal Rig at temperatures up to 1073 K. These experiments did not control the mass flow rate of the Aerothermal Rig in any way. Due to the constant mass flow rate used, as the temperature was increased the velocity of particles striking the coupon also increased. This was very problematic as it meant that the velocity and temperature effects on particle impact were coupled and there was no way to isolate the effects of temperature. One of the first and most important projects undertaken to upgrade the test facility was to create a method to control the mass flow rate of the inlet air.

The compressor supplies a fixed output of approximately 0.15 kg/s of air. If the flow rate of air is constricted below this the compressor will raise the pressure in the buffer tank to 120psi then shut off until the pressure has fallen below 95 psi. The means that pressure in the tank takes on a saw-tooth form as a function of time at lower mass flow rates. This in turn caused the mass flow rate to take on a periodic function form. To prevent this, a series of pressure regulators, seen in Figure D-1, were installed to remove all of the periodic nature of the mass flow rate.

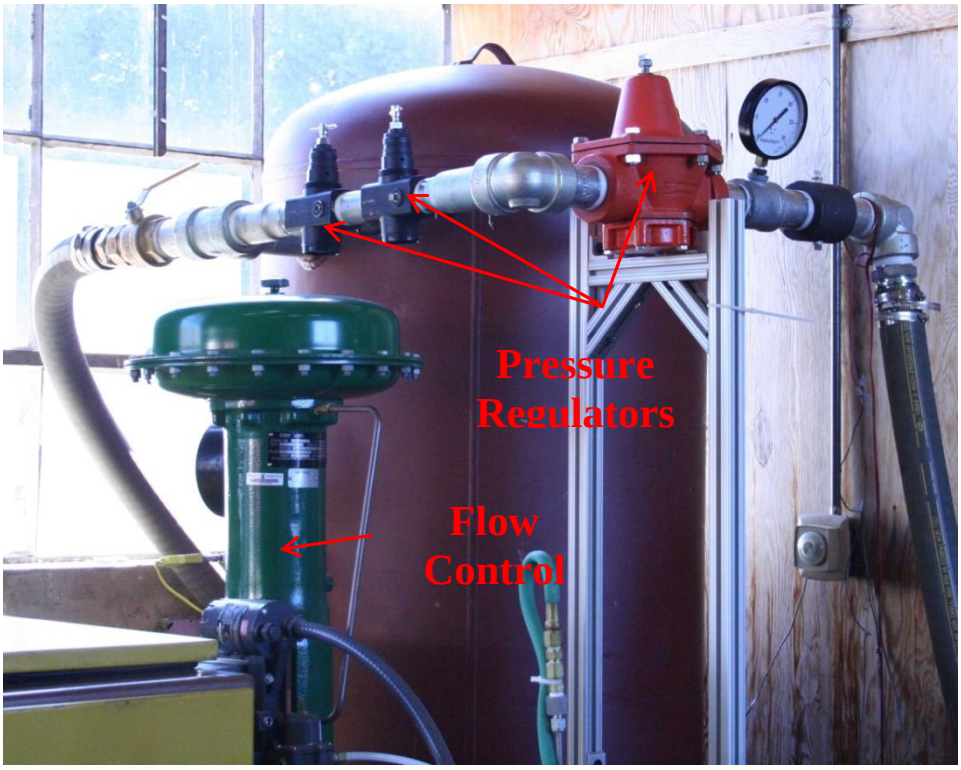

Figure D-1. Pressure regulator and flow control valve setup

Once the pressure seen by the control valve could be held constant despite the fluctuations within the buffer tank, it was relatively simple to use the control valve in conjunction with the final output pressure of the regulators to achieve any mass flow rate that was desired. Velocity of the air striking the coupon as measured by a pitot-static probe mounted to a traverse in the parameter that is used to determine the amount of flow rate to set in the rig. The temperature of the air leaving the buffer tank does still fluctuate due to the changes of pressure in the buffer tank. This fluctuation in temperature leads to a slight periodic fluctuation in density of the air leaving the buffer tank. This in turn leads to a very slight periodic fluctuation of the mass flow rate, but this fluctuation is on the order of 1%, or less, so is neglected.

Downstream of the pressure regulators a section of straight pipe was installed, and a velocity monitoring pitot-static probe was installed. The velocity at the centerline of the pipe is taken constantly while the rig is being run. This velocity can then be used to estimate the mass flow rate through the metering section by using a $1/7^{th}$ power law velocity profile. This is done in order to gain a continuous estimate of the mass flow rate without resorting to expensive or

high pressure loss methods of measuring the mass flow rate. Before each run the pitot-static probe mounted to the traverse is used to verify the velocity at the coupon. This pitot-static probe must be withdrawn via the traversing mechanism to avoid damage by the sand particles during actual test runs.

6.2.2 Equilibration Tube Design

One of the major features of any test setup meant to study particle interactions is the need for a straight section to allow for the particles to accelerate to the velocity of the flow. In the case of heated experiments this section also allows the particles to reach an equilibrium temperature. Because of this dual acceleration and particle heating the term "equilibration tube" is used for the section of pipe. For our experiments a 3 in diameter stainless steel pipe was chosen for this. The pipe was made from 310H stainless steel which exhibits good oxidation resistance up to temperatures of approximately 1423 K. This temperature limit allowed for some bulk temperature decrease from the inlet of the equilibration tube to the temperature at which the flow impinges on the target coupon due to heat transfer losses.

The length of the equilibration tube is extremely important to insuring that all of the particles injected into the flow reach equilibrium temperature and pressure before striking the target coupon. Figure D-2 below shows the results calculations for the distance traveled down the equilibration tube versus the percentage of temperature and velocity rise. Drag was calculated using stokes drag law of 24/Re. The length of equilibration tube used for these experiments was 2.1 m. This allowed plenty of length for the 40 μm ARD sand particles to accelerate and reach equilibrium velocity. The length is deliberately oversized to accommodate future larger particle sizes, higher temperatures, and faster velocities, all of which require longer equilibration tube lengths. In the Figure D-2 below the worst case heat transfer line is the heating curve of the particle if there is only conduction heat transfer from the surrounding air, with no radiation of convective heat transfer.

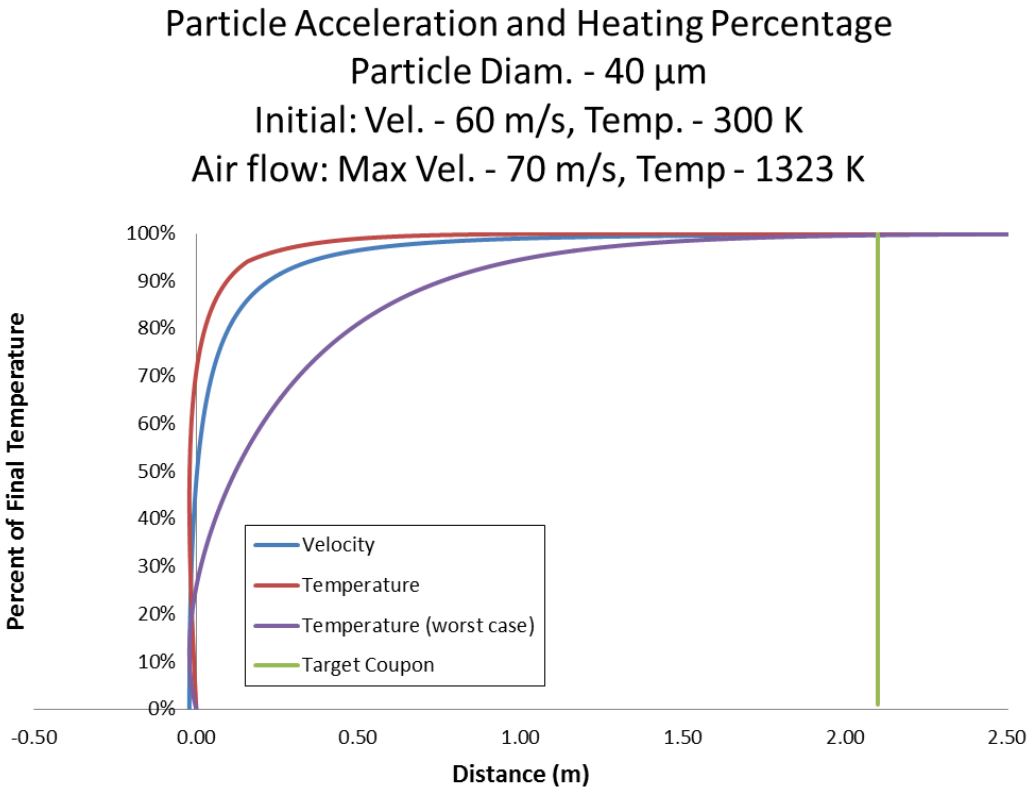

Figure D-2. Graph of the percentage of air flow velocity and temperature versus position of target particle

6.2.3 Expanding the Operating Envelop

During the course of running the test matrix at 28m/s velocity, a serious problem was encountered with the burner's operating envelop. Previously tests had been run at conditions with no control of the mass flow rate; this led to the velocity increasing as the temperature increased. In order to decouple these effects it was necessary to reduce the mass flow of the air through the test rig at the higher temperatures. The mass flow rate necessary to obtain a temperature of 1073 K at 28 m/s is 0.04 kg/s. As the temperature was brought up to this temperature it became apparent that the rig was burning fuel at stoichiometric ratios, as adding more fuel would cause a sharp decrease in temperature. Using these boundaries we were able to establish an operating envelop map of the temperatures and mass flow rates for the burner. This envelope map can be seen in Figure D-3. The envelop is bounded at the high temperatures by the limit of stainless steel 310H piping used in the equilibration tube. This variety of stainless steel was selected for its very high oxidation resistance up to temperatures of 1323 K.

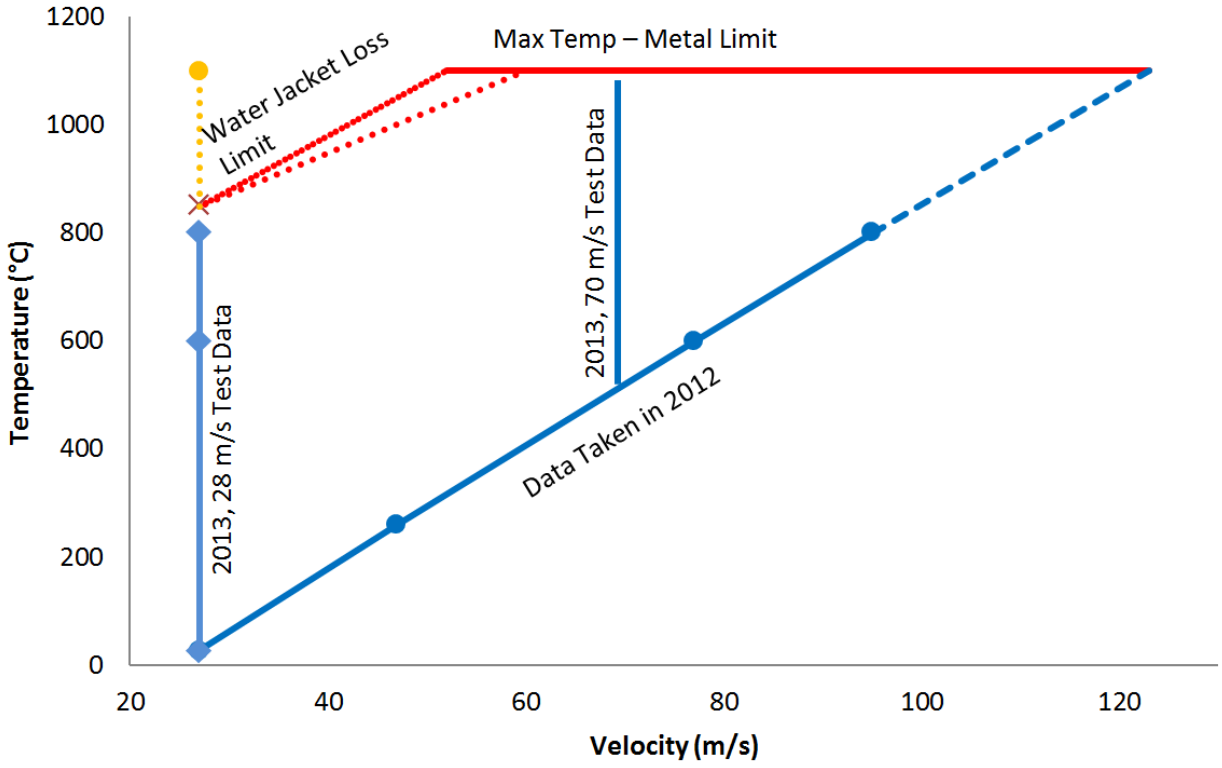

Figure D-3. Burner operation envelop in current configuration

As the limits of the burner at low mass flow rates were studied further it was realized that the limits were due to extremely high energy losses to the water jacket. The energy of the air was calculated based on the temperature of the air at the test section and tabulated enthalpy values using equation D-1. The energy in the water being cycled through the water jacket was measured by measuring the temperature of the water leaving the burner and the water returning from the cooling tower. This allowed the calculation of the energy in the water using equation D-2 shown below.

(D-1) $$\dot{Q}_{air} = \dot{m}_{air} * \Delta h_{air}$$

(D-2) $$\dot{Q}_{water} = \dot{m}_{water} * c_p * \Delta T_{water}$$

The calculations from these equations for the amount of energy in the water flow as compared to the energy in the air were completed and are shown in Table D-1. The total energy

leaving the burner through the water is over 70%, meaning that only a fraction of the energy from the combusted fuel remains in the heated air being used for the test. This is because the water jacket is in direct contact with the metal wall of the combustor. This means that metal is only a few degrees warmer than the water itself. Various solutions were tried such as reducing the flow rate of the water, and slowing the cooling tower fan speed to increase the water temperature. While these did have small effects on the energy loss they decrease in energy loss to the water was not significant enough to allow runs at 1073 K at 28 m/s.

Table D-6-1. Air energy compared to water energy at 1073 K and 28 m/s

	Air Properties	**Water Properties**
$\dot{m}$ (kg/s)	0.04	11.39
h_1 (kJ/kg)	300.19	--
h_2 (kJ/kg)	910.56	--
c_p (kJ/kg*K)	--	4.18
T_1 (°C)	20	20
T_2 (°C)	800	21.333
Energy (kW)	24.41	63.46

It was determined that by inserting a stainless steel liner pipe into the burner that we could create an small air gap between the water jacket and the combustion products leaving the burner. A conceptual image of this is shown in Figure D-4. Due to the presence of a constriction turbulator in the rig it was not possible to slide a pipe completely into the rig burner section, but only up to the turbulator. This was acceptable due to the extremely high temperature in the forward section of the burner where more of the combustion processes were taking place. A piece of 10 in diameter stainless steel pipe was selected for the combustor liner. Holes were drilled and tapped into it to allow for standoff bolts which allowed for the concentric location of the combustor liner. The liner was installed, as seen in Figure D-5 and an immediate 200 K increase in the operating envelope was immediately noticed. This increase allowed for the test run at 28 m/s and 1073 K to be conducted. Additionally this allowed for the expansion of the burner envelop in the higher velocity regions, so that in the future higher temperatures can be reached at lower velocities. It is possible that in the future the temperatures of the burner will be such that it will be necessary to remove the burner liner to prevent its melting.

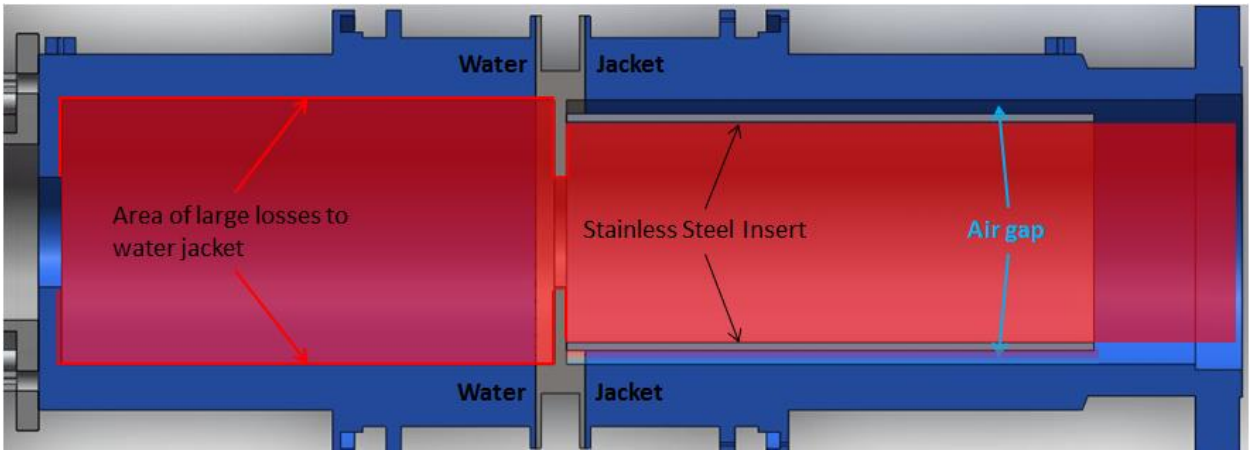

Figure D-4. Stainless steel burner insert with areas of high energy losses shown

Figure D-5. Finished combustor liner as installed in the VT Aerothermal Rig

6.2.4 Camera Cooling Modifications

The Dantec Dynamics® FlowSense camera used to capture the images of the particles has a maximum operating temperature of 50°C above which the camera sensor chip can suffer damage. Early during the setup for these high temperature experiments a Type K thermocouple was placed on the camera body to monitor the temperature of the metal casing in which the sensor chip is housed. It is especially important to monitor the temperature of the camera because it is underneath a blackout shield which prevents any ambient light from entering the test setup and contaminating the images. This shroud setup can be seen in Figure D-6 While this shroud is very effective at keeping any light from entering the test section of the rig it also does a very good job of trapping heat which rises from the hot test rig.

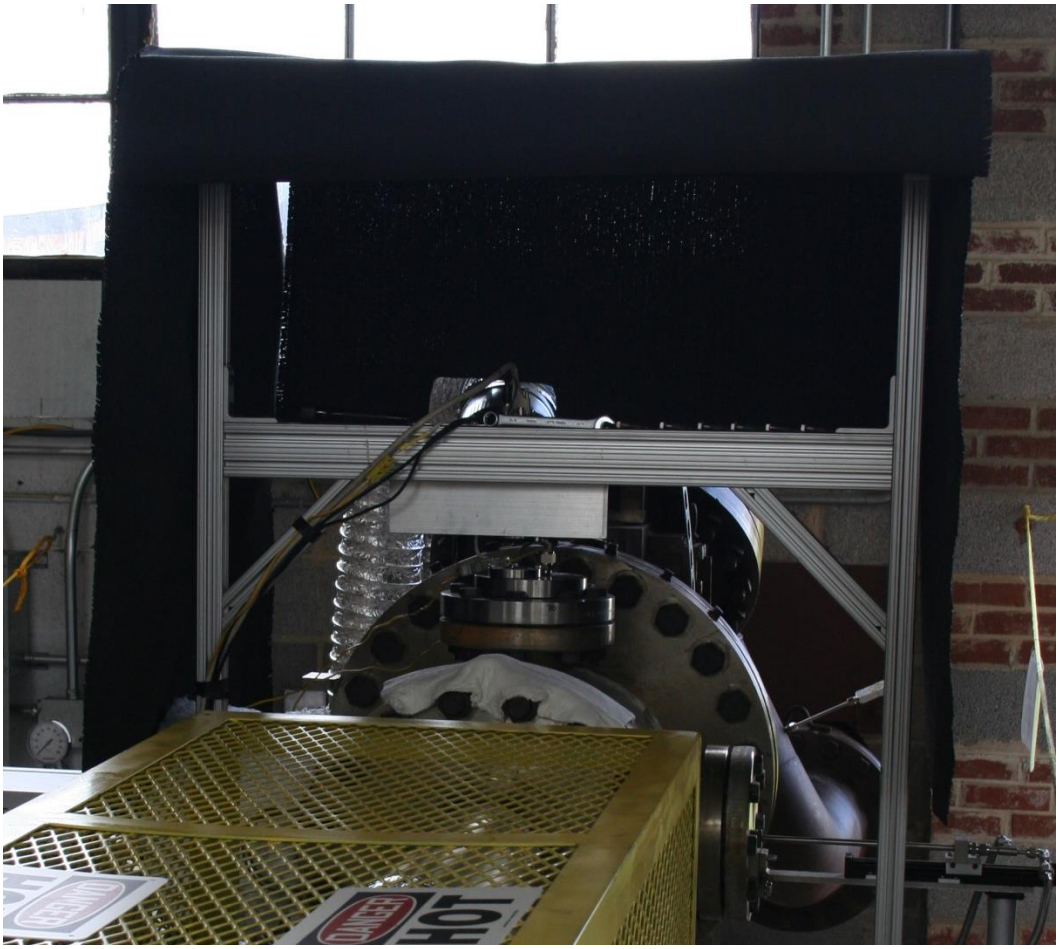

Figure D-6. Camera blackout shroud

Previously the test rig had been fired to temperatures of 1073 K. At these temperatures the exterior of the test rig would become extremely hot, and after a single run the camera

temperature was often approaching the 50°C temperature limit. During our experimental runs often it is most efficient to run multiple runs back to back. This caused extremely high temperatures of the camera. A fan was purchased and installed to blow air over the camera, and a duct was utilized to bring cool air from outside of the building to the camera. This was effective for multiple runs of 1073 K, but only barely capable of sustaining those temperatures.

It was decided that it would be necessary to purchase and air conditioning unit in order to cool the air that was being blown on the camera. This was difficult to do due to the rules but in place by Virginia Tech about purchasing air conditioning units. After a great deal of difficulty an air-conditioning unit was purchased. The air duct was rerouted and attached to the camera shroud as seen Figure D-7. This setup vastly improved our ability to run higher temperatures and no problems were encountered at the 1323 K test runs even when many test runs were conducted back to back.

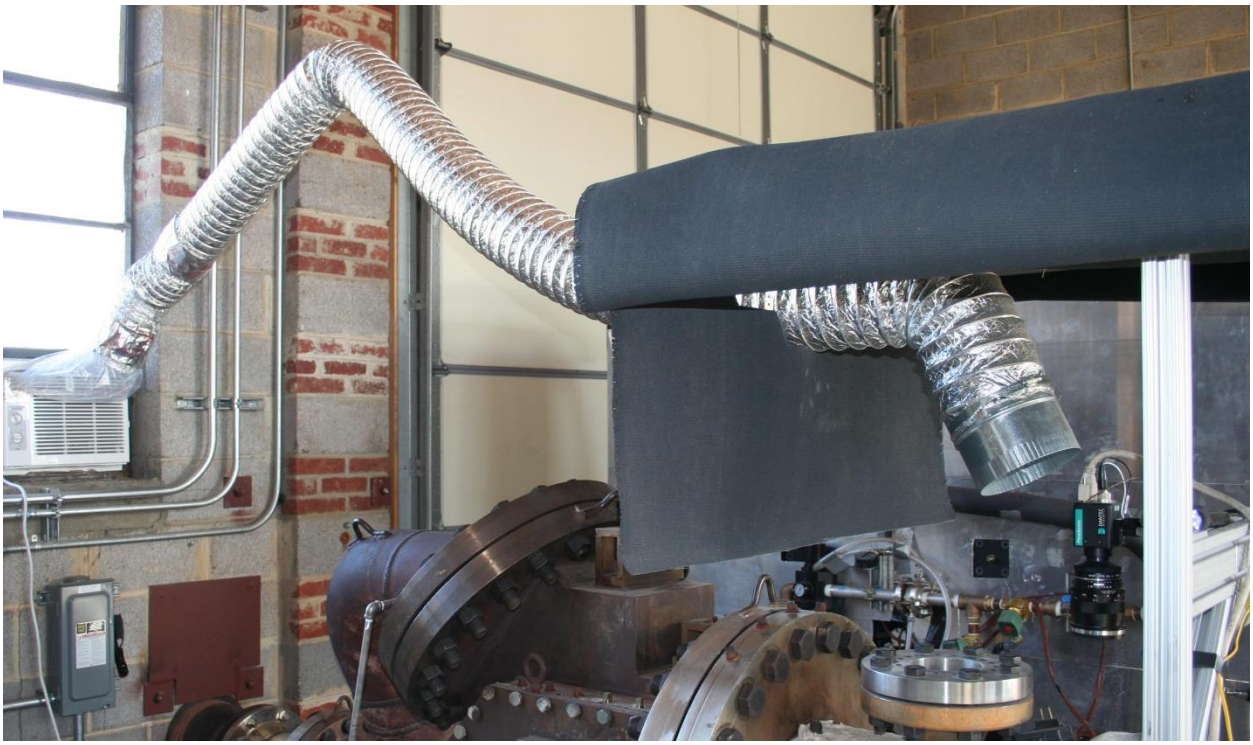

Figure D-7. Cooling air routed to camera

6.2.5 Exhaust Quenching System

In order to operate the rig at temperatures above 1073 K it was necessary to consider the temperature of the exhaust gases leaving the building. The exhaust stack and other downstream components in the VT Aerothermal Rig are not made from stainless steel, but rather regular

carbon steel. As such these components cannot be subjected to the extreme temperatures of the remainder of the rig.

In order to decrease the temperature of the air leaving the test rig it was necessary to install an exhaust quenching system. A system was devised whereby a small amount of water was diverted immediately downstream of the water pump. The water is then passed through a filter to remove any large particles that might clog the water injection nozzles. Two ¼ in NPT port were conveniently located on the exhaust S-duct of the rig and stainless steel nozzle were purchased to allow for the water to be injected. The installed cooling system can be seen in Figure D-8. During the design phase it was necessary to design the nozzles to have a low enough flow rate of water so that all of the water entering the test rig would be vaporized and carried out of the exhaust stack. If this design requirement was not met then liquid water would build up in the exhaust stack. The nozzles are also interchangeable so that nozzles with larger capacity can be added to rig as the mass flow rate of air and thus the mass flow rate of water required is increased.

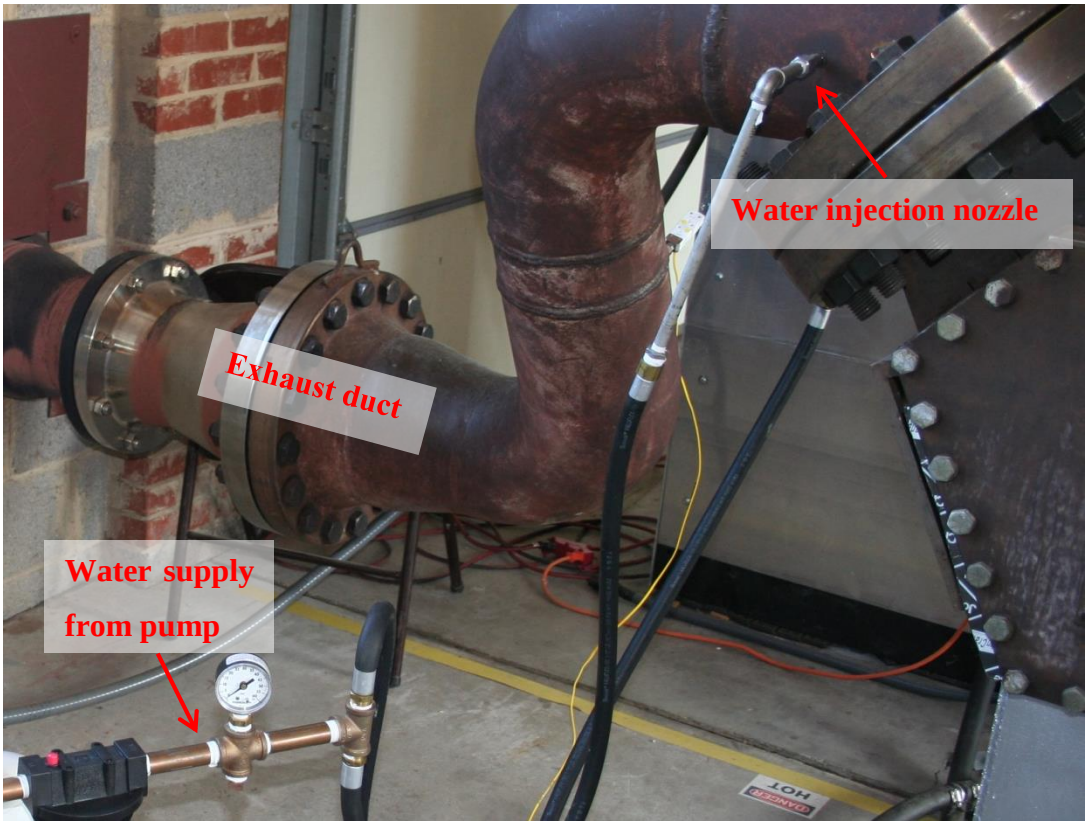

Figure D-8. Exhaust quenching system

6.2.6 Rig Controls

As the rig was upgraded, significant new instrumentation was installed on the rig. The monitoring of the mass flow rate, monitoring the metal temperature of the equilibration tube and other instruments were added. All of the new instrument readings needed to in placed in the control panel used to operate the rig. Great improvements were made to the controls of the rig by the author. Many small changes to make the controls user friendly and easy to read and operate were made, small things like allowing control of the traverse speed which was previously set at a very slow speed only, monitoring the temperature of the exhaust gases, and automatic over temperature shutoffs were added. LABVIEW control panel used to operate the VT Aerothermal Rig is show in its latest version in Figure D-9.

At the very low mass flow rate high temperature conditions the rig is operating very close to stoichiometric mixture of fuel and air. This means that with addition of more fuel at these conditions can lead to the flame being extinguished. When the fuel level is dropped the metal walls retain enough energy to reignite the air fuel mixture. This can lead to combustion momentarily occurring throughout the test rig. This is a condition that needs to be avoided at all costs.

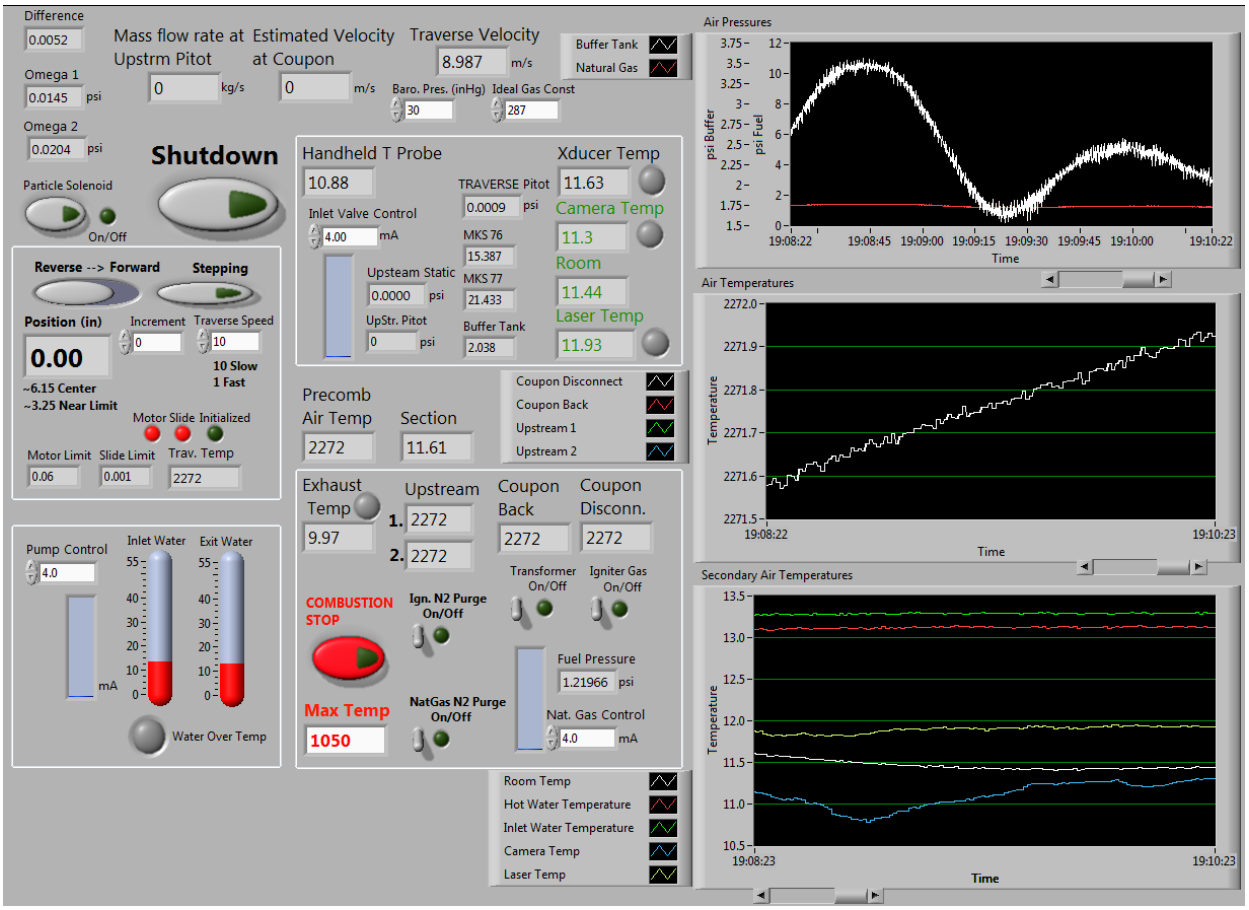

Figure D-9. Control panel used to operate the VT Aerothermal Rig

6.2.7 Hastelloy X Target Coupons

As the temperature at which the rig operated was raised to temperatures above 1073 K for the first time it was noticed that the 304 stainless steel was experiencing significant problems at these temperatures. At the extreme firing temperatures a thick oxide layer forms on the coupon. When the coupon cools the thermal expansion coefficient for the underlying substrate steel is larger than the surface oxide layer. This causes buckling and spallation of the surface oxide layer as the coupon is cooled. The spallation, known as "scaling," happens with enough force that small pieces of oxide layer dust can be visibly seen with the naked eye to break free and fly several inches into the air while the coupon is lying flat on the table. The scaling can be seen in Figure D-10 a where the light grey areas are remaining oxide layer and the darker grey areas are those areas where spallation has occurred. This does not affect the oxide layer while the coupon is at the elevated temperatures, and only caused the scaling to occur as the coupon is cooled.

This unfortunately means that it is impossible to evaluate the amount of deposition that occurs on the target coupon, because it is all broken loose during the scaling. Additionally stainless steel 304 is not used at the temperatures being seen in the rig due to the scaling that occurs. For these reasons it was decided to switch to and nickel based alloy exclusively for tests at temperatures above 1073 K. Hastelloy X was selected because of availability, high temperature limit, and its prevalent use in gas turbine applications. Figure D-10 b shows the Hastelloy X target coupon at 1323 K temperature.

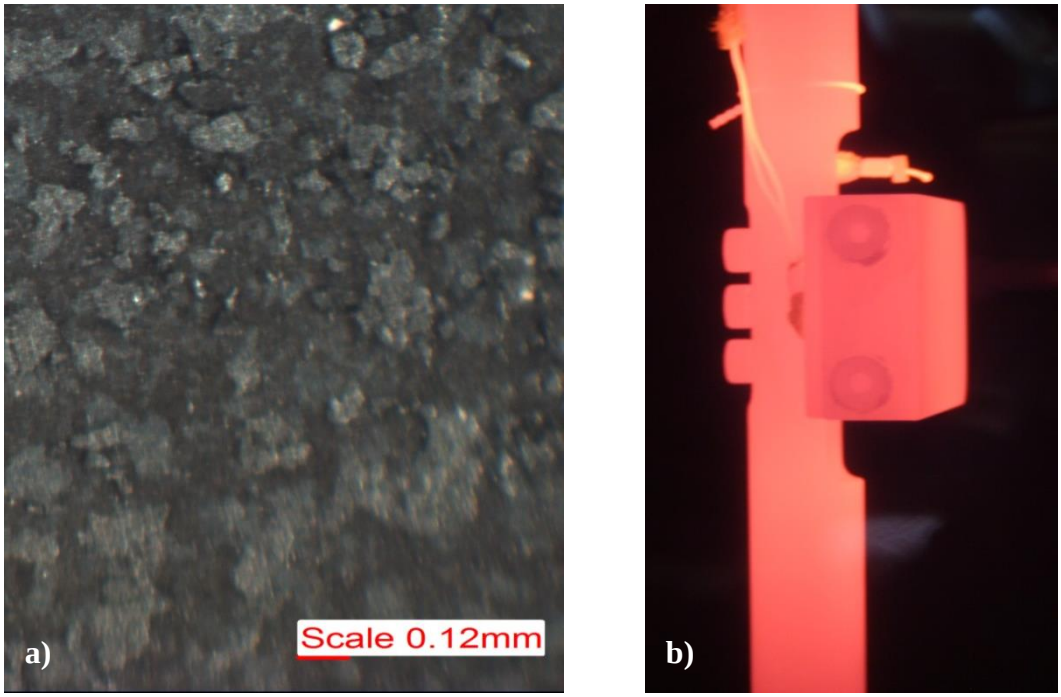

Figure D-10. a) Shows the scaling damage to the surface coating that occurs to stainless steel 304 after cooling. b) Shows the new visible light image of Hastelloy X coupon at 1323 K

6.3 Appendix E: Buckingham Pi Analysis of Impact Variables

As part of the analysis of the particle impact it was determined that it would be useful to perform a Buckingham Pi analysis to examine the non-dimensional groupings of variables. The variables listed below describe many of the important variables governing the impact of the sand particles on the target coupon. It should be noted that no fluid-particle interaction variables are expressed in this list. The variables are divided into three main categories. The first being the variables related to the particle kinetic energy. The second grouping of variables is the group related to the particle and the target's thermal energy. The third and final group of variables is related to the actual material properties of particle, metal, and oxide layer that play a role in the impact mechanics.

It is important to note that the actual value many of the different material properties are extremely difficult to measure. This is due to two reasons. The first reason is that most of the properties are a strong function of temperature and in the case of the oxide layer properties a function of the oxygen concentration in the air. Additionally all of these properties are commonly measured at relatively low strain rates. During a particle impact the rate at which the deformation mechanisms occurs is extremely fast. This speed of impact has been experimentally documented to create a dynamic Young's modulus, an impact hardness that differs from the standard impact measurement, and causes ductile materials to behave in a much more brittle manner.

Particle Kinetic Energy Variables

ρ_p	Particle density
$V_{p,in}$	Particle incoming velocity
$V_{p,out}$	Particle rebounding velocity
d_p	Particle diameter
Ω_{in}	Particle incoming rotational angular velocity
Ω_{out}	Particle rebounding rotational angular velocity

Thermal Energy Variables

$C_{p,p}$	Particle specific heat
T_p	Particle temperature
$C_{p,T}$	Target specific heat

T_T	Target temperature

Deformation Variables

$\sigma_{y,p}$	Particle yield strength
H_p	Particle hardness
E_p	Particle young's modulus
$K_{IC,p}$	Particle fracture toughness
$\sigma_{y,T}$	Target yield strength
H_T	Target hardness
E_T	Target young's modulus
$K_{IC,T}$	Target fracture toughness
ρ_T	Target density
$\sigma_{y,O}$	Oxide yield strength
H_O	Oxide hardness
E_O	Oxide young's modulus
$K_{IC,O}$	Oxide fracture toughness
ρ_O	Oxide density
L_O	Oxide thickness

Of these variables the particle density, particle incoming velocity, particle diameter, and the particle temperature were chosen to be the repeating variables. From the sum total of 24 variables 20 different pi groupings are then formed. The pi groups are listed below.

Resultant Pi Groups

$$\Pi_1 = \frac{V_{p,out}}{V_{p,in}}$$

$$\Pi_2 = \frac{d_p \Omega_{in}}{V_{p,in}}$$

$$\Pi_3 = \frac{d_p \Omega_{out}}{V_{p,in}}$$

$$\Pi_4 = \frac{C_{p,p} T_p}{{V_{p,in}}^2}$$

$$\Pi_5 = \frac{C_{p,T} T_p}{{V_{p,in}}^2}$$

$$\Pi_6 = \frac{T_T}{T_p}$$

$$\Pi_7 = \frac{\rho_T}{\rho_p}$$

$$\Pi_8 = \frac{\rho_O}{\rho_p}$$

$$\Pi_9 = \frac{L_O}{d_p}$$

$$\Pi_{10} = \frac{\sigma_{y,p}}{\rho_p V_{p,in}{}^2}$$

$$\Pi_{11} = \frac{H_p}{\rho_p V_{p,in}{}^2}$$

$$\Pi_{12} = \frac{E_p}{\rho_p V_{p,in}{}^2}$$

$$\Pi_{13} = \frac{K_{Ic,p}}{\rho_p V_{p,in}{}^2 d_p{}^{1/2}}$$

$$\Pi_{14} = \frac{\sigma_{y,T}}{\rho_p V_{p,in}{}^2}$$

$$\Pi_{15} = \frac{H_T}{\rho_p V_{p,in}{}^2}$$

$$\Pi_{16} = \frac{E_T}{\rho_p V_{p,in}{}^2}$$

$$\Pi_{17} = \frac{K_{Ic,T}}{\rho_p V_{p,in}{}^2 d_p{}^{1/2}}$$

$$\Pi_{18} = \frac{\sigma_{y,O}}{\rho_p V_{p,in}{}^2}$$

$$\Pi_{19} = \frac{H_O}{\rho_p V_{p,in}{}^2}$$

$$\Pi_{20} = \frac{E_O}{\rho_p V_{p,in}{}^2}$$

$$\Pi_{21} = \frac{K_{Ic,O}}{\rho_p V_{p,in}{}^2 d_p{}^{1/2}}$$

The first pi group is the velocity ratio or the COR which is the dimensionless variable reported in this paper. The second and third groups are the rotational velocity before and after impact. These three groups are useful to in determining how much kinetic energy is lost in the impact and where the particle will go following the impact. The COR term is the Pi group that contains the rebounding velocity and thus is dependent on the remaining Pi groups. Pi group four and five are both the ratio of thermal energy to the kinetic energy of the incoming particle,

while group six is the temperature ratio between particle and target. Groups six and seven are density ratios between the different materials which are likely not important by themselves, but interact with some of the other groups. The ninth group is likely very important and it contains the ratio between the depth of the oxide layer which forms on heated metal targets to the diameter of the particle. The depth of the oxide layer in itself is very important in determining what happens during the impact.

Pi groups from 10 through 21 all deal with the particle impact. Young's modulus and the yield strength terms deal with the elastic deformation that occurs during the particle impact how and plays a role in the restoring force. The terms containing hardness of the different materials deal with the ease with which plastic deformation can occur in the material. This hardness if quantified should probably be some type of impact hardness of the material as the hardness depends strongly on the dynamics of the impact. The final impact type terms are the fracture toughness terms. These terms relate the kinetic energy to the ease with which the material can be broken. The oxide layer and the particles themselves are the most likely to fail in this manner, as both are more brittle than the metal target.

6.4 Appendix F: Data Reduction Code

The data reduction code used to convert raw images captured by the Dantec Dynamics camera and into the COR of the particles is broken into three component codes. The first code used to reduce the data takes the raw images captured and applies an image mask to remove the coupon from the image. The code then applies a filter based on feature size to the image which eliminates all large features from the image. This also serves to eliminate any background noise from the image as well. Peaks in image brightness which represent particles are located and a calculation that locates the centroid of the particle to sub pixel accuracy. This particle location is compared between the two images of the image pair and the particle is paired with its nearest neighbor. If there are multiple neighbors within the possible circle of movement for the particle then that particle is disregarded to prevent false velocity vectors. The current version of the code used to reduce the data for the second and third papers is *ParticleTrack_v4.0*. Much of the underlying code is built on an open source particle tracking code by Grier, Crocker, and Weeks, and adapted for Matlab by Blair and Dufresne. The author was responsible for modifying the open source code and implementing the basic particle tracking routine the particle images generated from the experiments. The original open source code can be found at http://physics.georgetown.edu/matlab/

The second code in its current version used for this work is *TXTPostProcessing_ExtremeMods_v4.0*. This code is responsible for combing the particle velocity results from each of the 60 image pairs in a run into a single data file. The code also implements the velocity correction to the particle's impact location. This is the hybrid portion of the PTV/CFD technique used for calculating the COR. The output from this second code is a data file containing the location and velocity measure for each particle, as well as the location and velocity with which it impacted the target coupon. This second code is primarily the work of Colin Reagle; however, very significant changes were made by the author after the graduation of Colin to improve the quality. Improvements were made to reduce the computational time of this program by an order of magnitude. For the first paper presented as part of this dissertation this code also did some of the preliminary calculations used to determine the COR. All of the preliminary calculation portions of the code were removed as part of the change in COR calculation methodology discussed in the second paper.

The third code takes the output from the second code from each of the 10-12 runs at each angle and compiles them together. The code then calculates the COR using the rebound ratio method described in the second paper for each of the six different angles. The mean COR and the standard deviation of the COR are then plotted against the mean incoming angle and a power law curve fit is formed. The author of this work is the sole author of upwards of 95% of this code, with some minor assistance from Matt Murdock. The entirety of the third code *Post_Processing_v5.1* has been included in this appendix. The implementation of this data reduction code has been a major portion of this project, and represents a significant fraction of the time spent on this project.

As mentioned in the body of the dissertation significant advances in the data reduction technique were made by using the rebound ratio to calculate the COR. In order to use the rebound ratio the front face of the coupon was broken up into 2mm sections and all of the particles that impacted within that 2mm width were counted. To use the rebound ratio both the incoming and the rebounding particles must have a normal distribution. In order to make sure that these distributions were normal or at least close enough to normal that it could be statistically assumed to be normal a Lilliefors normality test was implemented in the code to check the normality of each incoming and rebounding distribution. The normal and tangential components of COR are calculated by splitting the incoming velocity vectors into the normal and tangential components. The same rebound ratio calculation used for the combined COR is then used for the normal and tangential components.

Additionally it was determined during the course of the experiments that there was a significant unsteadiness in the flow exiting the equilibration tube. It is believed that the globe valve used to control the inlet flow creates a very uneven velocity profile. This uneven profile causes some large scale low frequency hydrodynamic unsteadiness. This results in a relatively low frequency unsteady oscillation of the velocity. This effect was partially removed by the addition of a turbulence grid downstream of the inlet valve to promote mixing and a more uniform velocity profile. At 70 m/s velocity the standard deviation of the bulk velocity was found to be +/-3m/s. Since it is possible to estimate the bulk velocity of the flow by examining the mean measured velocity of all the incoming particles, it was decided to use this bulk velocity to remove the images taken at extreme velocities. This improved the scatter of the data, by reducing the variation in incoming velocity.

6.4.1 Post_Processing_*v5.1*

```
%% Post Processing Edge Data
close all
clear all
clc

%% Initialize
cstring='rgbmck';
set(0, 'DefaultAxesFontName', 'Arial');

i = 1;
filelist = [];
CORmag_totals = []; CORang_totals = [];
xpos_totals = []; inmag_totals = [];
rebound_totals = []; incoming_totals = [];
ang_totals_poly = []; in_totals_poly = [];
CORrebAngle = [];
% CORmag30deg = []; CORang30deg = [];
xpos30deg = []; inmag30deg = [];...
%     smoothrebEdge30deg = []; smoothinEdge30deg = [];
rebound30deg = [];...
%     rebEdge30deg = []; inEdge30deg = [];
incoming30deg=[];

% CORmag40deg = []; CORang40deg = [];
xpos40deg = []; inmag40deg = [];...
%     smoothrebEdge40deg = []; smoothinEdge40deg = [];
rebound40deg = [];...
%     rebEdge40deg = []; inEdge40deg = [];
incoming40deg=[];

% CORmag50deg = []; CORang50deg = [];
xpos50deg = []; inmag50deg = [];...
%     smoothrebEdge50deg = []; smoothinEdge50deg = [];
rebound50deg = [];...
%     rebEdge50deg = []; inEdge50deg = [];
incoming50deg=[];

% CORmag60deg = []; CORang60deg = [];
xpos60deg = []; inmag60deg = [];...
%     smoothrebEdge60deg = []; smoothinEdge60deg = [];
rebound60deg = [];...
%     rebEdge60deg = []; inEdge60deg = [];
incoming60deg=[];

% CORmag70deg = []; CORang70deg = [];
xpos70deg = []; inmag70deg = [];...
%     smoothrebEdge70deg = []; smoothinEdge70deg = [];
rebound70deg = [];...
%     rebEdge70deg = []; inEdge70deg = [];
incoming70deg=[];

%  CORmag80deg = []; CORang80deg = [];
xpos80deg = []; inmag80deg = [];...
%    smoothrebEdge80deg = []; smoothinEdge80deg = [];
rebound80deg = [];...
%     rebEdge80deg = []; inEdge80deg = [];
incoming80deg=[];

InNum80deg=[];InNum70deg=[];InNum60deg=[];InNum50deg=[];InNum40deg=[];...
    InNum30deg=[];
RebNum80deg=[];RebNum70deg=[];RebNum60deg=[];RebNum50deg=[];...
    RebNum40deg=[];RebNum30deg=[];
count80deg=0;count70deg=0;count60deg=0;count50deg=0;count40deg=0;...
    count30deg=0;

buttonBW = 'Yes';
root = '';
oldroot = 'init';
scrsz = get(0,'ScreenSize');
%% Load Data
count = 0;
legen = '';
```

```
figure('Position', scrsz); hold all
axis([0 90 0 2]);
set(gca, 'FontSize', 10)
xlabel('Angle of Impact'); ylabel('COR')


while (buttonBW == 'Yes')

    [file, root] = uigetfile([root '*.mat'], 'Select the results file...');
    load([root file])

    if (strfind(root, oldroot))
        disp('Duplicate file name')
    else
        count = count+1;

        %Find naming ... Degrees, Run, Unique
        degree = root(strfind(root, 'deg')-2:strfind(root, 'deg')+2);
        run = root(strfind(root, 'un')+2:strfind(root, 'un')+6);
        disp([degree run file])

        %mat file contains matrices: CORang, CORmag, smoothinEdge,
        %smoothrebEdge, incoming, rebound, rebEdge, and inEdge

        %Rename variables and set ang for Fitting
        filelist = [filelist; [degree '_' run]];

        % set up for normal/tan split
        rebound = sortrows(rebound,5);

        out  = isnan(CORmag);
        CORmag(out) = [];
        CORang(out) = [];
        smoothrebEdge(out,:) = [];
        rebound(out,:) = [];

        eval(['incoming' degree '_' run '= incoming;']);
        eval(['rebound' degree '_' run '= rebound;']);

        xpos = smoothinEdge(:,1);
        inmag = smoothinEdge(:,3);

        eval(['xpos' degree '_' run '= xpos;']);
        eval(['inmag' degree '_' run '= inmag;']);
        eval([['xpos' degree] '=' ['[xpos' degree ';' 'xpos];']]);
        eval([['inmag' degree] '=' ['[inmag' degree ';' 'inmag];']]);
        eval([['rebound' degree] '=' ['[rebound' degree ';' 'rebound];']]);
        eval([['incoming' degree] '=' ['[incoming' degree ';' 'incoming];']]);
        eval([['count' degree] '= [count' degree ']+1;' ]);
        eval([['RebNum' degree '(count' degree ')'] '=[size(rebound,1)];']);
        eval([['InNum' degree '(count' degree ')'] '=[size(incoming,1)];']);
        eval([['RebRatioNum' degree '(count' degree ')'] '= RebNum' degree '(count' degree ')./InNum' degree
'(count' degree ');']);

        xpos_totals = [xpos_totals; xpos];
        inmag_totals = [inmag_totals; inmag];
        rebound_totals = [rebound_totals; rebound];
        incoming_totals = [incoming_totals; incoming];

        legen = [legen; degree '-' run];
        oldroot = root;
        figure(1);
        plot(CORang, CORmag, 'Line', 'none', 'Marker', 'x',...
            'MarkerSize', 5, 'Color', cstring(mod(count,6)+1))
        legend(legen, 'Location', 'EastOutside')
    end
    buttonBW = questdlg('Input another file?', ' ', 'Yes', 'No ', 'No ');
end
hold off

clear CORang CORmag incoming rebound smoothinEdge smoothrebEdge...
    degree run rebEdge inEdge xpos inmag out Aggragate

%% Rebound Ratio Stuff

InNum=cat(2,InNum30deg,InNum40deg,InNum50deg,InNum60deg,InNum70deg,...
```

```
    InNum80deg);
RebNum=cat(2,RebNum30deg,RebNum40deg,RebNum50deg,RebNum60deg,...
    RebNum70deg,RebNum80deg);
RebRatioNum=cat(2,RebRatioNum30deg,RebRatioNum40deg,RebRatioNum50deg,...
    RebRatioNum60deg,RebRatioNum70deg,RebRatioNum80deg);




%% Ratio Distribution Calculations
    %Calculated Standard deviation of various things for each indivitual
    %angle.
    %REBRATIOa is the mean of the rebound ratios calculated at each
    %point on the coupon surface
    %REBRATIOr is the rebound ratio calculated from each individual run
    %REBRATIO is the mean rebound ratio calculated by averaging all the
    %run rebound ratios.
%********************** NOTE ***************************
Reb_n_Lim_upM=60;  %for calculating the rebound ratio
Reb_n_Lim_lowM=20;  %for calculating the rebound ratio
K=1.5;             %K factor for use in rebound ratio outlier removal
mm=2;              %number of X direction mm for each bin width
signif=.05;         %Significance level for Lilliefors Normality Test
%********************** NOTE ***************************

%30deg
%*****************************30deg*************************************
%************************Incoming 30deg*********************************
if (length(incoming30deg) >1)
    clear instats rebstats bins bins1 bin_AbP bin_AbA minx maxx cut m n ddi ddr
    angCoup=28;
    Reb_n_Lim_up=Reb_n_Lim_upM*angCoup/80;
    Reb_n_Lim_low=Reb_n_Lim_lowM*angCoup/80;
    instats(:,1:2) = incoming30deg(:,5:6);
    instats(:,3) = hypot(incoming30deg(:,7), incoming30deg(:,8));
    instats(:,4) = atan2(incoming30deg(:,8), incoming30deg(:,7))*180/pi+(angCoup-90);
    instats(:,5) = incoming30deg(:,10);
    instats2=instats;
    instats = sortrows(instats, 1);

    rebstats(:,1:2) = rebound30deg(:,5:6);
    rebstats(:,3) = hypot(rebound30deg(:,7), rebound30deg(:,8));
    rebstats(:,4) = atan2(rebound30deg(:,8), rebound30deg(:,7))*180/pi+(angCoup-90);
    rebstats = sortrows(rebstats, 1);

    for i=1:length(instats)-1;
        if instats(i,1)==instats(i+1,1)
           ddi(i)=i;
        end
    end
    if exist('ddi')
    instats(find(ddi),:)=[];
    end
    for i=1:length(rebstats)-1;
        if rebstats(i,1)==rebstats(i+1,1)
           ddr(i)=i;
        end
    end
    if exist('ddr')
    rebstats(find(ddr),:)=[];
    end

    StdInAngbyPos30=zeros(1,130);
    MeanInAngbyPos30=zeros(1,130);

    MeanInVelbyPos30=zeros(1,130);
    StdInVelbyPos30 = zeros(1,130);

    MeanInVelTbyPos30 = zeros(1,130);
    StdInVelTbyPos30=zeros(1,130);

    MeanInVelNbyPos30 = zeros(1,130);
    StdInVelNbyPos30=zeros(1,130);

    StdInVelbyAng30=zeros(1,130);
    LilltestInVelbyPos30=zeros(1,130);
    probin30=zeros(1,130);
    LilltestRebVelbyPos30=zeros(1,130);
```

```
    probreb30=zeros(1,130);

    bins=zeros(1,130);
    bins1=zeros(1,130);
    binsIN=zeros(1,130);
    for i = 1:size(instats,1)
        if round(instats(i,4))>0
        bin_VbA = round(instats(i,4));
        bins(bin_VbA)=bins(bin_VbA)+1;
        end
        bin_AbP = round(instats(i,1));
        bin_AbP = bin_AbP+40;
        bins1(bin_AbP)=bins1(bin_AbP)+1;
        if instats(i,5)<=Reb_n_Lim_up && instats(i,5)>=Reb_n_Lim_low
        binsIN(bin_AbP)=binsIN(bin_AbP)+1;
        end
    end
% % %     sorts the number of incoming particles from each run
    binsINr=zeros(1,size(InNum30deg,2));
    k=1;
    for i=1:size(InNum30deg,2)
        for j=1:InNum30deg(i)
            if instats2(k,5)<=Reb_n_Lim_up && instats2(k,5)>=Reb_n_Lim_low
            binsINr(1,i)=binsINr(1,i)+1;
            end
            k=k+1;
        end
    end


    %Calculating bin witdth for 2mm X direction bins for the Ratio Dist.
    bins1e=zeros(1,130);
    for i=1:mm:ceil(length(bins1))-1
       bins1e(ceil(i/mm))=bins1(i)+bins1(i+1);
    end
    n=1;
    for i=1: length(bins1e)

        if bins1e(i)>0   % this if statement removes outliers from the data set
%         if i>15 && i<=20
            clear bc
            Qr=quantile(instats(n:n+bins1e(i)-1,3),[0.25,0.75]);
            binsoutlierI(i)=length(find(instats(n:n+bins1e(i)-1,3)>=Qr(2)+K*(Qr(2)-Qr(1))...
            | instats(n:n+bins1e(i)-1,3)<=Qr(1)-K*(Qr(2)-Qr(1)) ));

            bc=find(instats(n:n+bins1e(i)-1,3)>=Qr(2)+K*(Qr(2)-Qr(1))...
            | instats(n:n+bins1e(i)-1,3)<=Qr(1)-K*(Qr(2)-Qr(1)));
            instats(n+bc-1,:)=[];
            bins1e(i)=bins1e(i)-binsoutlierI(i);
        end
        if bins1e(i)>4
            [LilltestInVelbyPos30(i),probin30(i)]= lillietest(instats(n:n+bins1e(i)-1,3)',signif);
        end
        StdInAngbyPos30(i) = std(instats(n:n+bins1e(i)-1,4));
        MeanInAngbyPos30(i) = mean(instats(n:n+bins1e(i)-1,4));
        StdInVelbyPos30(i) = std(instats(n:n+bins1e(i)-1,3));
        MeanInVelbyPos30(i) = mean(instats(n:n+bins1e(i)-1,3));
        MeanInVelTbyPos30(i) = mean(instats(n:n+bins1e(i)-1,3).*cosd(instats(n:n+bins1e(i)-1,4)));
        StdInVelTbyPos30(i) = std(instats(n:n+bins1e(i)-1,3).*cosd(instats(n:n+bins1e(i)-1,4)));
        MeanInVelNbyPos30(i) = mean(instats(n:n+bins1e(i)-1,3).*sind(instats(n:n+bins1e(i)-1,4)));
        StdInVelNbyPos30(i) = std(instats(n:n+bins1e(i)-1,3).*sind(instats(n:n+bins1e(i)-1,4)));

        n = n+bins1e(i);
        if isnan(StdInAngbyPos30(i))==1 || StdInAngbyPos30(i)==0
            StdInAngbyPos30(i)=0;
            MeanInAngbyPos30(i)=0;
            MeanInVelTbyPos30(i)=0;
            StdInVelTbyPos30(i)=0;
            StdInVelbyPos30(i) = 0;
            MeanInVelbyPos30(i) =0;
            MeanInVelNbyPos30(i)=0;
            StdInVelNbyPos30(i)=0;
        end
    end

%**********************Rebounding%30deg***********************************
    clear  bins bins2 bin_AbP bin_AbA
    rebstats(:,1:2) = rebound30deg(:,5:6);
    rebstats(:,3) = hypot(rebound30deg(:,7), rebound30deg(:,8));
```

```
rebstats(:,4) = atan2(rebound30deg(:,8), rebound30deg(:,7))*180/pi+(angCoup-90);
rebstats = sortrows(rebstats, 1);

StdRebAngbyPos30=zeros(1,130);
MeanRebAngbyPos30=zeros(1,130);

MeanRebVelbyPos30=zeros(1,130);
StdRebVelbyPos30 = zeros(1,130);

MeanRebVelTbyPos30 = zeros(1,130);
StdRebVelTbyPos30=zeros(1,130);

MeanRebVelNbyPos30 = zeros(1,130);
StdRebVelNbyPos30=zeros(1,130);

StdRebVelbyAng30=zeros(1,130);

bins=zeros(1,130);
bins2=zeros(1,130);

for i = 1:size(rebstats,1)
    if round(rebstats(i,4))>0
    bin_VbA = round(rebstats(i,4));
    bins(bin_VbA)=bins(bin_VbA)+1;
    end
    bin_AbP = round(rebstats(i,1));
    bin_AbP = bin_AbP+40;
    bins2(bin_AbP)=bins2(bin_AbP)+1;
end

%Calculating bin witdth for 2mm X direction bins for the Ratio Dist.
bins2e=zeros(1,130);
for i=1:mm:ceil(length(bins2))-1
   bins2e(ceil(i/mm))=bins2(i)+bins2(i+1);
end
n=1;
for i=1: length(bins2e)

    if bins2e(i)>0   % this if statement removes outliers from the data set
%       if i>15 && i<=20
          clear bc
          Qr=quantile(rebstats(n:n+bins2e(i)-1,3),[0.25,0.75]);
          binsoutlierR(i)=length(find(rebstats(n:n+bins2e(i)-1,3)>=Qr(2)+K*(Qr(2)-Qr(1))...
          | rebstats(n:n+bins2e(i)-1,3)<=Qr(1)-K*(Qr(2)-Qr(1)) ));

          bc=find(rebstats(n:n+bins2e(i)-1,3)>=Qr(2)+K*(Qr(2)-Qr(1))...
          | rebstats(n:n+bins2e(i)-1,3)<=Qr(1)-K*(Qr(2)-Qr(1)));
          rebstats(n+bc-1,:)=[];
          bins2e(i)=bins2e(i)-binsoutlierR(i);
    end
    if bins2e(i)>4
        [LilltestRebVelbyPos30(i),probreb30(i)]= lillietest(rebstats(n:n+bins2e(i)-1,3)',signif);
    end
    StdRebAngbyPos30(i) = std(rebstats(n:n+bins2e(i)-1,4));
    MeanRebAngbyPos30(i) = mean(rebstats(n:n+bins2e(i)-1,4));
    StdRebVelbyPos30(i) = std(rebstats(n:n+bins2e(i)-1,3));
    MeanRebVelbyPos30(i) = mean(rebstats(n:n+bins2e(i)-1,3));
    MeanRebVelTbyPos30(i) = mean(rebstats(n:n+bins2e(i)-1,3).*cosd(rebstats(n:n+bins2e(i)-1,4)));
    StdRebVelTbyPos30(i) = std(rebstats(n:n+bins2e(i)-1,3).*cosd(rebstats(n:n+bins2e(i)-1,4)));
    MeanRebVelNbyPos30(i) = mean(rebstats(n:n+bins2e(i)-1,3).*sind(rebstats(n:n+bins2e(i)-1,4)));
    StdRebVelNbyPos30(i) = std(rebstats(n:n+bins2e(i)-1,3).*sind(rebstats(n:n+bins2e(i)-1,4)));
    n = n+bins2e(i);

    if isnan(StdRebAngbyPos30(i))==1
        StdRebAngbyPos30(i)=0;
        MeanRebAngbyPos30(i)=0;
        MeanRebVelTbyPos30(i)=0;
        StdRebVelTbyPos30(i)=0;
        StdRebVelbyPos30(i) = 0;
        MeanRebVelbyPos30(i) =0;
        MeanRebVelNbyPos30(i)=0;
        StdRebVelNbyPos30(i)=0;
    end
end

%Ratio Distribution calculations
maxx=min(max(instats(:,1)),max(rebstats(:,1)))+40;
minx=max(min(instats(:,1)),min(rebstats(:,1)))+40;
```

```
    cut=(maxx-minx)/20;

    z=(-2:.001:4);
    pdfN30=zeros(130,length(z));
    pdfT30=zeros(130,length(z));
    pdf30=zeros(130,length(z));
    cor30=zeros(130,1);
    corN30=zeros(130,1);
    corT30=zeros(130,1);
    corStd30=zeros(130,1);
    corNStd30=zeros(130,1);
    corTStd30=zeros(130,1);
    ww30=zeros(130,1);

    for i=1:length(MeanRebVelNbyPos30)
        if (i>=(minx+cut)/mm && i<=(maxx-cut)/mm && abs(MeanRebVelbyPos30(i))>0 ...
            && LilltestRebVelbyPos30(i)<1 && LilltestInVelbyPos30(i)<1)

            p=ratio_of_normalpdf(z,abs(MeanRebVelbyPos30(i)),StdRebVelbyPos30(i),...
            abs(MeanInVelbyPos30(i)),StdInVelbyPos30(i));
            pdf30(i,:)=p;

            p=ratio_of_normalpdf(z,abs(MeanRebVelNbyPos30(i)),StdRebVelNbyPos30(i),...
            abs(MeanInVelNbyPos30(i)),StdInVelNbyPos30(i));
            pdfN30(i,:)=p;

            p=ratio_of_normalpdf(z,abs(MeanRebVelTbyPos30(i)),StdRebVelTbyPos30(i),...
            abs(MeanInVelTbyPos30(i)),StdInVelTbyPos30(i));
            pdfT30(i,:)=p;

            [~,n]=max(pdf30(i,:));
            cor30(i)=z(n);

            [~,n]=max(pdfT30(i,:));
            corT30(i)=z(n);

            [~,n]=max(pdfN30(i,:));
            corN30(i)=z(n);

            cd=cumtrapz(z,pdf30(i,:));
            [~,n] = min(abs(cd-.158));
            corStd30(i)=cor30(i)-z(n);

            cd=cumtrapz(z,pdfT30(i,:));
            [~,n] = min(abs(cd-.158));
            corTStd30(i)=corT30(i)-z(n);

            cd=cumtrapz(z,pdfN30(i,:));
            [~,n] = min(abs(cd-.158));
            corNStd30(i)=corN30(i)-z(n);
        end
    end
    vRatio30=bins2'./binsIN';
for i=1:130
    if cor30(i)<=0
        ww30(i) = i;
    end
end

if (length(instats)> length(rebstats))
    RebCor30=corr(instats([1:length(rebstats)],3),rebstats(:,3));
else
    RebCor30=corr(rebstats([1:length(instats)],3),instats(:,3));
end
MeanInAng30=MeanInAngbyPos30;
MeanInVel30=MeanInVelbyPos30;
MeanInVel30(find(ww30)) = [];
MeanInAng30(find(ww30)) = [];
cor30(find(ww30))=[];
corN30(find(ww30))=[];
corT30(find(ww30))=[];
corStd30(find(ww30))=[];
corNStd30(find(ww30))=[];
corTStd30(find(ww30))=[];
vRatio30(find(ww30))=[];
REBRATIOa30 = mean(vRatio30);
REBRATIO30 = length(rebstats)/sum(binsINr);
REBRATIOr30 = RebNum30deg./binsINr;
```

```
LillTotal(1,1)=sum(LilltestInVelbyPos30);
LillTotal(2,1)=sum(LilltestRebVelbyPos30);
end
%*************************40deg*****************************************
%*********************Incoming%40deg************************************
if (length(incoming40deg) >1)
    clear instats rebstats bins bins1 bin_AbP bin_AbA m n ddi ddr
    angCoup=38;
    Reb_n_Lim_up=Reb_n_Lim_upM*angCoup/80;
    Reb_n_Lim_low=Reb_n_Lim_lowM*angCoup/80;
    instats(:,1:2) = incoming40deg(:,5:6);
    instats(:,3) = hypot(incoming40deg(:,7), incoming40deg(:,8));
    instats(:,4) = atan2(incoming40deg(:,8), incoming40deg(:,7))*180/pi+(angCoup-90);
    instats(:,5) = incoming40deg(:,10);
    instats2=instats;
    instats = sortrows(instats, 1);

    rebstats(:,1:2) = rebound40deg(:,5:6);
    rebstats(:,3) = hypot(rebound40deg(:,7), rebound40deg(:,8));
    rebstats(:,4) = atan2(rebound40deg(:,8), rebound40deg(:,7))*180/pi+(angCoup-90);
    rebstats = sortrows(rebstats, 1);

    for i=1:length(instats)-1;
        if instats(i,1)==instats(i+1,1)
           ddi(i)=i;
        end
    end
    if exist('ddi')
    instats(find(ddi),:)=[];
    end
    for i=1:length(rebstats)-1;
        if rebstats(i,1)==rebstats(i+1,1)
           ddr(i)=i;
        end
    end
    if exist('ddr')
    rebstats(find(ddr),:)=[];
    end


    StdInAngbyPos40=zeros(1,130);
    MeanInAngbyPos40=zeros(1,130);

    MeanInVelbyPos40=zeros(1,130);
    StdInVelbyPos40 = zeros(1,130);

    MeanInVelTbyPos40 = zeros(1,130);
    StdInVelTbyPos40=zeros(1,130);

    MeanInVelNbyPos40 = zeros(1,130);
    StdInVelNbyPos40=zeros(1,130);

    LilltestInVelbyPos40=zeros(1,130);
    probin40=zeros(1,130);
    LilltestRebVelbyPos40=zeros(1,130);
    probreb40=zeros(1,130);

    StdInVelbyAng40=zeros(1,130);

    bins=zeros(1,130);
    bins1=zeros(1,130);
    binsIN=zeros(1,130);

    for i = 1:size(instats,1)
        if round(instats(i,4))>0
        bin_VbA = round(instats(i,4));
        bins(bin_VbA)=bins(bin_VbA)+1;
        end
        bin_AbP = round(instats(i,1));
        bin_AbP = bin_AbP+40;
        bins1(bin_AbP)=bins1(bin_AbP)+1;
        if instats(i,5)<=Reb_n_Lim_up && instats(i,5)>=Reb_n_Lim_low
        binsIN(bin_AbP)=binsIN(bin_AbP)+1;
        end
    end

    % % %     sorts the number of incoming particles from each run
    binsINr=zeros(1,size(InNum40deg,2));
```

```
    k=1;
    for i=1:size(InNum40deg,2)
        for j=1:InNum40deg(i)
            if instats2(k,5)<=Reb_n_Lim_up && instats2(k,5)>=Reb_n_Lim_low
            binsINr(1,i)=binsINr(1,i)+1;
            end
            k=k+1;
        end
    end

    %Calculating bin witdth for 2mm X direction bins for the Ratio Dist.
    bins1e=zeros(1,130);
    for i=1:mm:ceil(length(bins1))-1
       bins1e(ceil(i/mm))=bins1(i)+bins1(i+1);
    end
    n=1;
    for i=1: length(bins1e)

        if bins1e(i)>0   % this if statement removes outliers from the data set
%         if i>15 && i<=20
            clear bc
            Qr=quantile(instats(n:n+bins1e(i)-1,3),[0.25,0.75]);
            binsoutlierI(i)=length(find(instats(n:n+bins1e(i)-1,3)>=Qr(2)+K*(Qr(2)-Qr(1))...
            | instats(n:n+bins1e(i)-1,3)<=Qr(1)-K*(Qr(2)-Qr(1)) ));

            bc=find(instats(n:n+bins1e(i)-1,3)>=Qr(2)+K*(Qr(2)-Qr(1))...
            | instats(n:n+bins1e(i)-1,3)<=Qr(1)-K*(Qr(2)-Qr(1)));
            instats(n+bc-1,:)=[];
            bins1e(i)=bins1e(i)-binsoutlierI(i);
        end
        if bins1e(i)>4
            [LilltestInVelbyPos40(i),probin40(i)]= lillietest(instats(n:n+bins1e(i)-1,3)',signif);
        end
        StdInAngbyPos40(i) = std(instats(n:n+bins1e(i)-1,4));
        MeanInAngbyPos40(i) = mean(instats(n:n+bins1e(i)-1,4));
        StdInVelbyPos40(i) = std(instats(n:n+bins1e(i)-1,3));
        MeanInVelbyPos40(i) = mean(instats(n:n+bins1e(i)-1,3));
        MeanInVelTbyPos40(i) = mean(instats(n:n+bins1e(i)-1,3).*cosd(instats(n:n+bins1e(i)-1,4)));
        StdInVelTbyPos40(i) = std(instats(n:n+bins1e(i)-1,3).*cosd(instats(n:n+bins1e(i)-1,4)));
        MeanInVelNbyPos40(i) = mean(instats(n:n+bins1e(i)-1,3).*sind(instats(n:n+bins1e(i)-1,4)));
        StdInVelNbyPos40(i) = std(instats(n:n+bins1e(i)-1,3).*sind(instats(n:n+bins1e(i)-1,4)));

        n = n+bins1e(i);
        if isnan(StdInAngbyPos40(i))==1
            StdInAngbyPos40(i)=0;
            MeanInAngbyPos40(i)=0;
            MeanInVelTbyPos40(i)=0;
            StdInVelTbyPos40(i)=0;
            StdInVelbyPos40(i) = 0;
            MeanInVelbyPos40(i) =0;
            MeanInVelNbyPos40(i)=0;
            StdInVelNbyPos40(i)=0;

        end
    end

%**************************Rebounding 40deg*******************************
    clear bins bins2 bin_AbP bin_AbA

    StdRebAngbyPos40=zeros(1,130);
    MeanRebAngbyPos40=zeros(1,130);

    MeanRebVelbyPos40=zeros(1,130);
    StdRebVelbyPos40 = zeros(1,130);

    MeanRebVelTbyPos40 = zeros(1,130);
    StdRebVelTbyPos40=zeros(1,130);

    MeanRebVelNbyPos40 = zeros(1,130);
    StdRebVelNbyPos40=zeros(1,130);

    StdRebVelbyAng40=zeros(1,130);

    bins=zeros(1,130);
    bins2=zeros(1,130);

    for i = 1:size(rebstats,1)
        if round(rebstats(i,4))>0
```

```
        bin_VbA = round(rebstats(i,4));
        bins(bin_VbA)=bins(bin_VbA)+1;
        end
        bin_AbP = round(rebstats(i,1));
        bin_AbP = bin_AbP+40;
        bins2(bin_AbP)=bins2(bin_AbP)+1;
    end

      %Calculating bin witdth for 2mm X direction bins for the Ratio Dist.
    bins2e=zeros(1,130);

    for i=1:mm:ceil(length(bins2))-1
       bins2e(ceil(i/mm))=bins2(i)+bins2(i+1);
    end
    n=1;
    for i=1: length(bins2e)

        if bins2e(i)>0   % this if statement removes outliers from the data set
%         if i>15 && i<=20
            clear bc
            Qr=quantile(rebstats(n:n+bins2e(i)-1,3),[0.25,0.75]);
            binsoutlierR(i)=length(find(rebstats(n:n+bins2e(i)-1,3)>=Qr(2)+K*(Qr(2)-Qr(1))...
            | rebstats(n:n+bins2e(i)-1,3)<=Qr(1)-K*(Qr(2)-Qr(1)) ));

            bc=find(rebstats(n:n+bins2e(i)-1,3)>=Qr(2)+K*(Qr(2)-Qr(1))...
            | rebstats(n:n+bins2e(i)-1,3)<=Qr(1)-K*(Qr(2)-Qr(1)));
            rebstats(n+bc-1,:)=[];
            bins2e(i)=bins2e(i)-binsoutlierR(i);
%             figure
%             histfit(rebstats(n:n+bins2e(i)-1,3))

        end
        if bins2e(i)>4
            [LilltestRebVelbyPos40(i),probreb40(i)]= lillietest(rebstats(n:n+bins2e(i)-1,3)',signif);
        end
        StdRebAngbyPos40(i) = std(rebstats(n:n+bins2e(i)-1,4));
        MeanRebAngbyPos40(i) = mean(rebstats(n:n+bins2e(i)-1,4));
        StdRebVelbyPos40(i) = std(rebstats(n:n+bins2e(i)-1,3));
        MeanRebVelbyPos40(i) = mean(rebstats(n:n+bins2e(i)-1,3));
        MeanRebVelTbyPos40(i) = mean(rebstats(n:n+bins2e(i)-1,3).*cosd(rebstats(n:n+bins2e(i)-1,4)));
        StdRebVelTbyPos40(i) = std(rebstats(n:n+bins2e(i)-1,3).*cosd(rebstats(n:n+bins2e(i)-1,4)));
        MeanRebVelNbyPos40(i) = mean(rebstats(n:n+bins2e(i)-1,3).*sind(rebstats(n:n+bins2e(i)-1,4)));
        StdRebVelNbyPos40(i) = std(rebstats(n:n+bins2e(i)-1,3).*sind(rebstats(n:n+bins2e(i)-1,4)));



        n = n+bins2(i);
        if isnan(StdRebAngbyPos40(i))==1
            StdRebAngbyPos40(i)=0;
            MeanRebAngbyPos40(i)=0;
            MeanRebVelTbyPos40(i)=0;
            StdRebVelTbyPos40(i)=0;
            StdRebVelbyPos40(i) = 0;
            MeanRebVelbyPos40(i) =0;
            MeanRebVelNbyPos40(i)=0;
            StdRebVelNbyPos40(i)=0;

        end
    end

    %Ratio Distribution calculations
    maxx=min(max(instats(:,1)),max(rebstats(:,1)))+40;
    minx=max(min(instats(:,1)),min(rebstats(:,1)))+40;
    cut=(maxx-minx)/20;

    z=(-2:.001:4);

    pdfN40=zeros(130,length(z));
    pdfT40=zeros(130,length(z));
    pdf40=zeros(130,length(z));
    corN40=zeros(130,1);
    corT40=zeros(130,1);
    cor40=zeros(130,1);
    corNStd40=zeros(130,1);
    corTStd40=zeros(130,1);
    corStd40=zeros(130,1);
    ww40=zeros(130,1);

    for i=1:length(MeanRebVelNbyPos40)
```

```
        if (i>=(minx+cut)/mm && i<=(maxx-cut)/mm && abs(MeanRebVelbyPos40(i))>0 ...
            && LilltestRebVelbyPos40(i)<1 && LilltestInVelbyPos40(i)<1)
            p=ratio_of_normalpdf(z,abs(MeanRebVelbyPos40(i)),StdRebVelbyPos40(i),...
            abs(MeanInVelbyPos40(i)),StdInVelbyPos40(i));
            pdf40(i,:)=p;

            p=ratio_of_normalpdf(z,abs(MeanRebVelNbyPos40(i)),StdRebVelNbyPos40(i),...
            abs(MeanInVelNbyPos40(i)),StdInVelNbyPos40(i));
            pdfN40(i,:)=p;

            p=ratio_of_normalpdf(z,MeanRebVelTbyPos40(i),StdRebVelTbyPos40(i),...
            MeanInVelTbyPos40(i),StdInVelTbyPos40(i));
            pdfT40(i,:)=p;

            [~,n]=max(pdf40(i,:));
            cor40(i)=z(n);

            [~,n]=max(pdfT40(i,:));
            corT40(i)=z(n);

            [~,n]=max(pdfN40(i,:));
            corN40(i)=z(n);

            cd=cumtrapz(z,pdf40(i,:));
            [~,n] = min(abs(cd-.158));
            corStd40(i)=cor40(i)-z(n);

            cd=cumtrapz(z,pdfT40(i,:));
            [~,n] = min(abs(cd-.158));
            corTStd40(i)=corT40(i)-z(n);

            cd=cumtrapz(z,pdfN40(i,:));
            [~,n] = min(abs(cd-.158));
            corNStd40(i)=corN40(i)-z(n);
        end
    end
vRatio40=bins2'./binsIN';
for i=1:130
    if cor40(i)<=0
        ww40(i) = i;
    end
end
if (length(instats)> length(rebstats))
    RebCor40=corr(instats([1:length(rebstats)],3),rebstats(:,3));
else
    RebCor40=corr(rebstats([1:length(instats)],3),instats(:,3));
end

MeanInAng40=MeanInAngbyPos40;
MeanInVel40=MeanInVelbyPos40;
MeanInVel40(find(ww40)) = [];
MeanInAng40(find(ww40)) = [];
cor40(find(ww40))=[];
corN40(find(ww40))=[];
corT40(find(ww40))=[];
corStd40(find(ww40))=[];
corNStd40(find(ww40))=[];
corTStd40(find(ww40))=[];
vRatio40(find(ww40))=[];
REBRATIOa40 = mean(vRatio40);
REBRATIO40 = length(rebstats)/sum(binsINr);
REBRATIOr40 = RebNum40deg./binsINr;
LillTotal(1,2)=sum(LilltestInVelbyPos40);
LillTotal(2,2)=sum(LilltestRebVelbyPos40);
end
%************************50deg*******************************************
%********************Incoming 50deg*************************************
if (length(incoming50deg) >1)
    clear instats rebstats bins bins1 bin_AbP bin_AbA m n ddi ddr
    angCoup=48;
    Reb_n_Lim_up=Reb_n_Lim_upM*angCoup/80;
    Reb_n_Lim_low=Reb_n_Lim_lowM*angCoup/80;
    instats(:,1:2) = incoming50deg(:,5:6);
    instats(:,3) = hypot(incoming50deg(:,7), incoming50deg(:,8));
    instats(:,4) = atan2(incoming50deg(:,8), incoming50deg(:,7))*180/pi+(angCoup-90);
    instats(:,5) = incoming50deg(:,10);
    instats2=instats;
    instats = sortrows(instats, 1);
    rebstats(:,1:2) = rebound50deg(:,5:6);
```

```
    rebstats(:,3) = hypot(rebound50deg(:,7), rebound50deg(:,8));
    rebstats(:,4) = atan2(rebound50deg(:,8), rebound50deg(:,7))*180/pi+(angCoup-90);
    rebstats = sortrows(rebstats, 1);
    for i=1:length(instats)-1;
        if instats(i,1)==instats(i+1,1)
           ddi(i)=i;
        end
    end
    if exist('ddi')
    instats(find(ddi),:)=[];
    end
    for i=1:length(rebstats)-1;
        if rebstats(i,1)==rebstats(i+1,1)
           ddr(i)=i;
        end
    end
    if exist('ddr')
    rebstats(ddr,:)=[];
    end

    StdInAngbyPos50=zeros(1,130);
    MeanInAngbyPos50=zeros(1,130);

    MeanInVelbyPos50=zeros(1,130);
    StdInVelbyPos50 = zeros(1,130);

    MeanInVelTbyPos50 = zeros(1,130);
    StdInVelTbyPos50=zeros(1,130);

    MeanInVelNbyPos50 = zeros(1,130);
    StdInVelNbyPos50=zeros(1,130);

    StdInVelbyAng50=zeros(1,130);
    LilltestInVelbyPos50=zeros(1,130);
    probin50=zeros(1,130);
    LilltestRebVelbyPos50=zeros(1,130);
    probreb50=zeros(1,130);

    bins=zeros(1,130);
    bins1=zeros(1,130);
    binsIN=zeros(1,130);

    for i = 1:size(instats,1)
        if round(instats(i,4))>0
        bin_VbA = round(instats(i,4));
        bins(bin_VbA)=bins(bin_VbA)+1;
        end
        bin_AbP = round(instats(i,1));
        bin_AbP = bin_AbP+40;
        bins1(bin_AbP)=bins1(bin_AbP)+1;
        if instats(i,5)<=Reb_n_Lim_up && instats(i,5)>=Reb_n_Lim_low
        binsIN(bin_AbP)=binsIN(bin_AbP)+1;
        end
    end

 % % %     sorts the number of incoming particles from each run
    binsINr=zeros(1,size(InNum50deg,2));
    k=1;
    for i=1:size(InNum50deg,2)
        for j=1:InNum50deg(i)
            if instats2(k,5)<=Reb_n_Lim_up && instats2(k,5)>=Reb_n_Lim_low
            binsINr(1,i)=binsINr(1,i)+1;
            end
            k=k+1;
        end
    end

    %Calculating bin witdth for 2mm X direction bins for the Ratio Dist.
    bins1e=zeros(1,130);
    for i=1:mm:ceil(length(bins1))-1
       bins1e(ceil(i/mm))=bins1(i)+bins1(i+1);
    end
    n=1;
    for i=1: length(bins1e)

        if bins1e(i)>0   % this if statement removes outliers from the data set
%         if i>15 && i<=20
            clear bc
```

```
            Qr=quantile(instats(n:n+bins1e(i)-1,3),[0.25,0.75]);
            binsoutlierI(i)=length(find(instats(n:n+bins1e(i)-1,3)>=Qr(2)+K*(Qr(2)-Qr(1))...
            | instats(n:n+bins1e(i)-1,3)<=Qr(1)-K*(Qr(2)-Qr(1)) ));

            bc=find(instats(n:n+bins1e(i)-1,3)>=Qr(2)+K*(Qr(2)-Qr(1))...
            | instats(n:n+bins1e(i)-1,3)<=Qr(1)-K*(Qr(2)-Qr(1)));
            instats(n+bc-1,:)=[];
            bins1e(i)=bins1e(i)-binsoutlierI(i);
        end
        if bins1e(i)>4
            [LilltestInVelbyPos50(i),probin50(i)]= lillietest(instats(n:n+bins1e(i)-1,3)',signif);
        end
        StdInAngbyPos50(i) = std(instats(n:n+bins1e(i)-1,4));
        MeanInAngbyPos50(i) = mean(instats(n:n+bins1e(i)-1,4));
        StdInVelbyPos50(i) = std(instats(n:n+bins1e(i)-1,3));
        MeanInVelbyPos50(i) = mean(instats(n:n+bins1e(i)-1,3));
        MeanInVelTbyPos50(i) = mean(instats(n:n+bins1e(i)-1,3).*cosd(instats(n:n+bins1e(i)-1,4)));
        StdInVelTbyPos50(i) = std(instats(n:n+bins1e(i)-1,3).*cosd(instats(n:n+bins1e(i)-1,4)));
        MeanInVelNbyPos50(i) = mean(instats(n:n+bins1e(i)-1,3).*sind(instats(n:n+bins1e(i)-1,4)));
        StdInVelNbyPos50(i) = std(instats(n:n+bins1e(i)-1,3).*sind(instats(n:n+bins1e(i)-1,4)));


        n = n+bins1e(i);
        if isnan(StdInAngbyPos50(i))==1
            StdInAngbyPos50(i)=0;
            MeanInAngbyPos50(i)=0;
            MeanInVelTbyPos50(i)=0;
            StdInVelTbyPos50(i)=0;
            StdInVelbyPos50(i) = 0;
            MeanInVelbyPos50(i) =0;
            MeanInVelNbyPos50(i)=0;
            StdInVelNbyPos50(i)=0;

        end
    end


%**********************Rebounding 50deg***********************************
    clear bins bins2 bin_AbP bin_AbA

    StdRebAngbyPos50=zeros(1,130);
    MeanRebAngbyPos50=zeros(1,130);

    MeanRebVelbyPos50=zeros(1,130);
    StdRebVelbyPos50 = zeros(1,130);

    MeanRebVelTbyPos50 = zeros(1,130);
    StdRebVelTbyPos50=zeros(1,130);

    MeanRebVelNbyPos50 = zeros(1,130);
    StdRebVelNbyPos50=zeros(1,130);

    StdRebVelbyAng50=zeros(1,130);

    bins=zeros(1,130);
    bins2=zeros(1,130);

    for i = 1:size(rebstats,1)
        if round(rebstats(i,4))>0
        bin_VbA = round(rebstats(i,4));
        bins(bin_VbA)=bins(bin_VbA)+1;
        end
        bin_AbP = round(rebstats(i,1));
        bin_AbP = bin_AbP+40;
        bins2(bin_AbP)=bins2(bin_AbP)+1;
    end
     %Calculating bin witdth for 2mm X direction bins for the Ratio Dist.
    bins2e=zeros(1,130);

    for i=1:mm:ceil(length(bins2))-1
       bins2e(ceil(i/mm))=bins2(i)+bins2(i+1);
    end
    n=1;
    for i=1: length(bins2e)

        if bins2e(i)>0   % this if statement removes outliers from the data set
%         if i>15 && i<=20
```

```
        clear bc
        Qr=quantile(rebstats(n:n+bins2e(i)-1,3),[0.25,0.75]);
        binsoutlierR(i)=length(find(rebstats(n:n+bins2e(i)-1,3)>=Qr(2)+K*(Qr(2)-Qr(1))...
        | rebstats(n:n+bins2e(i)-1,3)<=Qr(1)-K*(Qr(2)-Qr(1)) ));

        bc=find(rebstats(n:n+bins2e(i)-1,3)>=Qr(2)+K*(Qr(2)-Qr(1))...
        | rebstats(n:n+bins2e(i)-1,3)<=Qr(1)-K*(Qr(2)-Qr(1)));
        rebstats(n+bc-1,:)=[];
        bins2e(i)=bins2e(i)-binsoutlierR(i);
    end
    if bins2e(i)>4
        [LilltestRebVelbyPos50(i),probreb50(i)]= lillietest(rebstats(n:n+bins2e(i)-1,3)',signif);
    end
    StdRebAngbyPos50(i) = std(rebstats(n:n+bins2e(i)-1,4));
    MeanRebAngbyPos50(i) = mean(rebstats(n:n+bins2e(i)-1,4));
    StdRebVelbyPos50(i) = std(rebstats(n:n+bins2e(i)-1,3));
    MeanRebVelbyPos50(i) = mean(rebstats(n:n+bins2e(i)-1,3));
    MeanRebVelTbyPos50(i) = mean(rebstats(n:n+bins2e(i)-1,3).*cosd(rebstats(n:n+bins2e(i)-1,4)));
    StdRebVelTbyPos50(i) = std(rebstats(n:n+bins2e(i)-1,3).*cosd(rebstats(n:n+bins2e(i)-1,4)));
    MeanRebVelNbyPos50(i) = mean(rebstats(n:n+bins2e(i)-1,3).*sind(rebstats(n:n+bins2e(i)-1,4)));
    StdRebVelNbyPos50(i) = std(rebstats(n:n+bins2e(i)-1,3).*sind(rebstats(n:n+bins2e(i)-1,4)));


    n = n+bins2e(i);
    if isnan(StdRebAngbyPos50(i))==1
        StdRebAngbyPos50(i)=0;
        MeanRebAngbyPos50(i)=0;
        MeanRebVelTbyPos50(i)=0;
        StdRebVelTbyPos50(i)=0;
        StdRebVelbyPos50(i) = 0;
        MeanRebVelbyPos50(i) =0;
        MeanRebVelNbyPos50(i)=0;
        StdRebVelNbyPos50(i)=0;
    end
end

 %Ratio Distribution calculations
maxx=min(max(instats(:,1)),max(rebstats(:,1)))+40;
minx=max(min(instats(:,1)),min(rebstats(:,1)))+40;
cut=(maxx-minx)/20;

z=(-2:.001:4);

pdfN50=zeros(130,length(z));
pdfT50=zeros(130,length(z));
pdf50=zeros(130,length(z));
corN50=zeros(130,1);
corT50=zeros(130,1);
cor50=zeros(130,1);
corNStd50=zeros(130,1);
corTStd50=zeros(130,1);
corStd50=zeros(130,1);
ww50=zeros(130,1);

for i=1:length(MeanRebVelNbyPos50)
    if (i>=(minx+cut)/mm && i<=(maxx-cut)/mm && abs(MeanRebVelbyPos50(i))>0 ...
        && LilltestRebVelbyPos50(i)<1 && LilltestInVelbyPos50(i)<1)

        p=ratio_of_normalpdf(z,abs(MeanRebVelbyPos50(i)),StdRebVelbyPos50(i),...
        abs(MeanInVelbyPos50(i)),StdInVelbyPos50(i));
        pdf50(i,:)=p;

        p=ratio_of_normalpdf(z,abs(MeanRebVelNbyPos50(i)),StdRebVelNbyPos50(i),...
        abs(MeanInVelNbyPos50(i)),StdInVelNbyPos50(i));
        pdfN50(i,:)=p;

        p=ratio_of_normalpdf(z,abs(MeanRebVelTbyPos50(i)),StdRebVelTbyPos50(i),...
        abs(MeanInVelTbyPos50(i)),StdInVelTbyPos50(i));
        pdfT50(i,:)=p;

        [~,n]=max(pdf50(i,:));
        cor50(i)=z(n);

        [~,n]=max(pdfT50(i,:));
        corT50(i)=z(n);

        [~,n]=max(pdfN50(i,:));
        corN50(i)=z(n);
```

```
            cd=cumtrapz(z,pdf50(i,:));
            [~,n] = min(abs(cd-.158));
            corStd50(i)=cor50(i)-z(n);

            cd=cumtrapz(z,pdfT50(i,:));
            [~,n] = min(abs(cd-.158));
            corTStd50(i)=corT50(i)-z(n);

            cd=cumtrapz(z,pdfN50(i,:));
            [~,n] = min(abs(cd-.158));
            corNStd50(i)=corN50(i)-z(n);
        end
    end
vRatio50=bins2'./binsIN';
for i=1:130
    if cor50(i)<=0
        ww50(i) = i;
    end
end

if (length(instats)> length(rebstats))
    RebCor50=corr(instats([1:length(rebstats)],3),rebstats(:,3));
else
    RebCor50=corr(rebstats([1:length(instats)],3),instats(:,3));
end
MeanInAng50=MeanInAngbyPos50;
MeanInVel50=MeanInVelbyPos50;
MeanInVel50(find(ww50)) = [];
MeanInAng50(find(ww50)) = [];
cor50(find(ww50))=[];
corN50(find(ww50))=[];
corT50(find(ww50))=[];
corStd50(find(ww50))=[];
corNStd50(find(ww50))=[];
corTStd50(find(ww50))=[];
vRatio50(find(ww50))=[];
REBRATIOa50 = mean(vRatio50);
REBRATIO50 = length(rebstats)/sum(binsINr);
REBRATIOr50 = RebNum50deg./binsINr;
LillTotal(1,3)=sum(LilltestInVelbyPos50);
LillTotal(2,3)=sum(LilltestRebVelbyPos50);
end

%***************************60deg*****************************************
%***********************Incoming 60deg************************************
if (length(incoming60deg) >1)
    clear instats rebstats bins bins1 bin_AbP bin_AbA m n ddi ddr
    angCoup=58;
    Reb_n_Lim_up=Reb_n_Lim_upM*angCoup/80;
    Reb_n_Lim_low=Reb_n_Lim_lowM*angCoup/80;
    instats(:,1:2) = incoming60deg(:,5:6);
    instats(:,3) = hypot(incoming60deg(:,7), incoming60deg(:,8));
    instats(:,4) = atan2(incoming60deg(:,8), incoming60deg(:,7))*180/pi+(angCoup-90);
    instats(:,5) = incoming60deg(:,10);
    instats2=instats;
    instats = sortrows(instats, 1);
    rebstats(:,1:2) = rebound60deg(:,5:6);
    rebstats(:,3) = hypot(rebound60deg(:,7), rebound60deg(:,8));
    rebstats(:,4) = atan2(rebound60deg(:,8), rebound60deg(:,7))*180/pi+(angCoup-90);
    rebstats = sortrows(rebstats, 1);
    for i=1:length(instats)-1;
        if instats(i,1)==instats(i+1,1)
           ddi(i)=i;
        end
    end
    if exist('ddi')
    instats(find(ddi),:)=[];
    end
    for i=1:length(rebstats)-1;
        if rebstats(i,1)==rebstats(i+1,1)
           ddr(i)=i;
        end
    end
    if exist('ddr')
    rebstats(find(ddr),:)=[];
    end

    StdInAngbyPos60=zeros(1,130);
    MeanInAngbyPos60=zeros(1,130);
```

```
    MeanInVelbyPos60=zeros(1,130);
    StdInVelbyPos60 = zeros(1,130);

    MeanInVelTbyPos60 = zeros(1,130);
    StdInVelTbyPos60=zeros(1,130);

    MeanInVelNbyPos60 = zeros(1,130);
    StdInVelNbyPos60=zeros(1,130);

    StdInVelbyAng60=zeros(1,130);

    LilltestInVelbyPos60=zeros(1,130);
    probin60=zeros(1,130);
    LilltestRebVelbyPos60=zeros(1,130);
    probreb60=zeros(1,130);

    bins=zeros(1,130);
    bins1=zeros(1,130);
    binsIN=zeros(1,130);

    for i = 1:size(instats,1)
        if round(instats(i,4))>0
        bin_VbA = round(instats(i,4));
        bins(bin_VbA)=bins(bin_VbA)+1;
        end
        bin_AbP = round(instats(i,1));
        bin_AbP = bin_AbP+40;
        bins1(bin_AbP)=bins1(bin_AbP)+1;
        if instats(i,5)<=Reb_n_Lim_up && instats(i,5)>=Reb_n_Lim_low
        binsIN(bin_AbP)=binsIN(bin_AbP)+1;
        end
    end

    % % %     sorts the number of incoming particles from each run
    binsINr=zeros(1,size(InNum60deg,2));
    k=1;
    for i=1:size(InNum60deg,2)
        for j=1:InNum60deg(i)
            if instats2(k,5)<=Reb_n_Lim_up && instats2(k,5)>=Reb_n_Lim_low
            binsINr(1,i)=binsINr(1,i)+1;
            end
            k=k+1;
        end
    end

    %Calculating bin witdth for 2mm X direction bins for the Ratio Dist.
    bins1e=zeros(1,130);
    for i=1:mm:ceil(length(bins1))-1
       bins1e(ceil(i/mm))=bins1(i)+bins1(i+1);
    end
    n=1;
    for i=1: length(bins1e)

        if bins1e(i)>0   % this if statement removes outliers from the data set
%         if i>17 && i<=18
            clear bc
            Qr=quantile(instats(n:n+bins1e(i)-1,3),[0.25,0.75]);
            binsoutlierI(i)=length(find(instats(n:n+bins1e(i)-1,3)>=Qr(2)+K*(Qr(2)-Qr(1))...
            | instats(n:n+bins1e(i)-1,3)<=Qr(1)-K*(Qr(2)-Qr(1)) ));
            bc=find(instats(n:n+bins1e(i)-1,3)>=Qr(2)+K*(Qr(2)-Qr(1))...
            | instats(n:n+bins1e(i)-1,3)<=Qr(1)-K*(Qr(2)-Qr(1)));
            instats(n+bc-1,:)=[];
            bins1e(i)=bins1e(i)-binsoutlierI(i);
        end
        if bins1e(i)>4
            [LilltestInVelbyPos60(i),probin60(i)]= lillietest(instats(n:n+bins1e(i)-1,3)',signif);
        end
        StdInAngbyPos60(i) = std(instats(n:n+bins1e(i)-1,4));
        MeanInAngbyPos60(i) = mean(instats(n:n+bins1e(i)-1,4));
        StdInVelbyPos60(i) = std(instats(n:n+bins1e(i)-1,3));
        MeanInVelbyPos60(i) = mean(instats(n:n+bins1e(i)-1,3));
        MeanInVelTbyPos60(i) = mean(instats(n:n+bins1e(i)-1,3).*cosd(instats(n:n+bins1e(i)-1,4)));
        StdInVelTbyPos60(i) = std(instats(n:n+bins1e(i)-1,3).*cosd(instats(n:n+bins1e(i)-1,4)));
        MeanInVelNbyPos60(i) = mean(instats(n:n+bins1e(i)-1,3).*sind(instats(n:n+bins1e(i)-1,4)));
        StdInVelNbyPos60(i) = std(instats(n:n+bins1e(i)-1,3).*sind(instats(n:n+bins1e(i)-1,4)));

        n = n+bins1e(i);
```

```
        if isnan(StdInAngbyPos60(i))==1
            StdInAngbyPos60(i)=0;
            MeanInAngbyPos60(i)=0;
            MeanInVelTbyPos60(i)=0;
            StdInVelTbyPos60(i)=0;
            StdInVelbyPos60(i) = 0;
            MeanInVelbyPos60(i) =0;
            MeanInVelNbyPos60(i)=0;
            StdInVelNbyPos60(i)=0;
        end
    end

%************************Rebounding 60deg*********************************
    clear bins bins2 bin_AbP bin_AbA

    StdRebAngbyPos60=zeros(1,130);
    MeanRebAngbyPos60=zeros(1,130);

    MeanRebVelbyPos60=zeros(1,130);
    StdRebVelbyPos60 = zeros(1,130);

    MeanRebVelTbyPos60 = zeros(1,130);
    StdRebVelTbyPos60=zeros(1,130);

    MeanRebVelNbyPos60 = zeros(1,130);
    StdRebVelNbyPos60=zeros(1,130);

    StdRebVelbyAng60=zeros(1,130);

    bins=zeros(1,130);
    bins2=zeros(1,130);

    for i = 1:size(rebstats,1)
        if round(rebstats(i,4))>0
        bin_VbA = round(rebstats(i,4));
        bins(bin_VbA)=bins(bin_VbA)+1;
        end
        bin_AbP = round(rebstats(i,1));
        bin_AbP = bin_AbP+40;
        bins2(bin_AbP)=bins2(bin_AbP)+1;
    end

      %Calculating bin witdth for 2mm X direction bins for the Ratio Dist.
    bins2e=zeros(1,130);

    for i=1:mm:ceil(length(bins2))-1
       bins2e(ceil(i/mm))=bins2(i)+bins2(i+1);
    end
    n=1;
    for i=1: length(bins2e)

        if bins2e(i)>0   % this if statement removes outliers from the data set
%         if i>15 && i<=20
            clear bc
            Qr=quantile(rebstats(n:n+bins2e(i)-1,3),[0.25,0.75]);
            binsoutlierR(i)=length(find(rebstats(n:n+bins2e(i)-1,3)>=Qr(2)+K*(Qr(2)-Qr(1))...
            | rebstats(n:n+bins2e(i)-1,3)<=Qr(1)-K*(Qr(2)-Qr(1)) ));

            bc=find(rebstats(n:n+bins2e(i)-1,3)>=Qr(2)+K*(Qr(2)-Qr(1))...
            | rebstats(n:n+bins2e(i)-1,3)<=Qr(1)-K*(Qr(2)-Qr(1)));
            rebstats(n+bc-1,:)=[];
            bins2e(i)=bins2e(i)-binsoutlierR(i);
        end
        if bins2e(i)>4
            [LilltestRebVelbyPos60(i),probreb60(i)]= lillietest(rebstats(n:n+bins2e(i)-1,3)',signif);
        end
        StdRebAngbyPos60(i) = std(rebstats(n:n+bins2e(i)-1,4));
        MeanRebAngbyPos60(i) = mean(rebstats(n:n+bins2e(i)-1,4));
        StdRebVelbyPos60(i) = std(rebstats(n:n+bins2e(i)-1,3));
        MeanRebVelbyPos60(i) = mean(rebstats(n:n+bins2e(i)-1,3));
        MeanRebVelTbyPos60(i) = mean(rebstats(n:n+bins2e(i)-1,3).*cosd(rebstats(n:n+bins2e(i)-1,4)));
        StdRebVelTbyPos60(i) = std(rebstats(n:n+bins2e(i)-1,3).*cosd(rebstats(n:n+bins2e(i)-1,4)));
        MeanRebVelNbyPos60(i) = mean(rebstats(n:n+bins2e(i)-1,3).*sind(rebstats(n:n+bins2e(i)-1,4)));
        StdRebVelNbyPos60(i) = std(rebstats(n:n+bins2e(i)-1,3).*sind(rebstats(n:n+bins2e(i)-1,4)));

        n = n+bins2e(i);
        if isnan(StdRebAngbyPos60(i))==1
            StdRebAngbyPos60(i)=0;
```

```
            MeanRebAngbyPos60(i)=0;
            MeanRebVelTbyPos60(i)=0;
            StdRebVelTbyPos60(i)=0;
            StdRebVelbyPos60(i) = 0;
            MeanRebVelbyPos60(i) =0;
            MeanRebVelNbyPos60(i)=0;
            StdRebVelNbyPos60(i)=0;
        end
    end

    %Ratio Distribution calculations
    maxx=min(max(instats(:,1)),max(rebstats(:,1)))+40;
    minx=max(min(instats(:,1)),min(rebstats(:,1)))+40;
    cut=(maxx-minx)/20;

    z=(-2:.001:4);

    pdf60=zeros(130,length(z));
    pdfN60=zeros(130,length(z));
    pdfT60=zeros(130,length(z));
    cor60=zeros(130,1);
    corN60=zeros(130,1);
    corT60=zeros(130,1);
    corStd60=zeros(130,1);
    corNStd60=zeros(130,1);
    corTStd60=zeros(130,1);
    ww60=zeros(130,1);

    for i=1:length(MeanRebVelNbyPos60)
        if (i>=(minx+cut)/mm && i<=(maxx-cut)/mm && abs(MeanRebVelbyPos60(i))>0 ...
            && LilltestRebVelbyPos60(i)<1 && LilltestInVelbyPos60(i)<1)
            p=ratio_of_normalpdf(z,abs(MeanRebVelbyPos60(i)),StdRebVelbyPos60(i),...
            abs(MeanInVelbyPos60(i)),StdInVelbyPos60(i));
            pdf60(i,:)=p;

            p=ratio_of_normalpdf(z,abs(MeanRebVelNbyPos60(i)),StdRebVelNbyPos60(i),...
            abs(MeanInVelNbyPos60(i)),StdInVelNbyPos60(i));
            pdfN60(i,:)=p;

            p=ratio_of_normalpdf(z,abs(MeanRebVelTbyPos60(i)),StdRebVelTbyPos60(i),...
            abs(MeanInVelTbyPos60(i)),StdInVelTbyPos60(i));
            pdfT60(i,:)=p;

            [~,n]=max(pdf60(i,:));
            cor60(i)=z(n);

            [~,n]=max(pdfT60(i,:));
            corT60(i)=z(n);

            [~,n]=max(pdfN60(i,:));
            corN60(i)=z(n);

            cd=cumtrapz(z,pdf60(i,:));
            [~,n] = min(abs(cd-.158));
            corStd60(i)=cor60(i)-z(n);

            cd=cumtrapz(z,pdfT60(i,:));
            [~,n] = min(abs(cd-.158));
            corTStd60(i)=corT60(i)-z(n);

            cd=cumtrapz(z,pdfN60(i,:));
            [~,n] = min(abs(cd-.158));
            corNStd60(i)=corN60(i)-z(n);
        end
    end
vRatio60=bins2'./binsIN';
for i=1:130
    if cor60(i)<=0
        ww60(i) = i;
    end
end
if (length(instats)> length(rebstats))
    RebCor60=corr(instats([1:length(rebstats)],3),rebstats(:,3));
else
    RebCor60=corr(rebstats([1:length(instats)],3),instats(:,3));
end

MeanInAng60=MeanInAngbyPos60;
```

```
MeanInVel60=MeanInVelbyPos60;
MeanInVel60(find(ww60)) = [];
MeanInAng60(find(ww60)) = [];
cor60(find(ww60))=[];
corN60(find(ww60))=[];
corT60(find(ww60))=[];
corStd60(find(ww60))=[];
corNStd60(find(ww60))=[];
corTStd60(find(ww60))=[];
vRatio60(find(ww60))=[];
REBRATIOa60 = mean(vRatio60);
REBRATIO60 = length(rebstats)/sum(binsINr);
REBRATIOr60 = RebNum60deg./binsINr;
LillTotal(1,4)=sum(LilltestInVelbyPos60);
LillTotal(2,4)=sum(LilltestRebVelbyPos60);
end

%************************70deg*****************************************
%********************Incoming 70deg*************************************
if (length(incoming70deg) >1)
    clear instats rebstats bins bins1 bin_AbP bin_AbA m n ddi ddr
    angCoup=68;
    Reb_n_Lim_up=Reb_n_Lim_upM*angCoup/80;
    Reb_n_Lim_low=Reb_n_Lim_lowM*angCoup/80;
    instats(:,1:2) = incoming70deg(:,5:6);
    instats(:,3) = hypot(incoming70deg(:,7), incoming70deg(:,8));
    instats(:,4) = atan2(incoming70deg(:,8), incoming70deg(:,7))*180/pi+(angCoup-90);
    instats(:,5) = incoming70deg(:,10);
    instats2=instats;
    instats = sortrows(instats, 1);
    rebstats(:,1:2) = rebound70deg(:,5:6);
    rebstats(:,3) = hypot(rebound70deg(:,7), rebound70deg(:,8));
    rebstats(:,4) = atan2(rebound70deg(:,8), rebound70deg(:,7))*180/pi+(angCoup-90);
    rebstats = sortrows(rebstats, 1);
    for i=1:length(instats)-1;
        if instats(i,1)==instats(i+1,1)
           ddi(i)=i;
        end
    end
    if exist('ddi')
    instats(find(ddi),:)=[];
    end
    for i=1:length(rebstats)-1;
        if rebstats(i,1)==rebstats(i+1,1)
           ddr(i)=i;
        end
    end
    if exist('ddr')
    rebstats(find(ddr),:)=[];
    end

    StdInAngbyPos70=zeros(1,130);
    MeanInAngbyPos70=zeros(1,130);

    MeanInVelbyPos70=zeros(1,130);
    StdInVelbyPos70 = zeros(1,130);

    MeanInVelTbyPos70 = zeros(1,130);
    StdInVelTbyPos70=zeros(1,130);

    MeanInVelNbyPos70 = zeros(1,130);
    StdInVelNbyPos70=zeros(1,130);

    StdInVelbyAng70=zeros(1,130);
    LilltestInVelbyPos70=zeros(1,130);
    probin70=zeros(1,130);
    LilltestRebVelbyPos70=zeros(1,130);
    probreb70=zeros(1,130);

    bins=zeros(1,130);
    bins1=zeros(1,130);
    binsIN=zeros(1,130);

    for i = 1:size(instats,1)
        if round(instats(i,4))>0
        bin_VbA = round(instats(i,4));
        bins(bin_VbA)=bins(bin_VbA)+1;
        end
        bin_AbP = round(instats(i,1));
```

```
        bin_AbP = bin_AbP+40;
        bins1(bin_AbP)=bins1(bin_AbP)+1;
        if instats(i,5)<=Reb_n_Lim_up && instats(i,5)>=Reb_n_Lim_low
        binsIN(bin_AbP)=binsIN(bin_AbP)+1;
        end
    end

    % % %     sorts the number of incoming particles from each run
    binsINr=zeros(1,size(InNum70deg,2));
    k=1;
    for i=1:size(InNum70deg,2)
        for j=1:InNum70deg(i)
            if instats2(k,5)<=Reb_n_Lim_up && instats2(k,5)>=Reb_n_Lim_low
            binsINr(1,i)=binsINr(1,i)+1;
            end
            k=k+1;
        end
    end

    %Calculating bin witdth for 2mm X direction bins for the Ratio Dist.
    bins1e=zeros(1,130);
    for i=1:mm:ceil(length(bins1))-1
       bins1e(ceil(i/mm))=bins1(i)+bins1(i+1);
    end
    n=1;
    for i=1: length(bins1e)

        if bins1e(i)>0   % this if statement removes outliers from the data set
%         if i>15 && i<=20
            clear bc
            Qr=quantile(instats(n:n+bins1e(i)-1,3),[0.25,0.75]);
            binsoutlierI(i)=length(find(instats(n:n+bins1e(i)-1,3)>=Qr(2)+K*(Qr(2)-Qr(1))...
            | instats(n:n+bins1e(i)-1,3)<=Qr(1)-K*(Qr(2)-Qr(1)) ));

            bc=find(instats(n:n+bins1e(i)-1,3)>=Qr(2)+K*(Qr(2)-Qr(1))...
            | instats(n:n+bins1e(i)-1,3)<=Qr(1)-K*(Qr(2)-Qr(1)));
            instats(n+bc-1,:)=[];
            bins1e(i)=bins1e(i)-binsoutlierI(i);
        end
        if bins1e(i)>4
            [LilltestInVelbyPos70(i),probin70(i)]= lillietest(instats(n:n+bins1e(i)-1,3)',signif);
        end
        StdInAngbyPos70(i) = std(instats(n:n+bins1e(i)-1,4));
        MeanInAngbyPos70(i) = mean(instats(n:n+bins1e(i)-1,4));
        StdInVelbyPos70(i) = std(instats(n:n+bins1e(i)-1,3));
        MeanInVelbyPos70(i) = mean(instats(n:n+bins1e(i)-1,3));
        MeanInVelTbyPos70(i) = mean(instats(n:n+bins1e(i)-1,3).*cosd(instats(n:n+bins1e(i)-1,4)));
        StdInVelTbyPos70(i) = std(instats(n:n+bins1e(i)-1,3).*cosd(instats(n:n+bins1e(i)-1,4)));
        MeanInVelNbyPos70(i) = mean(instats(n:n+bins1e(i)-1,3).*sind(instats(n:n+bins1e(i)-1,4)));
        StdInVelNbyPos70(i) = std(instats(n:n+bins1e(i)-1,3).*sind(instats(n:n+bins1e(i)-1,4)));

        n = n+bins1e(i);
        if isnan(StdInAngbyPos70(i))==1
            StdInAngbyPos70(i)=0;
            MeanInAngbyPos70(i)=0;
            MeanInVelTbyPos70(i)=0;
            StdInVelTbyPos70(i)=0;
            MeanInVelNbyPos70(i)=0;
            StdInVelNbyPos70(i)=0;
            StdInVelbyPos70(i) = 0;
            MeanInVelbyPos70(i) =0;
        end
    end

%********************Rebounding 70deg*********************************
    clear bins bins2 bin_AbP bin_AbA

    StdRebAngbyPos70=zeros(1,130);
    MeanRebAngbyPos70=zeros(1,130);

    MeanRebVelbyPos70=zeros(1,130);
    StdRebVelbyPos70 = zeros(1,130);

    MeanRebVelTbyPos70 = zeros(1,130);
    StdRebVelTbyPos70=zeros(1,130);

    MeanRebVelNbyPos70 = zeros(1,130);
    StdRebVelNbyPos70=zeros(1,130);
```

```
    StdRebVelbyAng70=zeros(1,130);

    bins=zeros(1,130);
    bins2=zeros(1,130);

    for i = 1:size(rebstats,1)
        if round(rebstats(i,4))>0
        bin_VbA = round(rebstats(i,4));
        bins(bin_VbA)=bins(bin_VbA)+1;
        end
        bin_AbP = round(rebstats(i,1));
        bin_AbP = bin_AbP+40;
        bins2(bin_AbP)=bins2(bin_AbP)+1;
    end
    %Calculating bin witdth for 2mm X direction bins for the Ratio Dist.
    bins2e=zeros(1,130);

    for i=1:mm:ceil(length(bins2))-1
       bins2e(ceil(i/mm))=bins2(i)+bins2(i+1);
    end
    n=1;
    for i=1: length(bins2e)

        if bins2e(i)>0   % this if statement removes outliers from the data set
%         if i>15 && i<=20
            clear bc
            Qr=quantile(rebstats(n:n+bins2e(i)-1,3),[0.25,0.75]);
            binsoutlierR(i)=length(find(rebstats(n:n+bins2e(i)-1,3)>=Qr(2)+K*(Qr(2)-Qr(1))...
            | rebstats(n:n+bins2e(i)-1,3)<=Qr(1)-K*(Qr(2)-Qr(1)) ));
            bc=find(rebstats(n:n+bins2e(i)-1,3)>=Qr(2)+K*(Qr(2)-Qr(1))...
            | rebstats(n:n+bins2e(i)-1,3)<=Qr(1)-K*(Qr(2)-Qr(1)));
            rebstats(n+bc-1,:)=[];
            bins2e(i)=bins2e(i)-binsoutlierR(i);
        end
        if bins2e(i)>4
            [LilltestRebVelbyPos70(i),probreb70(i)]= lillietest(rebstats(n:n+bins2e(i)-1,3)',signif);
        end

        StdRebAngbyPos70(i) = std(rebstats(n:n+bins2e(i)-1,4));
        MeanRebAngbyPos70(i) = mean(rebstats(n:n+bins2e(i)-1,4));
        StdRebVelbyPos70(i) = std(rebstats(n:n+bins2e(i)-1,3));
        MeanRebVelbyPos70(i) = mean(rebstats(n:n+bins2e(i)-1,3));
        MeanRebVelTbyPos70(i) = mean(rebstats(n:n+bins2e(i)-1,3).*cosd(rebstats(n:n+bins2e(i)-1,4)));
        StdRebVelTbyPos70(i) = std(rebstats(n:n+bins2e(i)-1,3).*cosd(rebstats(n:n+bins2e(i)-1,4)));
        MeanRebVelNbyPos70(i) = mean(rebstats(n:n+bins2e(i)-1,3).*sind(rebstats(n:n+bins2e(i)-1,4)));
        StdRebVelNbyPos70(i) = std(rebstats(n:n+bins2e(i)-1,3).*sind(rebstats(n:n+bins2e(i)-1,4)));

        n = n+bins2e(i);
        if isnan(StdRebAngbyPos70(i))==1
            StdRebAngbyPos70(i)=0;
            MeanRebAngbyPos70(i)=0;
            MeanRebVelTbyPos70(i)=0;
            StdRebVelTbyPos70(i)=0;
            StdRebVelbyPos70(i) = 0;
            MeanRebVelbyPos70(i) =0;
            StdRebVelNbyPos70(i) = 0;
            MeanRebVelNbyPos70(i) =0;
        end
    end

    %Ratio Distribution calculations
    maxx=min(max(instats(:,1)),max(rebstats(:,1)))+40;
    minx=max(min(instats(:,1)),min(rebstats(:,1)))+40;
    cut=(maxx-minx)/20;

    z=(-2:.001:4);

    pdfN70=zeros(130,length(z));
    pdfT70=zeros(130,length(z));
    pdf70=zeros(130,length(z));
    corN70=zeros(130,1);
    corT70=zeros(130,1);
    cor70=zeros(130,1);
    corNStd70=zeros(130,1);
    corTStd70=zeros(130,1);
    corStd70=zeros(130,1);
    ww70=zeros(130,1);
```

```
    for i=1:length(MeanRebVelNbyPos70)
        if (i>=(minx+cut)/mm && i<=(maxx-cut)/mm && abs(MeanRebVelbyPos70(i))>0 ...
            && LilltestRebVelbyPos70(i)<1 && LilltestInVelbyPos70(i)<1)
            p=ratio_of_normalpdf(z,abs(MeanRebVelbyPos70(i)),StdRebVelbyPos70(i),...
            abs(MeanInVelbyPos70(i)),StdInVelbyPos70(i));
            pdf70(i,:)=p;

            p=ratio_of_normalpdf(z,abs(MeanRebVelNbyPos70(i)),StdRebVelNbyPos70(i),...
            abs(MeanInVelNbyPos70(i)),StdInVelNbyPos70(i));
            pdfN70(i,:)=p;

            p=ratio_of_normalpdf(z,abs(MeanRebVelTbyPos70(i)),StdRebVelTbyPos70(i),...
            abs(MeanInVelTbyPos70(i)),StdInVelTbyPos70(i));
            pdfT70(i,:)=p;

            [~,n]=max(pdf70(i,:));
            cor70(i)=z(n);

            [~,n]=max(pdfT70(i,:));
            corT70(i)=z(n);

            [~,n]=max(pdfN70(i,:));
            corN70(i)=z(n);

            cd=cumtrapz(z,pdf70(i,:));
            [~,n] = min(abs(cd-.158));
            corStd70(i)=cor70(i)-z(n);

            cd=cumtrapz(z,pdfT70(i,:));
            [~,n] = min(abs(cd-.158));
            corTStd70(i)=corT70(i)-z(n);

            cd=cumtrapz(z,pdfN70(i,:));
            [~,n] = min(abs(cd-.158));
            corNStd70(i)=corN70(i)-z(n);
        end
    end
vRatio70=bins2'./binsIN';
for i=1:130
    if cor70(i)<=0
        ww70(i) = i;
    end
end
if (length(instats)> length(rebstats))
    RebCor70=corr(instats([1:length(rebstats)],3),rebstats(:,3));
else
    RebCor70=corr(rebstats([1:length(instats)],3),instats(:,3));
end

MeanInAng70=MeanInAngbyPos70;
MeanInVel70=MeanInVelbyPos70;
MeanInVel70(find(ww70)) = [];
MeanInAng70(find(ww70)) = [];
cor70(find(ww70))=[];
corN70(find(ww70))=[];
corT70(find(ww70))=[];
corStd70(find(ww70))=[];
corNStd70(find(ww70))=[];
corTStd70(find(ww70))=[];
vRatio70(find(ww70))=[];
REBRATIOa70 = mean(vRatio70);
REBRATIO70 = length(rebstats)/sum(binsINr);
REBRATIOr70 = RebNum70deg./binsINr;
LillTotal(1,5)=sum(LilltestInVelbyPos70);
LillTotal(2,5)=sum(LilltestRebVelbyPos70);
end

%***************80deg*************************************************
%*************Incoming 80deg*****************************************
if (length(incoming80deg) >1)
    clear instats rebstats bins bins1 bin_AbP bin_AbA m n  ddi ddr
    angCoup=78;
    Reb_n_Lim_up=Reb_n_Lim_upM*angCoup/80;
    Reb_n_Lim_low=Reb_n_Lim_lowM*angCoup/80;
    instats(:,1:2) = incoming80deg(:,5:6);
    instats(:,3) = hypot(incoming80deg(:,7), incoming80deg(:,8));
    instats(:,4) = atan2(incoming80deg(:,8), incoming80deg(:,7))*180/pi+(angCoup-90);
```

```
instats(:,5) = incoming80deg(:,10);
instats2=instats;
instats = sortrows(instats, 1);
rebstats(:,1:2) = rebound80deg(:,5:6);
rebstats(:,3) = hypot(rebound80deg(:,7), rebound80deg(:,8));
rebstats(:,4) = atan2(rebound80deg(:,8), rebound80deg(:,7))*180/pi+(angCoup-90);
rebstats = sortrows(rebstats, 1);

for i=1:length(instats)-1;
    if instats(i,1)==instats(i+1,1)
       ddi(i)=i;
    end
end
if exist('ddi')
instats(find(ddi),:)=[];
end
for i=1:length(rebstats)-1;
    if rebstats(i,1)==rebstats(i+1,1)
       ddr(i)=i;
    end
end
if exist('ddr')
rebstats(find(ddr),:)=[];
end

StdInAngbyPos80=zeros(1,130);
MeanInAngbyPos80=zeros(1,130);

MeanInVelbyPos80=zeros(1,130);
StdInVelbyPos80 = zeros(1,130);

MeanInVelTbyPos80 = zeros(1,130);
StdInVelTbyPos80=zeros(1,130);

MeanInVelNbyPos80 = zeros(1,130);
StdInVelNbyPos80=zeros(1,130);

StdInVelbyAng80=zeros(1,130);
invelbypos80=zeros(500,130);

LilltestInVelbyPos80=zeros(1,130);
probin80=zeros(1,130);
LilltestRebVelbyPos80=zeros(1,130);
probreb80=zeros(1,130);


bins=zeros(1,130);
bins1=zeros(1,130);
binsIN=zeros(1,130);

for i = 1:size(instats,1)
    if round(instats(i,4))>0
    bin_VbA = round(instats(i,4));
    bins(bin_VbA)=bins(bin_VbA)+1;
    end
    bin_AbP = round(instats(i,1));
    bin_AbP = bin_AbP+40;
    bins1(bin_AbP)=bins1(bin_AbP)+1;
    if instats(i,5)<=Reb_n_Lim_up && instats(i,5)>=Reb_n_Lim_low
    binsIN(bin_AbP)=binsIN(bin_AbP)+1;
    end
end

% % %     sorts the number of incoming particles from each run
binsINr=zeros(1,size(InNum80deg,2));
k=1;
for i=1:size(InNum80deg,2)
    for j=1:InNum80deg(i)
        if instats2(k,5)<=Reb_n_Lim_up && instats2(k,5)>=Reb_n_Lim_low
        binsINr(1,i)=binsINr(1,i)+1;
        end
        k=k+1;
    end
end
%Calculating bin witdth for 2mm X direction bins for the Ratio Dist.
bins1e=zeros(1,130);
for i=1:mm:ceil(length(bins1))-1
   bins1e(ceil(i/mm))=bins1(i)+bins1(i+1);
```

```
    end
    n=1;
    for i=1: length(bins1e)

        if bins1e(i)>0   % this if statement removes outliers from the data set
%         if i>12 && i<=15
            clear bc
            Qr=quantile(instats(n:n+bins1e(i)-1,3),[0.25,0.75]);
            binsoutlierI(i)=length(find(instats(n:n+bins1e(i)-1,3)>=Qr(2)+K*(Qr(2)-Qr(1))...
            | instats(n:n+bins1e(i)-1,3)<=Qr(1)-K*(Qr(2)-Qr(1)) ));
            bc=find(instats(n:n+bins1e(i)-1,3)>=Qr(2)+K*(Qr(2)-Qr(1))...
            | instats(n:n+bins1e(i)-1,3)<=Qr(1)-K*(Qr(2)-Qr(1)));
%         ntest=n;
%         itest=i;
            instats(n+bc-1,:)=[];
            bins1e(i)=bins1e(i)-binsoutlierI(i);
        end
        if bins1e(i)>4
            [LilltestInVelbyPos80(i),probin80(i)]= lillietest(instats(n:n+bins1e(i)-1,3)',signif);
        end


        StdInAngbyPos80(i) = std(instats(n:n+bins1e(i)-1,4));
        MeanInAngbyPos80(i) = mean(instats(n:n+bins1e(i)-1,4));
        StdInVelbyPos80(i) = std(instats(n:n+bins1e(i)-1,3));
        MeanInVelbyPos80(i) = mean(instats(n:n+bins1e(i)-1,3));
%               invelbypos80(:,i)= instats(n:n+bins2(i)-1,3);
        MeanInVelTbyPos80(i) = mean(instats(n:n+bins1e(i)-1,3).*cosd(instats(n:n+bins1e(i)-1,4)));
        StdInVelTbyPos80(i) = std(instats(n:n+bins1e(i)-1,3).*cosd(instats(n:n+bins1e(i)-1,4)));
        MeanInVelNbyPos80(i) = mean(instats(n:n+bins1e(i)-1,3).*sind(instats(n:n+bins1e(i)-1,4)));
        StdInVelNbyPos80(i) = std(instats(n:n+bins1e(i)-1,3).*sind(instats(n:n+bins1e(i)-1,4)));

        n = n+bins1e(i);
        if isnan(StdInAngbyPos80(i))==1
            StdInAngbyPos80(i)=0;
            MeanInAngbyPos80(i)=0;
            MeanInVelTbyPos80(i)=0;
            StdInVelTbyPos80(i)=0;
            MeanInVelNbyPos80(i)=0;
            StdInVelNbyPos80(i)=0;
            StdInVelbyPos80(i) = 0;
            MeanInVelbyPos80(i) =0;
        end
    end

%******************Rebounding 80deg**********************************
    clear bins bins2 bin_AbP bin_AbA

    StdRebAngbyPos80=zeros(1,130);
    MeanRebAngbyPos80=zeros(1,130);

    MeanRebVelbyPos80=zeros(1,130);
    StdRebVelbyPos80 = zeros(1,130);

    MeanRebVelTbyPos80 = zeros(1,130);
    StdRebVelTbyPos80=zeros(1,130);

    MeanRebVelNbyPos80 = zeros(1,130);
    StdRebVelNbyPos80=zeros(1,130);

    StdRebVelbyAng80=zeros(1,130);

    prob=zeros(1,130);

    bins=zeros(1,130);
    bins2=zeros(1,130);

    for i = 1:size(rebstats,1)
        if round(rebstats(i,4))>0
        bin_VbA = round(rebstats(i,4));
        bins(bin_VbA)=bins(bin_VbA)+1;
        end
        bin_AbP = round(rebstats(i,1));
        bin_AbP = bin_AbP+40;
        bins2(bin_AbP)=bins2(bin_AbP)+1;
    end
```

```
    %Calculating bin witdth for 2mm X direction bins for the Ratio Dist.
    bins2e=zeros(1,130);

    for i=1:mm:ceil(length(bins2))-1
       bins2e(ceil(i/mm))=bins2(i)+bins2(i+1);
    end
    n=1;
    for i=1: length(bins2e)

        if bins2e(i)>4   % this if statement removes outliers from the data set
%         if i>12 && i<=15
            clear bc
            Qr=quantile(rebstats(n:n+bins2e(i)-1,3),[0.25,0.75]);
            binsoutlierR(i)=length(find(rebstats(n:n+bins2e(i)-1,3)>=Qr(2)+K*(Qr(2)-Qr(1))...
            | rebstats(n:n+bins2e(i)-1,3)<=Qr(1)-K*(Qr(2)-Qr(1)) ));
            bc=find(rebstats(n:n+bins2e(i)-1,3)>=Qr(2)+K*(Qr(2)-Qr(1))...
            | rebstats(n:n+bins2e(i)-1,3)<=Qr(1)-K*(Qr(2)-Qr(1)));
            rebstats(n+bc-1,:)=[];

%             ntest=n;
%             itest=i;
            bins2e(i)=bins2e(i)-binsoutlierR(i);
%             figure
%             histfit(rebstats(n:n+bins2e(i)-1,3))
        end
        if bins2e(i)>4
            [LilltestRebVelbyPos80(i),probreb80(i)]= lillietest(rebstats(n:n+bins2e(i)-1,3)',signif);
        end



        StdRebAngbyPos80(i) = std(rebstats(n:n+bins2e(i)-1,4));
        MeanRebAngbyPos80(i) = mean(rebstats(n:n+bins2e(i)-1,4));
        StdRebVelbyPos80(i) = std(rebstats(n:n+bins2e(i)-1,3));
        MeanRebVelbyPos80(i) = mean(rebstats(n:n+bins2e(i)-1,3));
        MeanRebVelTbyPos80(i) = mean(rebstats(n:n+bins2e(i)-1,3).*cosd(rebstats(n:n+bins2e(i)-1,4)));
        StdRebVelTbyPos80(i) = std(rebstats(n:n+bins2e(i)-1,3).*cosd(rebstats(n:n+bins2e(i)-1,4)));
        MeanRebVelNbyPos80(i) = mean(rebstats(n:n+bins2e(i)-1,3).*sind(rebstats(n:n+bins2e(i)-1,4)));
        StdRebVelNbyPos80(i) = std(rebstats(n:n+bins2e(i)-1,3).*sind(rebstats(n:n+bins2e(i)-1,4)));

        n = n+bins2e(i);
        if isnan(StdRebAngbyPos80(i))==1
            StdRebAngbyPos80(i)=0;
            MeanRebAngbyPos80(i)=0;
            MeanRebVelTbyPos80(i)=0;
            StdRebVelTbyPos80(i)=0;
            MeanRebVelNbyPos80(i)=0;
            StdRebVelNbyPos80(i)=0;
            StdRebVelbyPos80(i) = 0;
            MeanRebVelbyPos80(i) =0;
        end
    end

     %Ratio Distribution calculations
    maxx=min(max(instats(:,1)),max(rebstats(:,1)))+40;
    minx=max(min(instats(:,1)),min(rebstats(:,1)))+40;
    cut=(maxx-minx)/20;

    z=(-2:.001:4);

    pdfN80=zeros(130,length(z));
    pdfT80=zeros(130,length(z));
    pdf80=zeros(130,length(z));
    corN80=zeros(130,1);
    corT80=zeros(130,1);
    cor80=zeros(130,1);
    corNStd80=zeros(130,1);
    corTStd80=zeros(130,1);
    corStd80=zeros(130,1);
    ww80=zeros(130,1);

    for i=1:length(MeanRebVelNbyPos80)
        if (i>=(minx+cut)/mm && i<=(maxx-cut)/mm && abs(MeanRebVelbyPos80(i))>0 ...
            && LilltestRebVelbyPos80(i)<1 && LilltestInVelbyPos80(i)<1)
            p=ratio_of_normalpdf(z,abs(MeanRebVelbyPos80(i)),StdRebVelbyPos80(i),...
            abs(MeanInVelbyPos80(i)),StdInVelbyPos80(i));
            pdf80(i,:)=p;
```

```
            p=ratio_of_normalpdf(z,abs(MeanRebVelNbyPos80(i)),StdRebVelNbyPos80(i),...
            abs(MeanInVelNbyPos80(i)),StdInVelNbyPos80(i));
            pdfN80(i,:)=p;

            p=ratio_of_normalpdf(z,abs(MeanRebVelTbyPos80(i)),StdRebVelTbyPos80(i),...
            abs(MeanInVelTbyPos80(i)),StdInVelTbyPos80(i));
            pdfT80(i,:)=p;

            [~,n]=max(pdf80(i,:));
            cor80(i)=z(n);

            [~,n]=max(pdfT80(i,:));
            corT80(i)=z(n);

            [~,n]=max(pdfN80(i,:));
            corN80(i)=z(n);

            cd=cumtrapz(z,pdf80(i,:));
            [~,n] = min(abs(cd-.158));
            corStd80(i)=cor80(i)-z(n);

            cd=cumtrapz(z,pdfT80(i,:));
            [~,n] = min(abs(cd-.158));
            corTStd80(i)=corT80(i)-z(n);

            cd=cumtrapz(z,pdfN80(i,:));
            [~,n] = min(abs(cd-.158));
            corNStd80(i)=corN80(i)-z(n);
        end
    end
vRatio80=bins2'./binsIN';
for i=1:130
    if cor80(i)<=0
        ww80(i) = i;
    end
end
if (length(instats)> length(rebstats))
    RebCor80=corr(instats([1:length(rebstats)],3),rebstats(:,3));
else
    RebCor80=corr(rebstats([1:length(instats)],3),instats(:,3));
end

MeanInAng80=MeanInAngbyPos80;
MeanInVel80=MeanInVelbyPos80;
MeanInVel80(find(ww80)) = [];
MeanInAng80(find(ww80)) = [];
cor80(find(ww80))=[];
corN80(find(ww80))=[];
corT80(find(ww80))=[];
corStd80(find(ww80))=[];
corNStd80(find(ww80))=[];
corTStd80(find(ww80))=[];
vRatio80(find(ww80))=[];
clear n
REBRATIOa80 = mean(vRatio80);
REBRATIO80 = length(rebstats)/sum(binsINr);
REBRATIOr80 = RebNum80deg./binsINr;
LillTotal(1,6)=sum(LilltestInVelbyPos80);
LillTotal(2,6)=sum(LilltestRebVelbyPos80);
end



%% OVERALL CALCULATIONS WITH RATIO DISTRIBUTION COR
clear fit PLCoef
arb90=1:1:90;
MeanInAng=[];
cor =[];
corN=[];
corT=[];
corStd=[];
corNStd=[];
corTStd=[];

PLCoef=zeros(9,3);

REBratioCompiled=cat(1,REBRATIO30,REBRATIO40,REBRATIO50,REBRATIO60,...
    REBRATIO70,REBRATIO80);
```

```
MeanInAng=cat(2,MeanInAng30, MeanInAng40, MeanInAng50, MeanInAng60,...
    MeanInAng70,MeanInAng80);
MeanInVel=cat(2,MeanInVel30, MeanInVel40, MeanInVel50, MeanInVel60,...
    MeanInVel70,MeanInVel80);
RebCorComp=cat(1,RebCor30, RebCor40, RebCor50, RebCor60,...
    RebCor70,RebCor80);
cor=cat(1,cor30,cor40,cor50,cor60,cor70,cor80);
corN=cat(1,corN30,corN40,corN50,corN60,corN70,corN80);
corT=cat(1,corT30,corT40,corT50,corT60,corT70,corT80);
corStd=cat(1,corStd30,corStd40,corStd50,corStd60,corStd70,corStd80);
corNStd=cat(1,corNStd30,corNStd40,corNStd50,corNStd60,corNStd70,corNStd80);
corTStd=cat(1,corTStd30,corTStd40,corTStd50,corTStd60,corTStd70,corTStd80);
MeanInAngWo80=cat(2,MeanInAng30, MeanInAng40, MeanInAng50, MeanInAng60,...
    MeanInAng70);
corTWo80=cat(1,corT30,corT40,corT50,corT60,corT70);
corTStdWo80=cat(1,corTStd30,corTStd40,corTStd50,corTStd60,corTStd70);
MeanInAngWo80=MeanInAngWo80';

MeanInAng=MeanInAng';
MeanInVel=MeanInVel';
%Power Law Fits
%Combined COR
f=fit(MeanInAng,cor,'power1');
PLCoef(1,[1,2])=coeffvalues(f);
meanCOR=feval(f,arb90);
%Mean COR Standard Deviations
f=fit(MeanInAng,cor-corStd,'power1');
PLCoef(2,[1,2])=coeffvalues(f);
meanCOR_minusStd=feval(f,arb90);
f=fit(MeanInAng,cor+corStd,'power1');
PLCoef(3,[1,2])=coeffvalues(f);
meanCOR_plusStd=feval(f,arb90);

% % tan COR fit with out 80deg data
% f=fit(MeanInAngWo80,corTWo80,'power2');
% meanCOR_t=feval(f,arb90);
% %Tangential COR Standard Deviations
% f=fit(MeanInAngWo80,corTWo80-corTStdWo80,'power2');
% meanCOR_t_minusStd=feval(f,arb90);
% f=fit(MeanInAngWo80,corTWo80+corTStdWo80,'power2');
% meanCOR_t_plusStd=feval(f,arb90);

% tan COR fit
f=fit(MeanInAng,corT,'power1');
PLCoef(4,[1,2])=coeffvalues(f);
meanCOR_t=feval(f,arb90);
%Tangential COR Standard Deviations
f=fit(MeanInAng,corT-corTStd,'power2');
PLCoef(5,:)=coeffvalues(f);
meanCOR_t_minusStd=feval(f,arb90);
f=fit(MeanInAng,corT+corTStd,'power2');
PLCoef(6,:)=coeffvalues(f);
meanCOR_t_plusStd=feval(f,arb90);

% normal COR fit
f=fit(MeanInAng,corN,'power1');
PLCoef(7,[1,2])=coeffvalues(f);
meanCOR_n=feval(f,arb90);
%Normal COR Standard Deviations
f=fit(MeanInAng,corN-corNStd,'power1');
PLCoef(8,[1,2])=coeffvalues(f);
meanCOR_n_minusStd=feval(f,arb90);
f=fit(MeanInAng,corN+corNStd,'power1');
PLCoef(9,[1,2])=coeffvalues(f);
meanCOR_n_plusStd=feval(f,arb90);

% %Polynomial Fit
% Ord=2; %Order of Curve Fit
% % Mean COR
% [COR_polycoefftest, ~] = polyfit(MeanInAng, cor, Ord);
% fit_c = polyval(COR_polycoefftest,MeanInAng);
% % tan COR poly fit
% [TanCOR_polycoeff, ~] = polyfit(MeanInAng, corT, Ord);
% fit_t = polyval(TanCOR_polycoeff,MeanInAng);
% % normal COR poly fit
% [NormCOR_polycoeff, S] = polyfit(MeanInAng, corN, Ord);
% fit_n = polyval(NormCOR_polycoeff,MeanInAng);
% %Mean COR Standard Deviations
% [COR_polycoefftest, S] = polyfit(MeanInAng, cor-corStd, Ord);
% fit_minusStd = polyval(COR_polycoefftest,MeanInAng);
```

```
% [COR_polycoefftest, S] = polyfit(MeanInAng, cor+corStd, Ord);
% fit_plusStd = polyval(COR_polycoefftest,MeanInAng);
% %Normal COR Standard Deviations
% [COR_polycoefftest, S] = polyfit(MeanInAng, corN-corNStd, Ord);
% fit_minusNStd = polyval(COR_polycoefftest,MeanInAng);
% [COR_polycoefftest, S] = polyfit(MeanInAng, corN+corNStd, Ord);
% fit_plusNStd = polyval(COR_polycoefftest,MeanInAng);
% %Tangential COR Standard Deviations
% [COR_polycoefftest, S] = polyfit(MeanInAng, corT-corTStd, Ord);
% fit_minusTStd = polyval(COR_polycoefftest,MeanInAng);
% [COR_polycoefftest, S] = polyfit(MeanInAng, corT+corTStd, Ord);
% fit_plusTStd = polyval(COR_polycoefftest,MeanInAng);
% [b, i , j] = unique(MeanInAng);
% % Mean COR
% meanCOR = interp1(b, fit_c(i), arb90);
% meanCOR_minusStd = interp1(b, fit_minusStd(i), arb90);
% meanCOR_plusStd = interp1(b, fit_plusStd(i), arb90);
% % Tangential COR
% meanCOR_t = interp1(b, fit_t(i), arb90);
% meanCOR_t_minusStd = interp1(b, fit_minusTStd(i), arb90);
% meanCOR_t_plusStd = interp1(b, fit_plusTStd(i), arb90);
% % Normal COR
% meanCOR_n = interp1(b, fit_n(i), arb90);
% meanCOR_n_minusStd = interp1(b, fit_minusNStd(i), arb90);
% meanCOR_n_plusStd = interp1(b, fit_plusNStd(i), arb90);

%BY VELOCITY

% Mean COR
[COR_polycoefftestV, ~] = polyfit(MeanInVel, cor, Ord);
fitV = polyval(COR_polycoefftestV,MeanInVel);

% tan COR poly fit
[TanCOR_polycoeffV, ~] = polyfit(MeanInVel, corT, Ord);
fit_tV = polyval(TanCOR_polycoeffV,MeanInVel);

% normal COR poly fit
[NormCOR_polycoeffV, S] = polyfit(MeanInVel, corN, Ord);
fit_nV = polyval(NormCOR_polycoeffV,MeanInVel);

%Mean COR Standard Deviations
[COR_polycoefftest, S] = polyfit(MeanInVel, cor-corStd, Ord);
fit_minusStdV = polyval(COR_polycoefftest,MeanInVel);

[COR_polycoefftest, S] = polyfit(MeanInVel, cor+corStd, Ord);
fit_plusStdV = polyval(COR_polycoefftest,MeanInVel);

%Normal COR Standard Deviations
[COR_polycoefftest, S] = polyfit(MeanInVel, corN-corNStd, Ord);
fit_minusNStdV = polyval(COR_polycoefftest,MeanInVel);

[COR_polycoefftest, S] = polyfit(MeanInVel, corN+corNStd, Ord);
fit_plusNStdV = polyval(COR_polycoefftest,MeanInVel);

%Tangential COR Standard Deviations
[COR_polycoefftest, S] = polyfit(MeanInVel, corT-corTStd, Ord);
fit_minusTStdV = polyval(COR_polycoefftest,MeanInVel);

[COR_polycoefftest, S] = polyfit(MeanInVel, corT+corTStd, Ord);
fit_plusTStdV = polyval(COR_polycoefftest,MeanInVel);

[b, i , j] = unique(MeanInVel);
maxv=ceil(max(inmag_totals));
arb_V = [maxv-15:1:maxv+15];
% Mean COR
meanCORV = interp1(b, fitV(i), arb_V);
meanCOR_minusStdV = interp1(b, fit_minusStdV(i), arb_V);
meanCOR_plusStdV = interp1(b, fit_plusStdV(i), arb_V);
% Tangential COR
meanCOR_tV = interp1(b, fit_tV(i), arb_V);
meanCOR_t_minusStdV = interp1(b, fit_minusTStdV(i), arb_V);
meanCOR_t_plusStdV = interp1(b, fit_plusTStdV(i), arb_V);
% Normal COR
meanCOR_nV = interp1(b, fit_nV(i), arb_V);
meanCOR_n_minusStdV = interp1(b, fit_minusNStdV(i), arb_V);
meanCOR_n_plusStdV = interp1(b, fit_plusNStdV(i), arb_V);

% plot(arb90,meanCOR,arb90,meanCOR_plusStd,'-b',arb90,meanCOR_minusStd,'-b',MeanInAng,cor,'r*')
```

```
% Aggragate all needed vectors for easy of exportation
clear Aggragate
Aggragate(1,:)=arb90;
Aggragate(2,:)=meanCOR;
Aggragate(3,:)=meanCOR_plusStd;
Aggragate(4,:)=meanCOR_minusStd;
Aggragate(5,:)=meanCOR_n;
Aggragate(6,:)=meanCOR_n_plusStd;
Aggragate(7,:)=meanCOR_n_minusStd;
Aggragate(8,:)=meanCOR_t;
Aggragate(9,:)=meanCOR_t_plusStd;
Aggragate(10,:)=meanCOR_t_minusStd;
Aggragate=Aggragate';

clear AggragateRaw
AggragateRaw(1,:)=MeanInAng;
AggragateRaw(2,:)=cor;
AggragateRaw(3,:)=corStd;
AggragateRaw(4,:)=corN;
AggragateRaw(5,:)=corNStd;
AggragateRaw(6,:)=corT;
AggragateRaw(7,:)=corTStd;
AggragateRaw=AggragateRaw';

save('aggragate.txt','Aggragate','-ASCII');



%% COR Plots

maxv=ceil(max(inmag_totals));
%plot versus angle
figure; hold all
axis([0 90 -1 3]);
set(gca, 'FontSize', 20)
plot(MeanInAng, corT, 'Line', 'none',...
    'Marker', '*', 'MarkerSize', 6, 'Color', 'g')
plot(arb90, meanCOR_t, 'k', 'Linewidth', 5)
% plot(arb90, meanCORtbin, '*r')
plot(arb90, meanCOR_t_plusStd, 'k-.', 'Linewidth', 5)
plot(arb90, meanCOR_t_minusStd, 'k-.', 'Linewidth', 5)
xlabel('Angle of Impact'); ylabel('COR tangential')
legend('COR Data by Location','Mean', ' Mean \pm \sigma', 'Location', 'Best')
hold off

figure; hold all
axis([0 90 0 2]);
set(gca, 'FontSize', 20)
plot(MeanInAng, corN, 'Line', 'none',...
    'Marker', '*', 'MarkerSize', 6, 'Color', 'g')
plot(arb90, meanCOR_n, 'k', 'Linewidth', 5)
% plot(arb90, meanCORnbin, '*r')
plot(arb90, meanCOR_n_plusStd, 'k-.', 'Linewidth', 5)
plot(arb90, meanCOR_n_minusStd, 'k-.', 'Linewidth', 5)
xlabel('Angle of Impact'); ylabel('COR normal')
legend('COR Data by Location',' Mean', ' Mean \pm \sigma', 'Location', 'Best')
hold off

stdmeanp2=meanCOR+2*(meanCOR_plusStd-meanCOR);
stdmeanm2=meanCOR-2*(meanCOR-meanCOR_minusStd);
stdmeanp3=meanCOR+3*(meanCOR_plusStd-meanCOR);
stdmeanm3=meanCOR-3*(meanCOR-meanCOR_minusStd);

figure; hold all
set(gca, 'FontSize', 20, 'FontName', 'Helvetica')
axis([15 90 0 1.5]);
a1=plot(MeanInAng, cor, 'Line', 'none',...
    'Marker', '*', 'MarkerSize', 6, 'Color', 'g');
a2=plot(arb90, meanCOR, 'k', 'Linewidth', 5);
a3=plot(arb90, meanCOR_plusStd, 'k-.', 'Linewidth', 5);
plot(arb90, meanCOR_minusStd, 'k-.', 'Linewidth', 5)

% a4=plot(arb90, stdmeanp2, 'b-.', 'Linewidth', 5);
% plot(arb90, stdmeanm2, 'b-.', 'Linewidth', 5)
% a5=plot(arb90, stdmeanp3, 'r-.', 'Linewidth', 5);
% plot(arb90, stdmeanm3, 'r-.', 'Linewidth', 5)
xlabel('Angle of Impact'); ylabel('COR')
```

```
% legend('ARD 10-20{\mu}m Data', ' Mean',...
%     ' Mean \pm \sigma', 'Location', 'Best')
legend([a1,a2,a3], 'COR Data by Location',' Mean', ' Mean \pm \sigma', 'Mean \pm 2\sigma',' Mean \pm 3\sigma',
'Location', 'Best')
% legend([a1,a2,a3,a4,a5],'ARD 20-40{\mu}m Data', ' Mean', ' Mean \pm \sigma', 'Mean \pm 2\sigma',' Mean \pm
3\sigma', 'Location', 'Best')
hold off

%plot vs velocity component
figure; hold all
set(gca, 'FontSize', 20, 'FontName', 'Helvetica')
axis([0 maxv+15 0 2]);
plot(MeanInVel, corT, 'Line', 'none',...
    'Marker', '*', 'MarkerSize', 6, 'Color', 'g')
plot(arb_V, meanCOR_tV, 'k', 'Linewidth', 5)
% plot(arb90, meanCORbin, '*r')
% plot(arb90, std_pred_plus, 'k-.', 'Linewidth', 5)
% plot(arb90, std_pred_minus, 'k-.', 'Linewidth', 5)
xlabel('Tangential Impact Velocity'); ylabel('COR Tangential')
legend('COR Data by Location', ' Mean',...
    ' Mean \pm \sigma', 'Location', 'Best')
hold off

figure; hold all
axis([0 maxv+15 0 2]);
set(gca, 'FontSize', 20)
plot(MeanInVel, corN, 'Line', 'none',...
    'Marker', '*', 'MarkerSize', 6, 'Color', 'g')
plot(arb_V, meanCOR_nV, 'k', 'Linewidth', 5)
% plot(arb90, meanCORnbin, '*r')
% plot(arb90, std_pred_plus_n, 'k-.', 'Linewidth', 5)
% plot(arb90, std_pred_minus_n, 'k-.', 'Linewidth', 5)
xlabel('Normal Impact Velocity'); ylabel('COR Norm')
legend('COR Data by Location', ' Mean',...
    ' Mean \pm \sigma', 'Location', 'Best')
hold off
```